# MAGNETRON SPUTTERING OF THIN NITRIDE FILMS

**Presented by**

**PRASHANTHI VENEETHA KOLA**

**as the fulfilment of the requirement for the degree of**

**DOCTOR OF PHILOSOPHY**

**at**

**DUBLIN CITY UNIVERSITY**

**SCHOOL OF MECHANICAL & MANUFACTURING ENGG.**

**ACADEMIC SUPERVISORS:** **Prof. M.S.J. Hashmi**
**Dr. D.C. Cameron**

**SEPTEMBER 1995**

## DECLARATION

**I declare that all the unreferred work described in this thesis is entirely my own, and no portion of the work contained in this thesis has been submitted in support of an application for another degree or qualification of this or any other university or other institute of learning.**

SIGNED: Prashanthi V. Kola

**Prashanthi Veneetha Kola**

**I.D Number** 91700094

**To Dr. Prasuna Reddy Kola and Mr. Prabhakara Reddy Kola F.R.C.S.**
**(or Mom and Dad)**

**You who encouraged me to read and question, to seek**
**and to strive, I owe so much.**

***I do not know how I may appear to the world, but to myself I seem to have been only a boy playing on the sea-shore, and diverting myself in now and then finding a smoother pebble or a prettier shell than ordinary, whilst the great ocean of truth lay all undiscovered before me.***

*- Newton (1831).*

# ACKNOWLEDGEMENTS

My first vote of thanks must go to Dr. David Cameron, a man for whom I have the greatest respect and admiration. His guidance and supervision was invaluable. I am extremely grateful for all the advice and suggestions given towards the problems solved. I am privileged to have worked with you.

To Prof. M.S.J. Hashmi, I extend my gratitude for enabling me the opportunity to learn, and for the responsibility I was allowed to have on the project. My sincere thanks to him for all the direction and guidance given to me in the past four years.

Stephen Daniels, whose work towards commissioning the rig was a vital link to the project, deserves a special note of thanks.

To the two technicians - Mr. Liam Domican and Mr. Martin Johnson, whose technical support speeded things up considerably, my special thanks for doing more than was expected of them.

Lesley, Ian, Tommy, Stuart and Paul all deserve a thanks, not forgetting the school of electronic engineering, who put up with my constant raids on their supplies. To my fellow research students in D.C.U. - David Kennedy, Abdul Majid Hamouda, Muksad Helali, Michael Murphy, and the countless others, I appreciate their help and support.

Thanks also are due to my colleagues now - Denis, Tom, Kevin, Anthony and everyone else in Forbairt for encouraging me during this last furlong. I would also like to acknowledge Materials Ireland for funding this research, and the Ceramics Research Centre in Forbairt for enabling my use of several analytical tools as I put the finishing touches on the thesis.

My gratitude is also extended to Dr. David Doff (T.C.D.), Dr. Brian Lawless (D.C.U.), Dr. Brian Meenan (NIBEC) and Mr. Kaj Pischow for their analytical expertise.

My most sincere gratitude is extended to my parents and my brother, who have given their utmost support to all that I have tried to do. I can't ever repay them enough. Thanks for always encouraging me to learn, and I hope there's room in the family for one more doctorate!

Thank you.

Prashanthi V. Kola, August 1995.

# TABLE OF CONTENTS

| | | PG |
|---|---|---|
| **Abstract** | | 5 |
| **Bibliography of Abbreviations** | | 7 |
| **Chapter 1** | **Introduction** | 8 |
| **Chapter 2** | **Magnetron Sputtering** | 11 |
| 2.1 | Introduction | 11 |
| 2.2 | Deposition Technique - PVD vs. CVD | 11 |
| 2.3 | Sputtering | 13 |
| 2.3.1 | Magnetron Sputtering | 14 |
| 2.3.2 | Magnetrons | 15 |
| 2.3.3 | Unbalanced Magnetrons | 15 |
| 2.4 | Film Microstructure | 18 |
| 2.4.1 | Structural Zone Models | 18 |
| 2.4.2 | Ion Bombardment | 20 |
| 2.4.3 | Residual/Internal Stress | 21 |
| 2.4.4 | Substrate-Film Adhesion | 22 |
| 2.4.5 | Substrate Effects | 24 |
| **Chapter 3** | **Magnetron Sputtering Deposition System** | |
| 3.1 | Introduction | 33 |
| 3.1.1 | Equipment | 33 |
| 3.1.2 | Vacuum Chamber | 34 |
| 3.1.3 | Substrate Holder | 35 |
| 3.2 | Target Poisoning | 36 |
| 3.2.1 | Feedback Loop | 37 |

| | | |
|---|---|---|
| 3.3 | Pumpdown | 38 |
| 3.4 | Magnetrons | 38 |
| 3.4.1 | Closed Field System | 39 |

**Chapter 4 Measurement Techniques**

| | | |
|---|---|---|
| 4.1 | Introduction | 52 |
| 4.2 | Film Hardness | 52 |
| 4.2.1 | Vickers Hardness | 52 |
| 4.2.2 | Berkovich Hardness | 54 |
| 4.2.3 | Knoop Hardness | 54 |
| 4.3 | Film Thickness | 55 |
| 4.3.1 | Surface Profilometry and Thickness | 55 |
| 4.3.2 | Interferometry | 56 |
| 4.3.3 | Thickness - Ball Cratering | 57 |
| 4.4 | Wear - Abrasive Wheel | 58 |
| 4.5 | Friction - Pin-on-disk | 58 |
| 4.6 | Electrographic Printing | 59 |
| 4.7 | Ellipsometry | 60 |
| 4.8 | Infra-Red (IR) Spectroscopy | 62 |
| 4.9 | Raman Spectroscopy | 63 |
| 4.10 | X-Ray Diffraction | 63 |
| 4.11 | X-Ray Photoelectron Spectroscopy (XPS) | 64 |
| 4.12 | Atomic Force Microscopy (AFM) | 65 |
| 4.13 | Secondary Ion Mass Spectroscopy (SIMS) | 66 |

**Chapter 5 Magnetron Sputtered Titanium (Ti) and Titanium Nitride (TiN)**

| | | |
|---|---|---|
| 5.1 | Initial Commissioning | 76 |
| 5.2 | Current - Voltage Characteristic Curve | 77 |

| | | |
|---|---|---|
| 5.3 | TiN - Introduction | 77 |
| 5.3.1 | TiN - Wear Resistance | 78 |
| 5.3.2 | TiN - Tribological Properties | 78 |
| 5.3.3 | TiN - Crystal Structure | 79 |
| 5.3.4 | TiN - Film Microstructure | 80 |
| 5.3.5 | Hardness | 81 |
| 5.3.6 | Colour | 82 |
| 5.4 | Biocompatible Materials | 82 |
| 5.5 | TiN Biocompatible Coatings | 84 |
| 5.6 | Metallic Corrosion | 85 |
| 5.6.1 | Electrochemical Series | 85 |
| 5.6.2 | Corrosion Testing | 86 |
| 5.7 | Experimental Procedure | 87 |
| 5.8 | Experimental Data | 88 |
| 5.9 | Results | 88 |
| 5.10 | Discussion | 89 |

**Chapter 6 Carbon Nitride ($CN_x$) Deposition**

| | | |
|---|---|---|
| 6.1 | Introduction | 104 |
| 6.2 | Experimental Procedure | 106 |
| 6.3 | Results | 107 |
| 6.3.1 | Hardness | 107 |
| 6.3.2 | Ellipsometry | 108 |
| 6.3.3 | Infra-Red (IR) Spectroscopy | 109 |
| 6.3.4 | X-Ray Diffraction (XRD) | 110 |
| 6.3.5 | X-Ray Photoelectron Spectroscopy (XPS) | 111 |
| 6.3.6 | Raman Spectroscopy | 115 |

6.3.7 Atomic Force Microscopy (AFM), Surface Roughness, Secondary Ion Mass Spectroscopy (SIMS), and Resistivity 116
6.4 Discussion 117

**Chapter 7 $CN_x$ Deposition on Steel**

7.1 Introduction 140
7.2 Experimental Parameters 140
7.3 Results 141
7.3.1 Hardness 141
7.3.2 Thickness 142
7.3.3 Friction and Wear 143
7.4 Discussion 144

**Chapter 8 Conclusions**

8.1 Conclusions - TiN Biocompatible Coatings 151
8.2 Conclusions - $CN_x$ Thin Films 154
8.3 Recommended Work 156

**Appendix A** Glow Discharge Phenomenon A1

**Appendix B** Chamber and Peripheral Equipment Drawings A7

**Appendix C** Operational and Safety Procedure A26

**References** R1

**Published Work** P1

**ABSTRACT**

**Magnetron Sputtering of Thin Nitride Films**

**by**

**Prashanthi Veneetha Kola**

The objective in this investigation was to design and commission a magnetron sputter deposition system and investigate the properties of hard coatings for mechanical and biomedical applications. The deposition of titanium (Ti) and titanium nitride (TiN) was undertaken as part of the commissioning tests and further work was conducted on the effect of the deposition parameters on the properties of TiN, specifically for biocompatible applications. A thorough understanding of the deposition process, film microstructure and sample preparation was achieved, and several measurement techniques utilised in the characterisation of the films. The nature of TiN as a biocompatible coating, and the effect of the deposition parameters on the hermeticity of the film was investigated by using electrographic printing as a technique for observing the pinhole defects on the film surface. It was found however, that the fluid used in the printing method caused corrosion of the substrate material and hence may have caused increased pinhole size.

The second topic of investigation was the novel film carbon nitride ($CN_x$), a new and promising coating in the area of tribological coatings. Investigations were undertaken to deposit the theoretical coating $\beta$-$C_3N_4$, a material harder than diamond. The understoichiometric $CN_x$ form was deposited successfully, and the films characterised optically, structurally, compositionally and topographically. An investigation of the effect of the deposition parameters - magnetron current, substrate bias, system pressure and nitrogen partial pressure on film properties revealed that the films were amorphous in nature with nitrogen incorporation of upto 18.5 % atomic. The films showed evidence of carbon bonding ,as detected by infra-red spectroscopy. It was also found that increased graphitic bonding occurred during nitrogen partial pressure increase but that a reduction in the graphitic nature

was seen for films deposited at high magnetron current, low system pressure and high negative substrate bias, all of which affect the ion bombardment of the film. The film surface was smooth and featureless and brown in colour.

Tribological evaluation was undertaken of carbon nitride films deposited onto tool steel and surgical steel. It was found that the films possessed low coefficients of friction and good wear resistance, but these properties were dependent on the substrate material due to the thinness of the films. An investigation of adhesion promoted by interlayer growth was also conducted, and it was found for carbon nitride coatings on steel substrates, that Ti and TiN interlayers promoted adhesion, but there was no advantage in a TiC interlayer. Carbon nitride has good tribological properties, and could possibly be used in both mechanical and biomedical applications.

## BIBLIOGRAPHY OF ABBREVIATIONS

| | |
|---|---|
| PVD | Physical Vapour Deposition |
| CVD | Chemical Vapour Deposition |
| IR | Infra-Red (Spectroscopy) |
| XRD | X-Ray Diffraction |
| XPS | X-Ray Photoelectron Spectroscopy |
| AFM | Atomic Force Microscopy |
| SIMS | Secondary Ion Mass Spectroscopy |
| PACVD | Plasma Assisted Chemical Vapour Deposition |
| PAPVD | Plasma Assisted Physical Vapour Deposition |
| SZM | Structural Zone Models |
| HV | Vickers Hardness |
| PTFE | Polytetraflouroethane |
| HK | Knoop Hardness |
| HB | Berkovich Hardness |
| f.c.c. | Face-centred-cubic |
| UHMWPE | Ultra-high-molecular-weight-polyethylene |
| IBD | Ion Beam Deposition |
| IVD | Ion and Vapour Deposition |
| PECVD | Plasma Enhanced Chemical Vapour Deposition |
| EELS | Electron Energy Loss Spectroscopy |
| B.E. | Binding Energy |
| FWHM | Full Width at Half Maximum |
| DLC | Diamond Like Carbon |

# Chapter 1

# Introduction

# Chapter 1 Introduction

An interest in materials and material properties led to the commencement of this project at the Advanced Materials Processing Centre. Thin film technology was a facet of engineering not previously introduced in any great detail during undergraduate years, and this, coupled with an interest in learning a very practical field of science was the catalyst in starting on this long road.

The demands on the performance of components are ever-increasing, and homogenous materials are often unable to meet all the necessary requisites. Such a requirement of enhanced properties resulted in the development of coatings for the following applications:

corrosion resistance
thermal barrier properties
biocompatible applications
electronic applications
optical applications
decorative applications
tribological properties etc.

From a mechanical engineering viewpoint, reasons to coat cutting tools in a production situation include the need to increase tool life, to improve the surface quality of the product and to increase the production rate [1]. Of specific interest were the protective properties of coatings for biomedical use.

The objective of the work conducted at the Advanced Materials Processing Centre was to gain an understanding of vacuum technology, magnetron sputtering as a thin film deposition technique to deposit new and novel coatings, and to understand the analytical tools used in the characterisation of thin films. Initially, the project was started by undertaking a literature review of the deposition process, equipment, and typical operational parameters. Since the design of

the vacuum chamber was to be a large part of the project, much time was spent liaising with both supervisors and suppliers. One of the most fundamental aspects of the chamber design was the versatility required in a research environment. The peripheral equipment was purchased, and upon delivery of the chamber, the system was assembled. Initial tests to evaluate the operating parameters of the chamber and magnetrons were conducted. As proficiency in the use of the system increased, a specific coating, titanium nitride (TiN), was chosen to aid commissioning, as published results were readily available in literature in order to provide bench-marks against which to commission the sputtering system.

Once stoichiometric TiN had been successfully deposited, with properties comparable to those in literature, an investigation into the function of TiN as a protective biomedical coating was initiated. A literature review found that TiN was indeed biocompatible, and already in use in dental applications. However, it was found that a coating is only as good as its weakest point - the defects on the film surface. A method of pinhole defect visualisation was chosen from literature, and an experiment designed to investigate the effect of the deposition parameters on pinhole density. Samples were corroded in a solution similar to saliva.

As a result of this work, and from literature examination, it was found that of key importance was the metallic ion leaching prevalent in metal prostheses implanted into the body. A coating comprising non-metallic elements should therefore be of better biocompatibility that even TiN. In the subsequent literature search, a theoretical coating was in the developmental process, possessing hardness values in excess that of diamond, and comprising only carbon and nitrogen. This coating, in its stoichiometric form ($\beta C_3N_4$) had not yet been deposited, and little published information regarding the sub-stoichiometric version of carbon nitride ($CN_x$) was available. In pursuit of this superhard coating, initial reviews found that magnetron sputtering had been successfully employed in the deposition of carbon nitride. In addition, the availability of a high-purity graphite target was abundant.

Initial experiments were undertaken to characterise the carbon nitride coating in greater detail that had been found in literature, and so the films deposited were investigated optically, structurally, compositionally, and topographically with respect to the deposition parameters. Hardness values proved to be promising, and subsequent experiments on steel samples specifically for mechanical and biomedical use were examined tribologically and show that carbon nitride possess high wear resistance and low coefficient of friction. Although stoichiometric carbon nitride was not achieved, much detailed information regarding the characteristics of carbon nitride films has been gathered, and may provide a good stepping-stone for further research in this area.

# Chapter 2

# Magnetron Sputtering

# Chapter 2 Magnetron Sputtering

## 2.1 Introduction

A brief overview of the deposition technique used in this research is outlined below. It is one of several techniques currently in practice in the deposition of thin films and each has its own advantages. Primarily, the chosen technique should address the substrate material constraints, the rate of deposition and the reproducibility of results.

## 2.2 Deposition Technique - Physical Vapour Deposition (PVD) vs. Chemical Vapour Deposition (CVD)

In general, deposition processes may be principally divided into two main categories

1. those involving droplet transfer (e.g. plasma/arc spraying, detonation gun coating)
2. those involving atomic/molecular transfer mode (e.g. Physical Vapour Deposition (PVD), Chemical Vapour Deposition (CVD), electrodeposition)

All three atomic deposition processes involve a three-step sequence

1. the creation of the flux or particles of the source material

2. the transport of the species created from the source to the substrate

3. film growth at the substrate

The most commonly used deposition techniques for thin film deposition are Physical Vapour Deposition (PVD) and Chemical Vapour Deposition (CVD). Typical coating thicknesses vary from 1-10μm for PVD coatings and higher for CVD coatings [2].

In PVD, each of the three steps in the deposition process (particularly steps 1 and 3) can be controlled independently by varying the deposition parameters (e.g. cathode current, system pressure and substrate bias). A fundamental characteristic of PVD technology is that one or more of the reaction species undergoes sublimation from the solid or liquid phase to the vapour phase. This creation of flux from the source material can occur either by evaporation of the source material or by sputtering, which will be discussed later.

In CVD processes, all three steps in the deposition sequence occur simultaneously at the substrate and cannot be independently controlled. Primarily, the source flux is from a gaseous phase, and a chemical reaction takes place at the heated substrate. Substrates can be heated resistively, radiantly, or directly using a hot plate, but CVD is, in essence, a thermally-activated deposition process. Typical substrate temperatures are 800°C, and reactions are endothermic (or absorb heat energy) and tend to completion with increased temperature at the substrate. Little bombardment of the substrate takes place during film growth, hence the films have large-angled grain boundaries, as described later, resulting in softer coatings compared to PVD. In Plasma Assisted CVD (PACVD), the plasma serves only to produce chemically active species that subsequently react via conventional chemical pathways. Electron kinetic energy instead of thermal energy is now used as the driving force, hence reaction temperatures are much reduced, but still remain higher than PVD processes.

The main disadvantage associated with CVD is the high substrate temperature (>600 °C) required for many coatings. This can result in the softening and distortion of (e.g. high speed steel at ≈400°C) substrates. This can anneal out any beneficial compressive stresses in the uncoated tools. However, PVD techniques, in conjunction with plasma assistance results in coating deposition at temperatures below the softening temperature (≈ 400 °C) for high speed

steels, thus leaving the stress state of the substrate unaffected and eliminating any need for post-coating treatment.

The reader is referred to Bunshah [3], Vossen and Kern [4] and Scheugraf [5], for a comprehensive documentation of deposition techniques and their respective merits.

## 2.3 Sputtering

Sputtering is one method of creating the flux of source material in a PVD process. Although sputtering by ionic bombardment existed as early as the 1800's [6], the practical application of the sputtering phenomenon in the field of surface engineering did not emerge until the 1930's [7]. Evaporative source PVD technology, known as ion plating, was devised by Mattox [8] in the 1960's.

In sputtering, the creation of the condensable species occurs through the bombardment of the target material by positive ions of an inert gas (e.g. Argon) and ejection of atoms of the target by momentum transfer, *figure 2.1*. A typical sputtering system is depicted in *figure 2.2*. A brief review of glow discharge phenomena, which results when a high potential is applied between an anode and a cathode, resulting in ionisation of a gas (i.e. a plasma is generated), is given in Appendix A. The positively charged ions are accelerated towards the negatively biased cathode target, overcome the binding energy of the atoms in the target material, and hence cause ejection of these atoms which travel across the electrode separation distance and are deposited on the substrate. This release of particles from the surface of the cathode is due to the fact that sputtering typically utilises kinetic energies in the range 10-100 eV, whereas the atoms of the surface of a solid are bonded with (sublimation) energies of typically, 2-10 eV. Typical energies of sputtered atoms ejected from the target are in the range 10-40 eV or upto 100 eV in magnetron processes [9].

This sputtering mechanism allows some important effects to occur :

- the surface of the target can be cleaned of undesirable species prior to coating by a process called sputter etching.

- the continuous redistribution of surface coating atoms during film growth, which can aid film densification. The increased energy imparted to the surface atoms of the film causes increased adatom mobility, which aids in the "filling-in" of holes/pores on the film surface, thereby increasing the density of the film.

The target is generally a plate of the material to be deposited, either elemental or compound. Where heterogeneous materials are deposited, the other constituent is usually in the form of a reactive gas. The target flux interacts with the reactive gas and forms a film of the compound on the substrate surface. The stoichiometry of the deposited film can be closely controlled by varying the partial pressure of the reactive gas.

The advantages of reactive deposition are that many complex compounds can be formed using relatively standard metallic targets and that both conducting and insulating compounds can be deposited by sputtering (see Appendix A). It is generally thought that in reactive sputtering, the target material is atomistically ejected by momentum transfer and it is on the film surface that the main reaction resulting in film formation occurs [9]. Hence reactive sputtering is predominantly a surface effect, as evidenced by both film growth on the substrate and by the poisoning effect on the surface of the target, which will be discussed later.

### 2.3.1 Magnetron Sputtering

Magnetron Sputtering is one such plasma assisted PVD (PAPVD) technique, and was the one employed in the investigations undertaken, due to the ease of independent control of the deposition parameters, which is an important consideration in a research environment. Another advantage was the relative ease and cost at which target (or source) material could be obtained.

### 2.3.2 Magnetrons

A magnetron sputtering system is basically a diode structure, in which magnets are used in conjunction with the cathode surface to form electron traps which are configured so that the drift motion of an electron in an E x B field is confined in a closed loop path until ionising collisions occur. The electric (E) field is perpendicular to the cathode surface, and the magnetic field (B) emanates from the north pole to the south pole and is therefore parallel to the surface. Thus the E x B electron drift current follows a closed path, trapped within the E and B field. This increased path increases ionisation probability, *figure 2.3,* by increasing the probability of collisions between the electrons and atoms to create more ions, and by also preventing the recombination at the walls. This intense ionisation causes rapid sputtering. The main disadvantage of a simple diode (i.e. the low deposition rate obtained), can thus be overcome by the addition of magnetic fields [10]. The trapping of the electrons by the E x B fields results in lowered electron bombardment of the substrate and hence lower temperatures at the substrate surface. Ions however, are not trapped, and so beneficial ion bombardment of the film continues. The intense energies used in sputtering generate large amounts of heat at the target, and hence must be dissipated by water cooling of the magnetrons. The design of magnetrons for d.c. sputtering has been documented in detail by Almedie [11].

When the target material is in direct contact with the cooling water, a directly cooled magnetron results. For expensive materials, or ones in which rigidity is insufficient to provide adequate support, the material is attached to a backing plate by epoxy or screws. This is an indirectly cooled magnetron. Directly cooled magnetrons allow for higher deposition rates due to the more efficient heat dissipation [12].

### 2.3.3 Unbalanced Magnetrons

The main disadvantages associated with magnetron sputtering are

1. the strong decrease of the substrate ion current with increasing distance of substrates from the magnetron target, ($d_{s-t}$) due to electron and ion recombination at the chamber walls.

This can be rectified by

(i) additional gas ionisation e.g. by use of a hot cathode electron beam [13] or a hollow cathode arc electron source [14], which increases the ion current.

(ii) by the magnetic confinement of the plasma, using an unbalanced magnetron [15-21], which mitigates the electron-ion recombination effects.

2. compared to other deposition processes, it has relatively poor throwing power i.e. magnetron sputtering is fundamentally a line-of-sight type deposition process.

This can be rectified on a microscopic scale by

(i) increasing the substrate temperature (T)

(ii) applying a bias to the substrate ($V_s$)

(iii) increasing the system pressure ($P_T$)

These three parameters affect greatly the energy of the atoms on the surface of the films. This energy is imparted thermally in case i), and by ion bombardment in case ii) and iii). This increased energy, once imparted to the atoms on the film can aid adatom mobility and hence diffusion of the surface atoms, thereby promoting even coverage of the substrate. Ion bombardment is increased due to the acceleration of ions across the plasma when a negative substrate bias is applied, resulting in more energetic collisions. Increasing the system pressure reduces the mean free path of the gaseous species, due to collisions with the chamber walls and other gas atoms, promoting further ionisation and hence increased plasma density, bombardment of the film and reducing directionality.

On a macroscopic scale, throwing power can be enhanced by

(i) utilisation of more than one target, which provides a greater flux of source material, and can also cause increased plasma densification due to increased ionisation of the gases in the reaction chamber.

(ii) rotating the substrate, which promotes even coverage of the substrate by eliminating shadowing effects of the substrate.

(iii) increasing the system pressure [13]

(iv) confining the plasma between the substrate and target by using unbalanced magnetrons [22], which increases plasma density and ion bombardment of the film.

A balanced magnetron is one in which the magnetic fluxes of the opposing magnetic poles are equal. This is most easily achieved by ensuring that the surface areas of both north and south poles are equal. Conversely, an unbalanced magnetron is one in which the magnetic fluxes of the opposing magnetic poles are not equal, *figure 2.4*. This imbalance in the magnetic field strength can be achieved by either making the outer ring or inner ring of magnets the stronger. Conventionally, the outer ring is made the stronger of the two so that the magnetic field lines emanating from the edges of the magnetron are directed towards the substrate. This magnetic field line configuration serves to confine the plasma between the target and the substrate, thus providing high density, low-energy ion bombardment of the growing film, facilitating the deposition of thin films onto substrates more satisfactorily than by using balanced magnetrons. Increased target-to substrate distances of upto 200mm can be used [21] when unbalanced magnetrons are used, without compromising film stoichiometry.

The increased plasma ionisation caused by the both balanced and unbalanced magnetrons increases the sputter yield at a specific area between the two rings of magnets called the

racetrack, *figure 2.5*. The target utilisation is low due to the increased erosion in this racetrack region, as most of the target beyond the outer ring of magnets, and within the inner ring of magnets is not preferentially sputtered. Although the target utilisation is dependent on the configuration of the magnets, typically, only 30% of the target is used in magnetron sputtering [5].

## 2.4 Film Microstructure

The properties of the coating are highly dependent on the film microstructure, which in magnetron sputtering is dependent on the substrate bias, the target power, the total pressure, the substrate temperature [23,24] and also on the partial pressure of reactive gas [25-27]. The effects of these parameters on the film microstructure has been extensively published resulting in three microstructural models [28-30]. Greater ion bombardment of the film ensues from the increased plasma ionisation and confinement present in unbalanced magnetron configuration, thereby yielding denser coatings.

### 2.4.1 Structural Zone Models (SZM)

Movchan and Demchishin [28] were the pioneers in the classification of thin film microstructures, basing their structure zones on a function of $T/T_m$ ( where T is the temperature of the substrate surface and $T_m$ is the melting temperature of the material), *figure 2.6(a)*. Low temperature Zone 1 structure, corresponding to low adatom mobility consisting of tapered columns with domed tops and voided boundaries. Computer simulation adds that atomic shadowing is prevalent, which, combined with limited surface mobility explains the basic Zone 1 characteristics [31,32]. The crystal diameter increases as $T/T_m$ increases, implying a low activation energy and little surface diffusion. Typically, Zone 1 occurs for $T/T_m < 0.3$ (metals) and $< 0.26$ (oxides).

Zone T, included in *figure 2.6(a)*, is a result of the sputtering gas, and is attributed to Thornton [29], as explained later. It has been inserted to show where Zone T would be located in the original Movchan-Demchishin model.

In Zone 2, increasing temperature causes increased surface diffusion and resulted in a structure of straight columnar grains with a smooth topography. With increasing $T/T_m$, the atomic shadowing in Zone 1 is dispelled, and along with increasing surface diffusion, explains the movement of Zone 1 to Zone 2 microstructure [33]. Typically, for Zone 2, $0.3 < T/T_m \leq 0.45$ (metals) and $0.26 < T/T_m \leq 0.45$ (oxides).

By further increasing the temperature, Zone 3 structures are formed, characterised by equiaxed grains, due to the recrystallisation effects of such high temperatures. The coating is usually fully annealed. Typically, for Zone 3, $0.45 < T/T_m < 1.0$ (metals and oxides).

Although the temperature of the substrate plays an important role in the size of the crystallites formed, other conditions such as the deposition site and reactive gas partial pressure can also affect the shape and size of the crystallites [25,34].

Further work undertaken by Thornton [29] necessitated the inclusion of Zone T, which is present under the effects of a sputtering gas, *figure 2.6(b)*. Zone T consists of poorly defined fibrous grains. Zone I microstructures can tend towards Zone T by either thermal-induced adatom mobility or by ion bombardment, where momentum exchange causes the coating atoms to fill the boundaries of loosely packed Zone I columns. A new model developed Messier et al [30] accounts for both effects, *figure 2.6(c)*. In essence, this model shows that ion bombardment promotes Zone T type dense structures.

### 2.4.2 Ion Bombardment

The action of ion bombardment on the substrate prior to deposition (sputter etching/cleaning) has the effect of removing physically and chemically adsorbed layers, which may hinder adhesion. This sputter etching can also produce an atomistically rough surface on the substrate which aids mechanical bonding of the coating to the sample.

Film densification can be obtained in many ways. The electrons and negative ions in the plasma accelerate towards the substrate, causing ion and electron bombardment of the film. Biasing of the substrate at a small negative potential ( -20 to -200V ) can also enhance further bombardment. The more negative the substrate bias, the more energetic the bombardment. This can lead to other property modifications in addition to densification [35] e.g. increased gas incorporation in the film. D.C. negative biasing is prevalent for conducting films, whilst r.f. biasing is used for biasing of non-conducting films. D.C biasing is not effective when a non-conducting film is formed on a substrate. This is due to the charge build-up on the substrate resulting from positive ion attraction by the negatively-biased substrate. This build-up effectively repels any further ion bombardment, and so the d.c. bias can become redundant during the deposition of insulating coatings. In investigations [35,36], the deposition rate was seen to decrease as negative bias was applied to a substrate. This was related to the increased ion bombardment of the film. Three possible causes were cited:

1. increased film densification due to the filling in of interstitial voids and a general decrease in the crystallite size.
2. resputtering of the growing film.
3. selective removal of impurities (e.g. Oxygen) from the film.

Thus the thickness of the film decreased although the sputtering yield from the target remained the same.

In general, it is agreed that films deposited at low substrate bias possess open, porous structures whilst denser coating structures can be obtained at increasing negative bias voltages [37, 38].

In the use of unbalanced magnetrons, the d.c. biasing of the substrate above the voltage at which the ion current saturates ( approximately -50 V d.c.) does not cause further film densification. This is due to the fact that when a negative bias is applied to the substrate, it undergoes positive ion bombardment, however, a fixed amount of plasma ionisation occurs for any given potential across the electrodes. Hence the amount of ion bombardment due to substrate bias is also fixed, and increases in the negative substrate bias cannot serve to attract any more ions than are already available in the plasma. This ion current thus saturates at a given negative substrate bias. When a positive bias is applied to the subsrate, it undergoes both electron and negative ion bonbardment. This current, called the electron current, will also saturate, but only at a substrate bias gretaer than the plasma potential.

At low pressure, the mean free path of the gas is longer, due to fewer inelastic collisions and results in more energetic particles, which impart their energy into the growing film as heat, providing the activation energy required to promote surface diffusion. At high magnetron power, there is increased energy to the particles, and also a greater flux of sputtered atoms which increases the impingement rate at the substrate. The position of the substrate in relation to the target is also important, with samples placed close to the source encountering more energetic particles i.e. those that have not undergone collisional losses.
In addition, the substrate temperature affects the residual stress in the films due to recrystallizational annealing which occurs at higher substrate temperatures.

### 2.4.3 Residual/Internal Stress

It has been reported that levels of internal stress in the coating varied with position from the substrate surface, and the residual microstress was due to growth and thermal mismatch factors [39-41]. Close to the coating-substrate interface, the fine-grained crystallites supported high elastic stresses, which indicated that yield strength was high. As the coating got thicker, the yield strength fell due to the larger grain size, increased porosity and reduced internal stresses [42,43]. Compressive stress was also found to be greatest in films deposited at low system

pressure [44] and at high negative substrate bias [45,35,46,47] i.e. at high ion bombardment levels..

Hence residual stress is dependent on both the ion bombardment and the deposition environment, particularly the substrate geometry and the deposition temperature. Two main components exist in any measured stress [48]:

1. thermal stresses due to mismatch of the expansion coefficients of the coating and substrate.
2. growth stresses generated during film deposition due to the accumulation of crystallographic defects. These are a strong function of coating microstructure.

Argon gas incorporation into the growing film is another possible source of residual stress, distorting the lattice over a substantial volume of the film [49].

However, the open, porous columnar grain structure present in Zone I microstructures relieves the residual stress inherent in the coating as the grains are not closely packed together, and hence some stress relaxation can take place. A reduction in the hardness is apparent compared to Zone T microstructures. Substantial stresses are generated in Zone T structures leading to an increased stored elastic energy [39] by a reduction in the adhesion of the coating to the substrate.

### 2.4.4 Substrate-Film Adhesion

Adhesion, or the ability of two materials to remain in contact is dependent on the interfacial region between the coating and the substrate. It is also dependent on the bonding across this region. There are four main categories of interfacial region [9]

1. A mechanical interface. If the surface is rough or porous, mechanical interlocking can provide adhesion. No chemical reaction between the substrate and the coating occurs.
2. A monolayer-to-monolayer interface. This is seen as an abrupt change from the substrate material to the coating material. This occurs when there is no diffusion of the

depositing atom into the substrate material and little chemical reaction between atoms of the coating and substrate material.

3. A compound interface. When a constant composition formed by chemical interaction of the coating and substrate material exists.

4. A diffusion interface. This is a gradual change in the composition across the interfacial region. Diffusion between the coating and the substrate material occurs, but only when there is some degree of solubility of the materials and available energy to overcome the activation energy for bulk diffusion (1-5eV)

Magnetron sputtering facilitates several combinations of theses interfacial regions. A mechanical interfacial region is created when the substrate is sputter etched prior to film deposition by inducing a rough surface on which good mechanical interlocking of the film can occur. Ion bombardment during film growth can produce the diffusion (or graded) interface providing true metallurgical bonding and reducing the effects of interfacial stress due to the difference ion mechanical and thermal properties of the coating and substrate material [50]. These graded interfaces are most probably caused by the intermixing of atoms at the interface due to high energy impacts of ions and neutrals. This bombardment both imparts energy to the growing film increasing adatom mobility ad forward sputters material into voids and interstitial sites [44,51]. Intermediary or interlayers can also be beneficial by providing a more compliant region in which interfacial stress can be relieved. It may also provide a region where diffusion can occur between it and the substrate and the coating and interlayer, thus resulting in bonding of the coating to the substrate.

Consider the case of TiN deposited onto steel. It has been found [52] that a Ti interlayer deposited between the steel an the TiN significantly increases adhesion. It has been proposed that the Ti interlayer reacts with the weak iron oxide present on the surface of the steel substrate thus bonding the Ti to the steel. In turn, Ti can diffuse into the TiN and thereby increase adhesion at that interface [66]. This Ti interlayer avoids the abrupt change in composition (monolayer-to-monolayer) between the coating and the substrate [53,54]. However an optimum Ti interlayer thickness of between 0.1 - 0.15 μm exists [55,56], with

thicker Ti interlayers( greater than 0.2-0.3 μm) showing reduced adhesion strength [57] due to the low shearing strength of titanium. Another beneficial effect of using Ti interlayers is the chemical gettering effect of oxide layers at the surface of the sample.

### 2.4.5 Substrate Effects

Substrate effects are two-fold. The substrate crystal structure affects the growth habit of the deposited coating through changes in the distribution, orientation and size of the crystallites nucleated on the growing surface [45,58-60]. Secondly, the thermal expansivity of the substrate affects the level of internal stress in the film. This stress is compressive when $\alpha_f < \alpha_s$ and tensile when $\alpha_f > \alpha_s$ where $\alpha_f$ and $\alpha_s$ are the thermal expansion coefficients of the film and substrate [45,61,58]. It has also been suggested [39,45] that compressive internal stresses may be an important factor in determining the porosity of PVD coatings. Thus internal stress is another unconsidered degree of freedom in the construction of PVD SZMs [58].Both of these effects can be mitigated by the use of interlayers.

Orientation of the sample in relation to the target is also important as magnetron sputtering is principally a line-of-sight deposition technique. Turley [62], in his investigations reported that coating thicknesses on parts of a component parallel to the line of sight was only 35% as thick as those parts orthogonal to the target line-of-sight. In addition, the coating had a more open, porous structure parallel to the line of sight , but exhibited a dense morphology perpendicular to the line-of-sight. Deposition rate also decreased along the length of the sample, with columnar crystals nearest the magnetron, and finer-grained, columnar structures farther away from the magnetron.

Thus many different parameters affect film properties. The deposition technique, substrate material and orientation, the ion bombardment resulting from variations in the magnetron power, system pressure, target to substrate distance and substrate bias all play an important part in the adhesion and microstructure of the film.

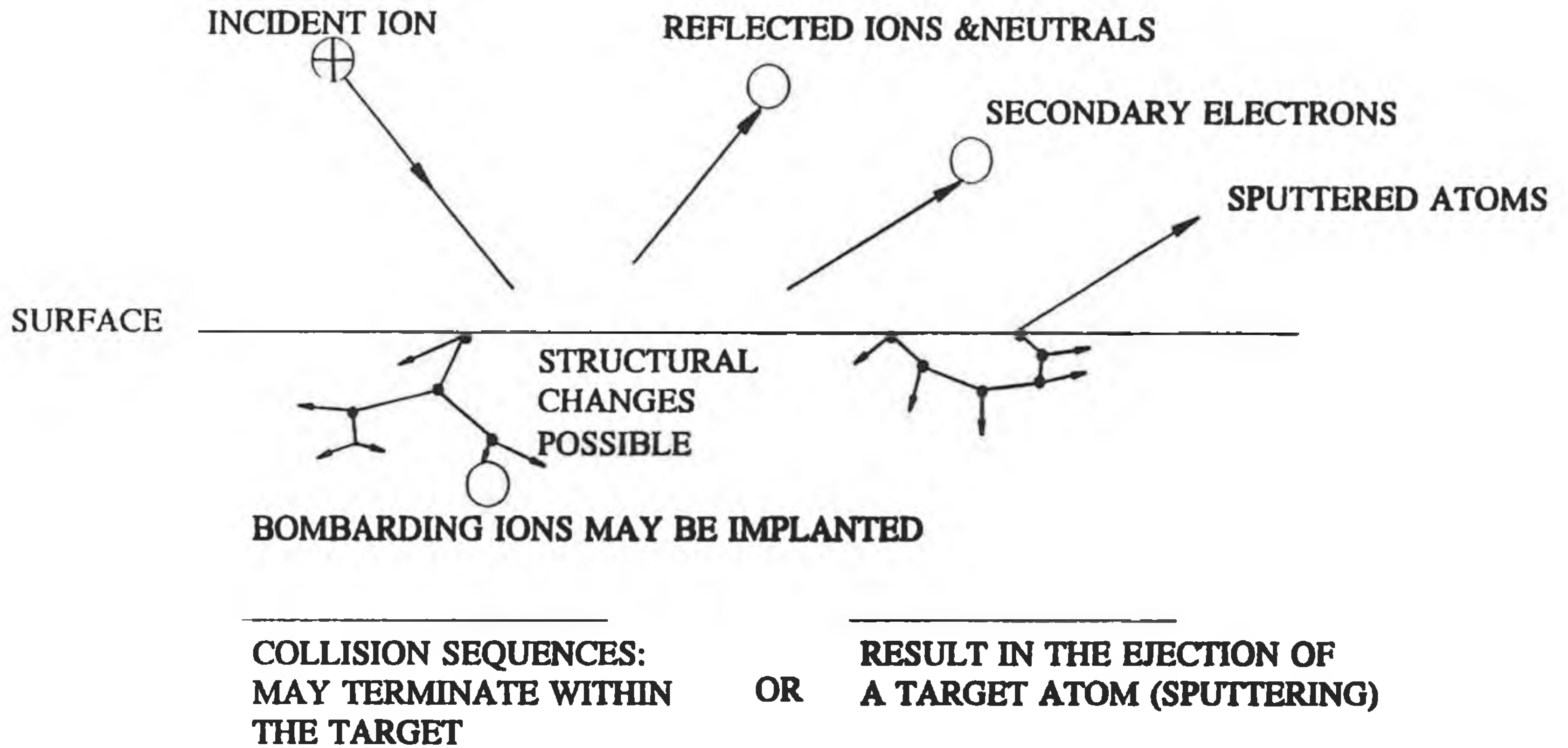


**Figure 2.1** **The Sputtering Process [170]**

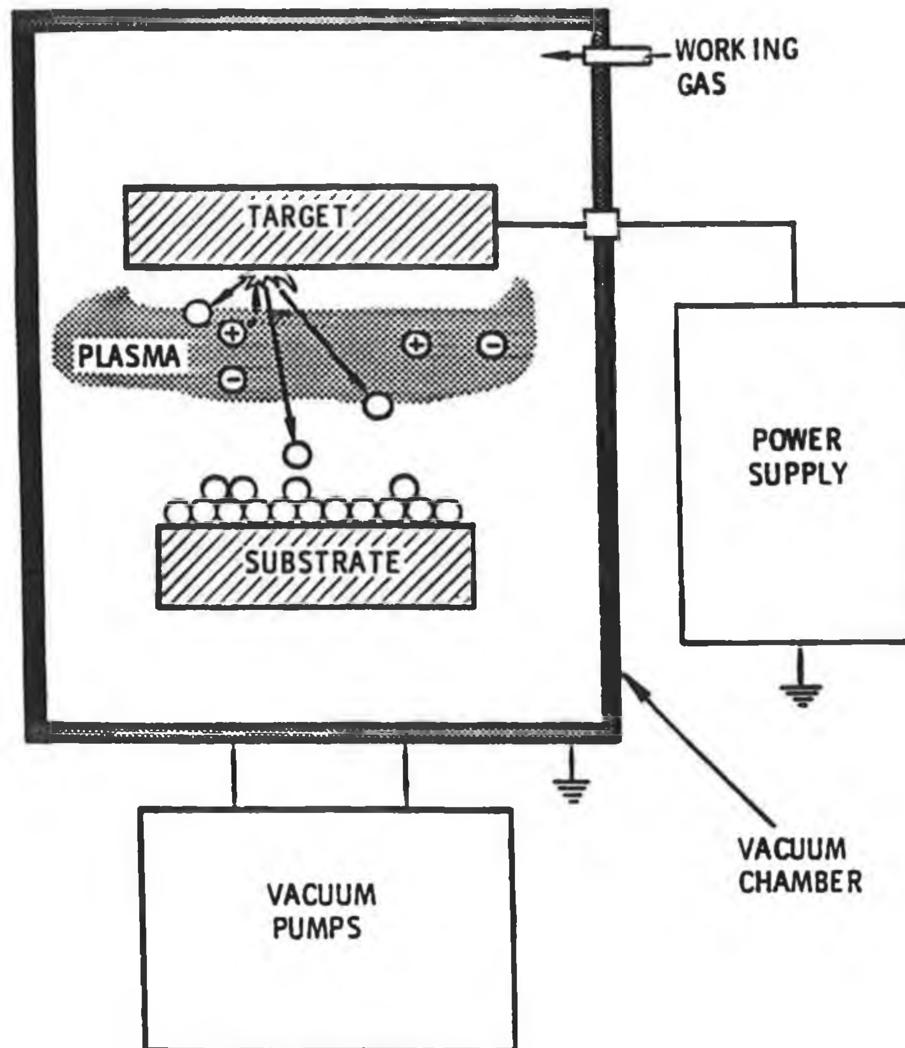


Figure 2.2 Schematic Diagram for Sputtering

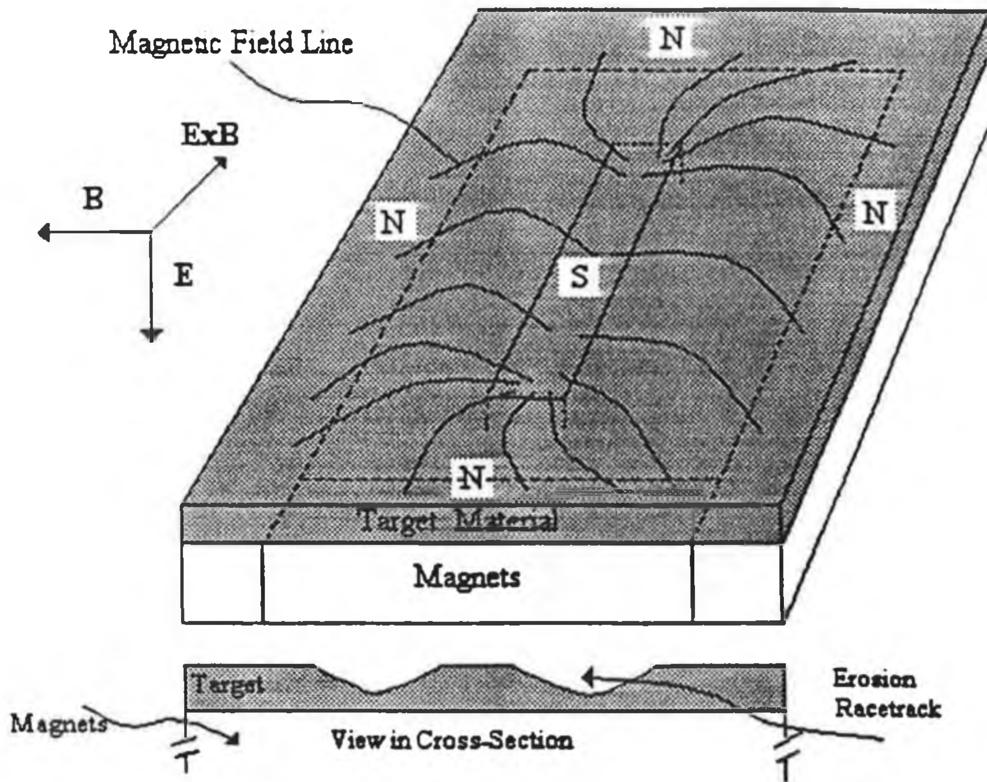


**Figure 2.3** **Planar Magnetron Configuration [66]**

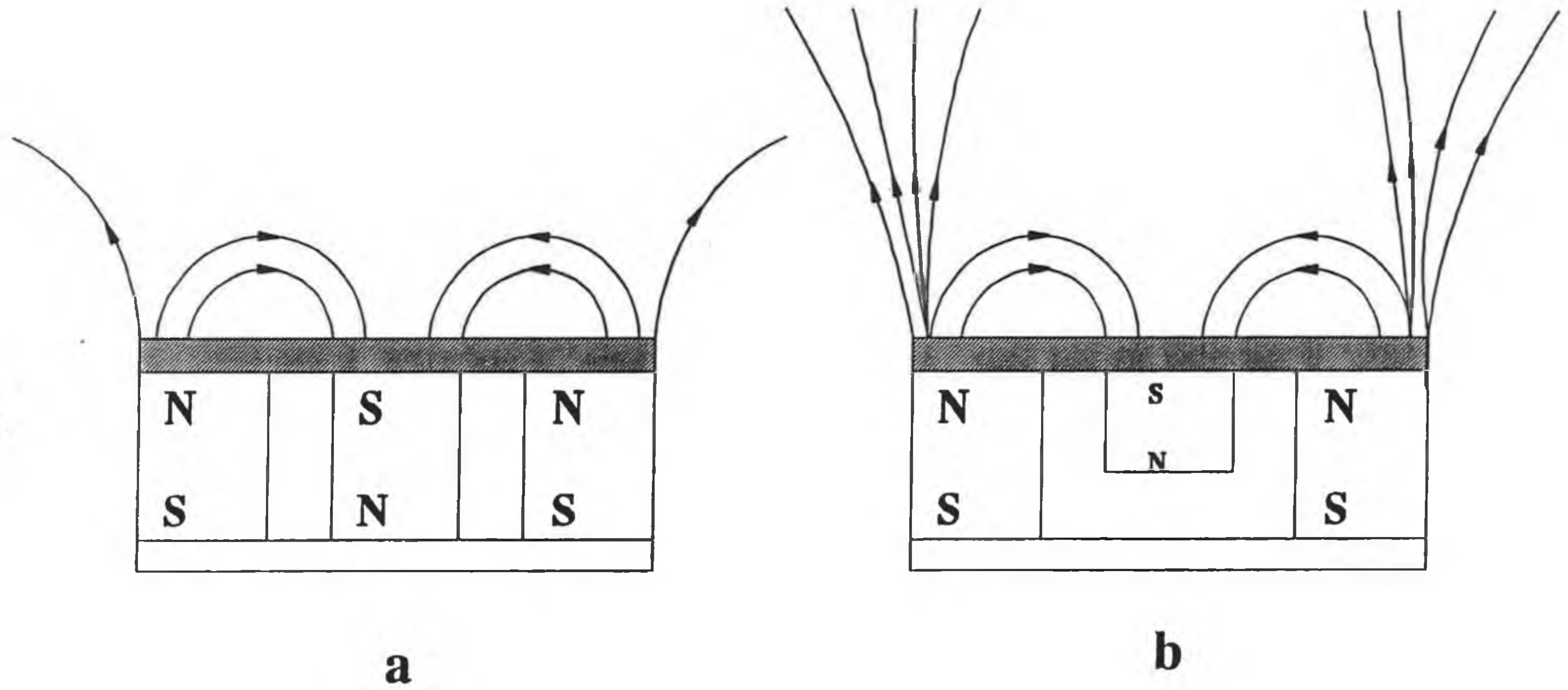


Figure 2.4 Balanced Magnetron (a)
Unbalanced Magnetron (b)

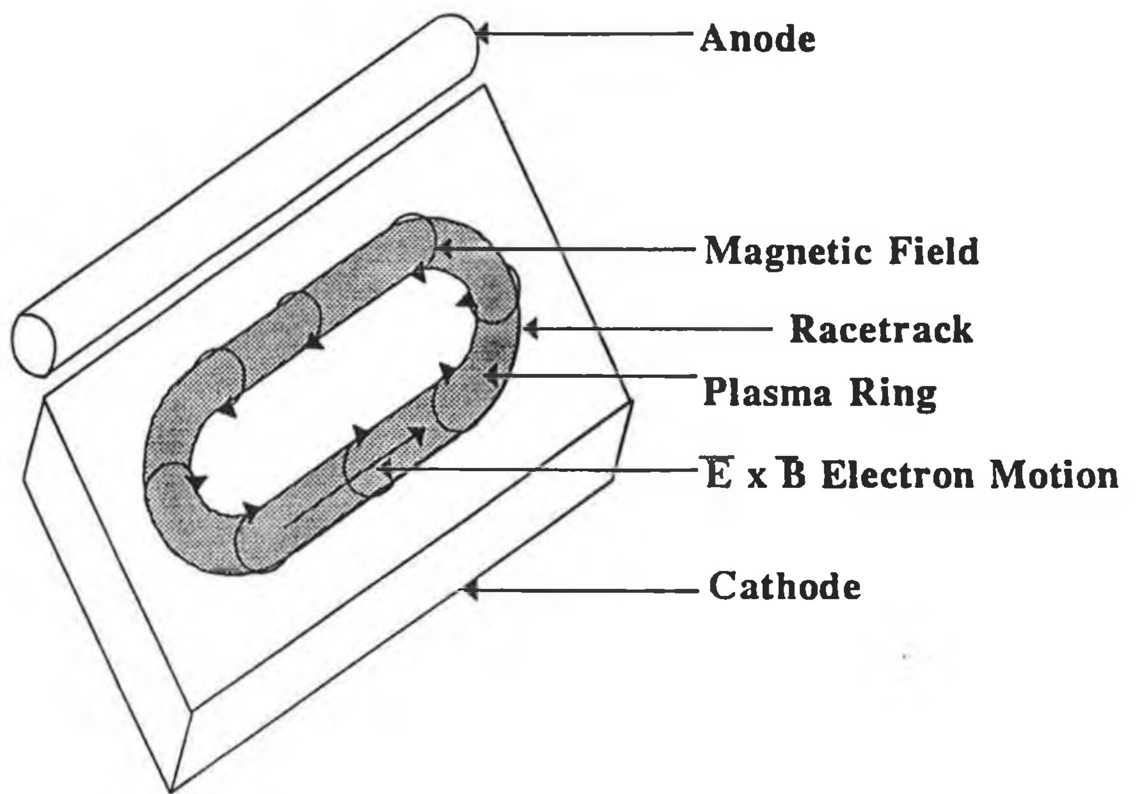


Figure 2.5 Planar Magnetron with Magnetic End Confinement

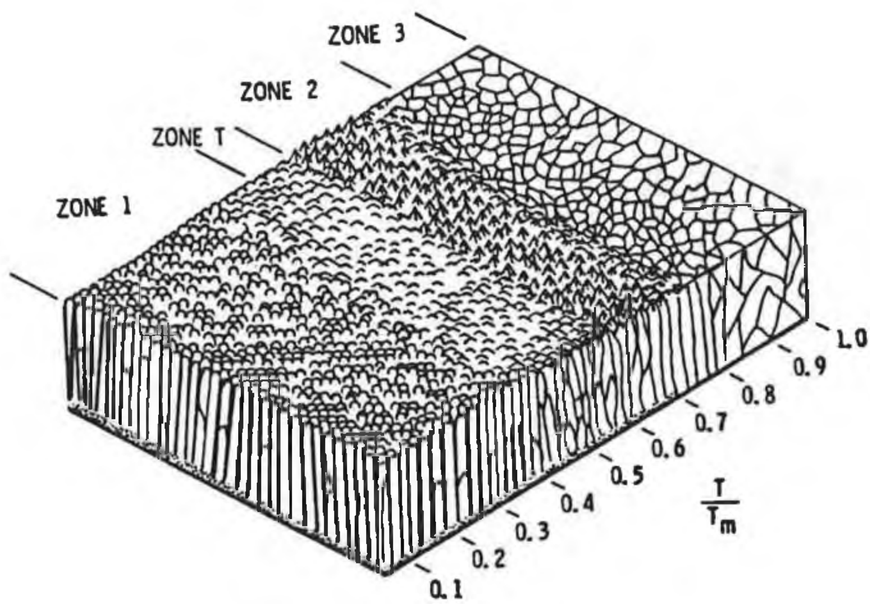


**Figure 2.6(a)** **Movchan-Demchishin Structural Zone Model**

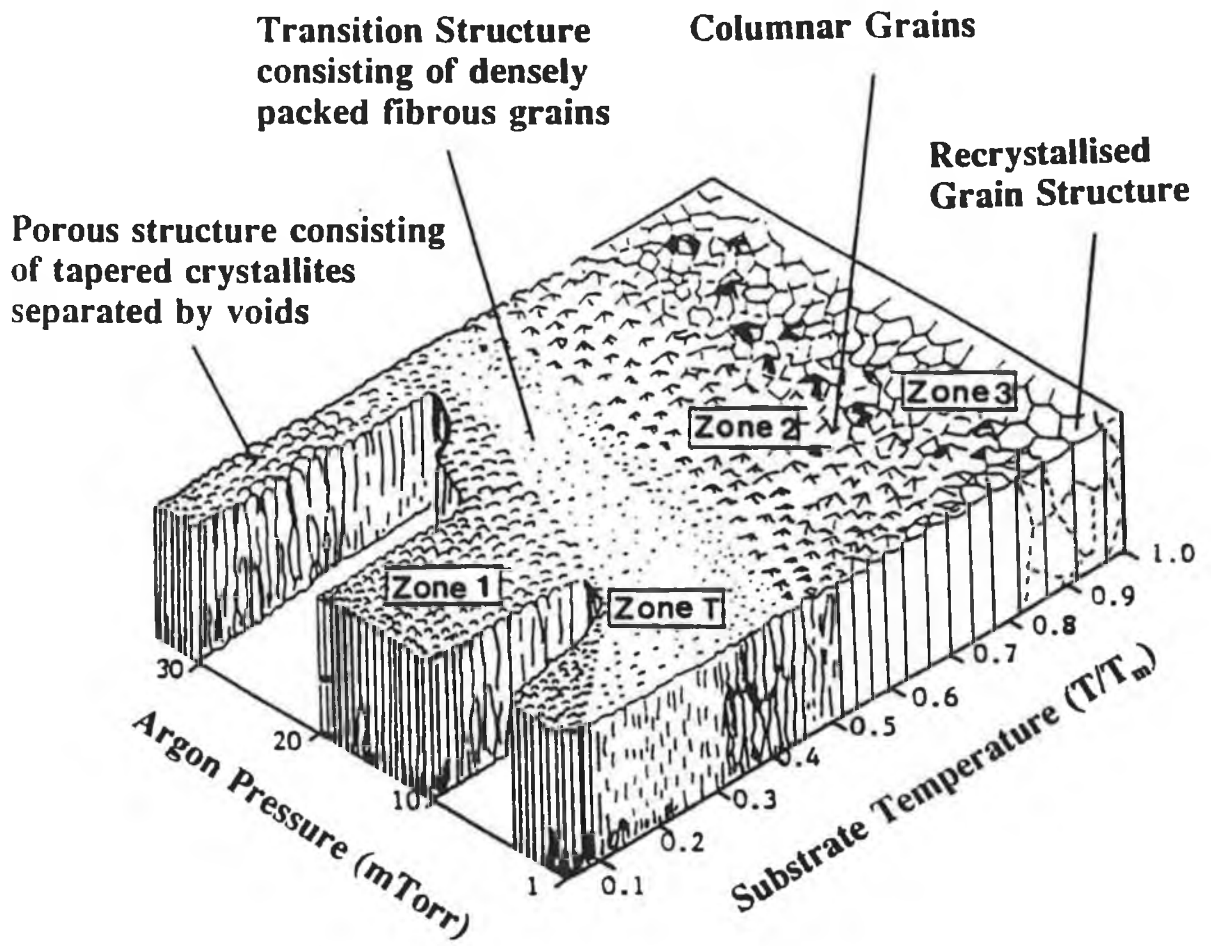


Figure 2.6(b) Thornton Structural Zone Model

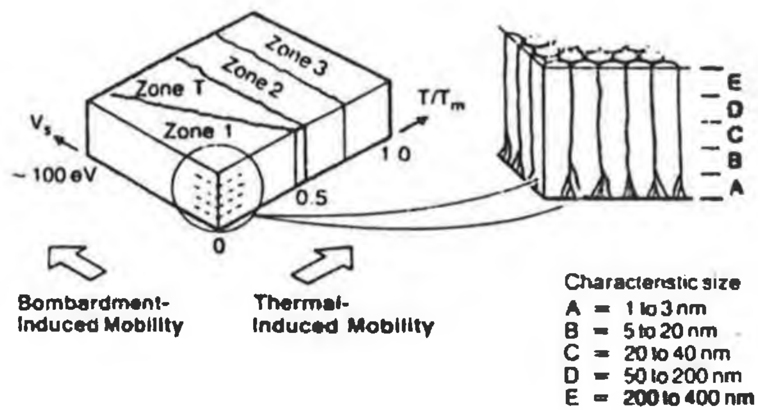


Figure 2.6(c) **Messier Structural Zone Model**

# Chapter 3

# Magnetron Sputtering Deposition System

# Chapter 3 Magnetron Sputtering Deposition System

## 3.1 Introduction

The magnetron sputtering system, which was constructed for the experimental work, comprised a vacuum chamber, standard high vacuum equipment, and magnetrons with power supplies. Whilst the vacuum equipment was generic, some important features of this system were the custom-built chamber, whose basic requirement was versatility and adaptability in a research environment. The system is depicted in *figure 3.1*.

### 3.1.1 Equipment

The system comprised a custom-built vacuum chamber, which was evacuated using a Varian VHS-6 diffusion pump (2,400 l/s) and backed by a Varian SD-700 rotary backing pump (765 l/min). A VAT Control Gate valve, Series 64 was used, together with Varian NW 40, A/O Block Valves for the control of the pumping sequence. A residual gas analyser (Spectrametrics Vacscan RGA) was utilised for gas analysis and leak detection. This was required to be differentially pumped, and so necessitated the use of a Varian V60 Turbomolecular pump (65 l/s) and a Varian SD40 rotary backing pump (40 l/m). A feedback control unit based on optical emission spectrometry was also incorporated into the system. This facilitated close control of the hysteresis loop dominant in the deposition of TiN by reactive magnetron sputtering. This will be discussed in further detail in section 2.2. A schematic diagram in *figure 3.2* depicts the system apparatus, *figure 3.3* shows the electrical wiring and *figure 3.4* depicts the water-cooling circuit.

The power supplies used for the magnetrons and for the substrate table biasing were Advanced Energy MDX 5kW Magnetron Drives. In addition, a Glassman High Voltage Inc. Series EW 0.6 A, 1 kV power supply was utilised for substrate biasing and argon sputter cleaning of the

samples. A larger, 60V, 30A Sorenson DCR 60-30 B power supply was used for the heating element used to heat the substrates prior to, and during, deposition.
The equipment also included an Advanced Energy RFX 1250 RF supply with an automatic matching unit, and was employed in substrate biasing.

The flow rates of both working gas and reactive gas were monitored by a Tylan mass flow controller (type FC280A) and a Tylan mass flow meter (type FM380A) respectively. The capacity of both the controller and the meter was 100sccm. A Reactaflo optical feedback control system was also incorporated, the operation of which is described later. Both the working gas and the reactive gas flow rates in standard cubic centimetres per minute (sccm) were displayed on a digital meter and the reactive gas was directed through a piezo-electric valve. The total pressure of the chamber was monitored by use of Edwards Penning and Pirani gauges, controlled through an Edwards Pirani/Penning controller, Type 1005. Another Pirani gauge monitored the pressure on the backing line. All valves were electro-pneumatic.

### 3.1.2 Vacuum Chamber

The chamber itself comprises a top plate (740 mm dia. x 25.4 mm), with one magnetron port (330 x 184 mm), and 8 rotatable shutter ports (50.8 mm dia.), 4 plasma emission spectrometer ports ( 50.8 mm dia.) and a bottom plate ( 740 mm x 25.4 mm ), with 2 pressure gauge flanges (KF16, KF25), 1 thermocouple feedthrough flange (KF25), 1 substrate table port ( 100m dia. ), in the centre of the base plate, 1 high vacuum port ( 200 mm dia. ), 1 backing line port (KF40), 8 rotatable shutter ports ( 50.8 mm dia. ) and 2 ( 6.35 mm ) Swagelok water inlet/outlet ports for water cooling of the substrate table. There are 4 magnetron ports on the cylindrical walls, along with 1 KF40 and 1 KF50 viewports, 1 KF25 optical pyrometer port, 2 rotatable magnetron shutter ports (for the top magnetron) and 1 plasma emission spectrometer port. The vacuum chamber was designed to maximise versatility. Thus, by using the four side magnetrons, large samples can be coated by rotating the sample in the chamber. By utilising only one or two magnetrons, smaller samples can be also be coated without rotation.

The flanges were all o-ring sealed, using either Viton® or Nitrile elastomers. KF clamping arrangements were employed to expedite the reconfigurement of apparatus when necessary. The chamber was fabricated using non-magnetic AISI 304 stainless steel. It was double skinned to enable the circulation of cooling water, supplied by a LAUDA UKT 1000P water cooler. Detailed drawings of the chamber can be found in Appendix B.

All peripheral blanking plates, magnetron shutters, Wilson seals etc. were designed and fabricated in-house. Detailed drawings of this peripheral equipment can be found in Appendix B.

The chamber top plate and walls could be raised by means of a pulley. A frame incorporated a linear slide rail in order to place the chamber walls and top plate on a resting area while maintenance and sample loading was undertaken. The frame was constructed of box section steel, and supported both the chamber, lifting device and peripheral equipment.

### 3.1.3 Substrate Holder

Initially, the substrate holder in place consisted of a stainless-steel frame upon which the substrates were clamped in a vertical position orthogonal to the side-magnetron target face. The heating of the substrate was achieved by radiant heating using a tungsten wire filament supported on a ceramic and steel frame. The independent use of heater and substrate holder enabled other holders to be used, specific to particular component/sample shapes and sizes. The distance from the target face could be adjusted by simply placing the table, holder and heater at the required distance, as shown in *figure 3.5*. Both the heater and the holder were electrically isolated from the earthed table by use of ceramic tiles. The temperature achieved by this method of radiant heating was greater than 400°C. Biasing of the substrate holder in order to sputter clean samples and bias during deposition was achieved by use of a Wilson seal with a copper rod. The Wilson seal was adapted such that a polytetraflouroethane (PTFE) sleeve fitted around the copper rod where it was in contact with the steel of the seal to prevent grounding. This proved most successful in applications.

The substrate holder, after modification now comprises a rotary Deublin feedthrough through which the table is water cooled. In addition, the table is biased by means of a single copper rod through the insulated shaft, as shown in Appendix B. The table top, inside the chamber, has a spoke-like arrangement, with individual holders machined suited to the substrate shape. These holders can be moved to any distance along the spoke, thus varying the substrate to target distance. They are orthogonal to the target face and positioned in the centre of the vertical axis of the magnetron. Simple rotation of the table by means of a d.c. stepping motor can provide for uniform coating of several components at a time, or the deposition of a multi-layered coating during each rotation of the table. As yet, this remains to be incorporated into the final design, but is depicted in *figure 19*, Appendix B..

## 3.2 Target Poisoning

As mentioned previously, two techniques exist for the deposition of compound films, one of which is reactive sputtering. In d.c. magnetron deposition, target poisoning is a common phenomenon. In order to deposit certain compound coatings by d.c. magnetron sputtering, the balance between the sputtered flux of target material and the arrival of the reactive gas at the target must be maintained at a precisely-controlled level. If this balance is not achieved, poisoning of the deposition source ensues, resulting in deposition of a film of the wrong stoichiometry. In the sputtering process, reactive gas is chemically pumped by reaction with the target, the sputtered metal at the chamber walls, and at the substrate [63]. Poisoning occurs when excess reactive gas in the chamber forms a compound on the target surface by reacting with the target. The film formed at the surface of the target is over stoichiometric and resistive, and can be difficult to sputter using a d.c. magnetron. As a result, the deposition rate drops and the cathode voltage rises. Thus, the flux, or amount of target material ejected from the target surface, is reduced due to target coverage, and the reactive gas pressure in the chamber rises.

A poisoned target reduces the speed of the chemical pump, so, to compensate for this, the partial pressure of reactive gas should be reduced until gas flow and pumping are balanced. This, however, creates an unstable condition and can make the deposition of some materials

(i.e. those that fall within the hysteresis loop) impossible. If the gas flow is reduced after the partial pressure rises above a certain level, the pressure-flow relationship will be different from that when the flow was increased, *figure 3.6(a)*. One solution to this hysteresis problem is to increase the system pumping capacity. If the pumping speed is greater that the rate of reactive gas consumed, no poisoning will occur.

Since optimisation of the deposition rate is usually a major concern, another solution is to monitor the partial pressure of reactive gas, *figure 3.6(b)*, thus maintaining the balance between target flux and reactive gas. Limiting the gas pressure ensures that the reactive gas admitted into the chamber either reacts with the target flux or is pumped out of the chamber and does not cause target poisoning.

The use of r.f. supplies to power the magnetrons would also minimise target poisoning, as both conducting and resistive materials can be successfully sputtered off the target. A very successful way of mitigating this target poisoning is to use feedback control.

### 3.2.1 Feedback Loop

As TiN was chosen as the initial coating with which to commission the rig, it was important to understand the deposition characteristics of this coating. TiN deposition is governed by a hysteresis loop where the reactive gas flow and reactive gas partial pressure differ as gas flow is increased from low to high levels to that value when gas flow is decreased from high to low levels. A TiN phase diagram is shown in *figure 3.7*, where stoichiometric TiN occurs between 38-50 atomic % nitrogen. During poisoning, the deposition rate falls, and the amount of unreacted reactive gas causes further target poisoning until the whole target becomes covered. This is a stable mode, and deposition can be undertaken in this mode, however the deposition rates are quite low (5 to 10 times lower than normal modes of deposition) and the resultant film is overstoichiometric.

Another stable mode of operation exists, in which the resultant film is understoichiometric. Thus, stoichiometric control would occur between these two stable modes of operation, *figure 3.8*. In order to maintain this stoichiometric control, the optical emission intensity of titanium was observed and monitored. The emission intensity of a species in a plasma is a good indication of the density of that species in the plasma. By setting the level of target poisoning such that deposition rate is optimised, the deviations from this set point as TiN is reactively sputtered are monitored and the fluctuations provide the feedback signal to the piezoelectric valve which admits the nitrogen gas into the chamber, *figure 3.9*.

The main advantage of using an optical emission spectrometer is that it allows for the rapid compensation in fluctuations of the plasma composition. The partial pressures of nitrogen and argon are monitored using the Reactaflo Reactive Sputtering Controller, *figure 3.10*. The dynamic control of the reactive gas flow eliminates pressure instabilities during target poisoning.

## 3.3 Pumpdown

The chamber, of approximately 200 litres (0.2 $m^3$) was evacuated using a combination of the rotary backing pump, which could rough pump the vacuum chamber from atmosphere to 0.03 bar in 5 minutes, and then high vacuum pumped using the diffusion pump to $5 \times 10^{-6}$ bar in a further 45 - 50 minutes. No cryogenic trap was employed. Leak detection was aided by the mass spectrometer and a helium sniffer. The ultimate pressure achieved was approximately $5 \times 10^{-7}$ mbar.

## 3.4 Magnetrons

The magnetrons employed in this project were supplied by D.G. Teer Coating Services Ltd., and comprised 3 directly cooled Feroba III magnetrons, and one indirectly cooled Neodymium-Iron-Boron (NdFeB) magnetron. The magnetron used during titanium and titanium nitride experimentation was a directly cooled Feroba III magnetron with a commercially pure Ti

target, and an indirectly cooled NdFeB magnetron with a pyrolitic graphite target (purity 99.75%).

### 3.4.1 Closed Field System

The magnetrons ordered were not only unbalanced, but they in themselves were of reversed polarities such that, for instance in the 4-magnetron case, a closed field arrangement ensued, where the magnetic field lines from the edges of one magnetron closed with the edge of the adjacent magnetron, as shown in *figure 3.11*. This effectively confines the plasma to the middle of the chamber where the substrate is placed [64,65]. A closed field system results in increased plasma densification and hence increased ionisation and ion bombardment of the growing film.

Initially, only two magnetrons were utilised to achieve this closed field ( both Feroba III type), and only one was energised during deposition, with the other one serving as a dummy to confine the plasma between the two magnetrons, *figure 3.12*.

Figure 3.1 Magnetron Sputtering System

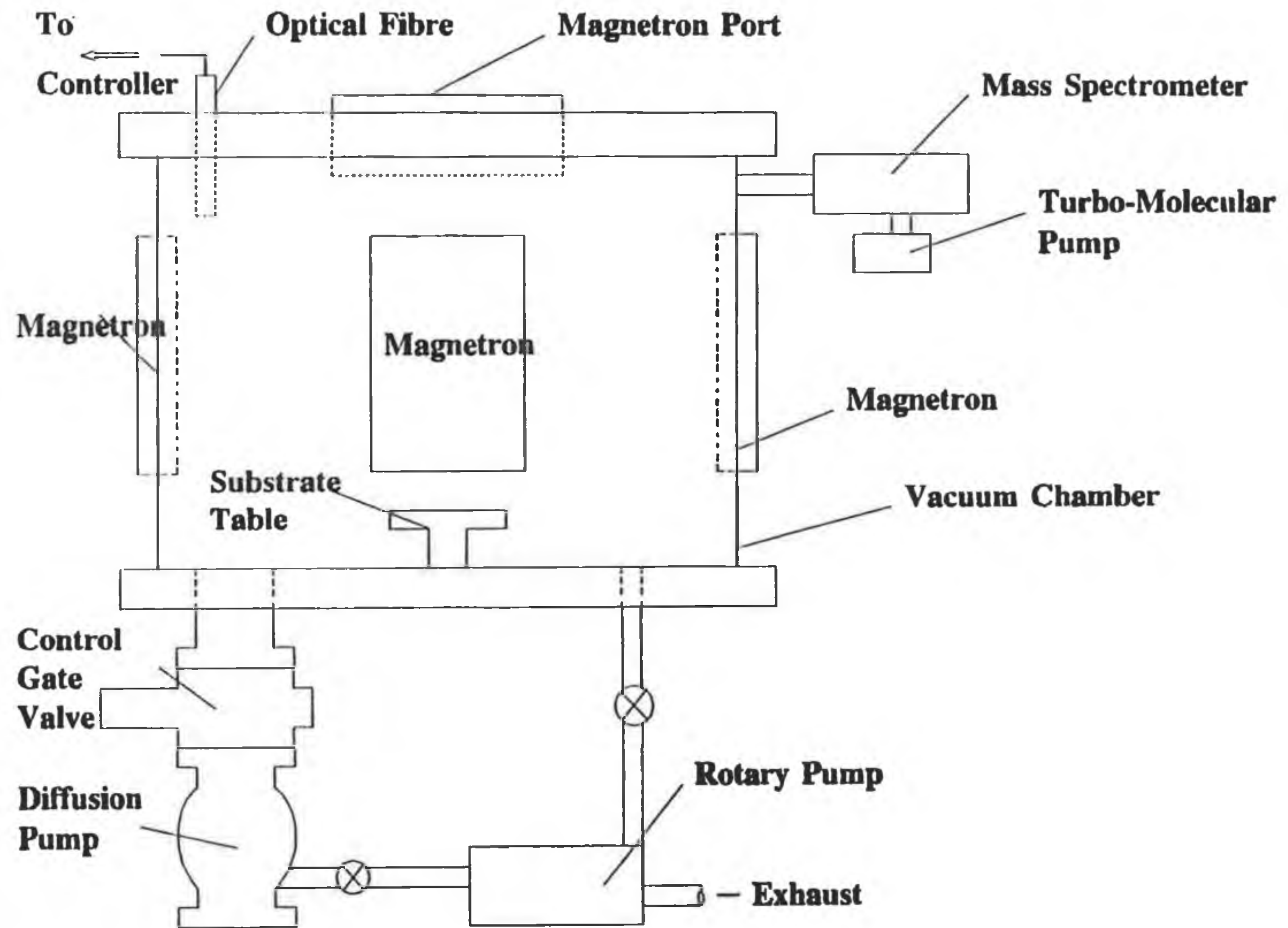


Figure 3.2 System Schematic

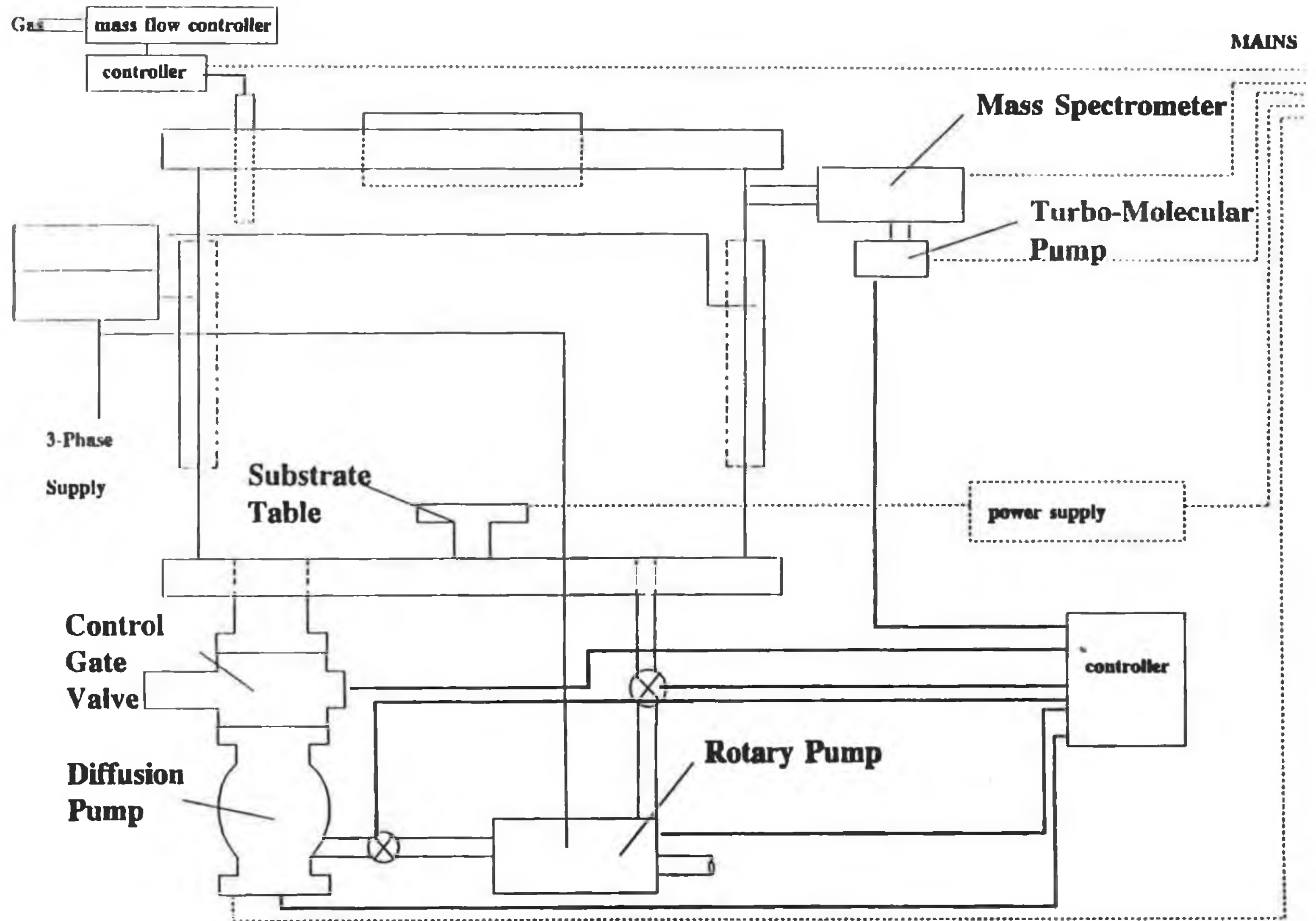


Figure 3.3 Electrical Circuit

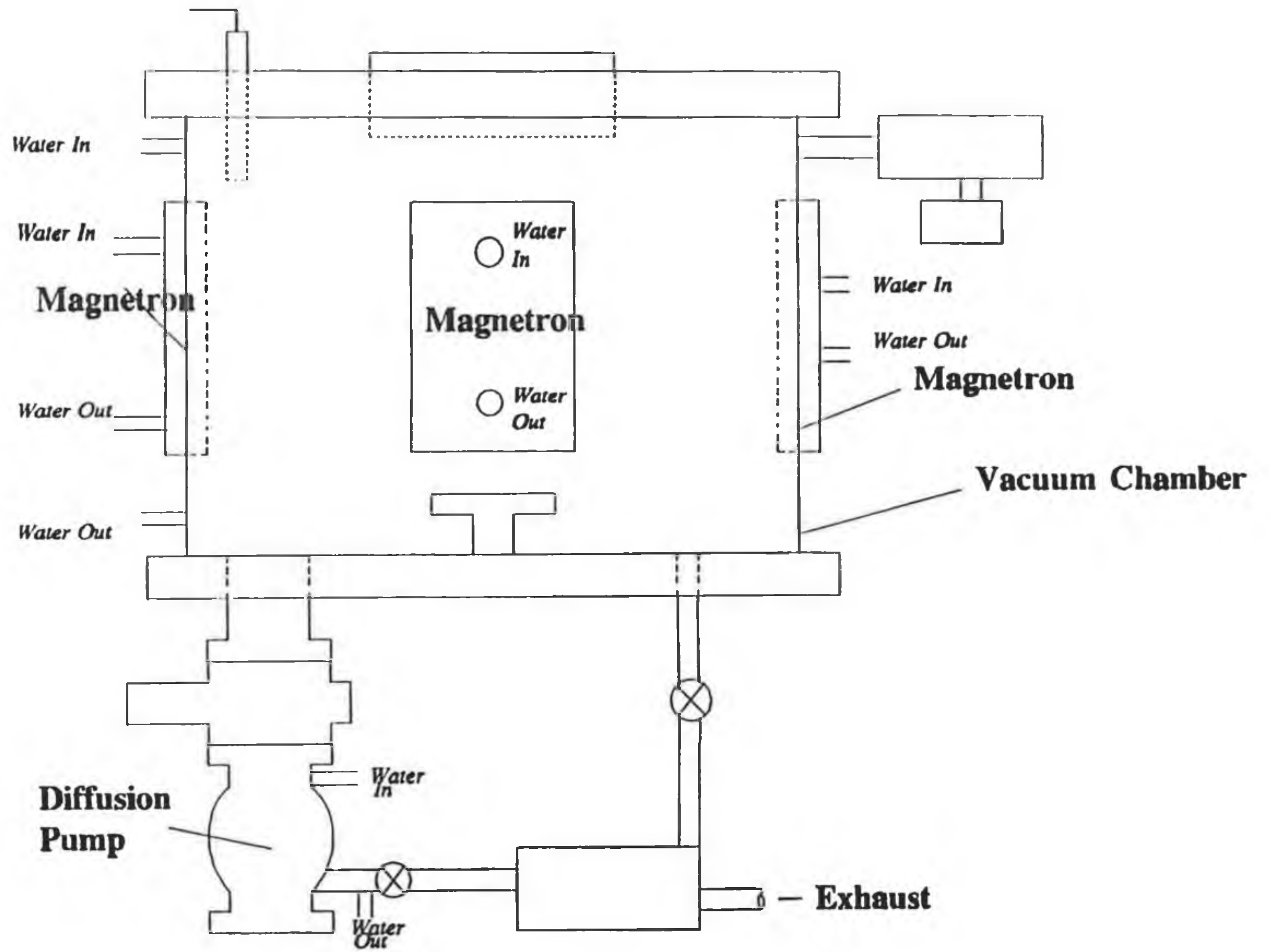


Figure 3.4 Cooling Circuit

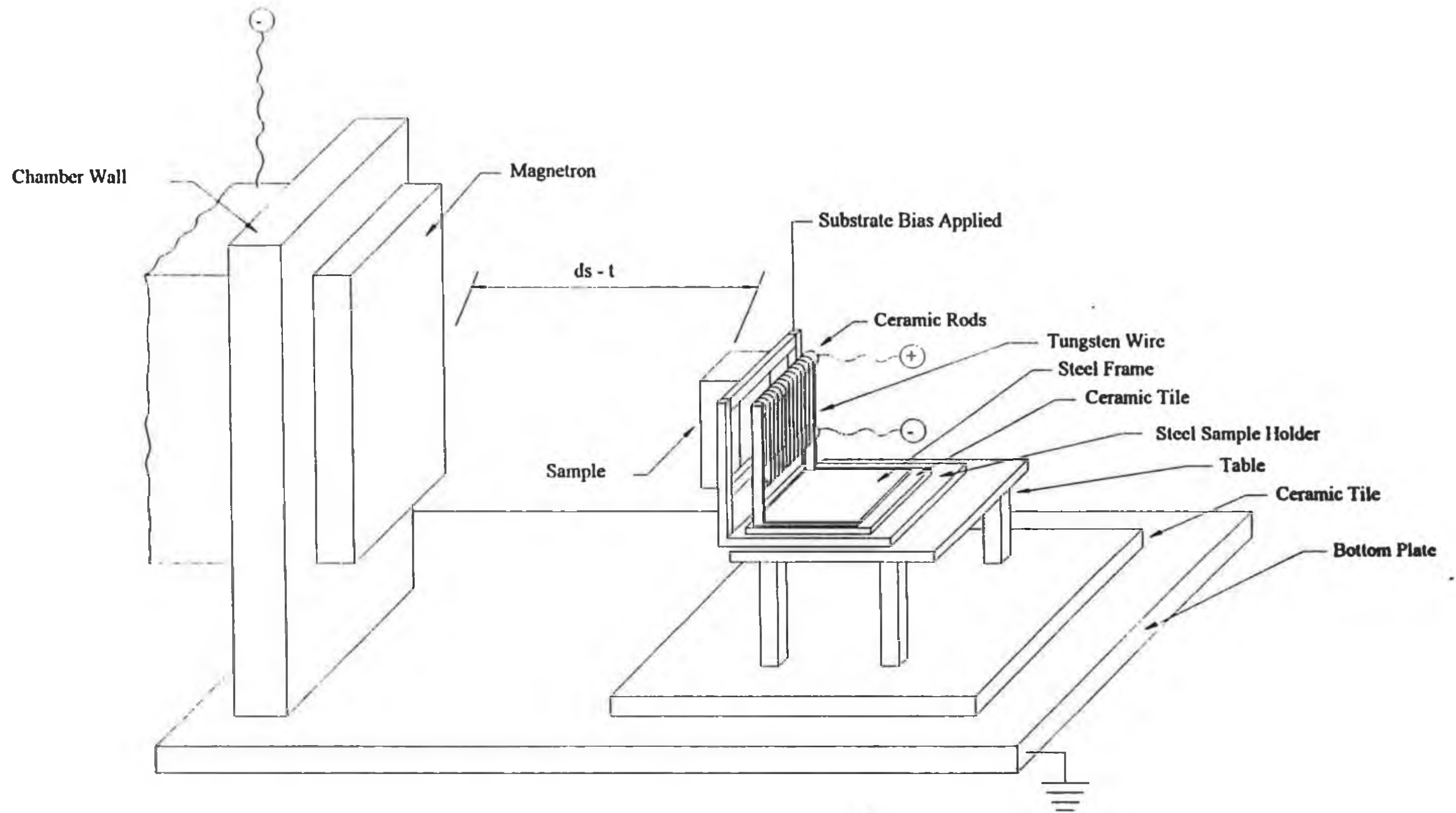


**Figure 3.5 Substrate Holder and Heater Configuration**

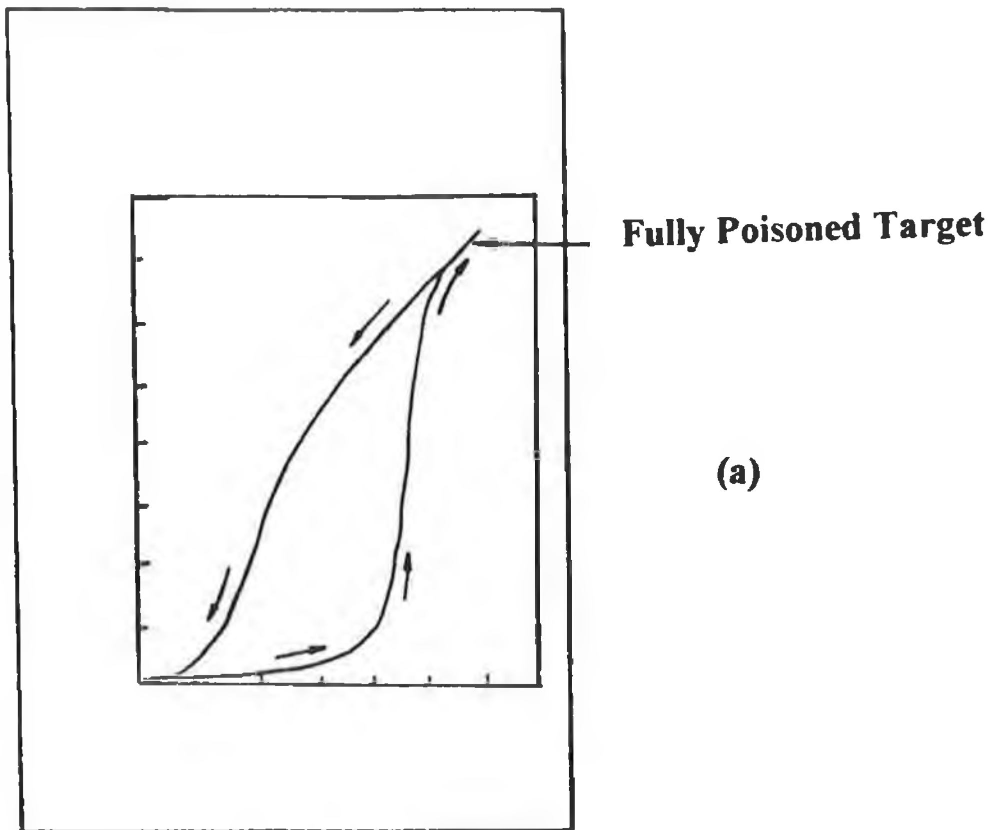


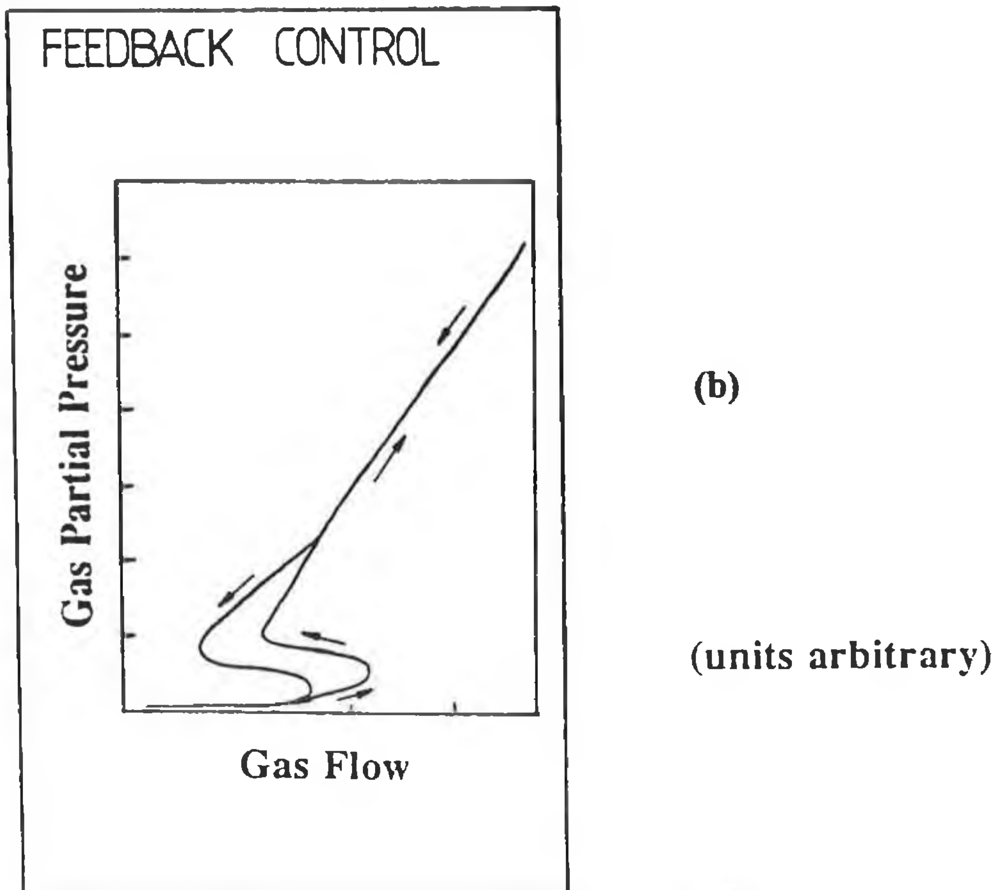


Figure 3.6 Hysteresis Loop [63]
**(a) total pressure control**
(b) partial pressure control

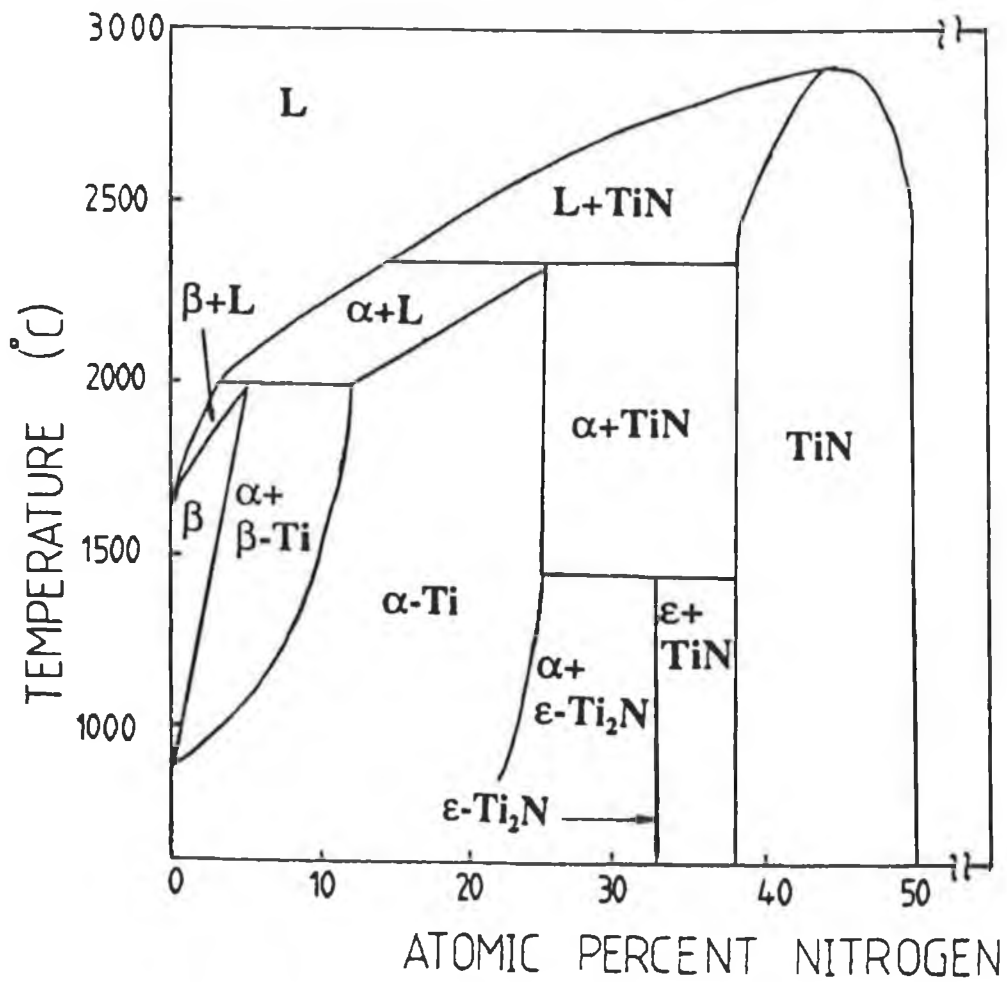


Figure 3.7 The equilibrium phase diagram for the Ti-N system [172]

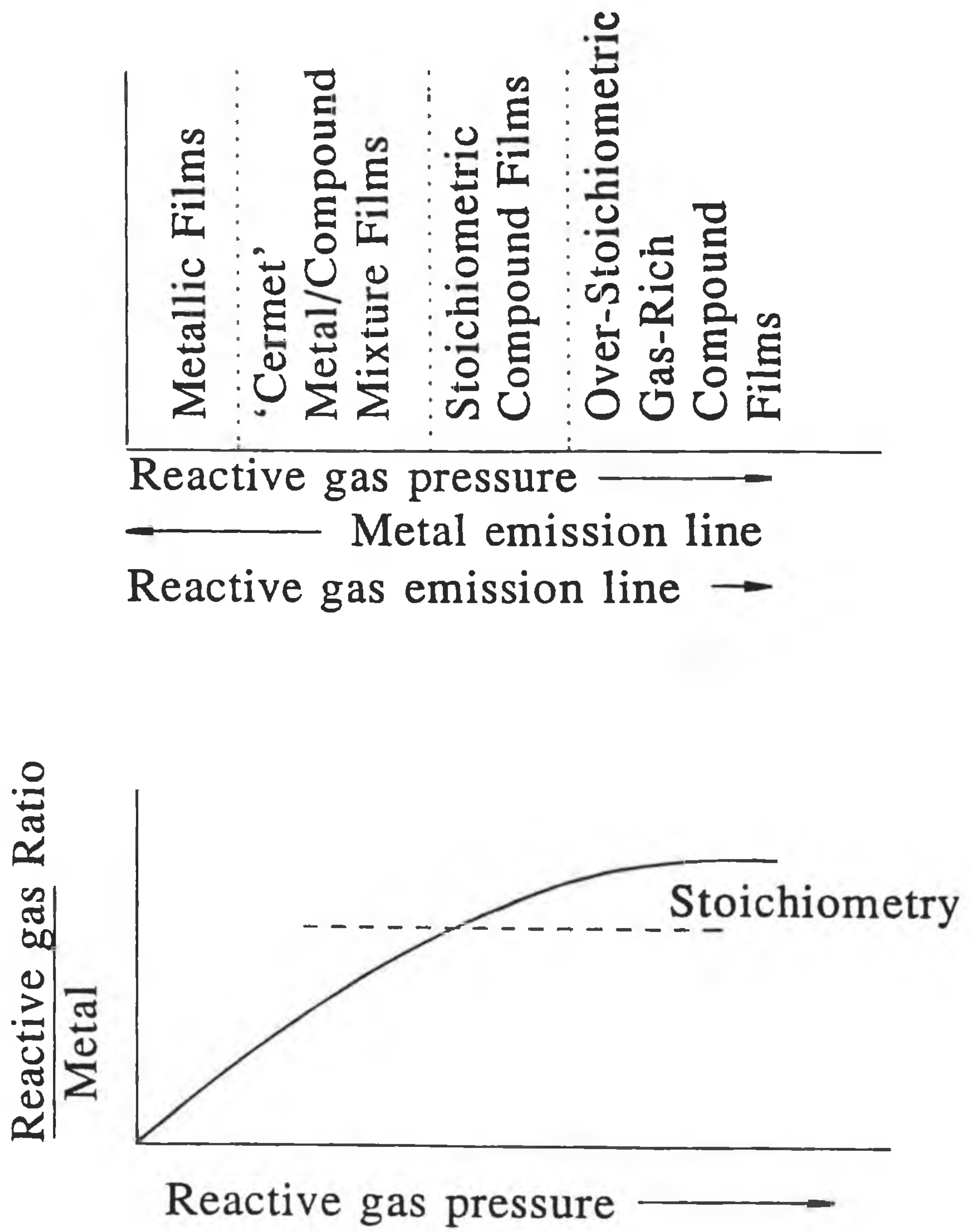


Figure 3.8 Relationship of set point to film composition

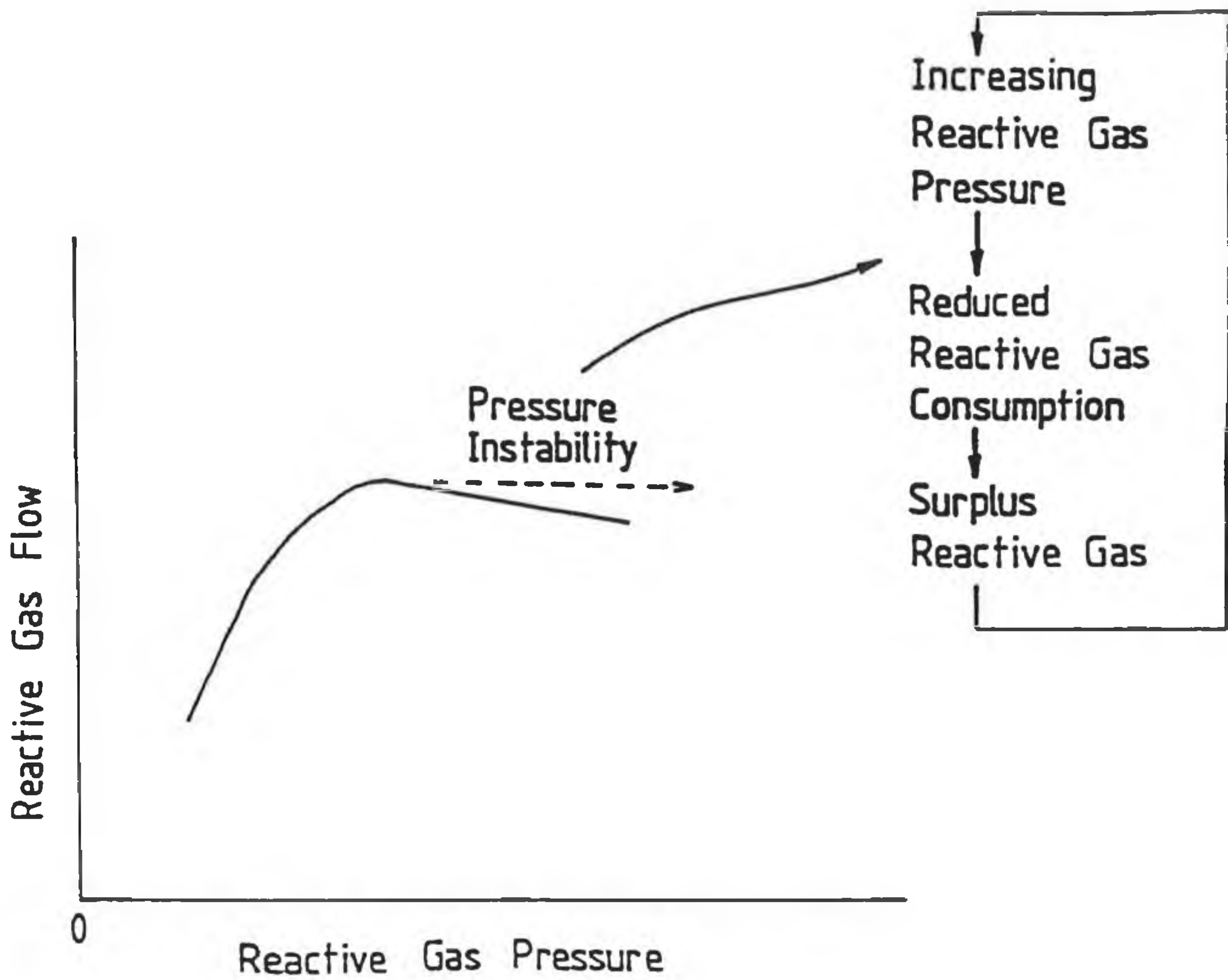


**Figure 3.9** **The mechanism that causes instability**

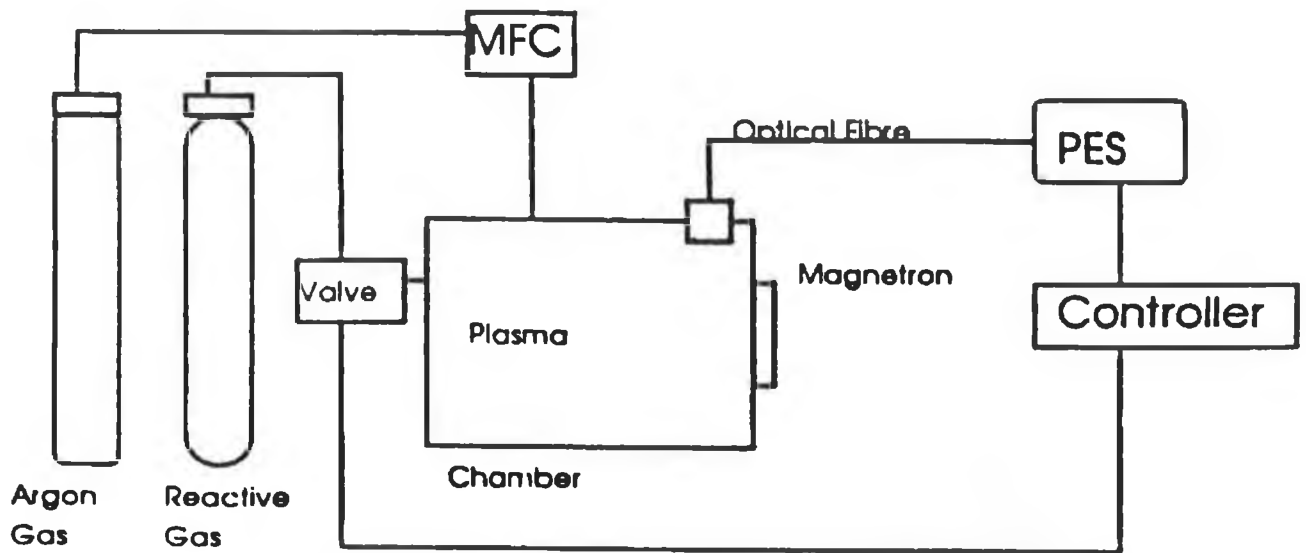


Figure 3.10 Optical Emission Feedback Loop
MFC = Mass Flow Controller
PES = Plasma Emission Spectrometer

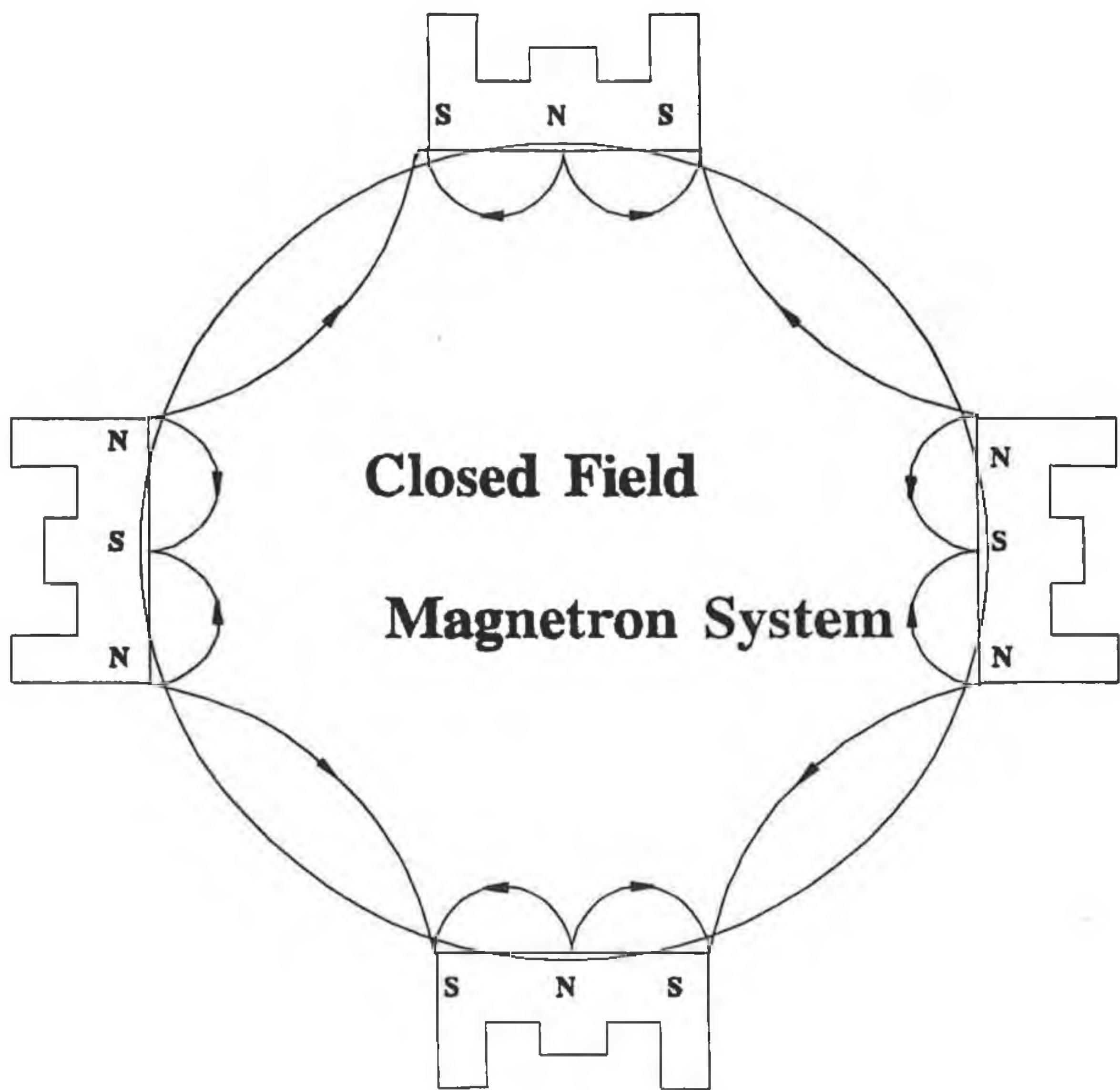


**Figure 3.11** **4-Magnetron Closed Field System**

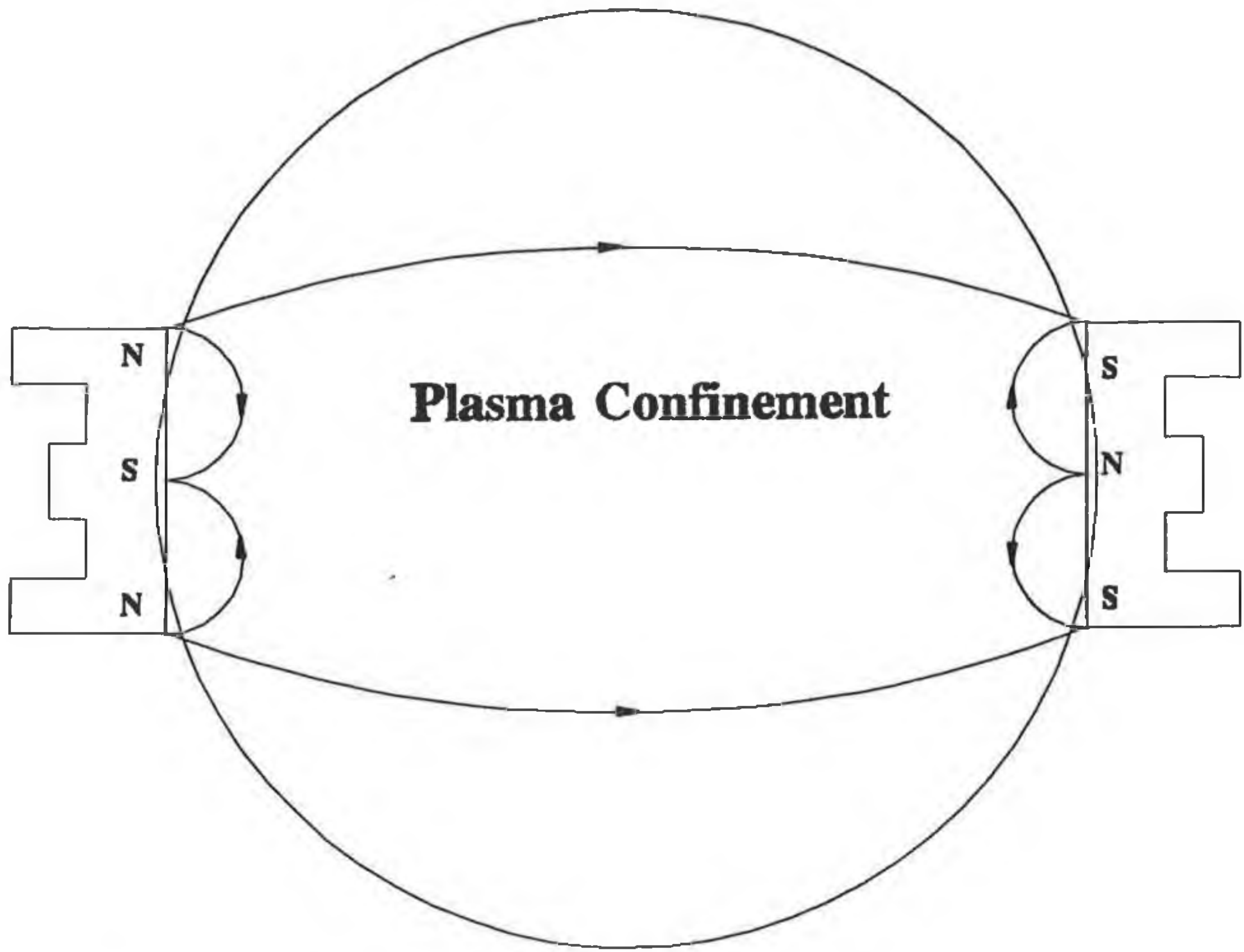


**Figure 3.12** **2-Magnetron Closed Field System**

# Chapter 4

# Measurement Techniques

# Chapter 4 Measurement Techniques

## 4.1 Introduction

The primary film properties of interest in the deposition of thin films are thickness, coating hardness, surface profile, step coverage, pinhole defects and tribological properties such as wear resistance and coefficient of friction. In addition, optical, structural, compositional and topographical information was required to assess the effect of the deposition parameters on the coating quality. Dependent on the application of the coating, different characterisation techniques were used. For some coatings, a broad spectrum of characteristics was required, necessitating the use of analytical equipment in other research institutions. In these cases, information regarding the general technique is given, whilst no specific instrument may be named.

## 4.2 Film Hardness

The hardness of a surface, defined as the average pressure under the indentor, is calculated as the applied force required to induce plastic penetration divided by the area of contact between the indentor and the specimen. Three different hardness measurement techniques were used in the characterisation of the magnetron sputtered thin films - Vickers Hardness (HV), Berkovich Hardness (HB) and Knoop Hardness (HK). In the case of Vickers Hardness, the actual surface area in used in the calculation of hardness, whereas in both Knoop and Berkovich Hardness, the projected area of contact is used. A brief outline of the calculation of the different hardness values in given below.

### 4.2.1 Vickers Hardness

The Vickers Hardness number (HV) is given by [66]

$$HV = \frac{2P \sin \theta/2}{d^2} \qquad ...(1)$$

where

| | | |
|---|---|---|
| $P$ | = | applied load (kg) |
| $d$ | = | mean diagonal of the square indenter (mm) |
| $\theta$ | = | angle between opposite faces of the diamond indenter (136°) |

The indentation cross-section for a Vickers diamond is as depicted 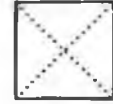

However, the Vickers hardness is found to be valid only for films where the indentation depth (d) is less than 10 times the film thickness (t). Therefore for thin films on soft substrates, a correction factor was utilised [67]. The hardness of the film was given by

$$H_f = H_s + \frac{D^2 (H_c - H_s)}{2DCt - (Ct)^2} \qquad ...(2)$$

where

| | | | |
|---|---|---|---|
| $H_f$ | = | hardness of the film ($kgfmm^{-2}$) | |
| $H_s$ | = | hardness of the substrate ($kgfmm^{-2}$) | |
| $D$ | = | normalised indentation depth (mm), ≈ 1/7 d [67] | |
| $d$ | = | measured indentation depth (mm) | |
| $H_c$ | = | hardness of the composite ($kgfmm^{-2}$) | |
| $t$ | = | film thickness (mm) | |
| $C$ | = | $Sin^2 22°$ | for plastically strained films |
| | | or | |
| | | $2 Sin^2 11°$ | for hard, brittle films on soft substrates |

### 4.2.2 Berkovich Hardness

It was found that, due to the large elastic recovery effects of the films, a more accurate hardness value could be attained by using a 3-sided Berkovich diamond pyramid indenter, where hardness is given by [9]

$$HB = \frac{P_{max}}{24.5\, h_p^2} \qquad ...(3)$$

where

$P_{max}$ = applied force (kg)

$h_p$ = plastic penetration (mm)

The indentation cross-section for a Berkovich diamond is as follows 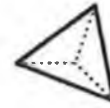

Indentation measurements were made with a commercially available ultra micro-indentation system (UMIS-2000) using a Berkovich indenter. Typically, 30 steps were used during both the loading and unloading stages with a dwell time of 0.1 seconds. The loads used were 1, 10, 30, 50 and 100 mN, with indentations made in an array of 20 at each load.

### 4.2.3 Knoop Hardness

Knoop indentation was also conducted using a pyramidal diamond having a ratio of 7 to 1 between the long and short diagonals. The longitudinal angle of 172° 30' and a transverse angle of 130° produces an indentation of approximately one thirtieth of its length. This in turn may assist in achieving a penetration depth of less than 10% of the film thickness. The Knoop hardness number (HK) is the ratio of the load applied to the indenter to the unrecovered projected area of indentation [68].

$$HK = P/A = P/(Cl)^2 \quad ...(4)$$

where $P$ = applied load (kg)

$A$ = unrecovered projected area ($mm^2$)

$l$ = measured length of the long diagonal (mm)

$C$ = 0.07028, a constant of the indenter

The indentation cross-section is as depicted 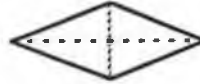

The values quoted were again subject to the correction for thin films as described in section 4.2.1

## 4.3 Film Thickness

Film thickness is a good indication of the deposition rate of a sputtered material, but due to the extremely thin coatings deposited in magnetron sputtering, several thickness measurement techniques were employed. Some proved to be more successful than others, but all reflected the difficulty in assessing accurately the thin film thicknesses. The techniques are outlined below.

### 4.3.1 Surface Profilometry and Thickness

A contact-type Surftest Profilometer was used to evaluate film thickness easily by measuring the step increase between the uncoated substrate and the coated substrate, *figure 4.1*. The procedure is the same as that in the measurement of surface roughness, which is measured along a single line profile, and is characterised as the arithmetic average of the heights of the peaks and troughs of the surface. The Surftest profiler measures the average height of the irregularities from the mean line along a specified sample length. The mean line is defined such

that the area between the surface profile above and below the mean line are equal. The stylus instrument amplifies and records the vertical motion of a stylus while moving at a constant velocity relative to the specimen surface. By positioning the stylus over the uncoated portion of the sample, and allowing it to traverse along a path such that it crossed the uncoated/coated boundary onto the coated sample side, a measure of the coating was given. However, it was found that the `step' was not as sharp or well-defined as anticipated, *figure 4.2*.

### 4.3.2 Interferometry

An interferometer was also used to measure the thickness of the deposited film. Interference occurs when radiation from the same source follows more than one path to the point of detection. When a path difference is present, a set of fringes can be seen as light and dark bands called interference fringes. This phenomenon is one illustration of the wave nature of light [69]. A sample is masked and coated, allowing a portion of the substrate to remain uncoated. An interferometric microscope is used to observe the fringe pattern obtained from the monochromatic light reflected from the uncoated and coated side of the sample. If there is a difference in height between the two sides of the specimen , the fringe pattern will appear to be shifted as it crosses the edge between them, figure 4.3. Two adjacent fringes are separated by half the wavelength of light ($\lambda/2$). The step on the specimen surface displays the fringe pattern and this is a measure of the difference in height between the coated and uncoated specimen sides. The coating thickness is measured as the displacement or shift of the fringe pattern at the step area. The shift in fringe patterns is counted and thickness calculated thus

$$t = d/s \times \lambda/2 \qquad \text{...(5)}$$

where d, s are as shown in *figure 4.3*

$\lambda$ = 550 nm, in this case

t = film thickness

This was a more convenient method of evaluating film thickness, although it is only really applicable where both the substrate and coating are reflective and film thickness is large (>0.2μm), enabling the interference patterns could be clearly distinguished.

### 4.3.3 Thickness - Ball Cratering

Film thickness for steel samples was measured using a ball cratering device as described in European Standard No. CEN/TC184/WG5. and is depicted in *figure 4.4*, where a hemispherical crater is worn onto the specimen at the contact point with a 50mm diameter steel ball. The ball sits in a V-groove on an axle, and a small amount of ¼μm diamond paste is placed on the ball which is friction driven and wears a hemispherical cap onto the sample. The lengths a and b *figure 4.4* were measured using an optical microscope and using the following equation, the thickness was calculated. R is the radius of the steel ball.

$$t = \left(R^2 - b^2\right)^{1/2} - \left(R^2 - a^2\right)^{1/2}$$

$$or$$

$$t = R\left(\left(1 - \frac{b^2}{R^2}\right)^{1/2} - \left(1 - \frac{a^2}{R^2}\right)^{1/2}\right)$$

$$If$$

$$\frac{a^2}{R^2} and \frac{b^2}{R^2} << 10^{-3}$$

then the following simplification can be used:

$$(1-e)^n = 1 - ne$$

$$\therefore t = \frac{1}{2R}\left(a^2 - b^2\right)$$

...(6)

## 4.4 Wear - Abrasive Wheel

Abrasive wear tests were conducted on a modified ASTM G105-89 rubber wheel abrasion tester, *figure 4.5*. The rubber wheel consisted of a 5mm neoprene rubber layer chemically anchored to the outer rim of an aluminium disc. The rate of revolution of the wheel remained constant under load, and a wheel revolution counter was used to count the number of revolutions to failure. Wear resistance of the sample was defined as the number of revolutions required to achieve penetration of the film. The specimen holder was attached to the lever arm to which a 1 kg weight was added. The slurry chamber was filled with 5.4 litres of deionised water to which 3 kg of 1$\mu$m alumina powder had been added. The test specimen was pressed against the wheel while the grit abraded the sample.

Failure of the sample was difficult to ascertain, and the test produced qualitative results, subject to human operation. However, all the tests were conducted in the same manner and all wear scars were of similar appearance.

## 4.5 Friction - Pin-on-disk

The coefficient of friction was measured on an Implant Sciences Corporation ISC-200PC Tribometer. This was a pin-on-disk type wear and friction measurement system, consisting of a tribometer and a computer for data acquisition. A test disk mounted in a cup that revolved on a vertical axis, came in contact with a pin attached to a precision balanced lever arm which was

used to apply vertical loads to the pin and to read the friction force on the pin. A load cell on the top platform measured the reaction friction force when hooked to the lever arm. The analog friction output signal was transmitted to the computer, and a friction coefficient was displayed on the screen. Information on the pin/disk material can be entered into the computer for Hertzian pressure calculation between the pin and disk. The apparatus is shown in *figure 4.6*.

## 4.6 Electrographic Printing

In order to assess the protective properties of a film in a corrosive environment, it is important to know the defects present on the film surface. These are all possible locations for coating failure by the loss of adhesion or corrosion initiation. Electrographic printing is a technique used in the visual assessment of such defects on the films. The technique is outlined below.

If the sample material can be anodically dissolved, and this reaction is followed by a colour coupling reaction specific to the generated metallic ions of the sample material, and if this coloured reaction product can be fixed on a substrate, the method is called autography or electrographic printing [70-73].

The apparatus and materials for imaging of Fe/TiN systems are:

1) a hydraulic press
2) dye transfer paper (Kodak, Type F)
3) Nitroso-R-Salt in water (1g/l)(1-Nitroso-2-Naphthol-3,6-Disulphonic Acid-Disodium Salt,1% in water)
4) Filter Paper
5) a membrane filter (Millipore type HA 0.45μm)
6) a power supply

Printing results are ruled by the sensitivity i.e. colour density per consumed iron ions. The larger the defect/pore/pinhole, then the more iron ions consumed, and the more noticeable the colour, So, the points of colour (green for Fe and Nitroso-R-Salt) are the locations and sites/shapes of the pinhole defects.

The basic process is as follows. A piece of dye transfer photographic paper is soaked in a dilute electrolyte solution and pressed firmly against the surface to be examined. A potential of between 0.5V to 10V d.c. is applied for several seconds to a few minutes across a sandwich formed by the sample (anode), and a metal cathode separated by filter paper soaked in dilute electrolytic solution, as shown in *figure 4.7*. The Millipore membrane filter is placed on the gelatinous side of the dye-transfer paper.

Cations from the underlying metal at pores or cracks in protective coatings, *figure 4.8*, are formed under the influence of the applied potential. These enter the gelatinous surface of the dye transfer paper and react with the chemicals to form coloured precipitates or soluble complexes. Cracks are shown on the print [73] as coloured lines, while pores appear as coloured dots. Mirror images of crack patterns and pore sites are produced. In order to avoid lateral diffusion of the coloured precipitates, excess electrolyte must be removed by subjecting the printing paper to pressures of up to 170 bar.

## 4.7 Ellipsometry

To measure the refractive index of the materials sputtered, thin films were deposited onto soda-lime glass slides for examination by ellipsometry.

Ellipsometry is a technique for the contact-less and non-destructive characterisation of surfaces. Measurements on thin films are made under the assumption that there is an abrupt interface between the substrate and the film. When two linearly polarised light waves with the same wavelength are combined in phase, the resultant wave is also linearly polarised. However, when

two linearly polarised beams are combined out of phase, they appear, when viewed end on, to follow an elliptical path. If the phase difference is 90°, the wave takes on a circular path. Ellipsometry is based on the fact that a monochromatic and linearly polarised electromagnetic wave changes its state of polarisation if it strikes an interface between two dielectric media in a non-perpendicular fashion. When light passes from one medium to another, some of the incident light is reflected whilst some enters the second medium. We denote the phase difference between the parallel component and the perpendicular component of the incident wave as $\delta_1$ and the phase difference between the parallel component and the perpendicular component or the outgoing wave $\delta_2$, *figure 4.9*. Then delta ($\Delta$) is given as [74]

$$\Delta = \delta_1 - \delta_2 \qquad \text{...(7)}$$

or the change in phase difference that occurs upon reflection. Ellipsometry, based on the reflection of light from the surface of a sample, measures the change in phase difference ($\Delta$) between the incident and reflected waves, and the ratio of the magnitudes of the total reflection coefficients ($\Psi$) such that [74]

$$\tan \Psi \, e^{j\Delta} = \frac{R^p}{R^s} \qquad \text{...(8)}$$

where

| | | |
|---|---|---|
| $R^p$ | = | Reflectance in plane of incidence |
| $R^s$ | = | Reflectance normal to plane of incidence |
| $e^{j\Delta}$ | = | exponential complex notation of $\Delta$ |
| $\Delta$ | = | phase difference between incident and reflected waves |

Calculations based on $\Delta$ and $\Psi$ and the index of refraction (n) for the substrate and the angle of incidence of the light beam ($\phi$) will yield values for the index of refraction (n) and the coefficient of extinction (k) for a film on a substrate.

Based on plots of $\Delta$ vs. $\Psi$, with different incident beam wavelengths ($\lambda$) and incident angle ($\phi$), different values of n, the refractive index can be plotted . The curve on which the measured point, given by co-ordinates ($\Psi$,$\Delta$), falls, indicates the refractive index of the film. The position on which it falls indicates the thickness of the film [74,75].

Ellipsometric measurements were made on an Auto EL-3 Rudolph Research null ellipsometer.

## 4.8 Infra-Red (IR) Spectroscopy

To measure the absorption of thin films and to ascertain the bonds within the film, samples were deposited onto Si(100) samples. In infra red spectroscopy, the molecule is irradiated with a whole range of infra-red frequencies but is only capable of absorbing radiation energy at specific frequencies which match the natural vibrational frequencies of the molecule and these occur in the infra-red region of the electromagnetic spectrum. The dipole moment is defined as the magnitude of either charge in the dipole multiplied by the charge spacing. If an atom has the same number of protons and electrons, it is electrically neutral and does not contribute to the dipole moment. However, chemical forces in the molecule tend to redistribute the electrons so that a given atom may have a little electron excess or deficiency, and may be considered a particle with a small negative or positive charge. Unlike the fixed charge on an electron or proton, the charge on an atom may change due to molecular vibration induced by IR excitation. If the negatively charged atom vibrates in one direction, and the positively charged one in the opposite direction, the vibration is IR active. If, however, the vibrationally-distorted molecule retains the centre of symmetry so that the dipole moment is unchanged, the vibration is IR inactive. The natural symmetry in molecules is affected by in-phase stretching, bending and rotational effects, all of which are IR active. In polyatomic molecules, where there is no symmetry, IR inactive vibrations arise [76]. Anti-symmetric vibrations however, are IR active. IR measurements were conducted on a Nicolet 205 Fourier Transform Infra Red instrument.

## 4.9 Raman Spectroscopy

Further examination of the absorption of films was conducted using Raman spectroscopy. If the sample is irradiated with an intense source of monochromatic radiation, whose frequency is generally much higher that the vibrational frequencies, radiation scattering occurs. The Raman effect is the inelastic collision between incident photons and the molecules where, as a result of the collision, the vibrational or rotational energy of the molecule is changed by an amount $\Delta E_m$. The energy of the scattered photon $hv_s$ must be different from the energy of the incident photon $hv_i$ by an amount equal to $\Delta E_m$. In Raman scattering, the frequency of the incident photon is usually much greater than the molecular frequency $v_m$. If a molecule gains energy then $\Delta E_m$ is positive and $v_s < v_i$ which results in Stokes lines in the Raman spectrum. If a molecule loses energy, $\Delta E_m$ is negative and $v_s > v_i$ which results in anti-Stokes lines in the Raman spectrum. In order for a molecular vibration to be Raman active, the vibration must be accompanied by a change in the polarizability of the molecule [76].

Raman data were recorded using a Renishaw Raman Imaging Microscope, with an operating range of $\approx$150-7000cm$^{-1}$. Acquisition times were kept short (typically 10s) to avoid, as much as possible, surface damage.

## 4.10 X-Ray Diffraction (XRD)

A Phillips XRD was used in the standard powder diffraction mode, using 40kV at 20mA current.

XRD is a non-destructive method of structural analysis of thin films [77]. The analysis of the angular position and intensity of X-rays diffracted by crystalline material can reveal information on the crystal structure and crystalline phases present in the sample. X-ray diffraction occurs when the Bragg requirement satisfies [77]

$$n\lambda = 2d\sin\theta \qquad ...(9)$$

where $\lambda$ = x-ray wavelength (nm)

$d$ = interplanar spacing (nm)

$\theta$ = Bragg diffraction angle

$n$ = integer giving order of the diffraction

The diffractometer is designed to disperse x-rays of a single wavelength by diffracting them from planes of different spacings.

## 4.11 X-Ray Photoelectron Spectroscopy (XPS)

When high energy photons in the X-ray range are used, and electrons are emitted, the technique is called X-ray Photoelectron Spectroscopy (XPS). This is used to define the electronic structure of solid surfaces as well as to chemically identify surface components.

The bombardment of material by X-rays result in the ejection of electrons from the material. When monoenergetic X-rays are used, the kinetic energy of the ejected electrons $E_k$ is determined by the difference between the binding energy of the electron $E_b$ and the energy of the X-ray photon hv. If the kinetic energy of the ejected electron is determined, the binding energy of the electrons can be evaluated from [78]

$$E_b = hv - E_k \qquad ...(10)$$

The radiation is obtained from X-ray tubes with Al or Mg anodes which give lines at 1487eV and 1254 eV respectively. This technique can be used to identify atoms at surfaces by comparing the lines observed with either calculated core level binding energies or experimentally derived spectra from standards [78].

Low-energy resolution XPS was conducted using a Kratos XSAM 800 instrument, with spectra recorded using a non-monochromated MgKα X-rays (hν = 1253.6eV) at an anode operating power level of 240W (20mA emission current, 12kV applied voltage, respectively). The electron take-off angle was 90° with reference to the incident beam. The depth of the analysis was typically ≈30-50 Angstroms.

High-energy resolution XPS spectra were recorded using a Scienta ESCA 300 Instrument, using monochromated AlKα X-rays (hν=1486.6eV), at an operating power level of 2.8kW (200mA emission current, 12kV applied voltage). The electron take-off angle in this instance was 45°. In both cases a low energy electron flood source was used to compensate for charge build-up during spectral acquisition and all peaks were additionally charge compensated by setting the lowest binding energy (B.E.) component of the C1s envelope to a value of 285.0eV and adjusting other spectral lines appropriately.

## 4.12 Atomic Force Microscopy (AFM)

AFM relies on the attractive or repulsive forces between the tip of a stylus and the underlying substrate. It can operate in the repulsive (or contact) mode or the attractive (or non-contact) mode. The repulsive mode is in essence a micro-profiler using forces of $10^{-8}$ to $10^{-9}$ N. In the non-contact mode, the tip is positioned 40-50 Angstroms above the surface. Because the tips are very light, they can be moved at high speed, and 3 dimensional images can be reconstructed at near video speeds [78].

AFM surface analysis of the films was performed using contact mode and normal pyramid-shaped micro fabricated tips on a Rasterscope instrument, which tends to give a rectangular shape to round perturbations having dimensions close to that of the tip radius (200 nm).

## 4.13 Secondary Ion Mass Spectroscopy (SIMS)

SIMS is a surface analytical technique which employs a beam of low energy ions to sputter secondary ions (neutrals and electrons are also produced) from a sample surface. The positive and negative ions are mass detected in a quadrupole mass spectrometer adjacent to the sample normal. SIMS has a surface sensitivity in the parts per million range with high spatial and depth resolution [78]. SIMS can be operated in either a static or dynamic mode. In static SIMS, a low current density is employed so that the analysis is confined to the detailed chemical state of the outermost layer. In dynamic SIMS, high ion current densities erode the surface enabling depth profiles of thin films to be obtained. This mode is a destructive analytical technique.

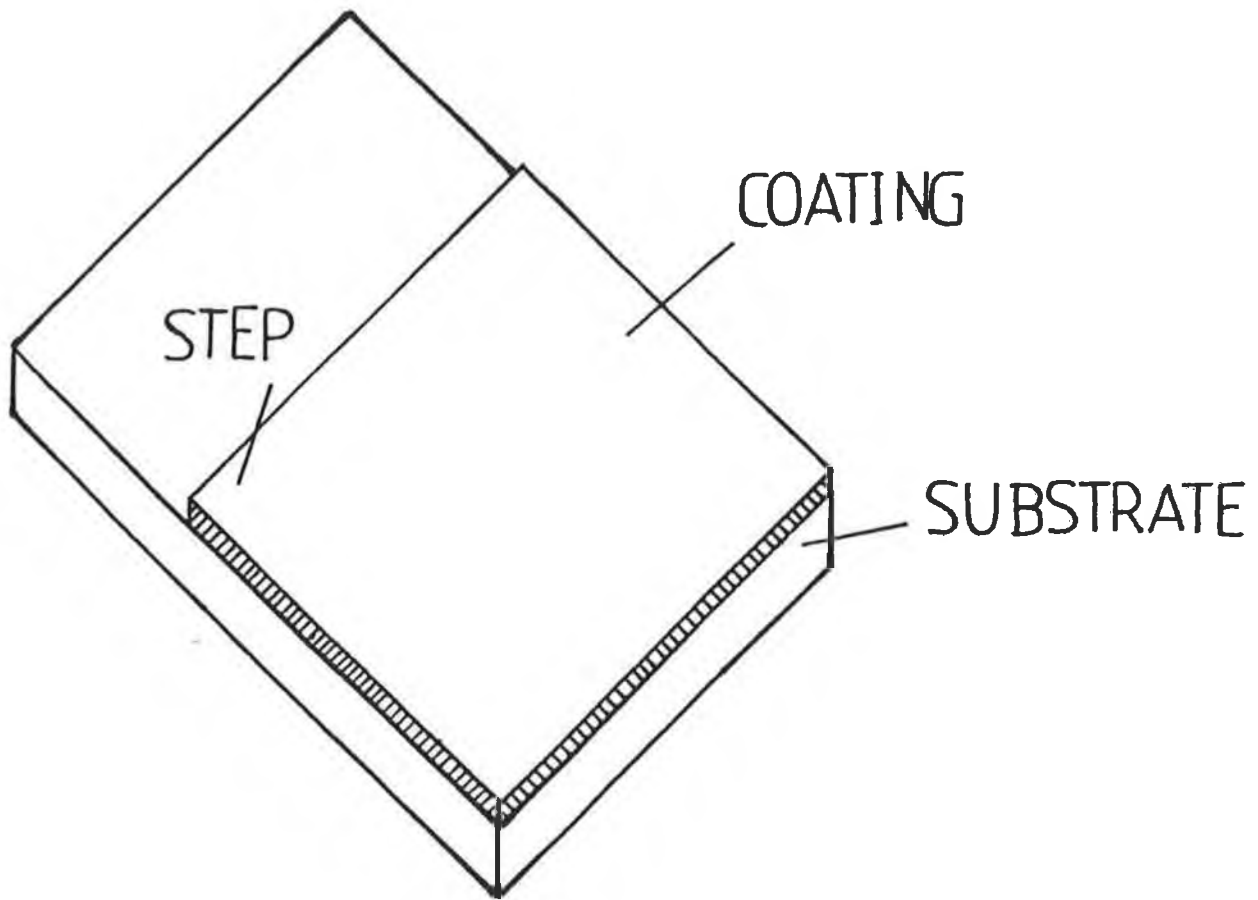


**Figure 4.1** **Step Coverage**

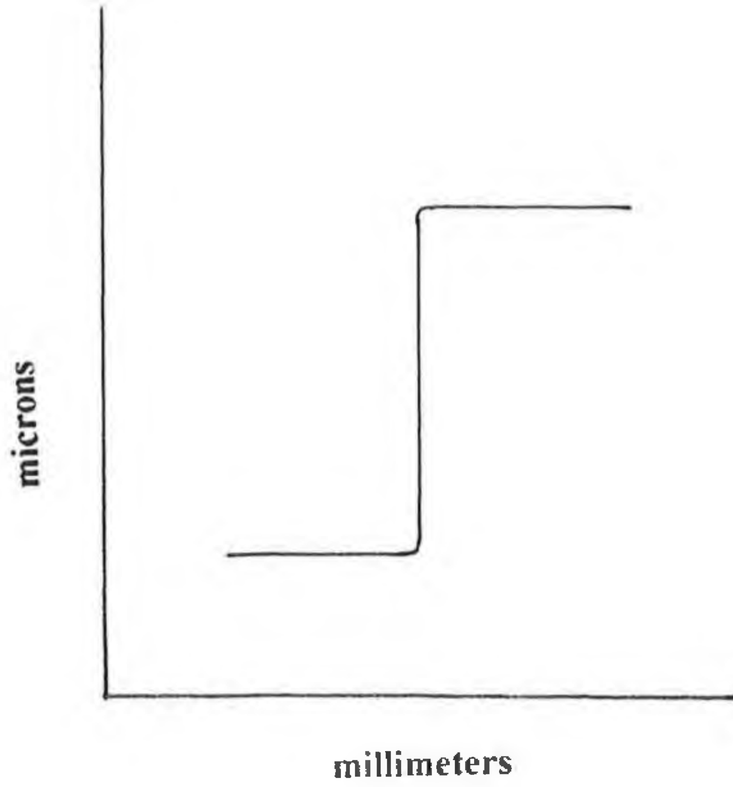


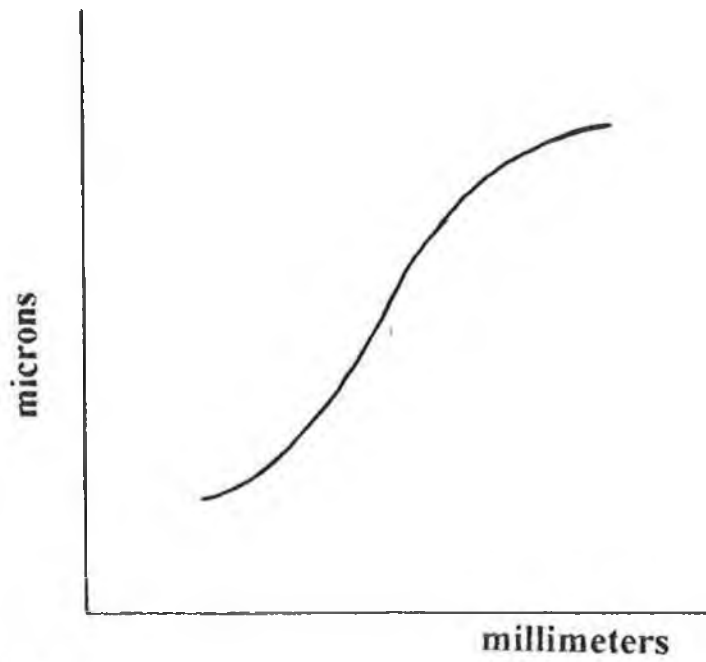


Figure 4.2 **Step Coverage**
**(a) Theoretical**
**(b) Surftest Profile Actual**

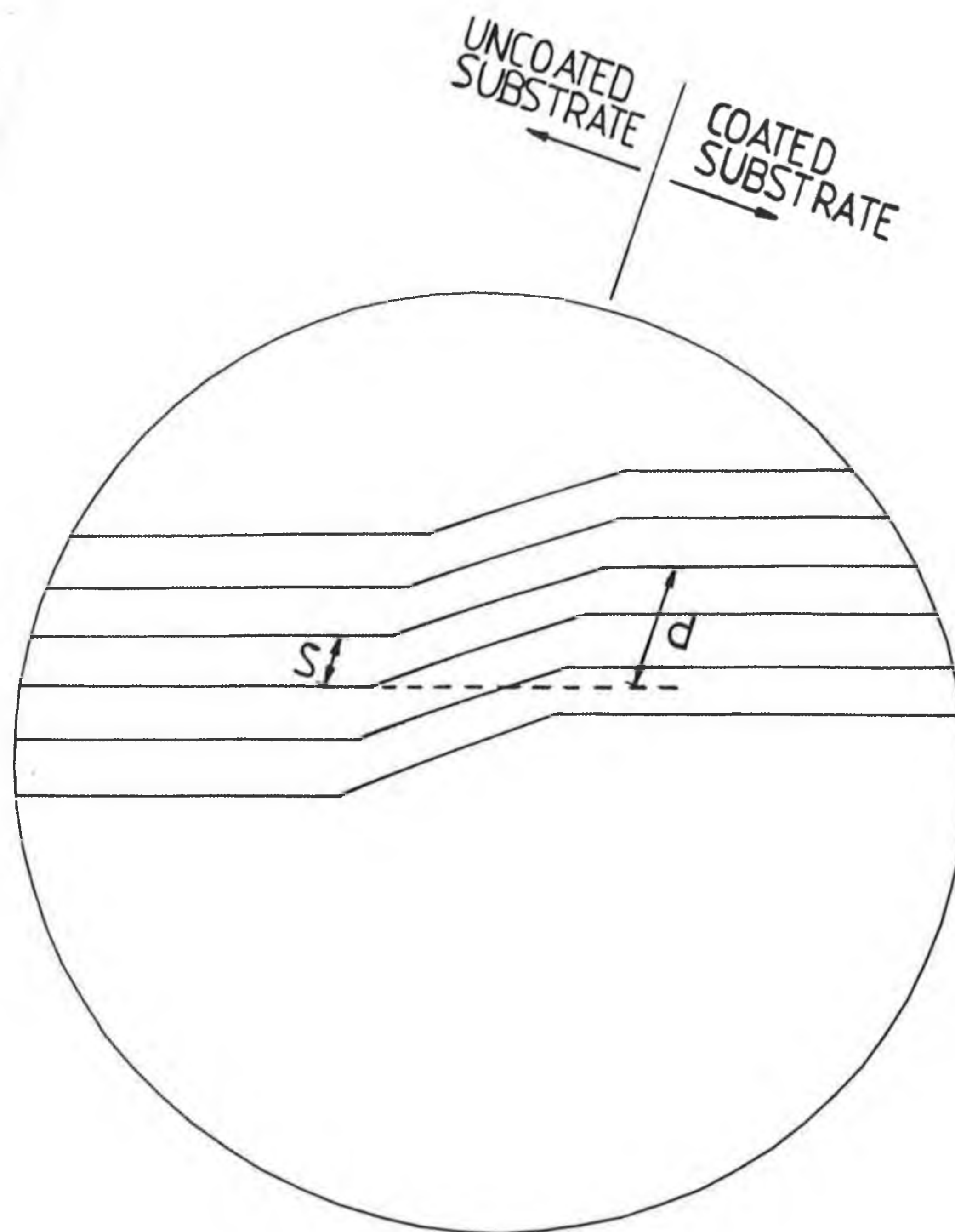


**Figure 4.3** **Interference Patterns**

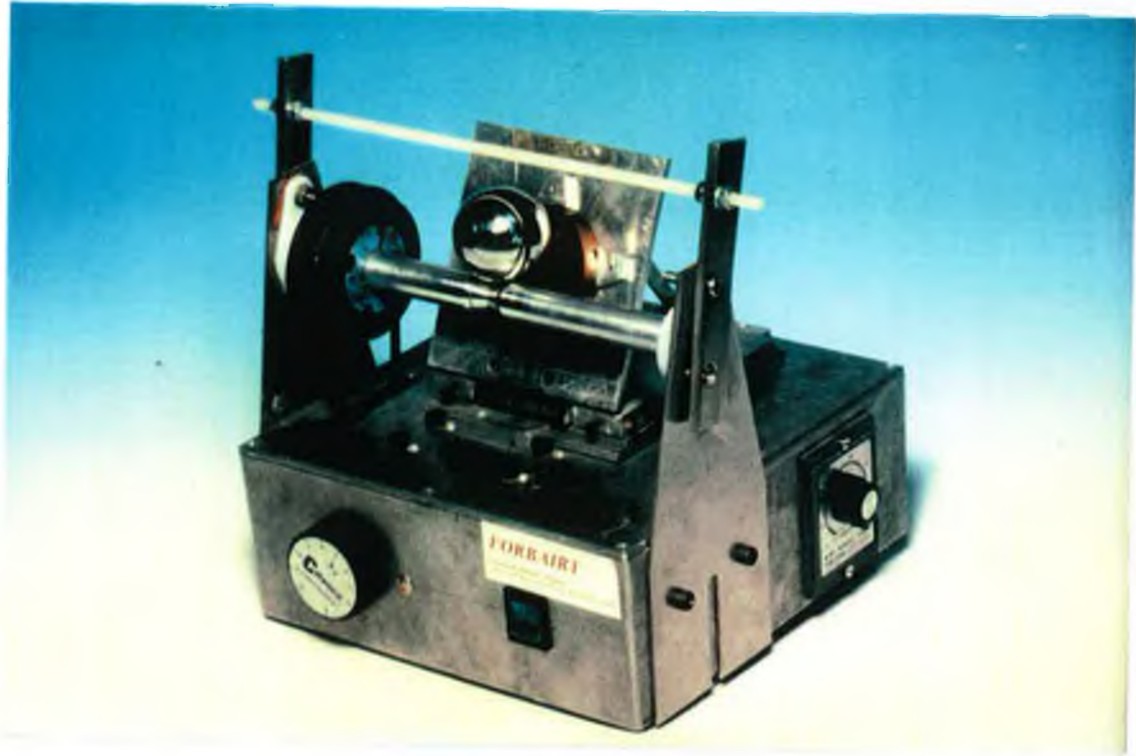

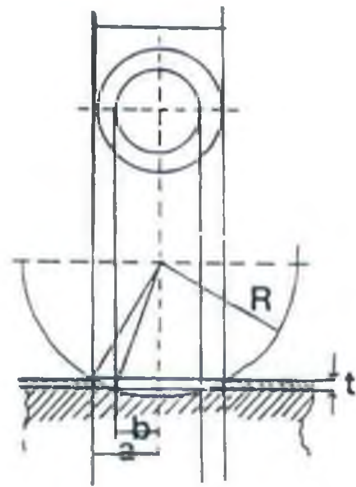


Figure 4.4 Ball Cratering Device

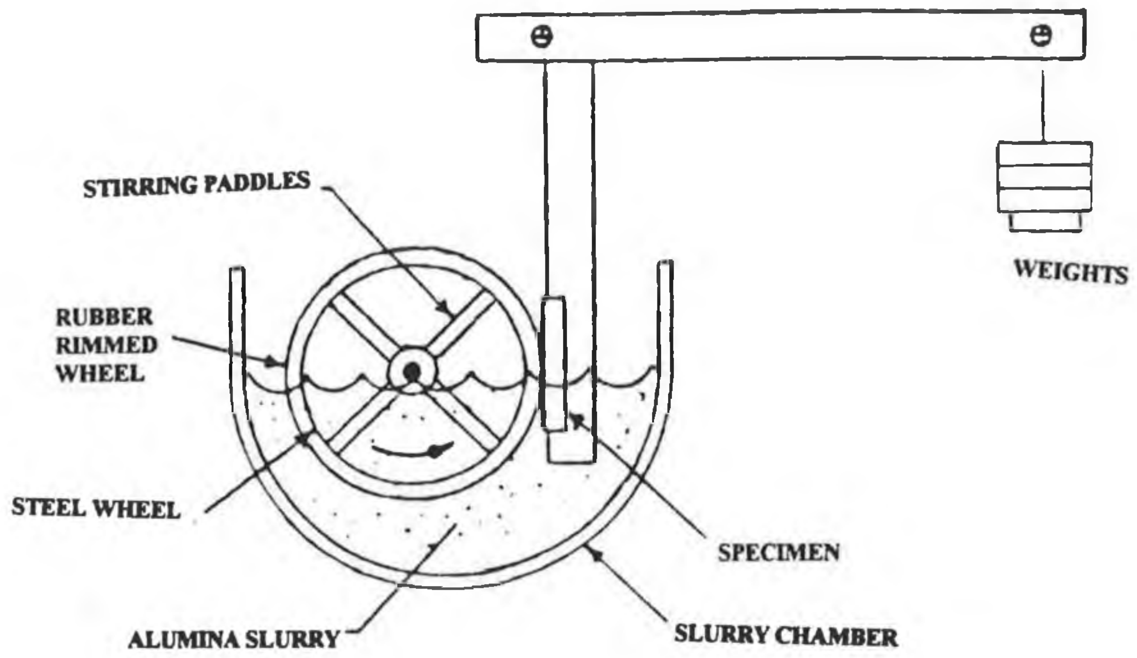


Figure 4.5 Abrasive Wheel Tester

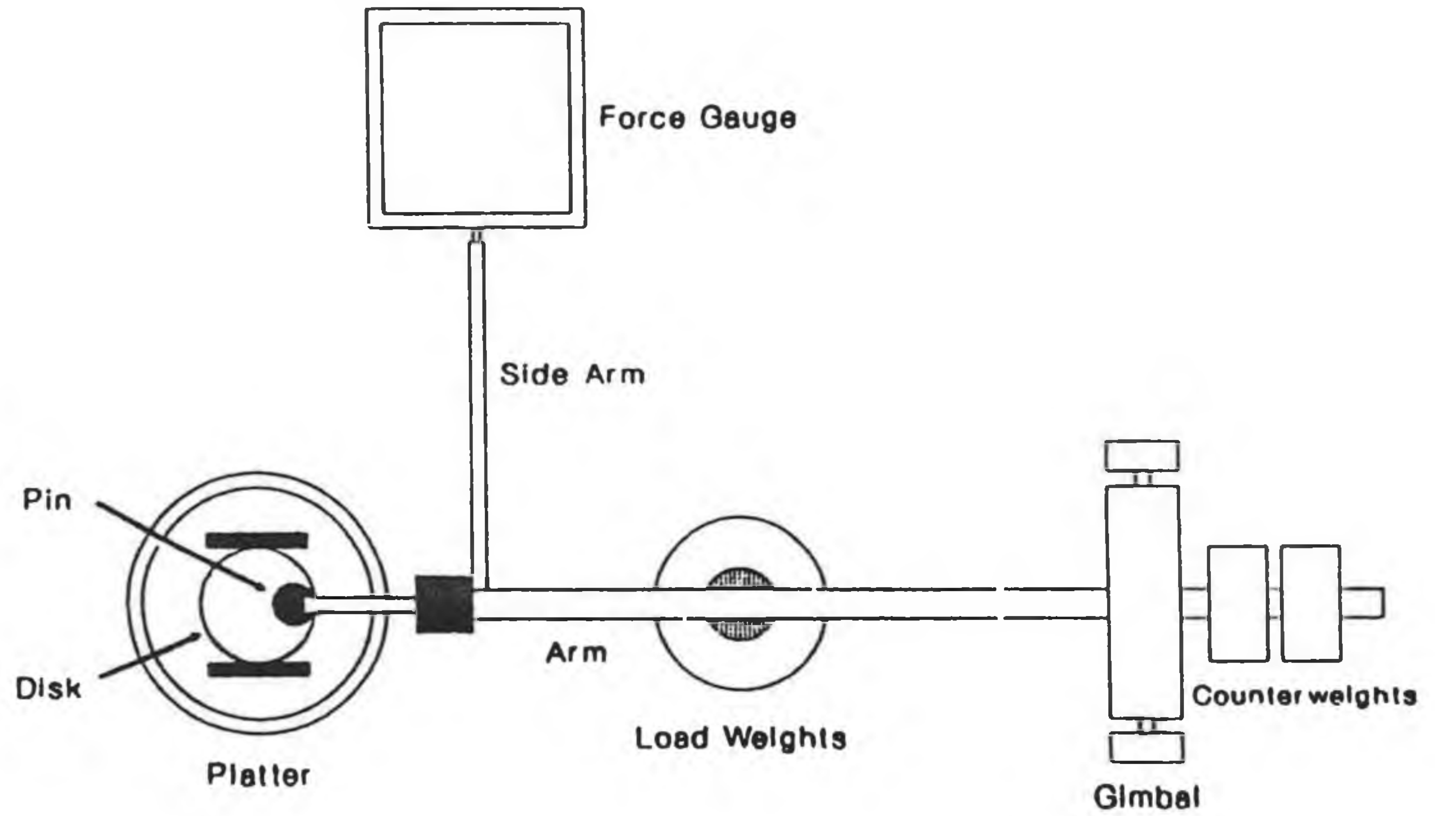


**Figure 4.6** **Pin-on-disk Tester**

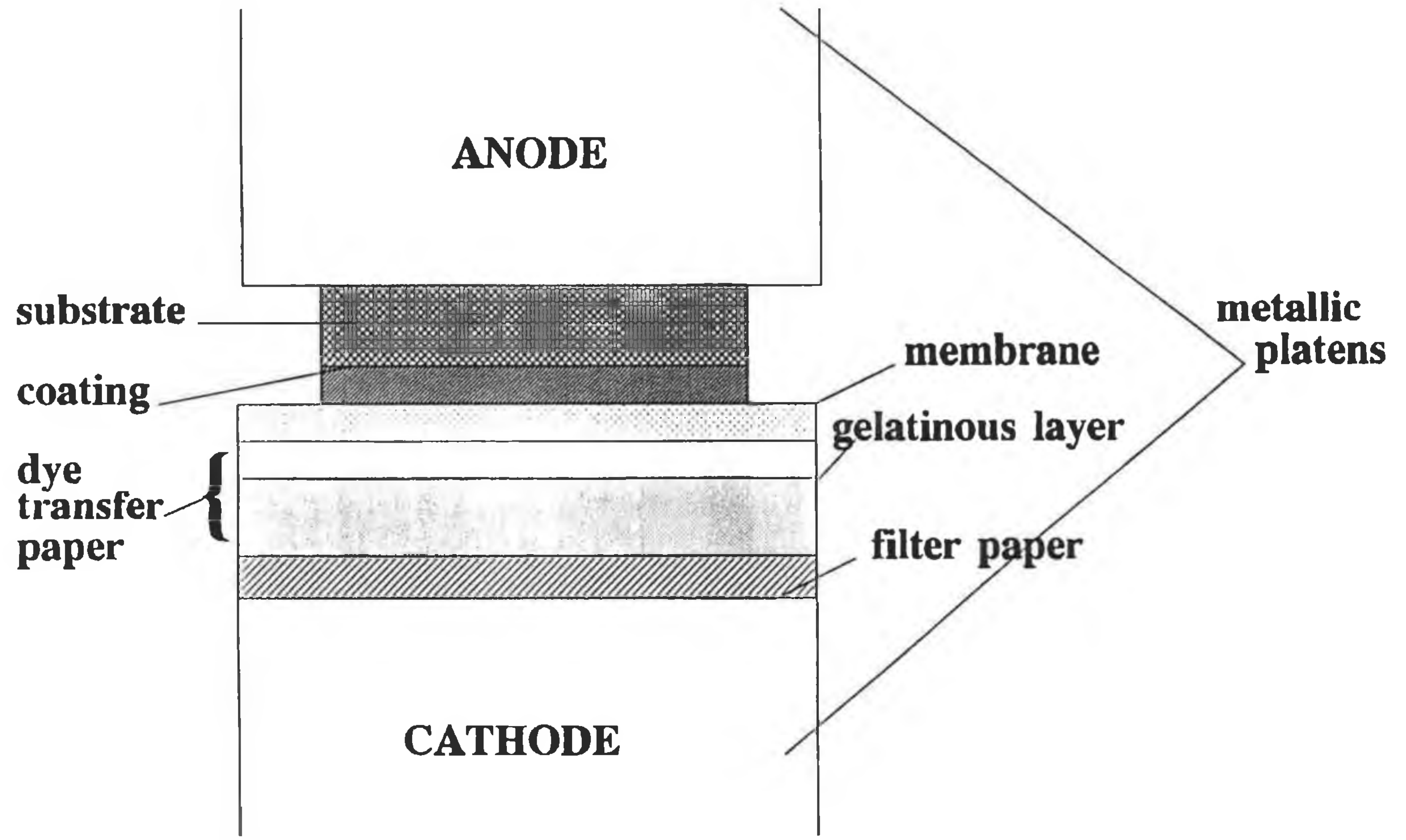


Figure 4.7 Electrographic Printing

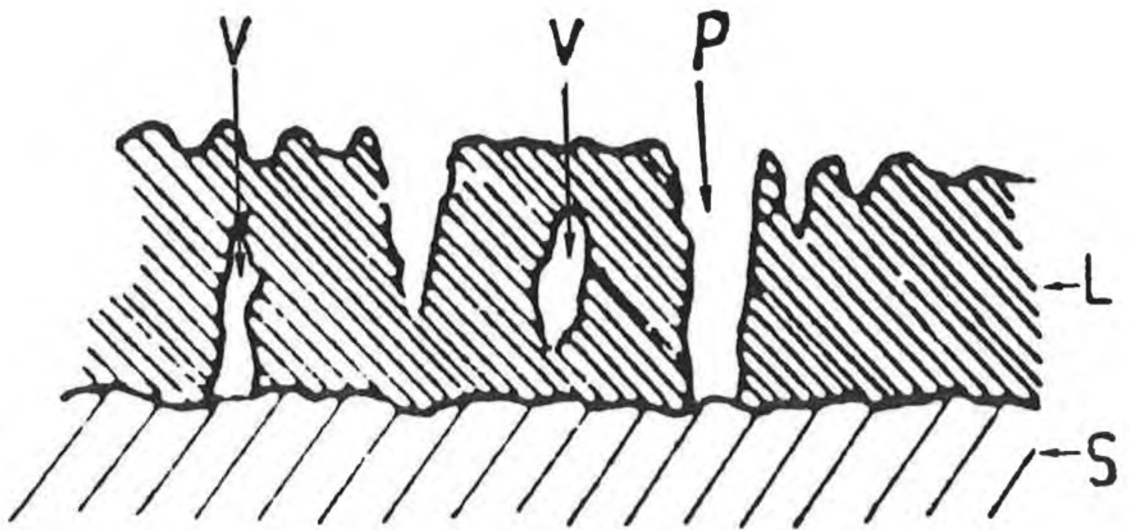


Figure 4.8 Cross section of the model of a thin film L on a substrate S

| | | | |
|---|---|---|---|
| L | Layer | P | Hole |
| S | Substrate | V | Void |

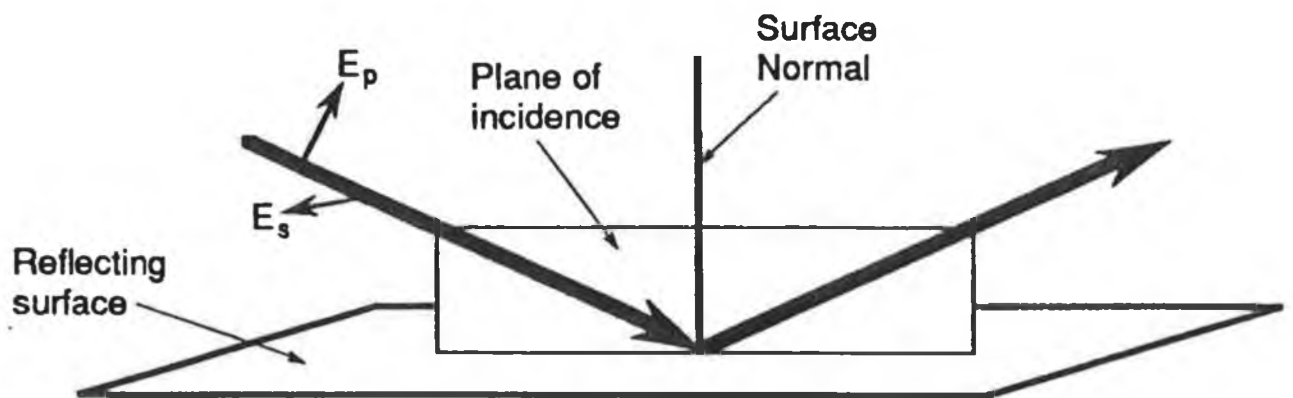


Figure 4.9 Reflection of a light beam from a surface
The plane incidence contains both the incoming and the outgoing beam.

# Chapter 5

# Magnetron Sputtered Titanium and Titanium Nitride

# Chapter 5 Magnetron Sputtered Titanium and Titanium Nitride

## 5.1 Initial Commissioning - Magnetron Sputtered Titanium

Initial experiments were conducted on Si(100) samples to investigate the deposition rate of Ti with respect to the total system pressure, the target to substrate distance and the magnetron power. All samples were ultrasonically degreased in 1,1,1 trichloroethane and then in acetone prior to deposition. Deposition rate vs. system pressure is depicted in *figure 5.1*. Points plotted represent an average of 5 values. Results indicated that, within the $10^{-3}$ mbar pressure regime, there was little effect on the deposition rate, as pressure was increased from $4 \times 10^{-3}$ to $1 \times 10^{-2}$ mbar. This is consistent with other reports [79]. In the graph of deposition rate vs. magnetron current, *figure 5.2*, it was found that there was a three-fold increase in the deposition rate as the magnetron current was doubled. Target to substrate distance was also an important factor in the deposition rate. The film deposition rate was found to be related to target to substrate distance according to the following equation, which was similar to a standard inverse power law equation:

$$R = \frac{k}{d_{s-t}^{\ n}} \qquad ...(1)$$

where R is the deposition rate

k is a constant

$d_{s-t}$ is the target to substrate distance

n is a constant

In a plot of log t vs. log d, *figure 5.3*, it was found that k = 9.55 and n = 1.44. For a point source, thickness (where thickness divided by the deposition time would give deposition rate) should decrease at a rate proportional to $1/d^2$, (i.e. n = 2). An infinite source would have a relationship whereby thickness would remain constant as target to substrate distance increased.

However, the magnetron target is neither an infinite nor a point source and a value of n =1.44 showed that deposition rate decreased at a rate proportional to $1/d^{1.44}$.

## 5.2 Current (I) - Voltage (V) Characteristic

The plasma characteristics were measured by plotting a current-voltage characteristic curve by inserting a probe into the plasma in the luminous region, mimicking a substrate placed in the plasma, *figure 5.4*. Any body immersed into a glow discharge (unless grounded) will acquire a potential with respect to ground that is slightly negative. This is known as the floating potential $V_f$. The substrate, even when grounded, is at a negative potential with respect to the plasma at a value of $V_f$ for a floating substrate. As the negative voltage to the probe is increased, positive ions are attracted to the probe and as a result, an ion current flows. However, the number of positive ions in the plasma is fixed for any given voltage applied across the electrodes and so the number of positive ions attracted to the probe does not rise appreciably, hence the ion current saturates.

As the voltage on the probe is increased positively, the electron and negative ions are attracted to the probe and the probe is at the same potential as the plasma at point $V_p$. The electron current is much greater than the ion current due to the greater mobility of electrons in the plasma. At potentials higher than $V_p$, the electron current will also saturate.

## 5.3 TiN - Introduction

One of the most commonly used PVD protective coating in mechanical applications is Titanium Nitride (TiN). TiN exhibits high hardness and adhesion, good ductility, excellent lubricity, high chemical stability and high resistance to wear, corrosion and temperature [1].

Benmalek et al. [46] found that TiN coatings deposited on similar substrates but deposited by different PVD techniques exhibited quite different properties. It was found that TiN deposited by magnetron sputtering produced very low values of surface roughness, which was also apparent in the topography of the coated sample. In addition, it was found that a dense compact Zone T type crystal structure was apparent, exhibiting high film hardness, and low starting coefficient of friction when tested against aluminium. So, it is evident that TiN has good tribological and hardness properties that can be utilised in mechanical situations.

### 5.3.1 TiN - Wear Resistance

The main requirement for wear resistance is high hardness [80], which reduces plastic deformation, and good adhesion, which can be enhanced by various surface preparation techniques including nitriding of steel substrates. It has been reported that hard (e.g. pre-nitrided) substrate increased wear resistance [81-83].

High temperatures are generated during frictional processes and the high hardness must be retained at these temperatures. Thus, the coating requirements are such that stability must be ensured at high temperatures, diffusion into the rubbing material must be avoided, and the material must be oxidation and corrosion resistant. A further advantage is gained if the coating is an efficient thermal barrier, helping to reduce tool-piece heating. Upton [44] reported that TiN has the lowest wear of drill bits coated with TiN, TiCN, TiZrN, TiAlN and TiAlN + TiN.

### 5.3.2 TiN - Tribological Properties

Current literature has established that the application of a TiN coating can improve the wear resistance of contacting surfaces. Many properties regarding wear and coating microstructure have been detailed by various authors. It has been shown [84], using a pin on disc wear test, that TiN coatings with a (200) orientation are more wear resistant than a corresponding

coating exhibiting (111) orientation, although both coatings had the same hardness. It has also been reported that for porous Zone I coatings, TiN is removed by a ploughing mechanism (abrasive wear), but as the coating becomes denser, and the structure tends towards Zone T, the wear rate dropped, but due to the increase of internal stress predominant in Zone T, there is a loss in abrasive wear resistance. Hence Zone T type microstructures with low levels of internal stress would be advantageous.

Zhu et al. [85] noted that TiN-coated ball bearings were significantly better in terms of scuffing resistance, temperature resistance and lower frictional forces without compromising tolerances.

### 5.3.3 TiN - Crystal Structure

It has been reported [59,60,84,86] that stoichiometric and substoichiometric TiN crystallises in a face-centred-cubic (f.c.c). structure, *figure 5.5.* High mechanical hardness relates predominantly covalent bonding, but enough metallic bonding exists so that electrical conductivity still remains high in TiN films [87].

The development of texture occurs in 3 stages [45,58]:

(i) Nucleation - crystallites are nucleated on the substrate from the vapour phase, the orientation, distribution and size of which are dependent on the substrate nature.

(ii) Competitive Growth - certain favourably-orientated nuclei will grow faster. This may or may not constitute the majority of nuclei population.

(iii) Steady Growth - once a preferred orientation has achieved dominance, steady state growth will occur.

The nucleation and growth processes are governed by the impingement rate and the substrate temperature, while further growth of the films is governed by impingement rate and surface diffusion [88].

Deposition conditions exert quite an influence on each of these stages and hence a large variety of textures and properties can result for nominally identical TiN thin films. Orientation was found to change from (111) to (220) due to increases in the ion current density [84,89]. It was also seen to change from (200) to (111) with increasing ion bombardment [90], increasing film thickness and decreasing substrate bias [42]. Thick coatings exhibit a (111) texture whilst thinner ones show (200) textures indicating that this orientation is predominant at nucleation. It has been further reported [39,42] that increasing the ion current density alters nucleation.

### 5.3.4 TiN - Film Microstructure

Experiments have shown that TiN films deposited by magnetron sputtering at low substrate bias are matt black and possess a porous microstructure and low microhardness [23]. However films deposited at higher substrate bias, and hence, subjected to increased levels of ion bombardment, produce TiN coatings of a dense compact golden-coloured nature, which posses low levels of carbon impurities.

The effect of increased substrate temperature increases the densification of the TiN coating, while at low temperatures, the coatings are more porous. Maheo and Poitevin [36] found that TiN coatings deposited at temperatures between 150-600°C had a columnar-type structure. At temperatures >670°C, grain sizes increased.

### 5.3.5 Hardness

The effect of increased hardness with elevated deposition temperatures occurs due to the decrease in defect concentration (which is related to material strength). Sundgren and Hentzell [9] expanded this explanation and found that at elevated temperatures, the grain boundaries in the film strengthen and are capable of increased load bearing capacity. Similar observations have been found by Burnett and Rickerby [92], with increased substrate bias voltage for TiN sputter coated samples.

Commissioning experiments conducted on TiN resulted in hard adherent films on AISI 304 stainless steel substrates in the as received ($R_a$ approximately 150μm) state. These samples had been thoroughly degreased in solvents and had been subjected to argon sputter cleaning for 30 minutes at 1 x$10^{-2}$ mbar. The samples had also undergone heating to a temperature of 400°C. Temperature was measured by fixing a type K thermocouple to a dummy sample which underwent identical deposition conditions. An interlayer of Ti with a gradual increase in the nitrogen partial pressure produced a graded interface to aid adhesion. The operating pressure was 4 x $10^{-3}$ mbar, with a film stoichiometry of 50% Ti/N using the Reactaflo feedback control system. This gave a partial pressure of 8% nitrogen at a magnetron power of 4kW and a target to substrate distance of 10cm. In an investigation of hardness vs. substrate bias, it was found that the substrate bias had a significant effect on the hardness of the film. There was an increase of 133% from 300HV at 0V d.c. substrate bias to 700HV at -50V d.c substrate bias, *figure 5.6*. Points plotted represent an average of 5 values. Similarly, it was found that a magnetron power of 5kW produced films possessing hardness values four times greater than films deposited (under similar deposition conditions as outlined above) at 2 kW magnetron power, *figure 5.7*.

### 5.3.6 Colour

Colour is a good indication of hardness [93,94] with colour tones varying from white to red gold dependent on concentrations of nitrogen in the coating process. In the deposition of transition metal nitrides and carbides, it was found that colour is mainly influenced by both the microstructure and the stoichiometry of the coating [95]. It was found that golden (stoichiometric) TiN plating had the greatest resistance to wear. Colour ranges from silver (for $Ti/N_x$ ratios $x < 0.6$) towards tones of brown in films with $x > 1$ for $TiN_x$ films [96]. *Figure 5.8* shows a summary of data on composition and colour of $TiN_x$ films in the range $0 < x < 1.2$ [97,98]. A decrease in microhardness has been observed by Manory [96] with increasing x in the range of gold colour. Matsumura [99] has documented the colour matching of TiN films in some detail, along with Beck et al. [100]. The films deposited in the magnetron sputtering system produced a spectrum of colours ranging from silver (Ti-rich), through yellow-gold, red-gold, bronze, brown, pink (nitrogen-rich) to blue (oxides). All these colours were easily obtained in tests by varying the nitrogen partial pressure.

## 5.4 Biocompatible Materials

There are three main classes of materials primarily used in biomedical applications - metals (e.g. Ti-6Al-4V, Ti, Co-Cr and stainless steels), plastics (e.g. Ultra High Molecular Weight Polyethylene (UHMWPE), Polytetraflouroethane (PTFE)) and ceramics (e.g. Hydroxyapatite [101-103], $Al_2O_3$ [104-106] and TiN).

Metals undergo pitting, galvanic corrosion, crevice corrosion and stress corrosion, limiting the life of a metallic implant. Another serious drawback is the increased metallic toxicity levels in body tissue in the hair, nails, spleen, liver and in dental tissues [107]. In addition, metals wear, and can cause debris deposition in surrounding tissue. However, metals possess good mechanical properties, and this is the major area of concern in the use of plastics [108]. Some plastics can also cause tumours and inflammation [109]. Ceramics are generally brittle in

nature, having low impact resistance, and a lack of mechanical reliability. particulate deposition in neighbouring lymph nodes [110] and low bonding rates with bone [111,112] can cause fixtures to become loose and eventually require replacement.

Newer materials in implant technology are carbon-reinforced hydroxyapatite [113], biodegradable (or material that the body can readily break down and dispose of) glass [114], and biodegradable polymers [115]. These are all materials available for implantation into the body. Prostheses for implantation into the human body must be biocompatible i.e. no dissolution of the material can occur in human tissue and also, the prostheses must be corrosion resistant. The two main concerns in prostheses usage are

1. Adhesion of the bone to the prostheses

2. Corrosion resistance of the implant

The former has been well documented in terms of inducing pore size in the implant of about 100μm [101], thus allowing bone ingrowth or osteoneogensis into the implant [116], whilst the corrosion resistance has been addressed in the development of new biocompatible, biodegradable materials. A further method of corrosion protection is in the use of inert protective coatings such as $Al_2O_3$, TiN, BN, $CN_x$, and diamond-like carbon [117] to encapsulate the metallic prostheses thereby increasing corrosion resistance, whilst at the same time mitigating metallic ion migration.

The investigation of the effectiveness of TiN as a biocompatible coating was undertaken.

### 5.5 TiN Biocompatible Coatings

In addition to TiN possessing good mechanical, corrosion resistant and aesthetic properties, which remain uncompromised in the oral cavity, TiN has been found to meet the requirements of a biocompatible coating [118], viz.:

- the absence of thrombogenic, toxic, allergic, or inflammatory reactions.
- no changes in plasma protein and enzymes
- no immunological reactions
- no carcinogenic effect
- no deterioration of adjacent tissue

Hence TiN can readily be utilised in dental prosthetics. The use of TiN coatings for orthopaedic prostheses [119], cardiac valves [120], and dental prostheses [121], has been well documented, along with the haemocompatibility of TiN [122-124], concluding that TiN is well tolerated by the human body. In the specific use of dental prostheses coated with TiN, Berhandt and Lunk [123] have found that TiN does not exhibit any cytotoxic effects. Further documentation available in Russian and German journals, found these prostheses to gain widespread acceptance by patients [125].

However, it has also been reported that leaching of the metal ions from metal prostheses can accumulate in the body to toxic levels [97]. The corrosion resistance of TiN coated prostheses, although reducing the number of base metal ions in the body, is strongly dependent on the porosity of the coating, thereby limiting the coating's protective qualities [126]. Porosity in the coating due to cracking of the TiN film etc. causes pitting and crevice corrosion in Co-Cr-Mo alloy substrates. Knotek et al. [121] reports that multi-layering of the TiN deposited by PVD,

and etching of each subsequent layer removes loosely bonded material and can aid densification of the coating. Wisby et al [119] found that pitting corrosion of Co-Cr-Mo alloys was significantly reduced on application of a thin TiN coating.

## 5.6 Metallic Corrosion

The corrosion of metallic implants in bodily fluid closely resembles that of corrosion of metals in seawater [127]. The effects of corrosion in the body are three-fold.

(i) electrical currents may effect cell behaviour

(ii) the chemical environment (pH, $pO_2$) may be altered due to the corrosion process

(iii) the metallic ions may affect cellular metabolism

The last scenario is of the most serious consequence.

### 5.6.1 Electrochemical Series

The reaction of metals in aqueous environs is electrochemical in nature, with the movement of metallic ions and electrons. The metallic implant (anode) oxidation reaction is balanced by the reduction of dissolved oxygen into hydroxyl ions (cathodic reaction).

$$\frac{1}{2}O_2 + H_2O + 2e^-_{metal} \rightarrow H_2 + 2OH^- \quad ...(2)$$

In the tissue or wound surrounding the implant, a dearth of oxygen exists, which may result in an alternative cathodic reaction in the reduction of water

$$2H_2O + 2e^-_{metal} \rightarrow H_2 + 2OH^- \quad ...(3)$$

The standard electrochemical series gives a listing of the normal electrode potentials of elemental metals referenced to the standard hydrogen electrode. More positive potential metals are nobler, and least reactive.

However, this standard series is not so relevant in implant conditions. In physiological environments, many different ions are present. Also the metal surface is free to form passivation oxide layers.

A more apt electrochemical series is that obtained for combinations of metals in seawater [127]. This galvanic series predicts qualitatively how two metals will interact with each other in a physiological environment. A comparison between theoretical biocompatibility scale (electromotive series, column(a) ), general passivation effect of the metals, not in the oral cavity (column(b) ) and the actual in vivo tested materials (column(c) ) are shown in *figure 5.9*. As can be seen, Ti exhibits the highest resistance, followed by Niobium and the Cobalt alloys.

### 5.6.2 Corrosion Testing

The initiation of the corrosion process is dependent on the presence of a defect in the coating which passes through the substrate material. These defects may result from cracks, pinholes or voids in the coating layer. Physiological saline solution is typically 0.9% NaCl. Corrosion tests were conducted at a concentration of 3% NaCl at room temperature with no agitation. Samples immersed in this solution were left for 48 hours and then printed electrographically. These prints were then compared to the control specimens.

## 5.7 Experimental Procedure

The operation and safety aspects of the sputtering system was followed according to the procedure outlined in Appendix C. AISI 316L samples 38.1mm in diameter by 6mm thick were ground and metallurgically polished by hand to a 0.25μm surface finish ($R_a$). Samples were then ultrasonically degreased in 1,1,1 trichloroethane and then in acetone. Specimens were loaded using 2 samples at a time into a closed field unbalanced magnetron sputtering system with one magnetron energised. One sample was to be the control, while the other underwent corrosion testing. Prior to deposition, the samples were heated for 1 hour using a tungsten filament radiant heater and argon sputter-cleaned for 20 minutes at $1x10^{-1}$ bar to remove debris and further heat the samples by ion bombardment. TiN was reactively sputtered onto samples with an interlayer of Ti of approximately 0.2μm between the steel and the TiN. Corrosion resistance is greatly improved with a Ti interlayer consistent with results by Massiani et al. [128,35,129], probably due to the passive $TiO_2$ layer formation. Deposition was undertaken at a pressure of $5 \times 10^{-3}$ bar. TiN was deposited until a layer thickness of 2.5μm was obtained at magnetron powers ranging from 1 to 3 kW. A substrate bias of between 0 to -40 V was applied to the substrate to further promote densification of the growing film by ion bombardment. The bombardment was enhanced by the closed field magnetron configuration due to the improved confinement of the plasma.

Stoichiometric control was achieved by the use of a plasma emission spectrometer feedback loop, controlling the flow rate of the reactive ($N_2$) gas by monitoring the Ti peak. The value returned by the emission spectrometer for a pure Ti peak height represented 100% (e.g. 8 mV) The setpoint was initially set to its maximum value indicating that no nitrogen was admitted into the chamber. Slowly, the setpoint was reduced such that the value returned by the emission spectrometer was 55% (i.e. 4.4 mV) of the original peak height. This ensured that the nitrogen admitted into the chamber was sufficient to deposit stoichiometric TiN. Samples were finally cooled for 2 hours in the chamber prior to unloading.

## 5.8 Experimental Data

The coated samples, both corroded and uncorroded were examined for pin-hole defects, which are noticeably obvious to the naked eye and further enhanced by the optical microscope. Photographs of these defects on the sample are shown in *figure 5.10*. Those defects which were larger than 1μm in diameter were counted and graphed with respect to the deposition parameters. Although there exists pin-hole defects of smaller dimensions than 1μm, these would not contribute as greatly to pronounced corrosion as the larger defects. Given time, these smaller pin-holes would also become larger, as corrosion of the base metal begins, and leads to flaking of the coating material at these corrosion sites, leading to enlargement of the defect and thus promoting further corrosion. Hence, over time, the size of the defect will increase. To obtain consistent results, those defects 1μm or greater in diameter were considered to be most significant. The thickness of each coating was approximately 2.5μm thick, thereby mitigating the strong dependence of pinhole density on coating thickness, with defects effectively smoothed out on thicker coatings.

## 5.9 Results

The variation of the pinhole density as a function of magnetron power and substrate bias are shown in *figures 5.11* and *5.12* respectively. In each case it can be seen that pinhole density is reduced where higher ion bombardment of the substrate is known to occur. This is consistent with the film densification that is known to occur from increased ion bombardment at high magnetron powers and high substrate bias. Increased ion bombardment also leads to higher substrate temperatures which also promotes densification. This is also apparent where the number of defects is plotted against the substrate bias, (*figure 5.12*) furnishing the result that as both power and bias are increased, film densification increases, leading to fewer pinhole

defects. *Figures 5.13* and *5.14* show the pinhole density in similar samples after corrosion testing, and indicate that bias is an important factor in promoting coating density.

## 5.10 Discussion

The combination of high power and high substrate bias serve to densify the film and reduce pinhole density. In a comparison of corroded and uncorroded samples, the influence of substrate bias plays an important role in the pinhole density at higher magnetron powers. Although the pinhole density is marginally increased for corroded samples, this may not necessarily be due to the salt solution but rather to the corrosive properties of the electrolyte, which promotes corrosion at the pinhole sites and causes the coating to flake off at these sites. Thus, the pinhole defects appear larger, and the enlargement of otherwise microscopic defects becomes more significant. The numbers of defects above 1μm are therefore increased and the pinhole density may not reflect the true corrosion resistance of the coating against the salt solution.

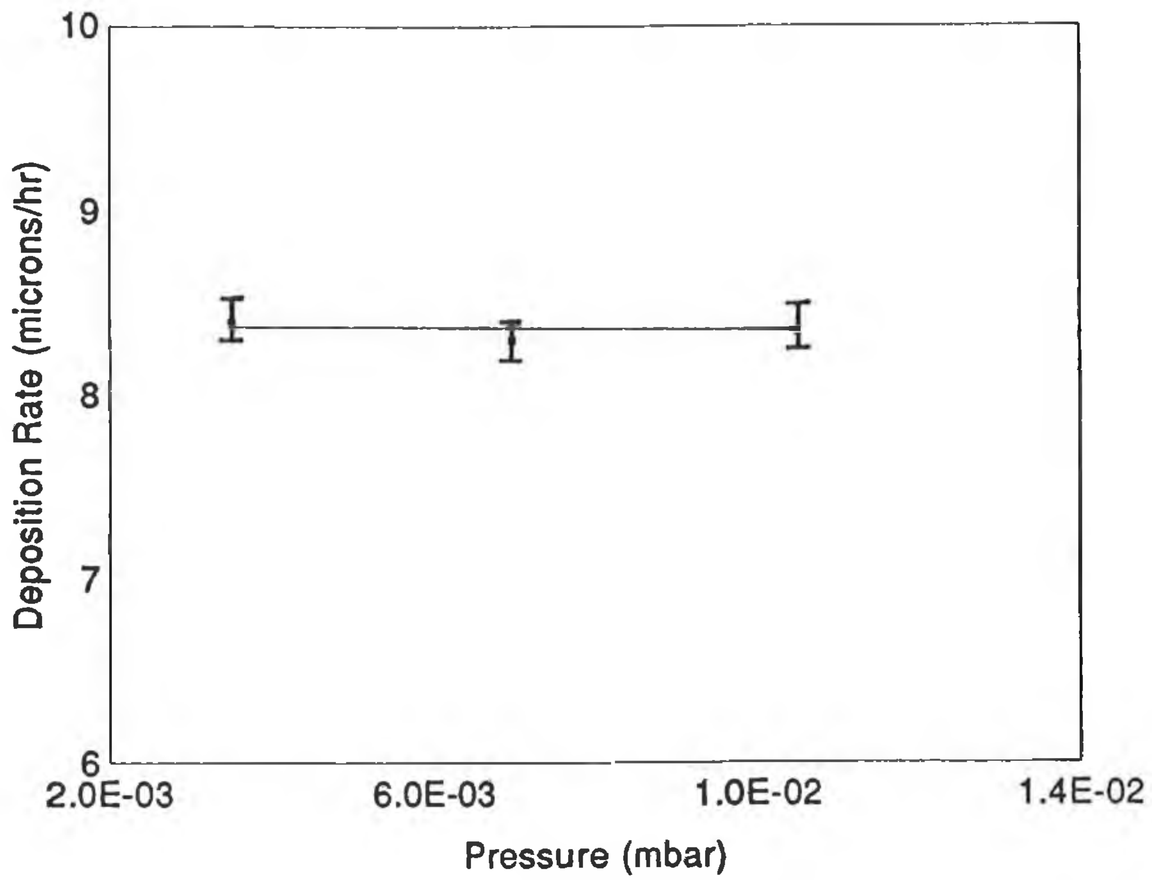


**Figure 5.1** **Deposition Rate vs. Pressure for Titanium**
**1.8kW magnetron power, 6cm $d_{s-t}$**

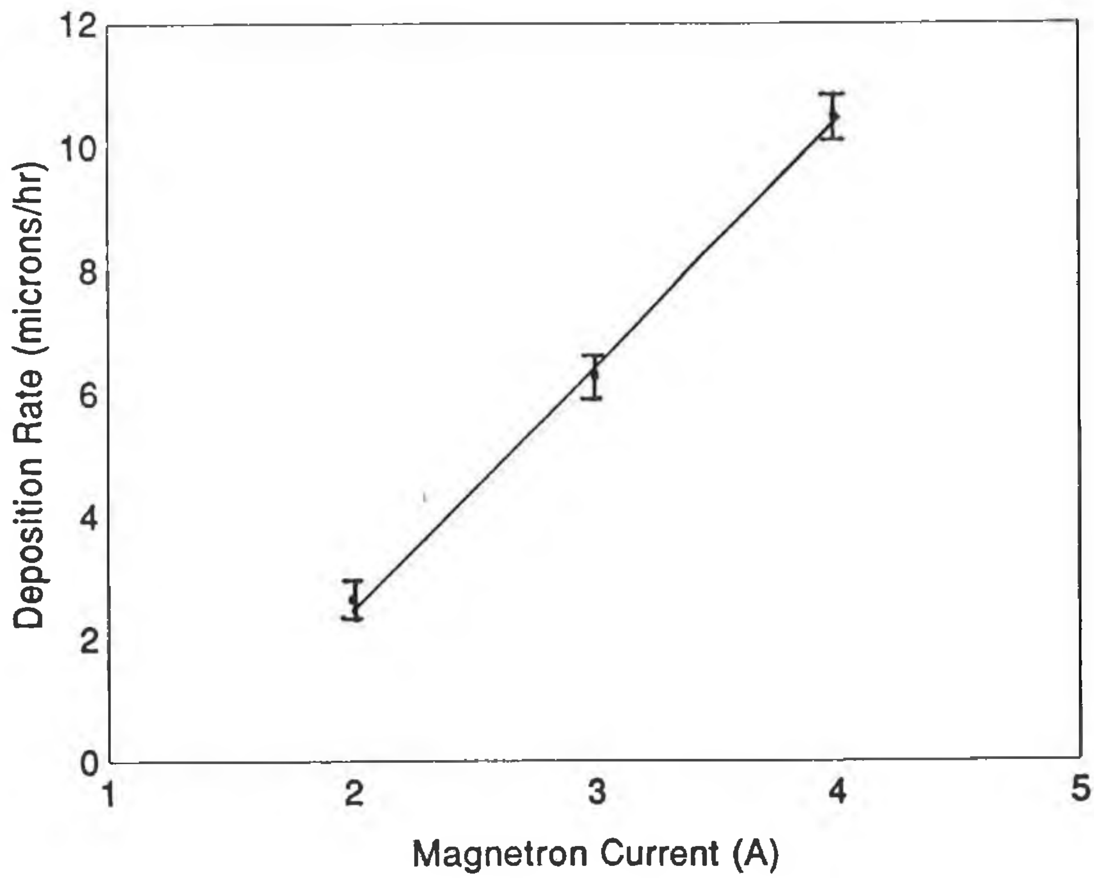


Figure 5.2 **Deposition Rate vs. Magnetron Current for Titanium 1.8kW magnetron power, 6cm $d_{s-t}$, $3.5 \times 10^{-3}$ mbar**

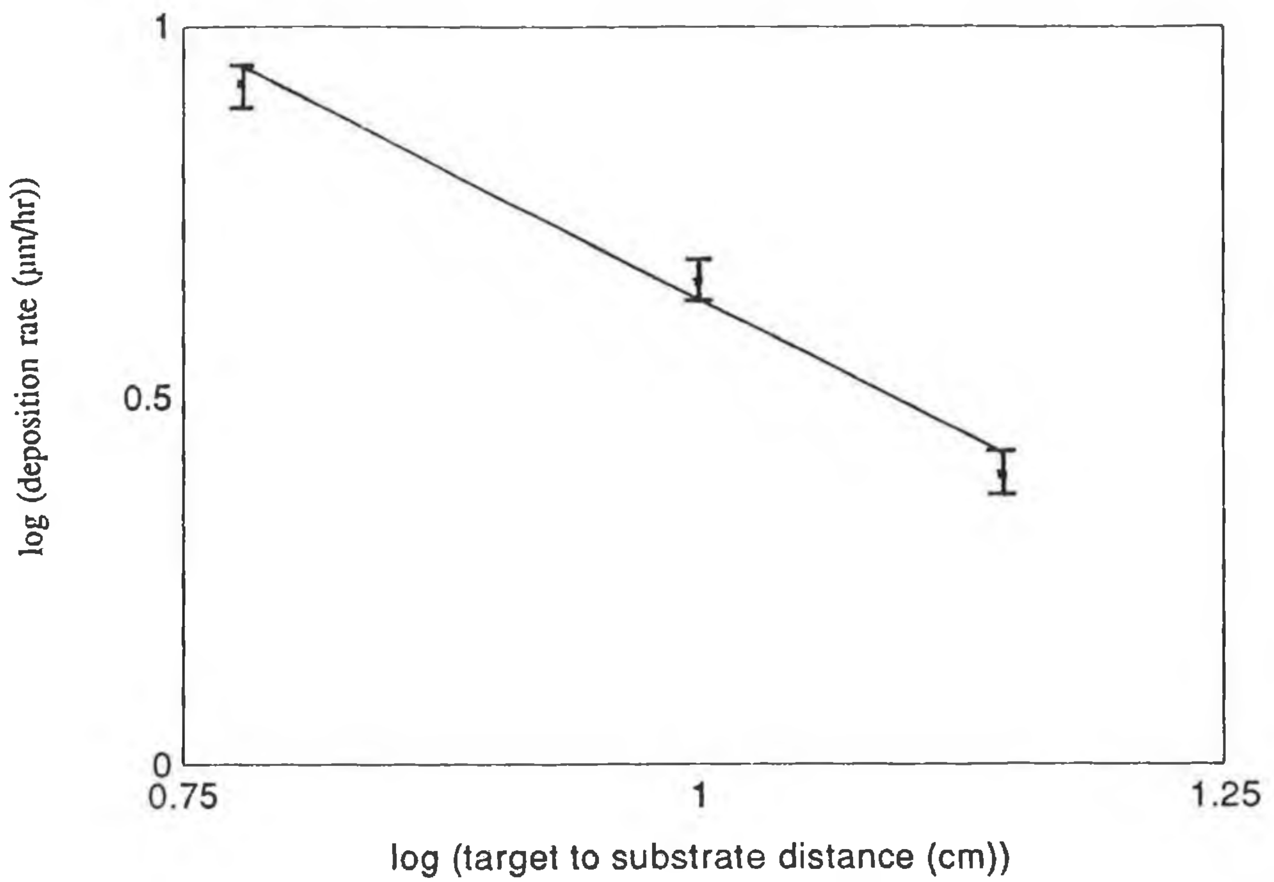


Figure 5.3 **Log of Deposition Rate vs. Log of Target to Substrate Distance for Titanium**
**1.8kW magnetron power, $3.5 \times 10^{-3}$ mbar**

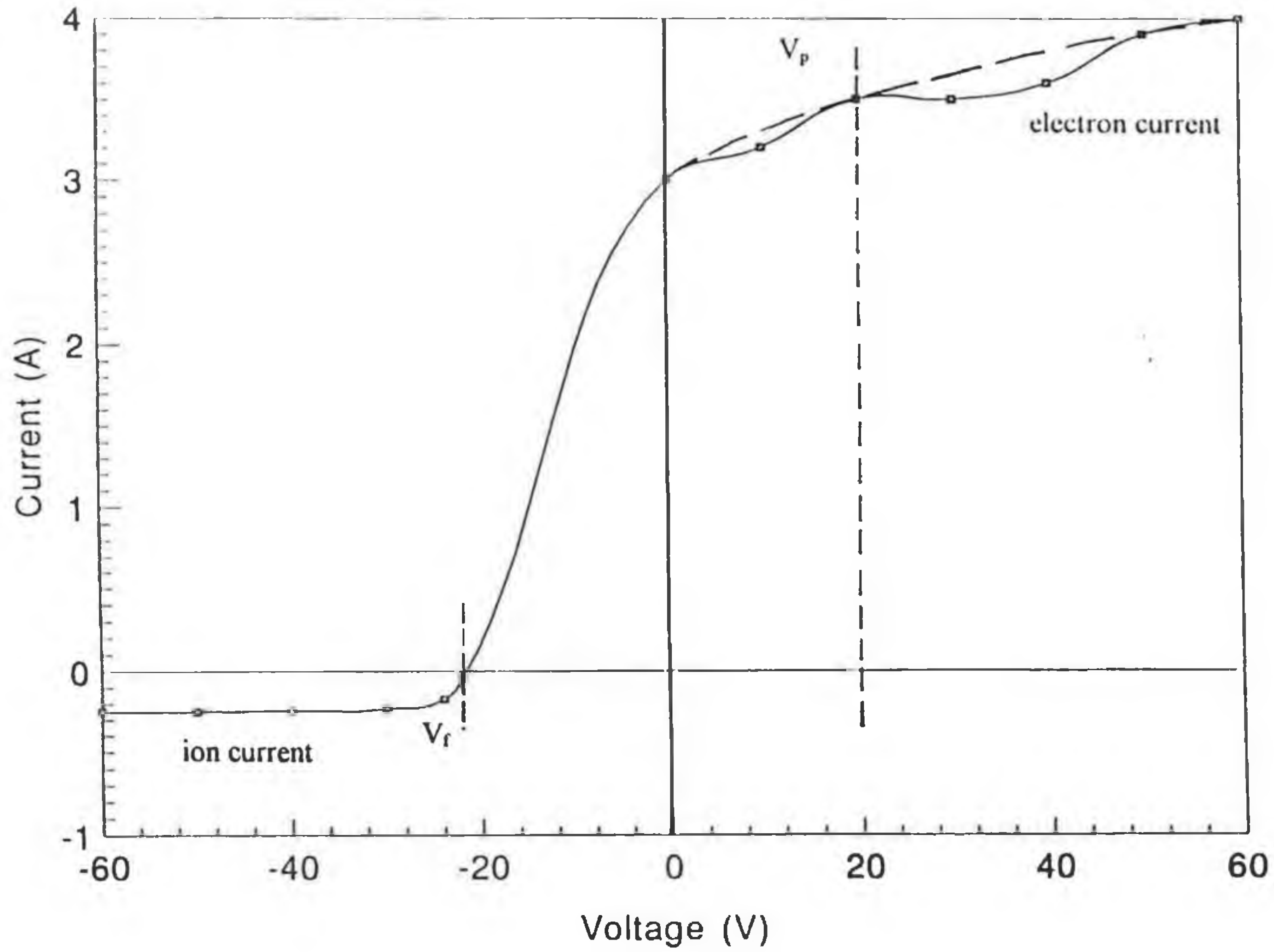


**Figure 5.4** **Graph of current-voltage characteristic**

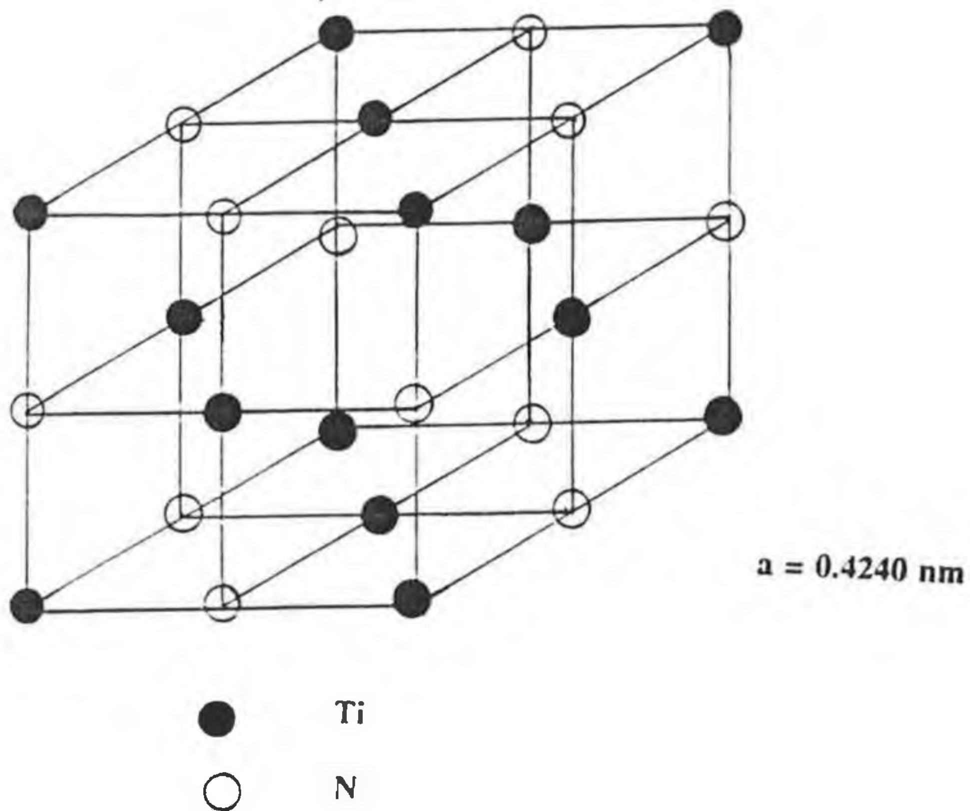


Figure 5.5 **The crystal structure of stoichiometric TiN**

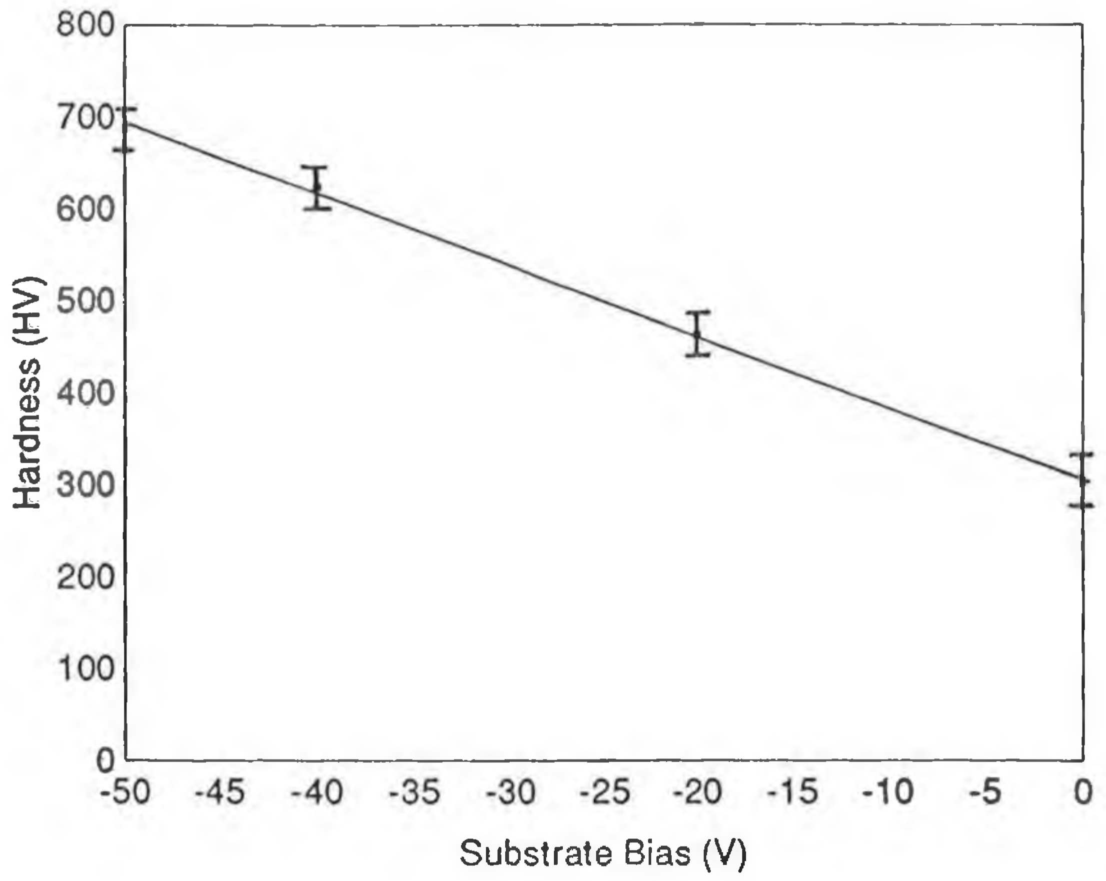


Figure 5.6 Hardness vs. Substrate Bias

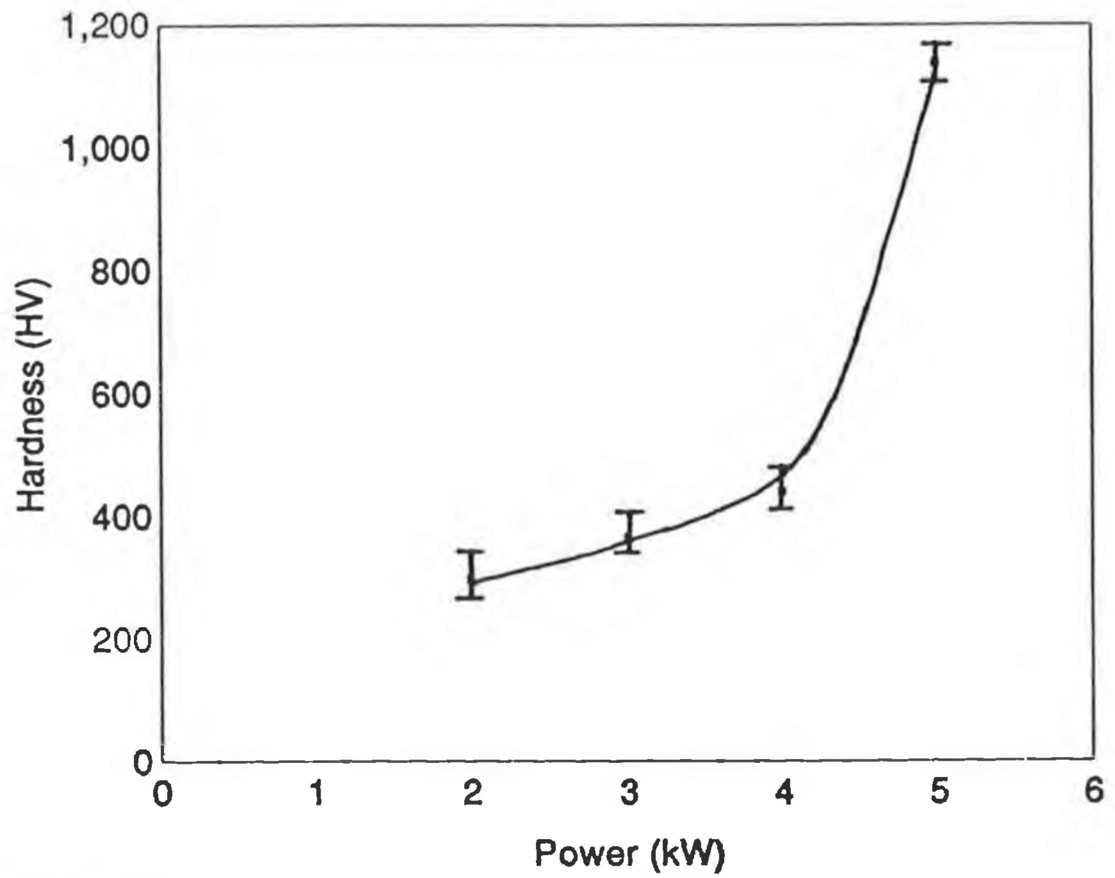


Figure 5.7 **Hardness vs. Magnetron Power**

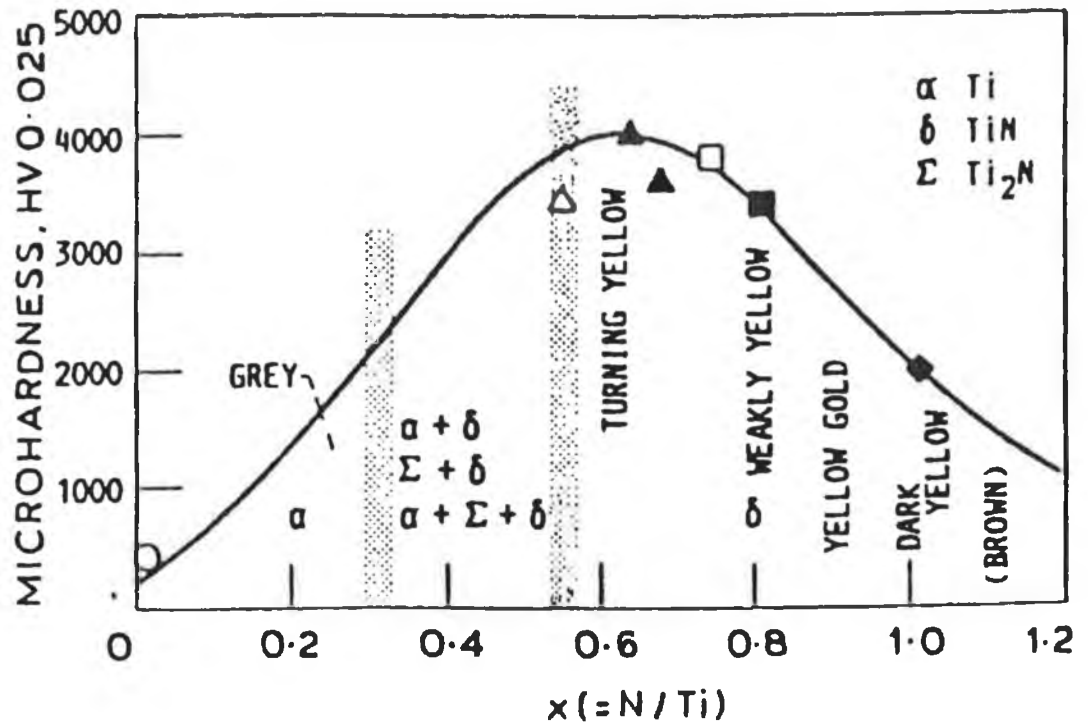


Figure 5.8 Microhardness, colours and phases of $TiN_x$ films as a function of nitrogen content [96]

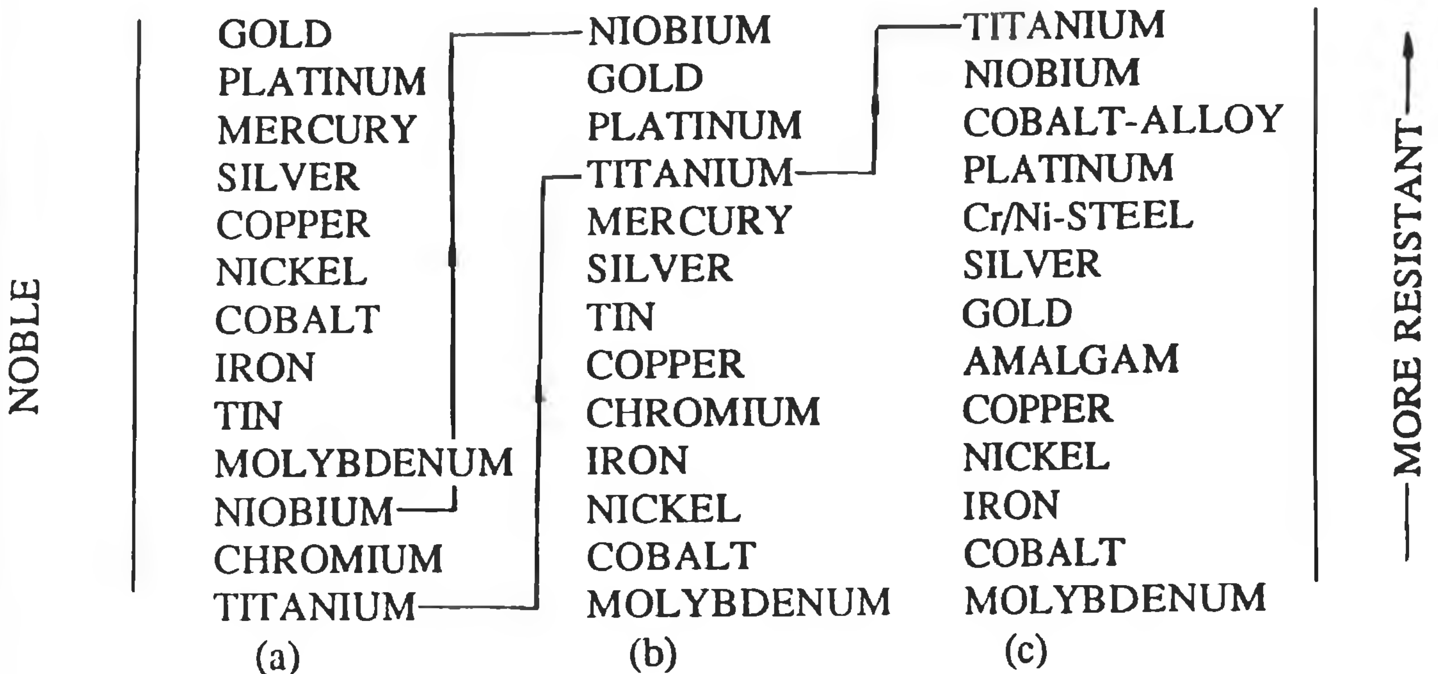


Figure 5.9 Resistance of materials in the oral cavity [127]

column (a) theoretical biocompatibility scale
column (b) general passivation effect of metals
column (c) in vivo tested materials
(note: column (a) & (b) not measured in the oral cavity)

(a) 2kW Power
0V Bias
uncorroded

(b) 3kW Power
0V Bias
uncorroded

(c) 1kW Bias
0V Bias
corroded

(d) 1kW
-40V Bias
corroded

Figure 5.10 Pin-Hole defects on the actual sample

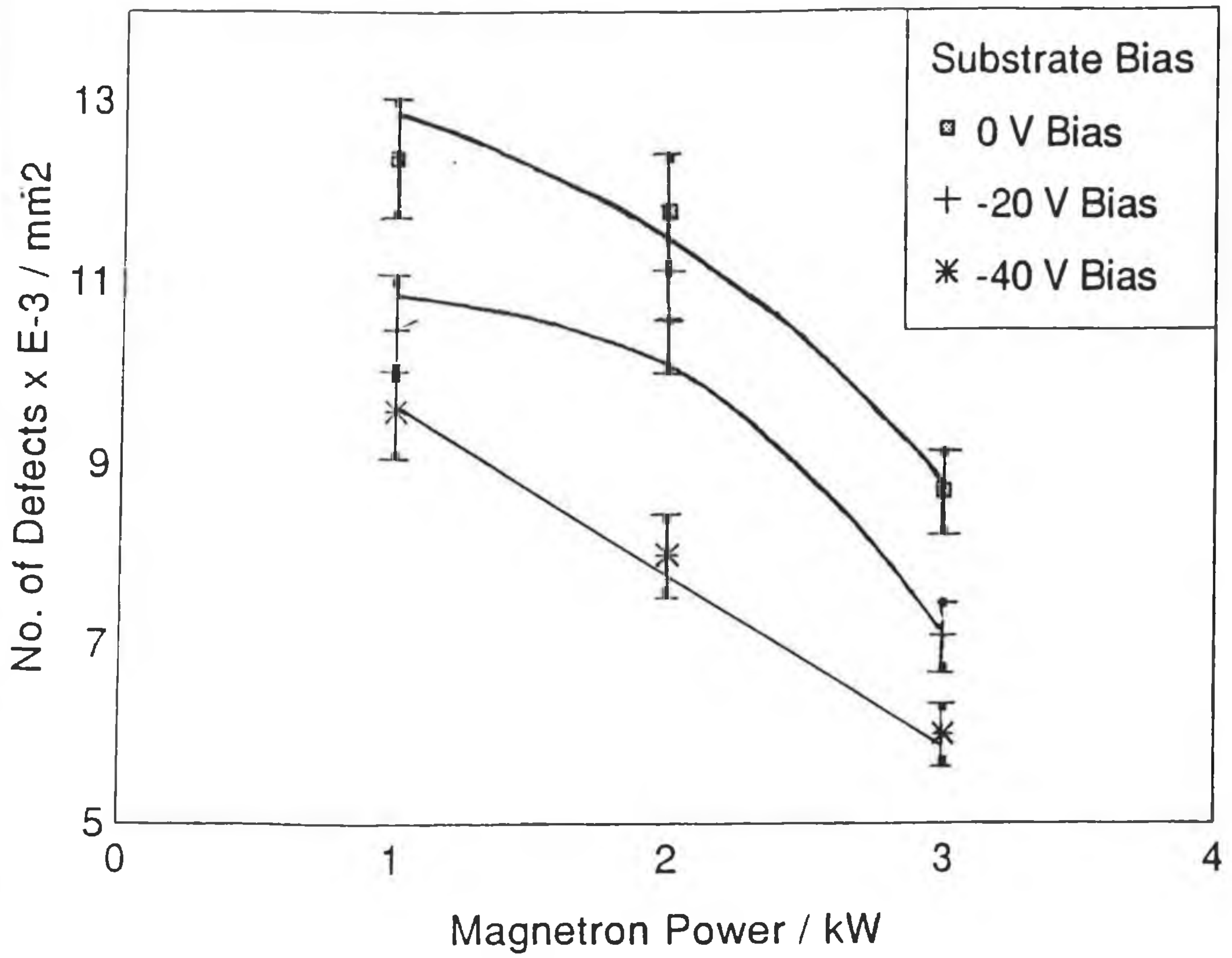


**Figure 5.11** **Number of defects vs. Power (non-corroded samples)**

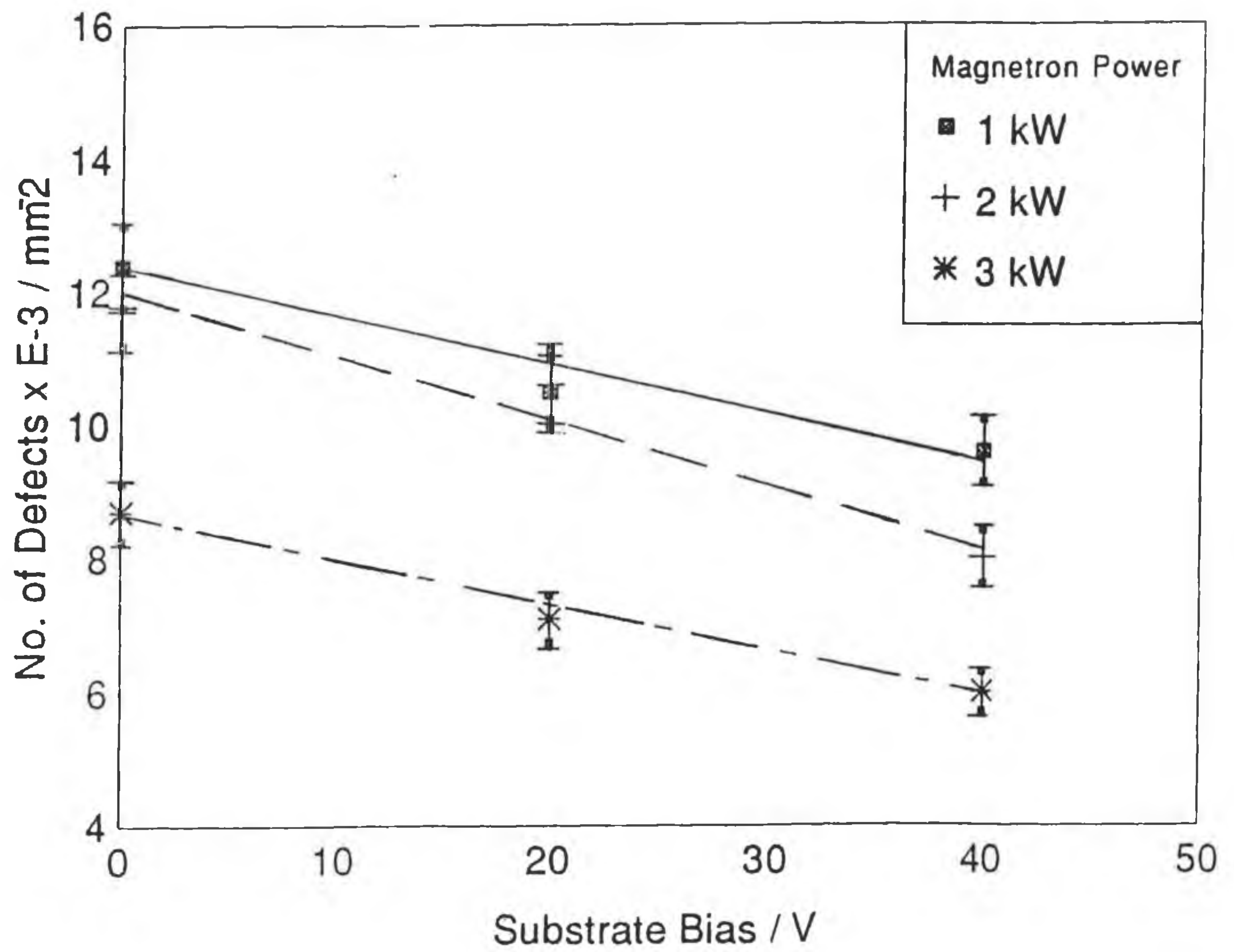


Figure 5.12 **Number of defects vs. Substrate Bias (non-corroded samples)**

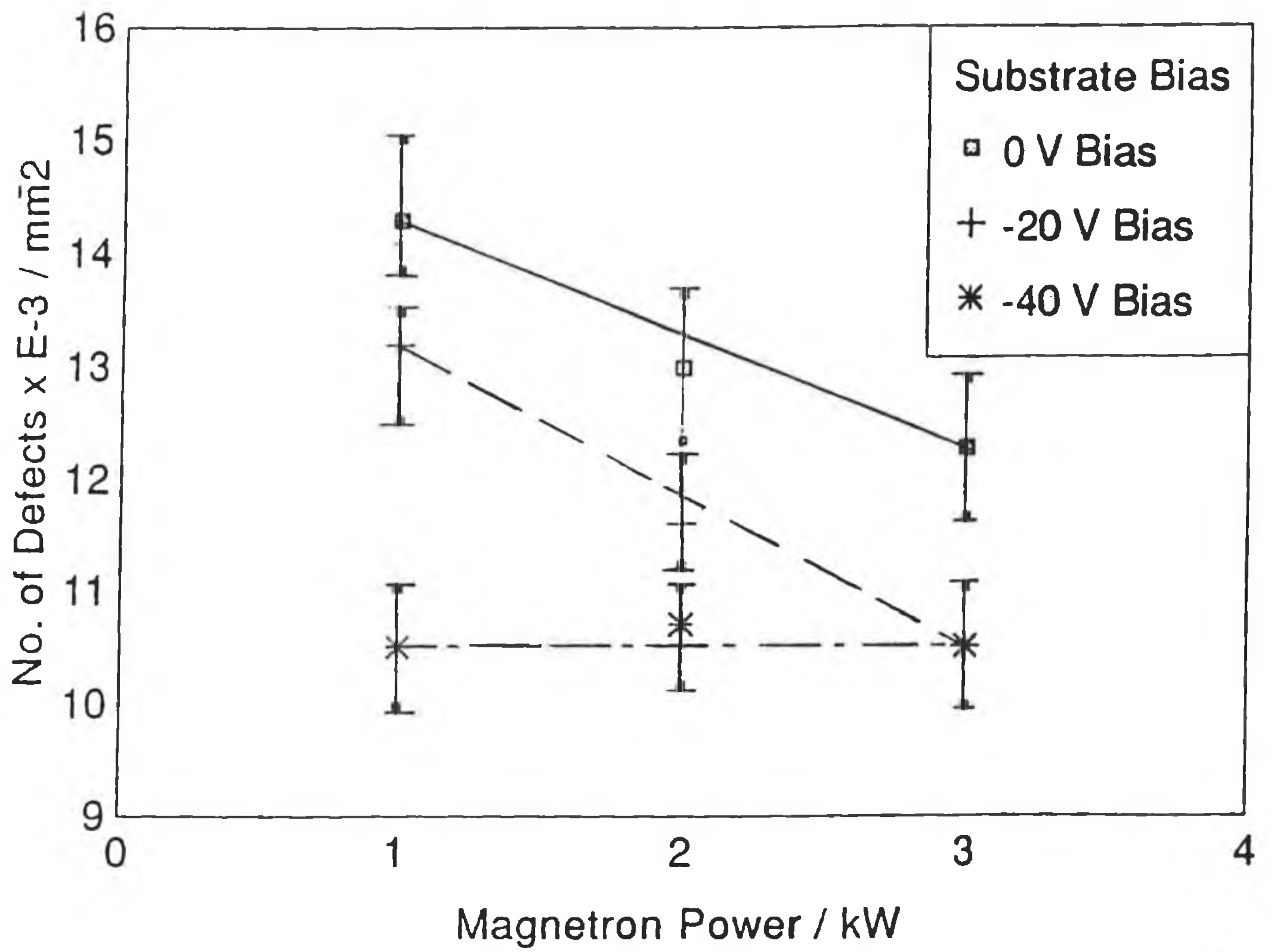


**Figure 5.13** **Number of defects vs. Power (corroded samples)**

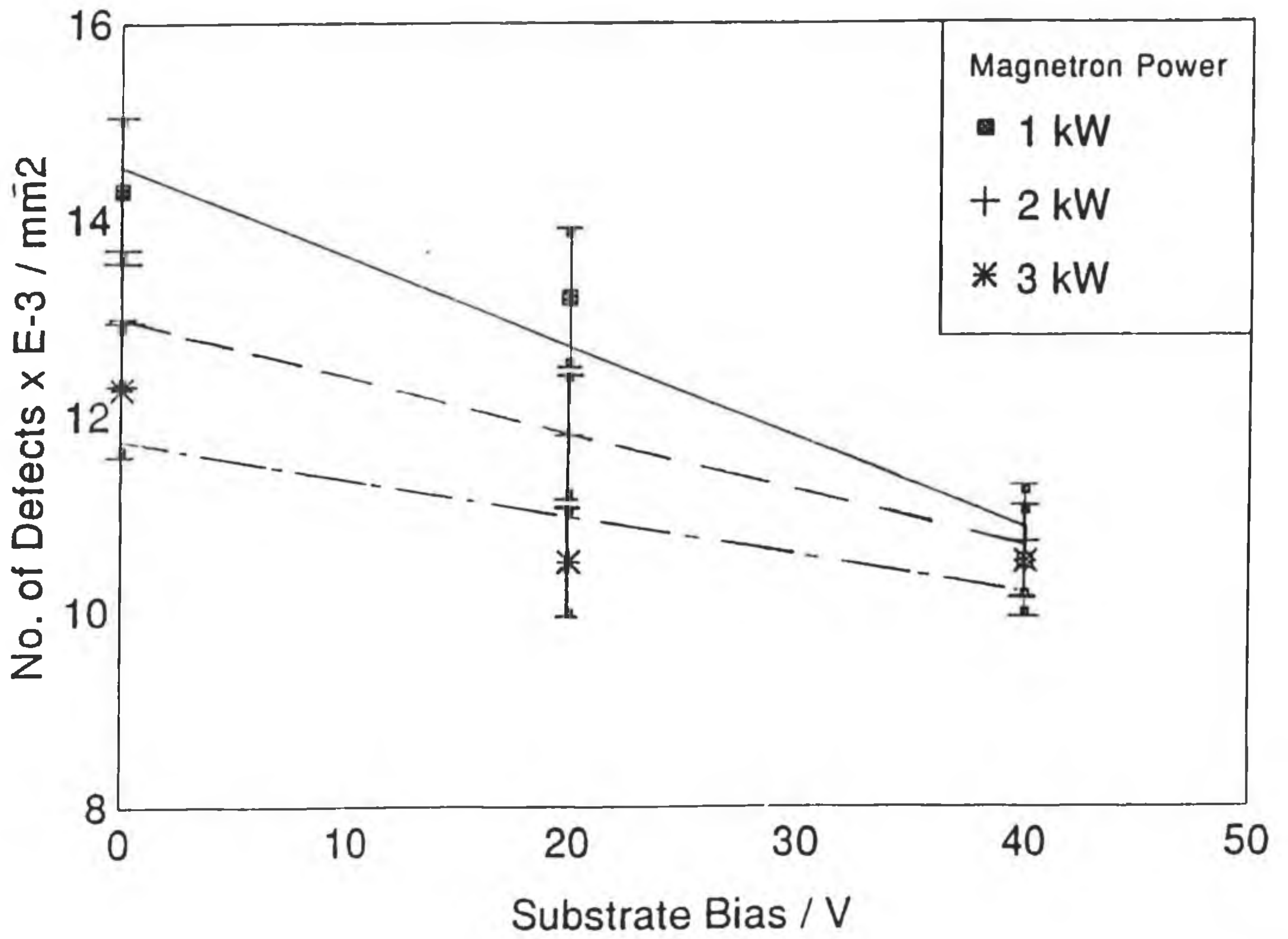


**Figure 5.14** **Number of defects vs. Substrate Bias (corroded samples)**

# Chapter 6

# Carbon Nitride ($CN_x$) Deposition on Silicon

## 6.1 Introduction

Calculations, based on a $\beta$-$Si_3N_4$ type structure, where carbon atoms were substituted for the silicon atoms ($\beta$-$C_3N_4$) predicted a material having hardness values in excess that of diamond [130,131]. The calculation is outlined below, where B, the bulk modulus (Mbar) is given as [130]

$$B = \frac{19.71 - 2.2\lambda}{d^{3.5}} \quad ...(1)$$

where d = bond length (Angstroms)

$\lambda$ = ionicity for diamond $\lambda = 0$

for III-IV compounds (e.g. BN) $\lambda = 1$

A comparison of bulk modulii for some materials calculated by this method is given below.

| Material | d(Angstroms) | ionicity ($\lambda$) | B (Mbar) |
|---|---|---|---|
| diamond | 1.54 | 0 | 4.35 |
| c-BN | 1.56 | 1 | 3.69 |
| $\beta Si_3N_4$ | 1.47 | 0.5 | 2.68 |
| $\beta C_3N_4$ | 1.74 | 0.5 | 4.83 |

Such coatings have many possibilities in the area of tribological and wear-resistant applications. Initial work on the deposition and characterisation of nitrogen-containing carbon films has been reported by many investigators [132-135]. Various deposition techniques have been employed by the different investigators, including magnetron sputtering [132,133,135,135-138], ion beam assisted magnetron sputtering [139], pulsed laser ablation

[140,141], ion beam deposition (IBD) [142,143], ion and vapour deposition (IVD) [144] and plasma enhanced chemical vapour deposition (PECVD) [145]. Carbon compound coatings can be produced by incorporating nitrogen either during their growth or by a post-deposition ion-beam treatment [146-148]. The maximum nitrogen incorporation to date has been less than the stoichiometric requirement of 57%.

Magnetron sputtering has successfully been employed in the deposition of non-stoichiometric carbon nitride films with nitrogen incorporation of upto 40% atomic [132]. In pursuit of this $\beta C_3N_4$, experiments were conducted to sputter graphite in an argon/nitrogen plasma to deposit carbon nitride films. The incorporation of nitrogen in the films during reactive sputtering depends on the competition between the trapping of nitrogen and the desorption of nitrogen-containing species from the growth surface. Thus both thermodynamics and kinetics will limit the nitrogen content in the films. The dominant mechanism of nitrogen incorporation in the films is a result of chemisorption of atomic nitrogen and/or low energy implantation of energetic nitrogen species impinging on the growth surface with an energy high enough to become implanted and trapped [150]. The loss of nitrogen-containing species from the growth surface will occur either through resputtering or through thermal desorption. It is suggested [150] that this extensive resputtering, together with a relatively low fraction of atomic nitrogen species in d.c. magnetron sputtering results in an upper limit of the maximum achievable nitrogen concentration. Several authors have reported levels of upto 50% atomic nitrogen in their films [132,140,143,149,151-153], but to date, only a few [144,157] have come close to depositing $\beta$-$C_3N_4$ in its stoichiometric form.

Structural, optical and compositional information from experiments conducted by other authors have been obtained using various techniques such as Electron Energy Loss Spectroscopy (EELS), X-ray Diffraction (XRD), Raman spectroscopy, X-ray Photoelectron Spectroscopy (XPS) and Infra-red (IR) spectroscopy. Although film properties can vary depending on both the deposition technique and parameters, little detailed information regarding magnetron sputtered carbon nitride films was found in the literature survey.

Using reactive d.c. magnetron sputtering of a graphite target in an Ar/$N_2$ plasma, the resultant film properties were investigated as a function of the deposition parameters. Optical, structural, mechanical and compositional information is presented here, building on work already reported by the previously mentioned authors.

## 6.2 Experimental Procedure

Silicon (100) substrates were ultrasonically degreased in 1,1,1-trichloroethane and then in acetone. The samples were then loaded into a closed-field unbalanced magnetron sputtering system with one magnetron energised. The target-to-substrate distance was 6cm. Prior to deposition, the samples were reverse sputter etched at -1000 V d.c. bias with 0.1 A magnetron current to enhance the plasma intensity, and also to degas the carbon target. This cleaning routine was conducted for 30 minutes at 6.5 x $10^{-3}$ mbar. Typical substrate temperature at this stage was approximately 330K. $CN_x$ films were deposited using a graphitic target (99.75% purity) energised using a d.c. power supply at magnetron currents of 1, 2 and 2.5 A, respectively, in an argon/nitrogen atmosphere using $N_2$ concentrations of 0%, 25%, 50%, and 75% of the total gas pressure, at 8x $10^{-3}$ bar and 5x $10^{-3}$ bar system pressure, and at both floating (approx. -17V) and -50V d.c. substrate bias, with the -50V bias being more negative than the bias at which the ion current saturated. Substrate temperatures at the end of the deposition process were typically below 370K.

Deposition times at the various magnetron currents were selected such that the resultant films were all approximately 1μm thick. After deposition, samples were cooled for 1 hour in the chamber to mitigate delamination due to thermal shock. The films deposited with 0% $N_2$ were representative of pure carbon films. The films were characterised by the use of ellipsometry, IR spectroscopy, XRD, XPS, Raman spectroscopy, Atomic Force Microscopy (AFM) and Secondary Ion Mass Spectroscopy (SIMS).

## 6.3 Results

Physically, $CN_x$ films were opaque, dark-brown/black in colour, which is a strong indication of their graphitic nature due to $sp^2$ bonding. Diamond, which is totally $sp^3$ bonded, is transparent, and by analogy, it would be expected that $\beta$-$C_3N_4$ films might also be transparent. The $CN_x$ films were smooth and featureless to the naked eye, with good adherence to the silicon substrate. The samples analysed by the various techniques employed were deposited under the parameters outlined in *Table 6.1*.

### 6.3.1 Hardness

Hardness testing of the films was carried out using a Vickers indenter. All hardness values were subject to the correction calculation outlined in section 4.2.1 for thin films. The films were brittle under load, and tended to fracture during indentation. Hence, it was difficult to estimate exactly the length of the indentation diagonals. There was considerable scatter in the results which ranged from 2000HV to 9000HV, with no obvious correlation with deposition conditions. However values in the range 8000 to 8500HV were consistently achieved. These are very high values and are likely to be inflated by the elastic recovery of the films.

Nano-indentation tests using a Berkovich indenter yielded equivalent Vickers hardness values in the range 1500HV to 2500HV for series G and showed large elastic recovery effects. Pure carbon films had the highest hardness value of 2500HV, and a general decrease in hardness occurred with increasing nitrogen content, as shown in *figure 6.1* (series G) down to approximately 1500HV. The points plotted are an average of 20 indentations. This is consistent with reports that hardness values increased as nitrogen partial pressure was decreased in samples at the same substrate bias (~-50V), with no strong dependence of hardness on the target power [141,151,155,156]. As the $sp^2$ bonding in $CN_x$ films increased with nitrogen partial pressure (as supported by XRD evidence later), the films exhibited lower hardness values. These values were always lower than those predicted for a film of $sp^3$ bonded carbon nitride.

### 6.3.2 Ellipsometry

The refractive index was measured by ellipsometry using λ=632.8nm. Three effects were observed

i) The refractive index of the $CN_x$ films was consistently lower than that of pure Carbon films grown under the same deposition conditions, as shown in *figure 6.2*.

ii) As the nitrogen content of the films grown under similar conditions was raised, there was a consequent slight increase in the refractive index.

iii) The most significant result was a reduction in refractive index as the magnetron current was increased as shown in *figure 6.3*. Films deposited at 1A magnetron current had the highest refractive index values. Little variation was evident between the refractive index values of films deposited at 2 and 2.5 A magnetron current.

Ellipsometry has shown that under fixed deposition conditions, the refractive index drops initially as nitrogen is introduced into the pure carbon film, and then steadily rises with nitrogen partial pressure. A possible explanation of this behaviour could be that as the $sp^2/sp^3$ ratio in hydrogenated amorphous carbon is increased, the refractive index is reduced [157]. XRD measurements, detailed later, have shown an increase in the $sp^2$ bonding nature with nitrogen partial pressure, which should lead to a continual decrease in refractive index with nitrogen partial pressure. Therefore the increase seen at higher $N_2/Ar$ ratios must be due to increasing nitrogen incorporation in the films. Sreenivas et al [158] also observed a similar decrease in refractive index of DLC films doped with nitrogen compared to pure DLC films. Similar values of refractive index to those obtained in these experiments have been reported by Grill et al [159] in his investigations of nitrogen-doped DLC films.

### 6.3.3 Infra-Red Spectroscopy

Infra-red spectroscopy was carried out over the range of 4000 $cm^{-1}$ to 600 $cm^{-1}$. Two main features emerged

i) As nitrogen concentration increased there was an increase in transmittance for wavenumbers greater than 1700 $cm^{-1}$ as shown in *figure 6.4*. The greatest increase was seen for films processed in 75% nitrogen partial pressure. The result is consistent with Li et al [155]. There was also a relative increase in the absorption in the 1200-1500 $cm^{-1}$ band, with the greatest increase from 0% to 25% nitrogen partial pressure. The films deposited at 25%, 50% and 75% nitrogen partial pressure all exhibited similar absorption in the 1200-1500 $cm^{-1}$ band.

ii) The transmittance depended on the magnetron current, with those films deposited at high magnetron current being more absorbing as shown in *figure 6.5* which showed a fourfold increase in absorption between films deposited at 2.5A and 1A current.

One of the most significant features to emerge from this study, as confirmed both by the XRD reflections and the absorption of the 1200-1500$cm^{-1}$ band in the IR is the increased occurrence of $sp^2$-type bonded carbon with increasing nitrogen partial pressure. Similar results have been reported by Mansour et al [160] and Friere et al [161], who found that nitrogen incorporation induced graphitization in amorphous carbon films. However, since the other deposition parameters can also effect this increased graphitization, the occurrence of $sp^2$ bonding may not indicate directly the levels of nitrogen incorporation into the $CN_x$ films.

Other features observed in the IR data were an absorption peak at 2200 $cm^{-1}$ attributed by Chen et al [132] to C≡N stretch, hence showing that nitrogen is chemically bonded to carbon. This peak increased with nitrogen partial pressure. A broad absorption band at 1200-1600 $cm^{-1}$

showed evidence for two peaks at 1300 $cm^{-1}$ and 1500 $cm^{-1}$ respectively, whose presence was independent of the nitrogen content. These peaks are attributable to C-C and C=C bonds [162]. Ricci et al [145] also found a broad absorbance at 1200-1600 $cm^{-1}$ , attributing C=N (imino) or $sp^2$ ν(C=C) at 1600$cm^{-1}$ and ν(C-N) at 1400$cm^{-1}$. Rossi et al [139] found similar absorbance in this region, and attributed it to ν(C-N) at 1220$cm^{-1}$, $sp^3$ C-C or ν(C=C) at 1390$cm^{-1}$ and ν(C=N) at 1625$cm^{-1}$. Han and Feldman [151] also found imino ν(C=N) and nitrile ν(C≡N) in the region 1600-2200$cm^{-1}$, and absorbance at 2100-2200$cm^{-1}$ due to isonitrile and nitrile when bound to an aromatic ring. Kaufman et al [163] corroborates this, and adds that absorbance at 2100-2200$cm^{-1}$ could be due to an sp-bonded region in the films. Chubaci et al [144], however, suggests that absorbance in this region could be due to the C≡N stretch mode only. Kumar et al [164] found an absorption peak at ≈ 2170 $cm^{-1}$ due to the stretching vibration of a C≡N, suggesting that C and N atoms are bonded in the film. Sreenivas et al [158] also found C≡N bonding at 2200$cm^{-1}$ which increased in intensity with increasing nitrogen incorporation, suggesting increased graphitisation.

The absence of absorption bands in the 3000$cm^{-1}$ region, characteristic of carbon-hydrogen bonding [132] is as expected, since no $H_2$ was used during deposition.

### 6.3.4 X-Ray Diffraction

X-ray diffraction of the films showed that they possessed an amorphous structure shown by a broad peak at $2\theta=27°$. The diffractograms exhibited some degree of ordering of the structure. *Figure 6.6* shows such a result obtained using Cukα radiation. The tabulated peak for graphite occurred at 26.5° thus a degree of graphitic-type bonding is evident. (The sharp peaks are due to the silicon substrate). As nitrogen concentration increased, this peak increased in size. *Figure 6.7* shows the height of this peak as a function of the nitrogen concentration indicating an increase in graphitic-type bonding. XRD peak intensity increased approximately linearly as nitrogen concentration was increased from 0% to 75% nitrogen partial pressure. Films

deposited at high magnetron current, (2.5A) possessed less ordered structure as indicated in, *figure 6.8*, by the XRD peak intensity. Peak intensity also increased by 45% as the substrate bias was made more negative from -15V to -50V d.c. *figure 6.9*. This peak increase was not so apparent on the increase in total system pressure, showing only an increase of 15%, *figure 6.10*.

In general, the $sp^2$ bonding structure or graphitic nature of the films is minimised under conditions of high magnetron current and low system pressure, both parameters affecting the degree of ion bombardment of the growing films. The substrate bias alters the $sp^2$ bonding content of the films in a contradictory manner to those previously mentioned since it would be expected that a more negative bias would also increase the amount of ion bombardment. This effect is relatively minor and its origin is unclear from the studies carried out to date. In a comparison of the relative percentages increase in XRD peak intensity dependent on deposition parameter, it was found that magnetron current produced the largest increase in peak intensity with films processed at 2.5A showing an increase of approximately 70% in comparison to film deposited at 2A.

### 6.3.5 X-ray Photoelectron Spectroscopy

Non-monchromated XPS spectra for an extended C1s (342-282 eV) region, the O1s (545-525 eV) region, the N1s (412-392 eV) region and a wide range (1100-0 eV) survey scan were recorded. The results for the extended C1s region show the expected photoelectron line (285.0 eV), with some asymmetry to the higher binding energy side, *figure 6.11*, due to the interaction with conduction band electrons. In all cases, the N1s peak increased with nitrogen partial pressure up to a maximum value of $\approx$ 18% atomic concentration. At the highest nitrogen partial pressure (75%), the nitrogen content of some of the films reduced below that for 50% nitrogen partial pressure films. At low deposition rate (1A magnetron current) there is some evidence of small concentrations of implanted Ar, but this is not observed at higher magnetron currents (2A).

The pronounced shoulder to the higher binding energy (B.E.) side of the main C1s photoelectron line, *figure 6.12*, due to the $\pi$-$\pi^*$ ($sp^2$) bonding can act as a general diagnostic for the presence of graphitic character in carbonaceous films. Additionally, the broad band feature centred at ≈30 eV above the C1s line is due to the presence of X-ray induced Electron Energy Loss (EEL) information. Similar EEL features at ≈27 eV (graphite) and 35 eV (diamond) have been reported [135-137,139]. The N1s region shows little or no peak intensity for the films deposited at 0% nitrogen partial pressure, however, a distinctive peak is observed in the samples processed in 25% nitrogen. A comparison of F0 with F1, J0 with J1, M0 with M1 and H0 with H1 in illustrates this, *Table 6.2*. A strong O1s peak is observed for all samples analysed at University of Ulster (section a). It was found that sputtering of the surface layer yielded lower O1s signals, indicating that the oxygen content is probably due in the main to surface absorption. It should be noted that XPS only samples the top 30-50 Angstroms and bulk compositions may differ.

The B.E. (eV) positions for C1s, O1s, N1s and where appropriate, Si2p peaks are given in *Table 6.2*. The full-width-at-half-maximum (FWHM) for each of the bands is also given in parenthesis. The area under each peak, for section (a), calculated after the removal of a suitable spectral background based on a Shirley-type integral yields an estimate of the "% atomic concentration" of each species detected.

From the spectra observed and the data in *Table 6.2*, section (a), a number of points can be made

i) The FWHM of the C1s band increases with nitrogen partial pressure for the three sets of samples (F, J and M) while the other varied parameters would seem to have no significant effect. This indicates that there may be more than one carbonaceous term present.

ii) The % atomic concentration of carbon decreases with increasing nitrogen partial pressure (series F, J and M).

iii) The B.E. position of the O1s line decreases with increasing nitrogen partial pressure while the corresponding FWHM increases. This change in B.E. and the overall peak shape suggests that the surface has less organic-type oxygen (C-OH, C=O, $COO^-$, etc) and that it may therefore be more inorganic in nature ($CO_3^-$,etc).

iv) The % atomic concentration of oxygen present rises steadily with the presence of 25% and 50% nitrogen for set J to a value of 13.4% but then falls again slightly when the sample is processed in 75% nitrogen to 9.5%.

v) The N1s peak position decreases in B.E. and the corresponding FWHM increases with increasing nitrogen. The most significant FWHM increase occurs with 25% nitrogen (4.3) and the peak width then stays at more-or-less this value as the nitrogen partial pressure is increased further (4.0 for both 50% and 75% nitrogen). The higher the B.E. for a certain peak, the higher the oxidation state. However, the converse cannot be directly inferred. Instead, the lower the B.E., the more indication there is of a pseudo-oxidation state.

vi) The % atomic concentration of nitrogen species in the surface region of the films increases dramatically with nitrogen content with similar changes resulting for all three (F, J and M) sets of samples studied.

vii) The small Si2p signal observed for some of the samples is assumed to be a result of a non-coherent film coverage. The most significant amount of silicon is observed for the sample M1 (2.2% atomic).

viii) The N1s B.E. of approximately ~ 399 eV is characteristic of covalent bonds. Similar B.E. values as those tabulated in *Table 6.2* for N1s have been reported [139,140,144,145,150] attributable to N≡C species.

ix) XPS measurements of physisorbed $N_2$ on graphite display a B.E. of ~ 404 eV, which is much larger than those obtained, thus suggesting that nitrogen atoms are not bonded in a molecular configuration. This is in agreement with other authors [167,166].

XPS shows us that the films contain carbon bonded to nitrogen and that the amount of nitrogen species in the coating is dependent mainly on the $N_2$ gas partial pressure. Although there is an indication of the presence of graphitic-type ($sp^2$) carbon from the asymmetry on the C1s peak and the EEL structure, the energy resolution is not good enough in these experiments to draw firm conclusions as to the degree of graphitisation present. The overlay plot for samples F1, F2 and F3 in *figure 6.11* shows the EEL and $\pi$-$\pi^*$ shoulder on the higher B.E. side of the C1s line at approximately 320eV on the horizontal axis. *Figure 6.12* shows the C1s peak itself, and *figure 6.13* shows the N1s peak for samples F1-F3. As can be seen in *figure 6.12* (a close-up of the higher binding energy side of the C1s peak), there is a slight change in the spectral envelop profile as a function of nitrogen partial pressure which shows a less pronounced, higher B.E. component for 75% nitrogen partial pressure (F3), at approximately 320eV. Likewise, there is a slight, but distinguishable, change in the $\pi$-$\pi^*$ shoulder on the C1s peak, as seen in *figures 6.11* ( ≅285eV) and *6.12* ( ≅ 290eV).

The N1s band for each of the samples, when shown in overlay *figure 6.13*, are very similar in form, and result from three chemically distinct species with two main components and one minor contribution on the higher B.E. side. In general, shifts to a higher B.E. in XPS spectra are a result of higher oxidation state environments.

A linear least squares fitting procedure was used to deconvolute the N1s spectra and the results are depicted in *figure 6.14* for sample F1. A comparison of the B.E., FWHM and %area for each of the samples F1-F3 fitted for three components after deconvolution shows that all three samples have very similar contributions from the individual components with only a small increase in the relative intensity of component 3 for the highest nitrogen partial pressure (75%). Component 1 is attributed to carbon-nitride bonding (C=N) while components 2 and 3 are attributed to oxy-carbon-nitrides (C-O-N) and (C-OO-N) respectively. Rossi [139], however, found evidence of only 2 components, and attributed component 1 to C=N and component 2 to C≡N.

### 6.3.6 Raman Spectroscopy

Raman spectroscopy affords a powerful tool in the determination of the $sp^2$ and $sp^3$ character in carbon-carbon bonding systems. The main feature observed is a very broad spectral envelop spanning 1150 - 1750 $cm^{-1}$ which has two major components centred at ≈ 1380 $cm^{-1}$ and 1560 $cm^{-1}$ respectively, as shown in *figure 6.15*. This overall structure is assigned to an $sp^2/sp^3$ carbon-carbon bonded structure similar to that obtained in the case of poorer quality diamond like carbon (DLC) materials. Cho et al [136,137] reported a similar peak at 1560 $cm^{-1}$ attributable to a graphite peak (G-peak). He also reported a disordered peak (D-peak) at 1350 $cm^{-1}$. Similar reports from Mendoza et al [167], Nemanich and Solin [168] and others [132,134,139,169] support the bonding structure observed in the samples studied here. Tuinstra and Koenig [170] have found that in mixed $sp^2/sp^3$ bonded carbon, the overall Raman spectra is dominated by the G-peak occurring in their films at 1575 $cm^{-1}$.

The spectral features seen for samples F1-F3 would therefore seem to be a result of the Graphite (G) and Disordered (D) peaks observed for graphite occurring at 1560 $cm^{-1}$ and 1380 $cm^{-1}$ respectively.

A second, much less intense, but equally important feature, is observed in the Raman spectra of samples F1-F3, i.e. those processed in nitrogen. This band, centred at ≈2200 $cm^{-1}$ is attributed to a ν(C≡N) mode and is found to increase in intensity with increase in nitrogen partial pressure. Note that no ν(C≡N) peak is observed in the case of sample F0, i.e. no nitrogen present in the processing gas atmosphere.

### 6.3.7 AFM, Surface Roughness, SIMS, and Resistivity measurements

The films as analysed by AFM are predominantly amorphous, as can be seen in *figure 6.16* (sample J1). The round features on the surface of the film show a globular morphology. Perturbations having larger lateral dimensions than the other regular features on the surface and having a height clearly exceeding the corrugation of the rest of the surface are termed macro-particles. *Figure 6.17* (sample E0) shows a large round macro-particle on a surface composed of round globules having different diameters, up to a few microns, and other, mainly roundish shapes. Three different surface topographies were found and are listed in order of abundance. Firstly a completely smooth, featureless topography, *figure 6.16* (J1), secondly, a topography composed of small roundish globules, as shown in *figure 6.17* (E0), and thirdly, a topography composed of irregularly shaped globules of differing dimensions, *figure 6.18* (K2). Different amounts of macro-particles were found on all these surfaces. These features were not correlated with the deposition parameters. The average roughness (Ra) values are calculated from a 5000x5000 $nm^2$ scan. No change in Ra was observed with varying nitrogen partial pressure. However, variation of the other deposition parameters did have an effect, namely:

i) In a comparison of films deposited under conditions of 1A magnetron current, $8x10^{-3}$ bar system pressure and floating bias (series D), with those deposited under the same magnetron current and system pressure, but instead at a substrate bias of -50 V d.c. (series K), a reduction in Ra was seen from an average value of 6nm to 2nm.

ii) Films deposited at 1A magnetron current, $5x10^{-3}$ bar system pressure, and -50V d.c. substrate bias (series G), when compared to films deposited under similar magnetron current and substrate bias, but at a system pressure of $8x10^{-3}$ mbar (series K), were seen to have higher Ra values, averaging 12nm compared to 2nm for the latter deposition conditions.

*Figure 6.19* (series G) shows the ratio of $^{14}N$ to $^{13}C$ signals as a function of nitrogen partial pressure for films deposited at 1A magnetron current, $5x10^{-3}$ bar system pressure and -50V d.c substrate bias obtained from the SIMS analysis. The carbon and nitrogen signals are uniform throughout the thickness of the film. Up to a nitrogen partial pressure of 50%, increased levels of nitrogen incorporation are seen in the films. However, for the sample representative of 75% nitrogen partial pressure, the ratio of nitrogen to carbon fell, compared to the sample deposited in a 50% nitrogen plasma. This result confirms the XPS results. A similar decrease in nitrogen incorporation has been reported by others [171].

Resistivity measurements have shown that the films had very low conductivity, which was difficult to quantify. This conductivity may, however, be sufficient to allow enough leakage current to flow, explaining the effect of applying the -50V d.c. bias to the substrate.

## 6.4 Discussion

The most significant feature to emerge from this study is the increased occurrence of $sp^2$-type bonded carbon with nitrogen content. This is confirmed both from the XRD reflections and the absorption of the 1200-1500 $cm^{-1}$ band in the infra-red. This cannot be used, however, as a measure of the nitrogen content since the other deposition conditions have an important influence on this parameter. It is clear that the graphitic-type content is minimised under conditions of high magnetron power and low pressure, which would maximise the ion bombardment of the growing films. Although the substrate bias alters the graphitic content of the films in a contradictory manner to the other parameters since more negative bias would also be expected to increase the ion bombardment, this effect is relatively minor. It is, however,

uncertain why this should occur. Resistivity measurements showed that the films had very low conductivity, although some conductivity was observed, which may account for any effect of the -50V d.c. bias. From the refractive index measurements shown in *figure 6.2 & 6.3* it is clear that under fixed conditions of magnetron current, pressure and bias, as nitrogen content is increased the index initially drops then rises steadily. An explanation of this behaviour can be given. Donnelly et al [157] have suggested that as $sp^2$ to $sp^3$ ratio in hydrogenated amorphous carbon is increased, the refractive index is reduced. Since the XRD measurements referred to previously show an increase in the graphitic nature with nitrogen content, this should lead to a continual decrease in refractive index with nitrogen content. Therefore the increase which is seen at higher $N_2/Ar$ ratios must be due to increasing nitrogen incorporation in the films.

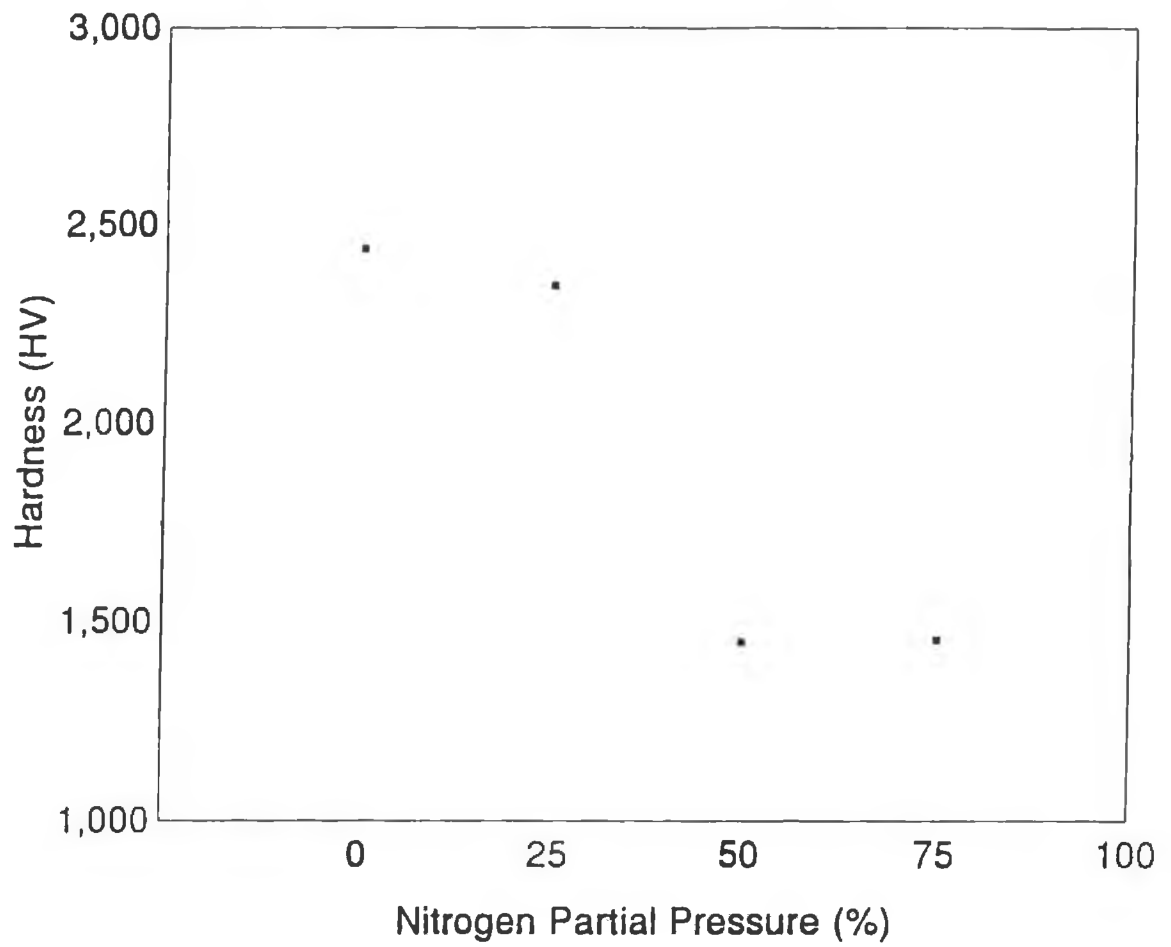


**Figure 6.1** **Hardness (HV) as a function of $N_2$% partial pressure for Series G**

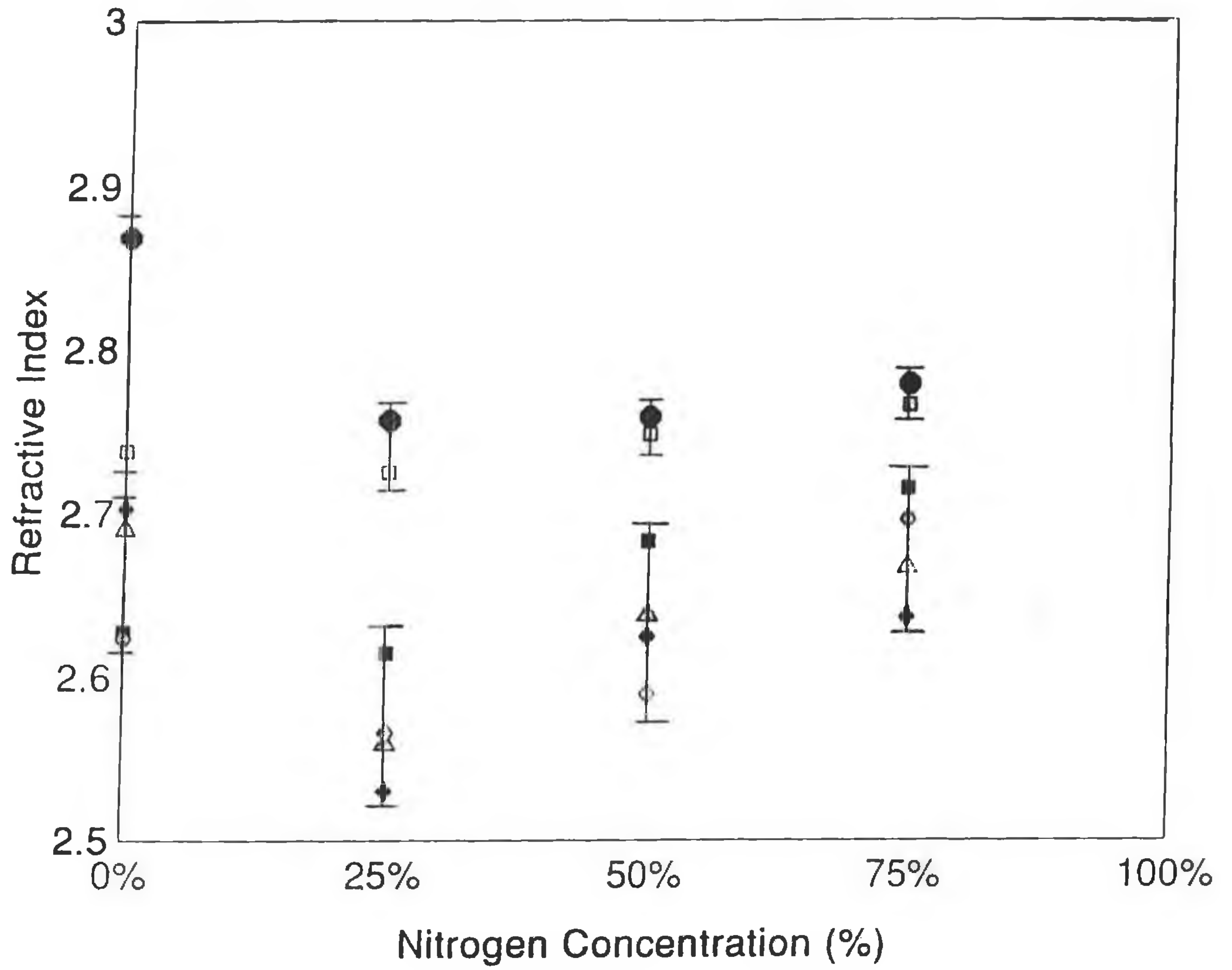


**Figure 6.2** **Refractive Index vs. Nitrogen Concentration (%) at -50V d.c.substrate bias.**

1A, $5x10^{-3}$ mbar
1A, $8x10^{-3}$ mbar
2A, $5x10^{-3}$ mbar
2A, $8x10^{-3}$ mbar
2.5A, $5x10^{-3}$ mbar
2.5A, $8x10^{-3}$ mbar

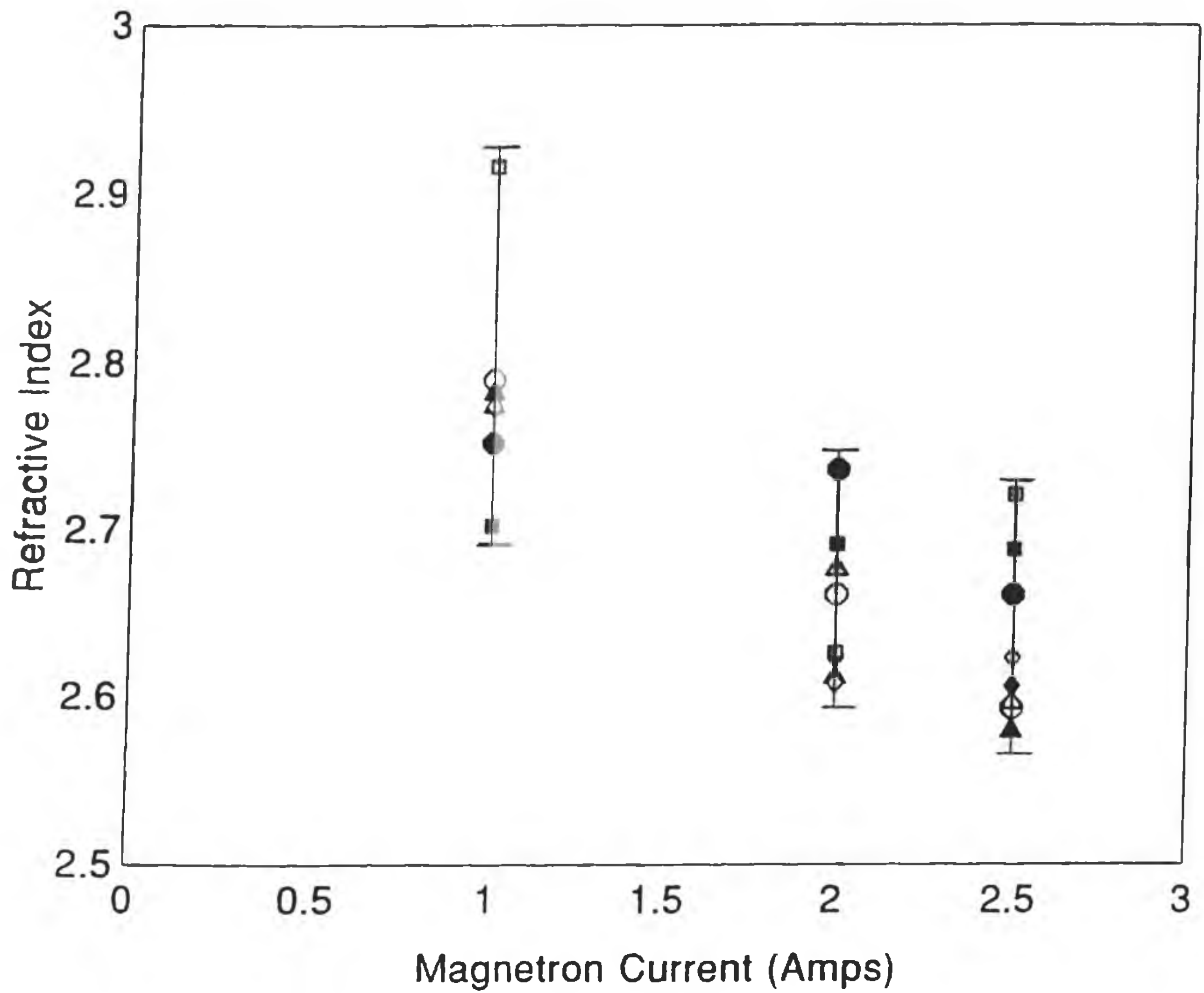


**Figure 6.3** **Refractive Index vs. Magnetron Current (Amps) at floating bias (approx. -17V d.c.).**

0% $N_2$, 5x$10^{-3}$ mbar — 25% $N_2$, 5x$10^{-3}$ mbar — 50% $N_2$, 5x$10^{-3}$ mbar
75% $N_2$, 8x$10^{-3}$ mbar — 0% $N_2$, 8x$10^{-3}$ mbar — 25% $N_2$, 8x$10^{-3}$ mbar
50% $N_2$, 8x$10^{-3}$ mbar — 75% $N_2$, 8x $10^{-3}$ mbar

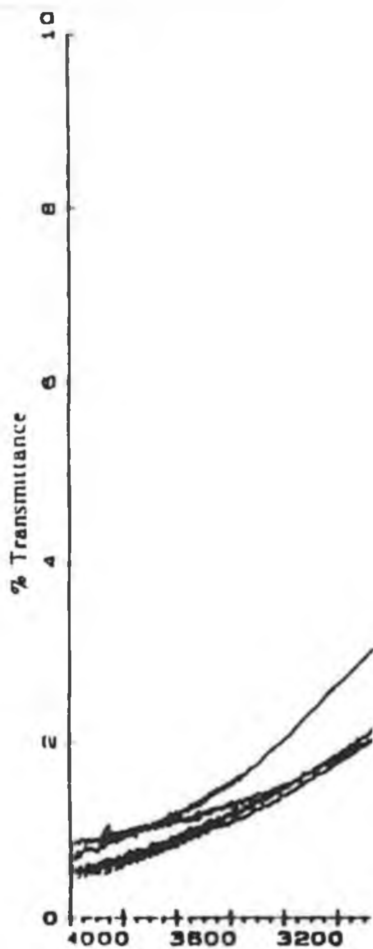


**Figure 6.4**

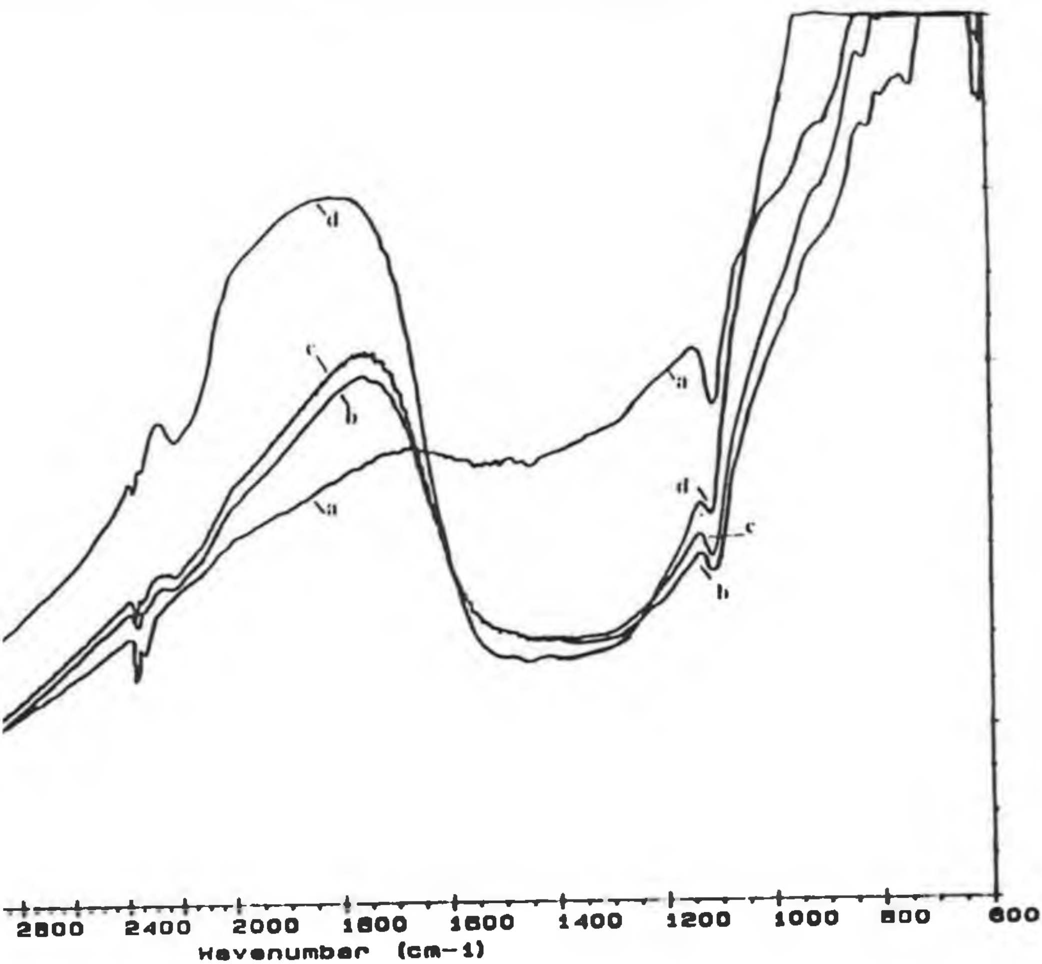


**Infra-red Transmittance as a function of the nitrogen concentration. Deposition parameters were -50V d.c. substrate bias, 1A magnetron current, $5 \times 10^{-3}$ mbar system pressure.**

**a 0% $N_2$ b 25% $N_2$ c 50% $N_2$ d 75% $N_2$**

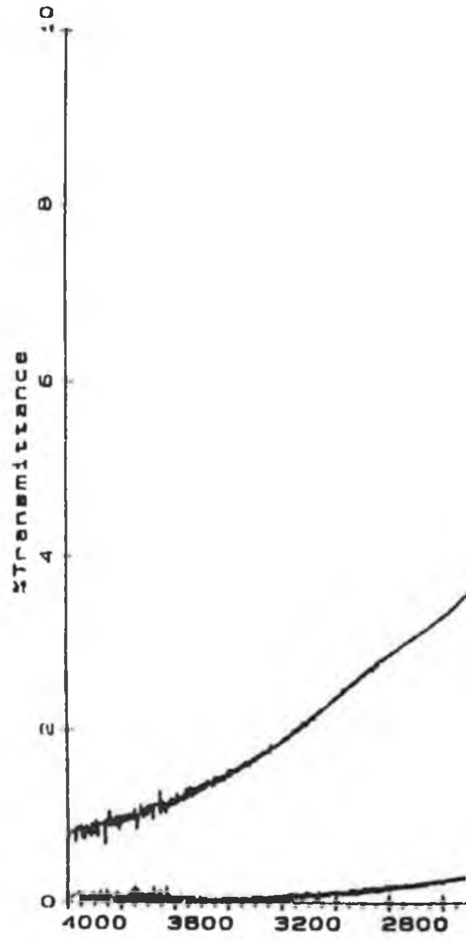


Figure 6.5

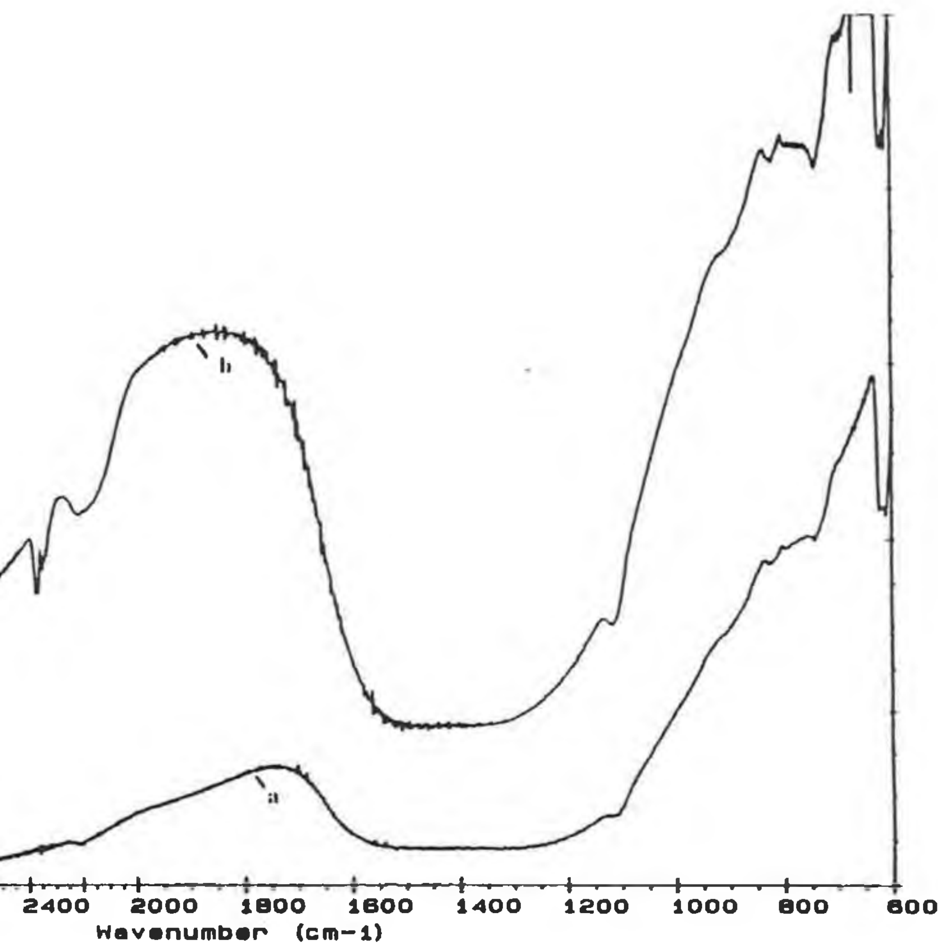


**Infra-red Transmittance as a function of the magnetron current.**

**Deposition parameters were 75% $N_2$, -50V substrate bias and $5x10^{-3}$ mbar system pressure.**

**a 2.5A b 1A**

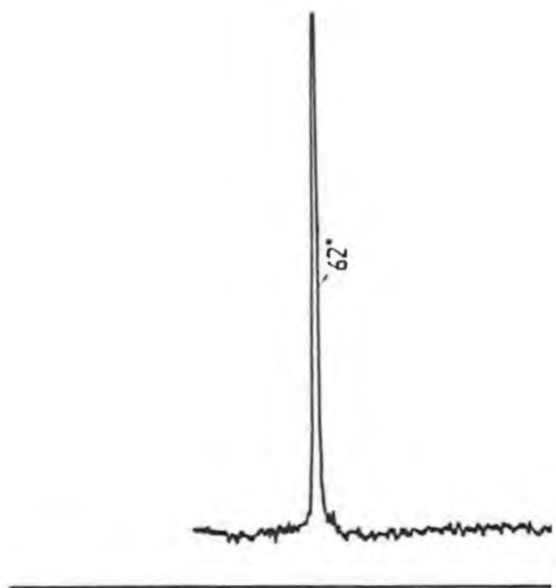

**Figure 6.6**

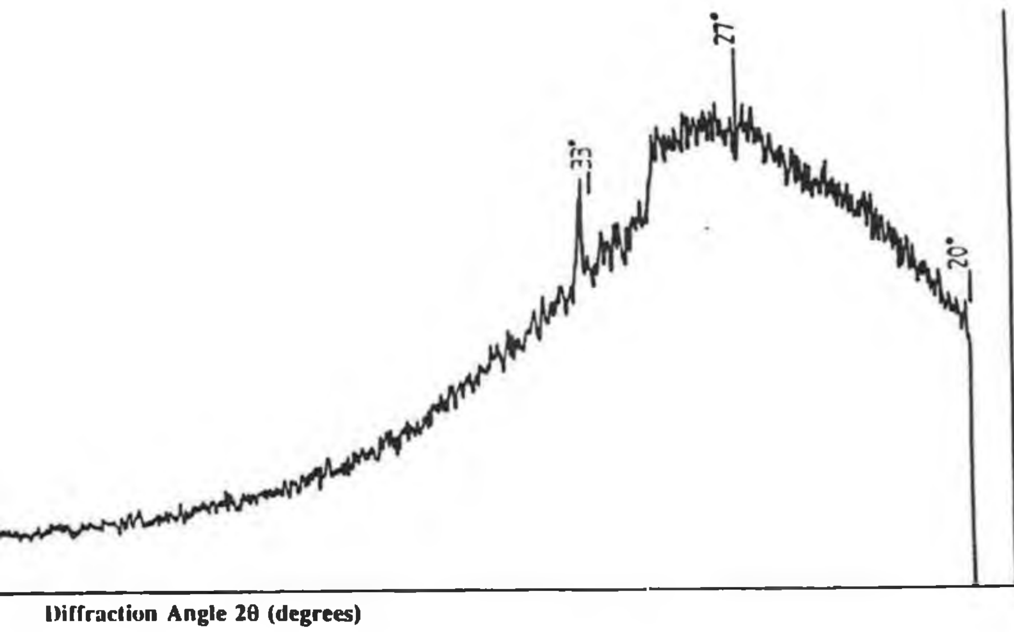


**An XRD diffractogram of a CN film deposited at -50V substrate bias, $5x10^{-3}$ mbar system pressure and 75% $N_2$ concentration.**

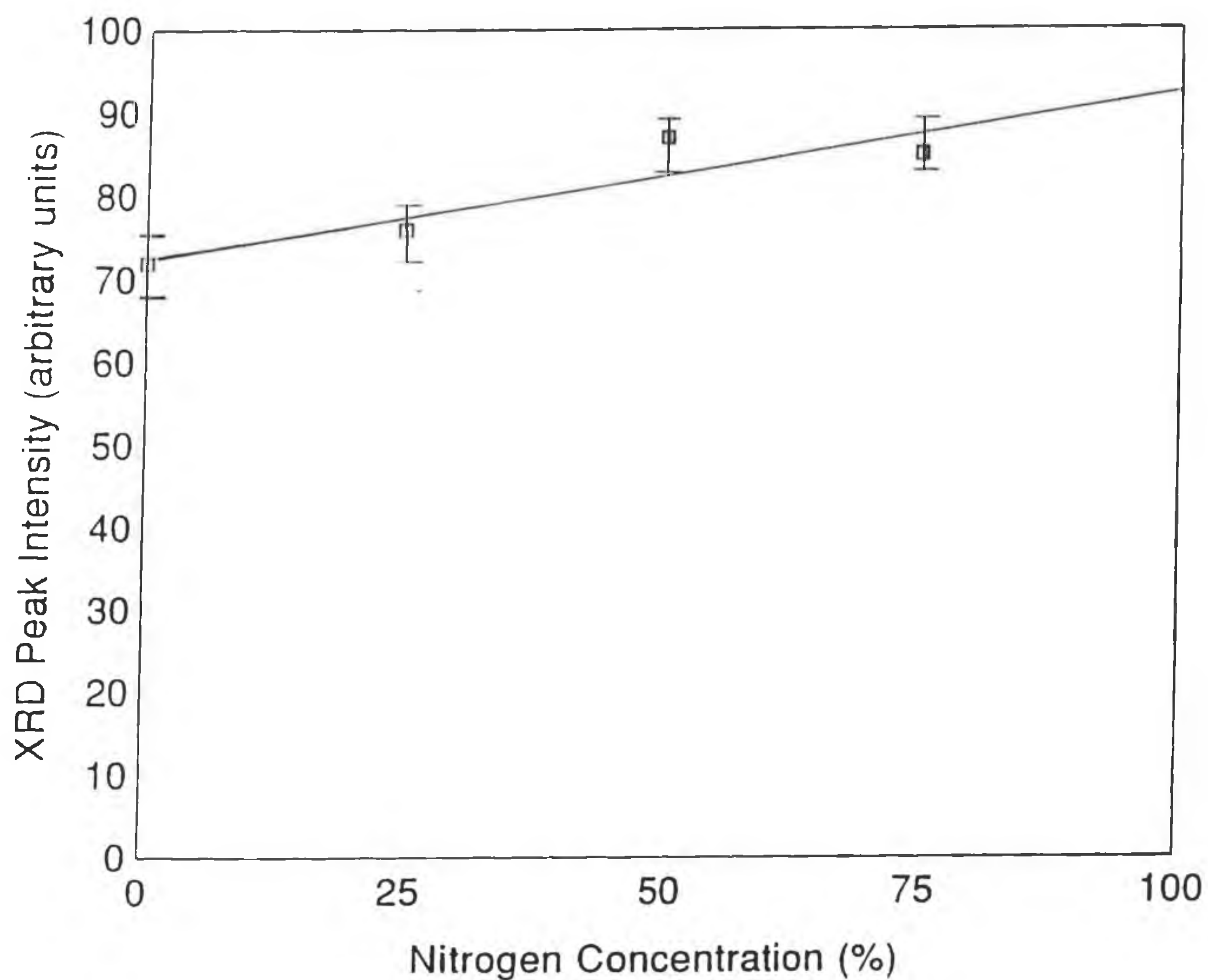


**Figure 6.7** **XRD Peak Intensity vs. Nitrogen Concentration (%). Deposition parameters were -50V substrate bias, 2A magnetron current and $5x10^{-3}$ mbar system pressure.**

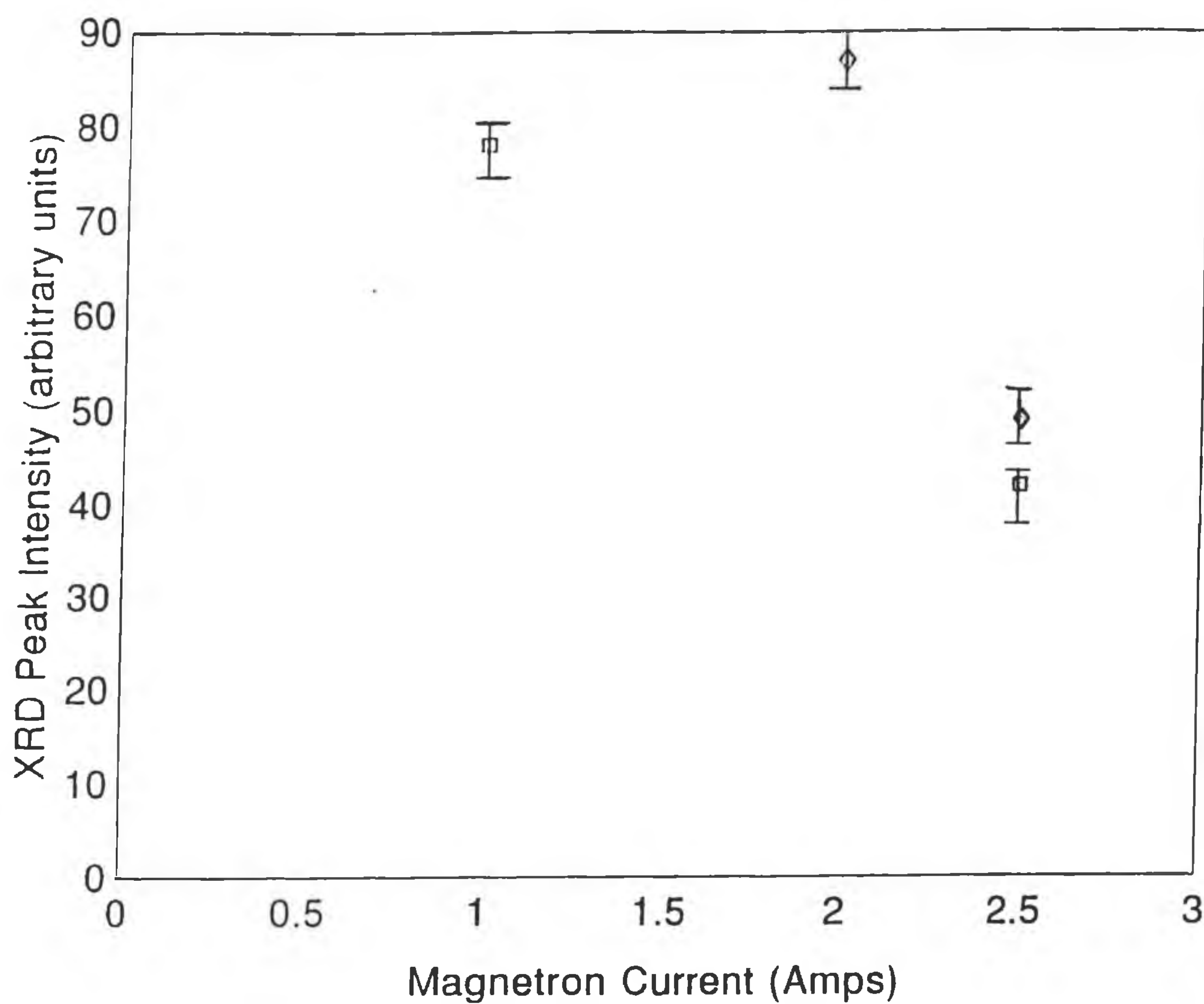


**Figure 6.8** **XRD Peak Intensity vs. Magnetron Current (Amps).**

□ **75% $N_2$, -50V bias and $8x10^{-3}$ mbar**
◊ **75% $N_2$, -50V bias and $5x10^{-3}$ mbar**

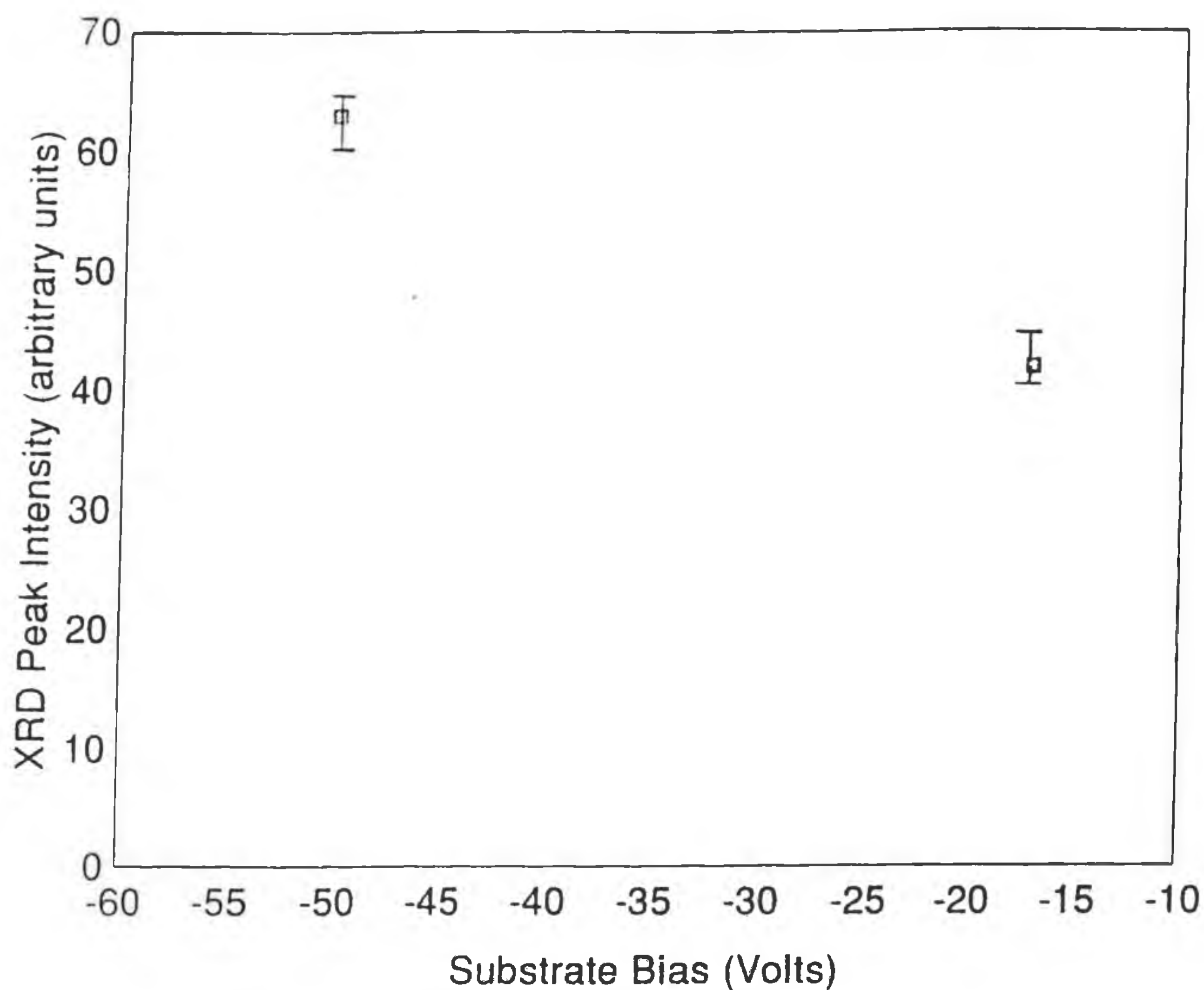


Figure 6.9 **XRD Peak Intensity vs. Substrate Bias (Volts). Deposition parameters were 50% $N_2$, 1A magnetron current and $5x10^{-3}$ mbar system pressure.**

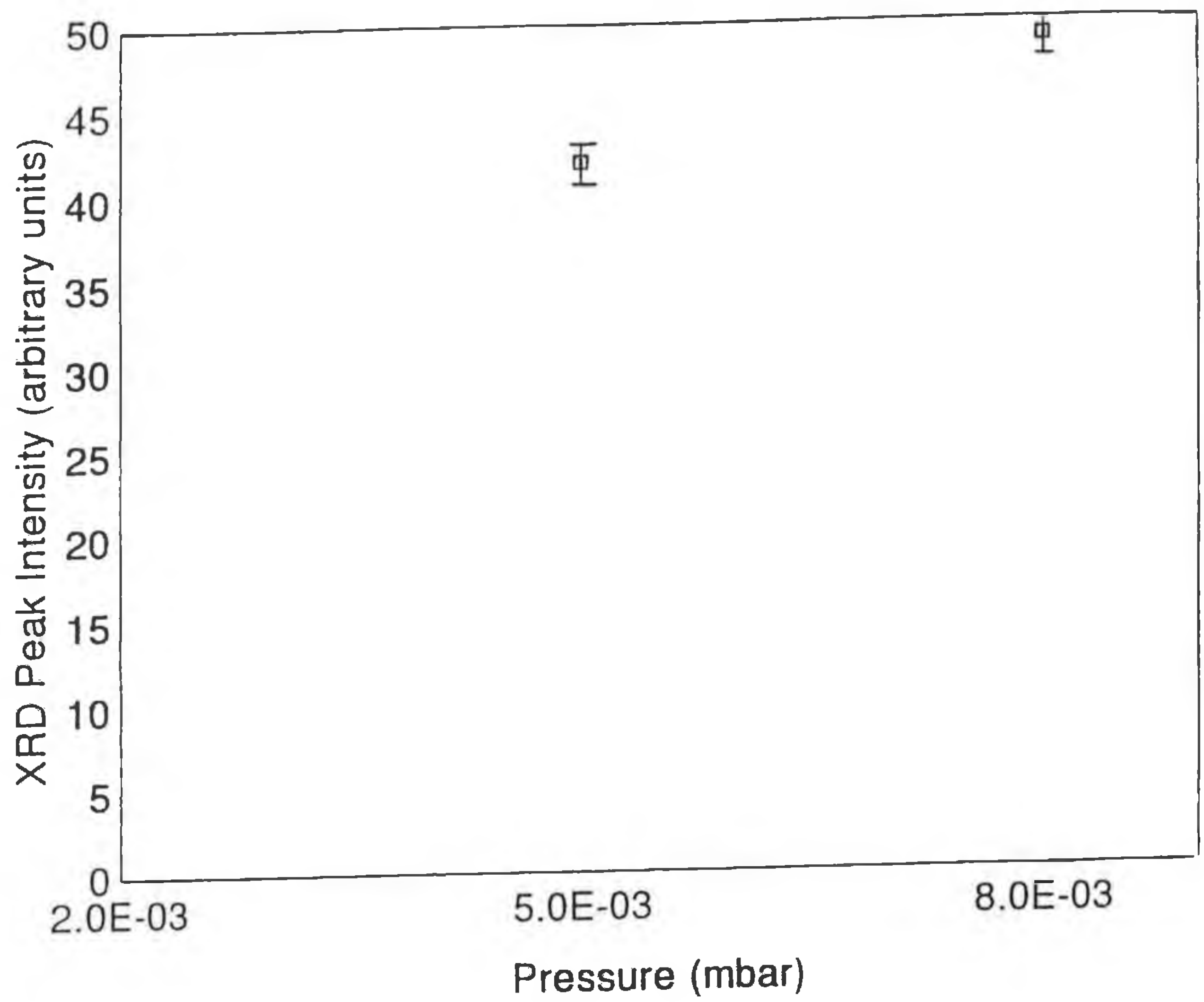


Figure 6.10 **XRD Peak Intensity vs. System Pressure (mbar). Deposition parameters were 75% $N_2$, -50V substrate bias and 2.5A magnetron current.**

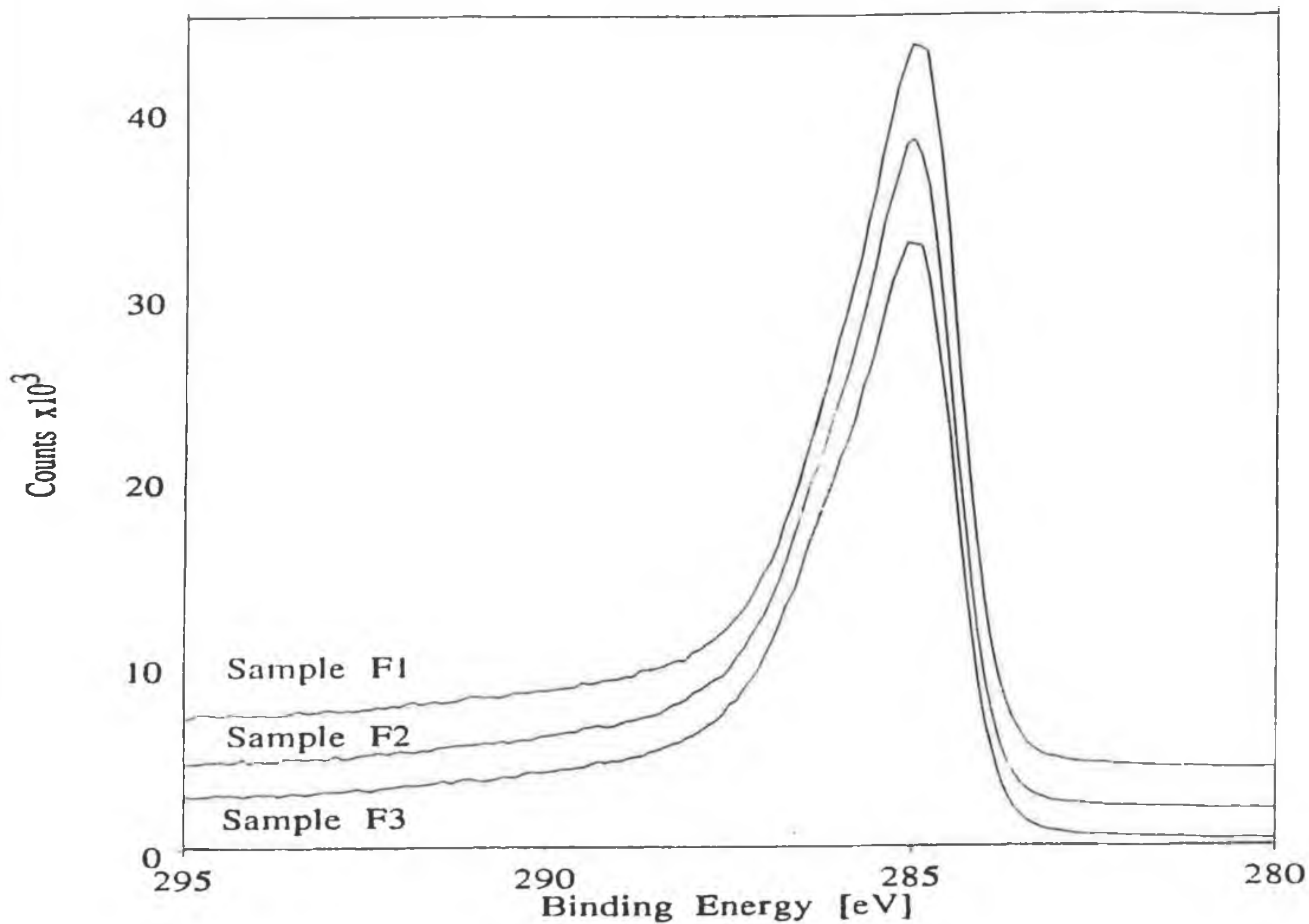


**Figure 6.11** **An overlay plot showing the EEL and $\pi-\pi^*$ shoulder on the C1s line of samples deposited at 2.5A magnetron current, $8x10^{-3}$ mbar system pressure and at floating bias with varying nitrogen partial pressure.**

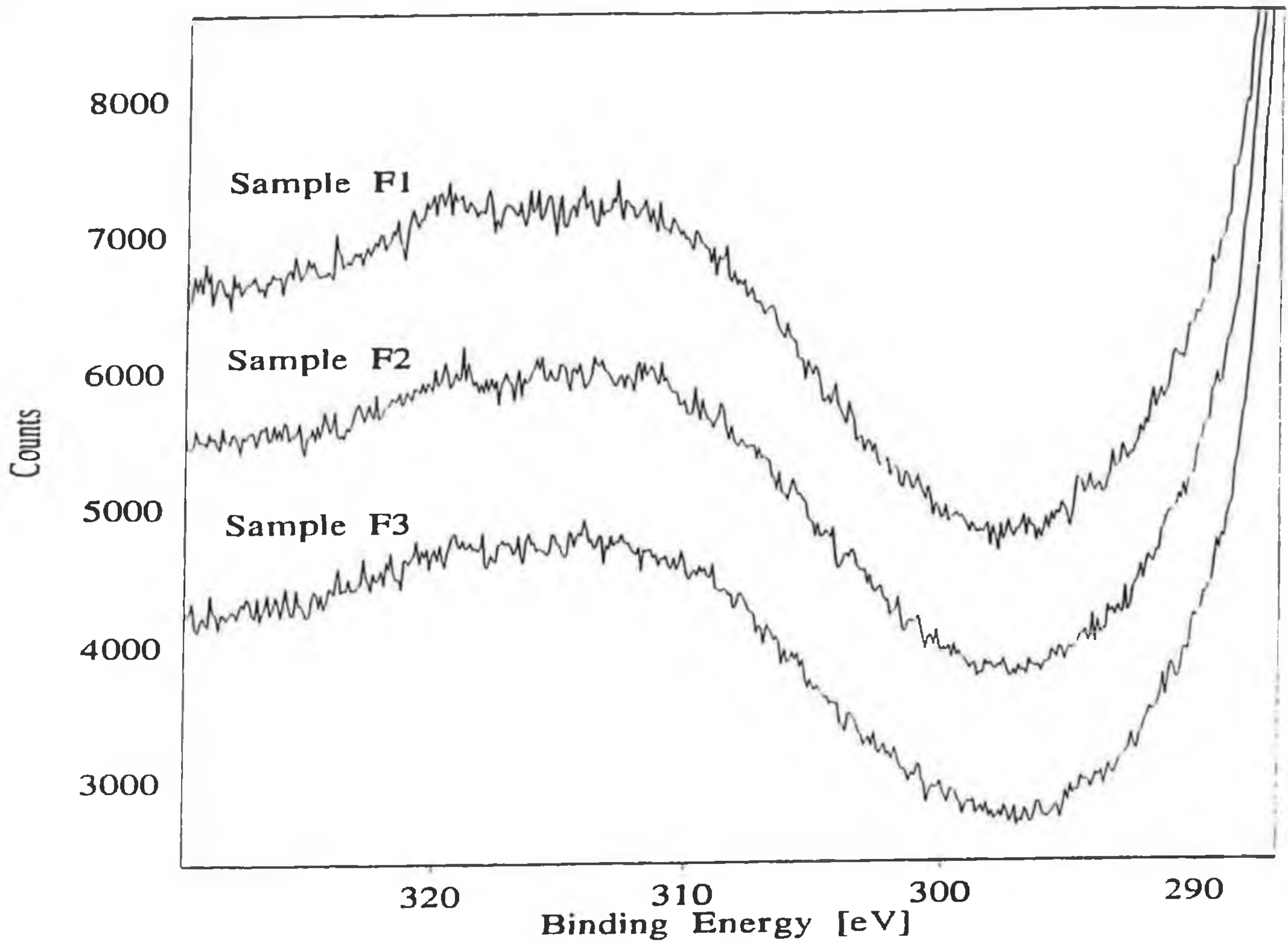


**Figure 6.12** **The XPS C1s peak for samples deposited at 2.5A magnetron current, $8x10^{-3}$ mbar system pressure and at floating bias with varying nitrogen partial pressure.**

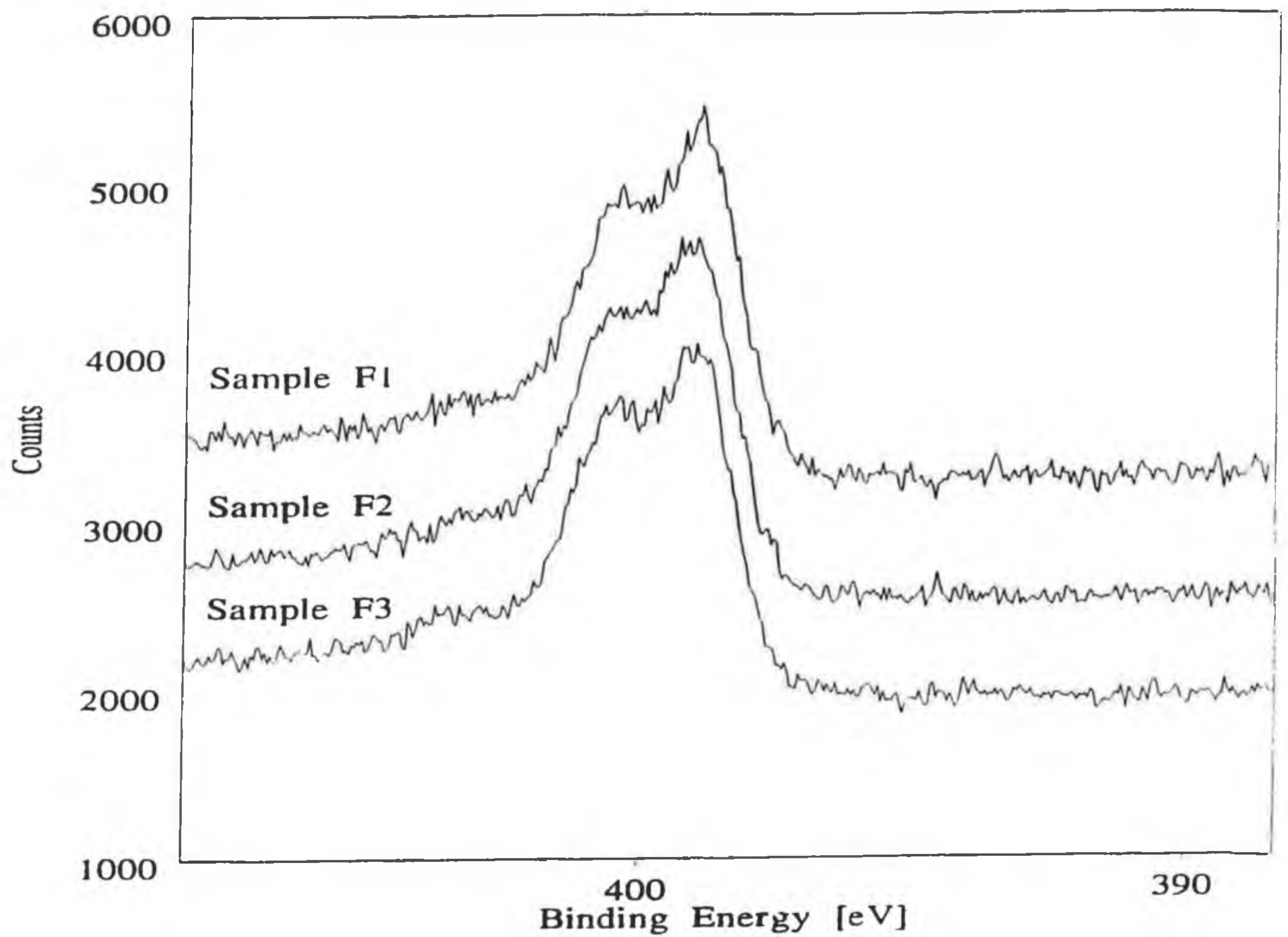


**Figure 6.13** **The XPS N1s peak for samples deposited at 2.5A magnetron current, $8x10^{-3}$ mbar system pressure and at floating bias with varying nitrogen partial pressure.**

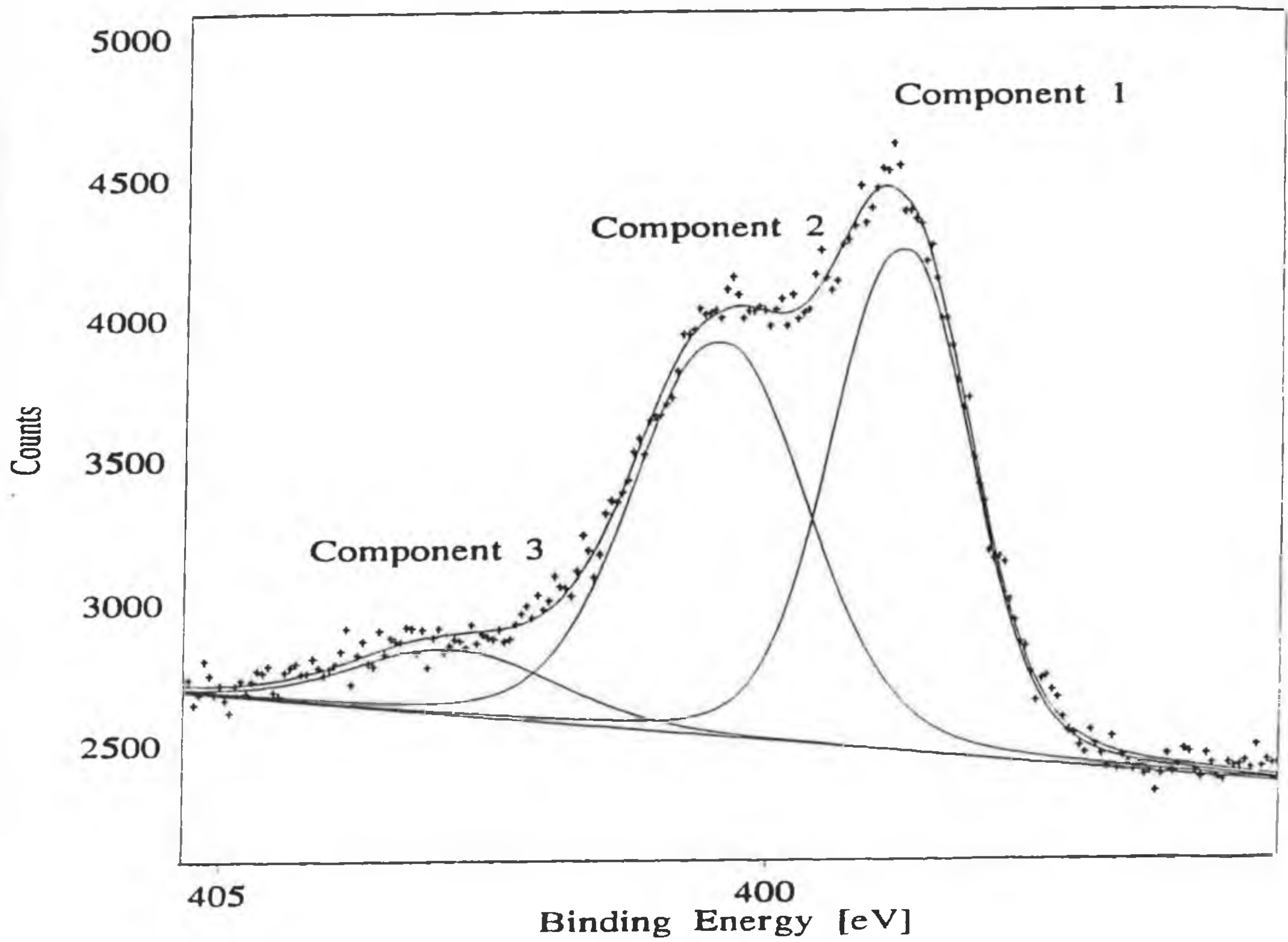


**Figure 6.14** **Deconvolution of the N1s peak, using a linear least squares fitting procedure, for samples deposited at 2.5A magnetron current, $8x10^{-3}$ mbar system pressure at floating bias, and 25% $N_2$ partial pressure.**

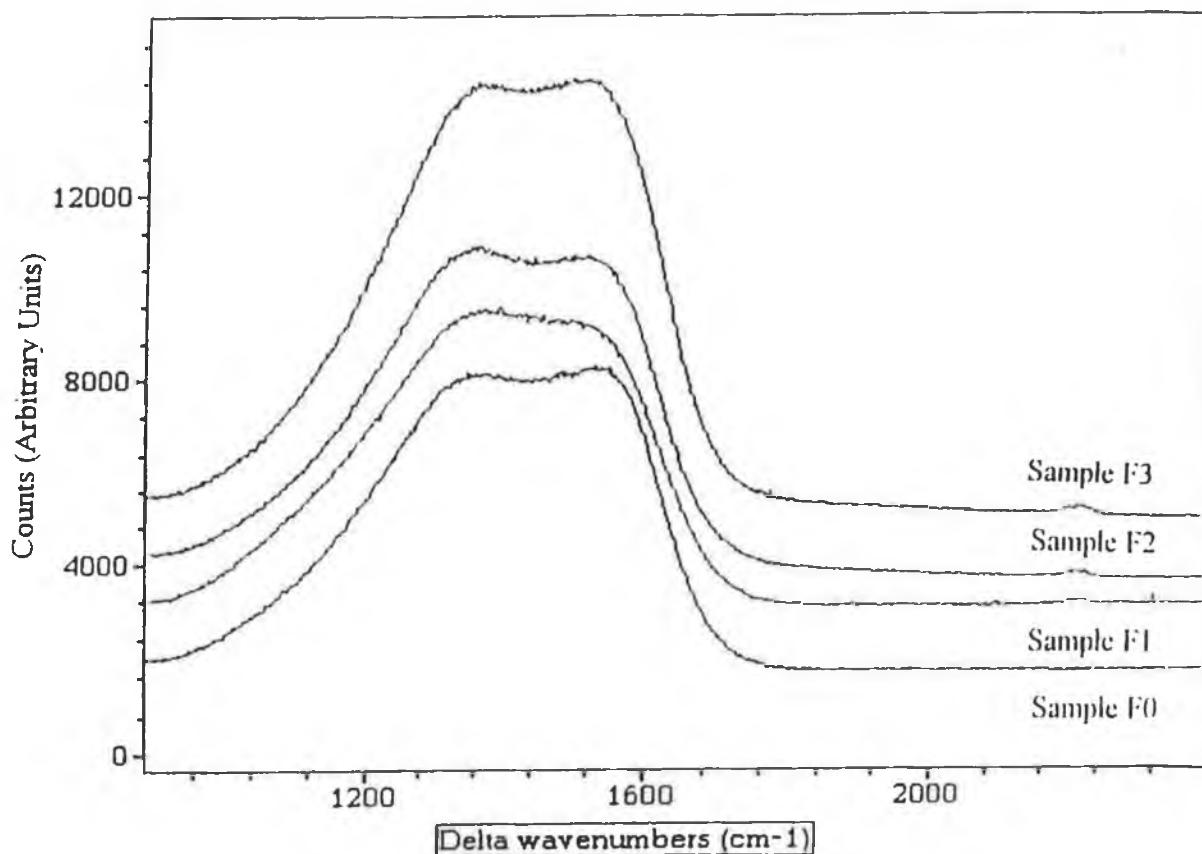


**Figure 6.15** **Raman spectral bands for samples deposited at 2.5A magnetron current, $8x10^{-3}$ mbar system pressure and at floating bias with varying nitrogen partial pressure.**

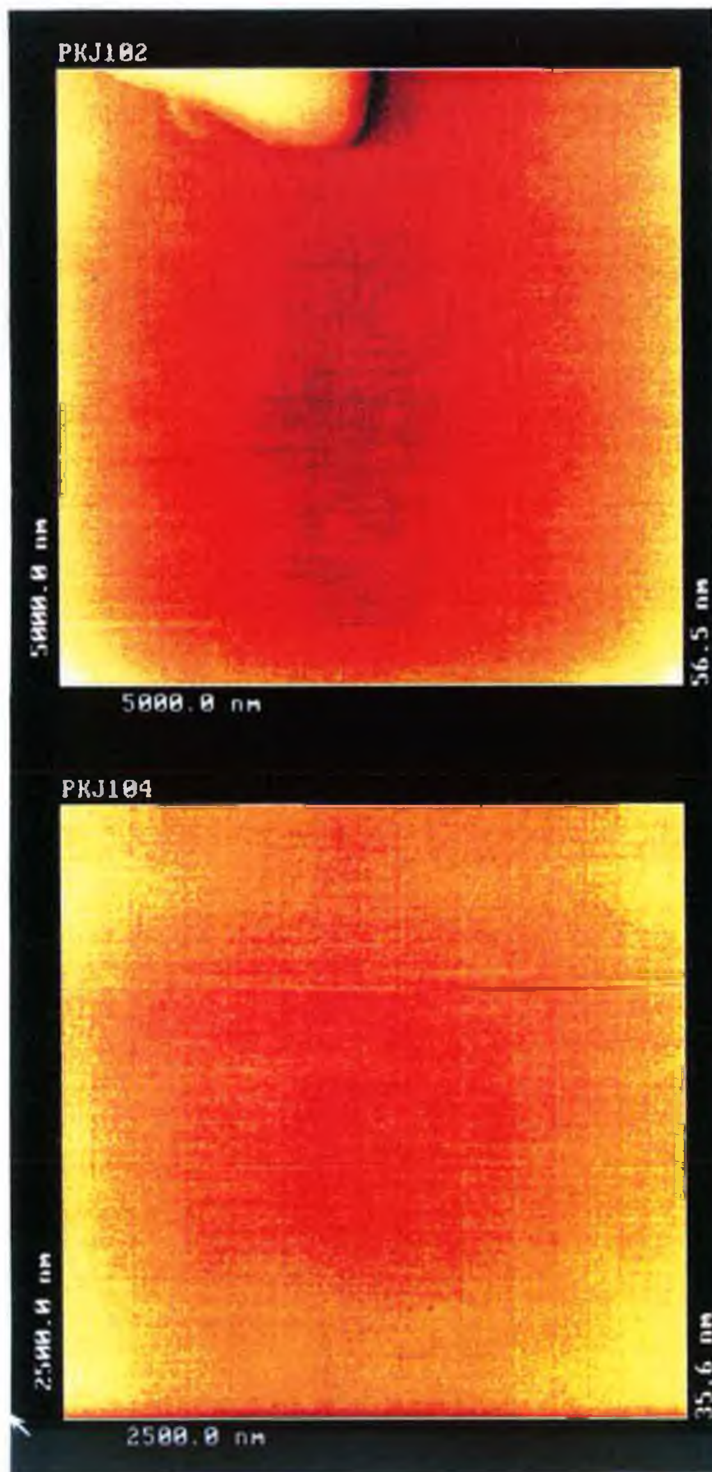


**Figure 6.16** **AFM micrograph of amorphous $CN_x$ films (J1)**

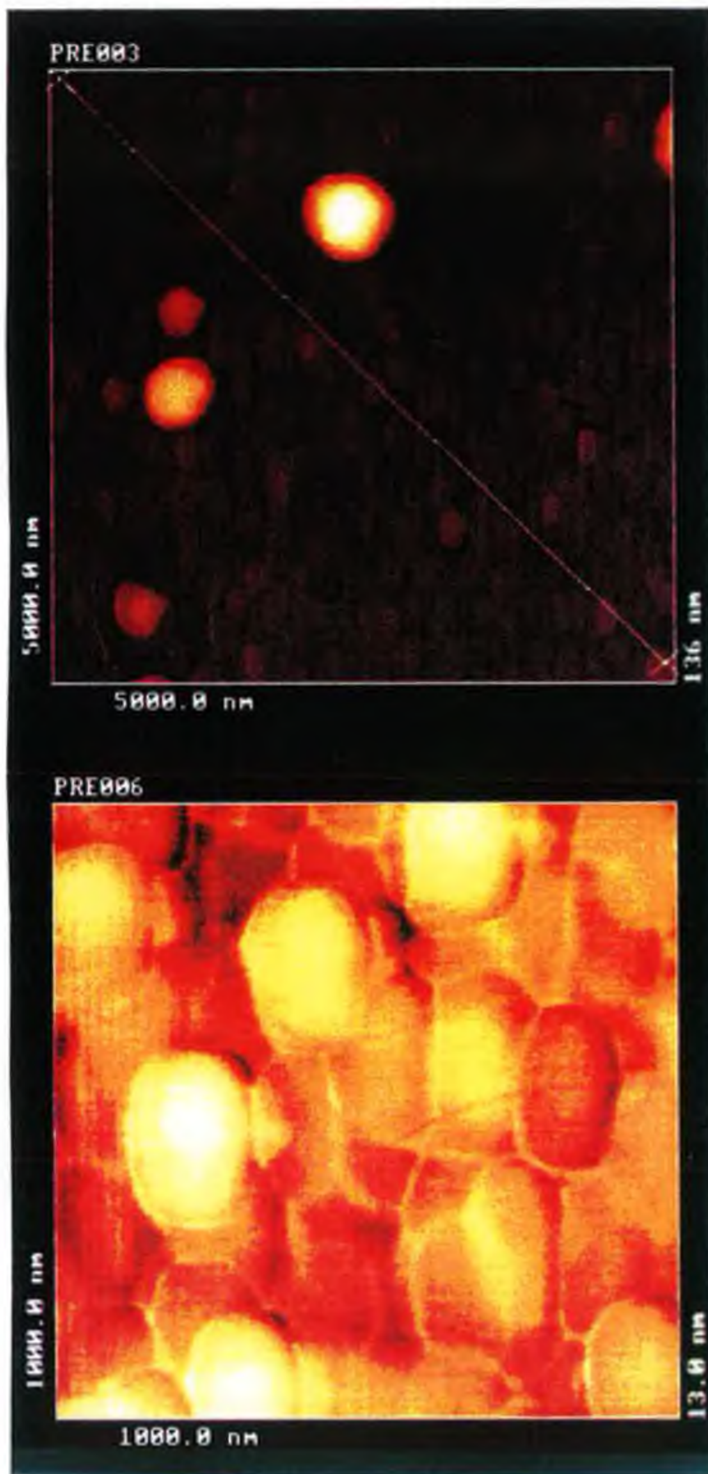


**Figure 6.17** **AFM micrograph of $CN_x$ films composed of small roundish grains≅200nm in size (E0)**

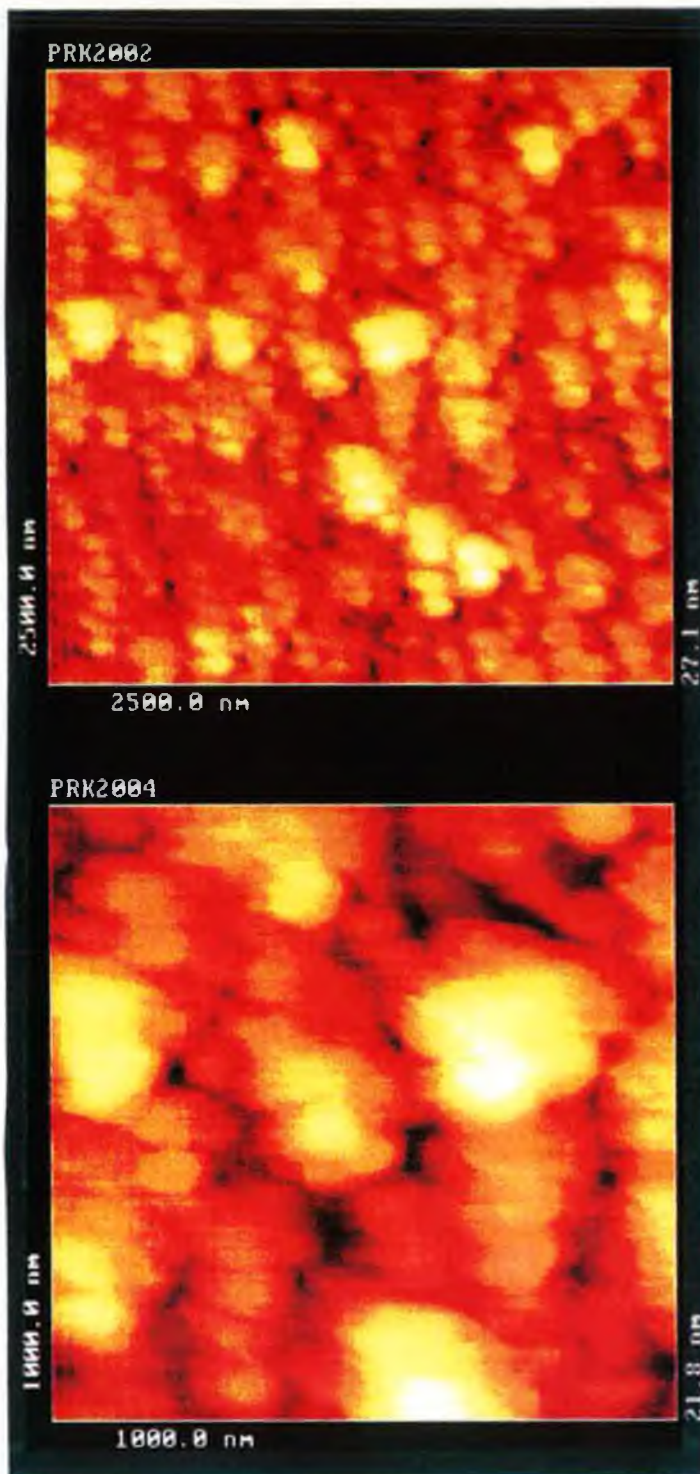


**Figure 6.18** **AFM micrograph of $CN_x$ films composed of irregularly-shaped grains of differing size (K2)**

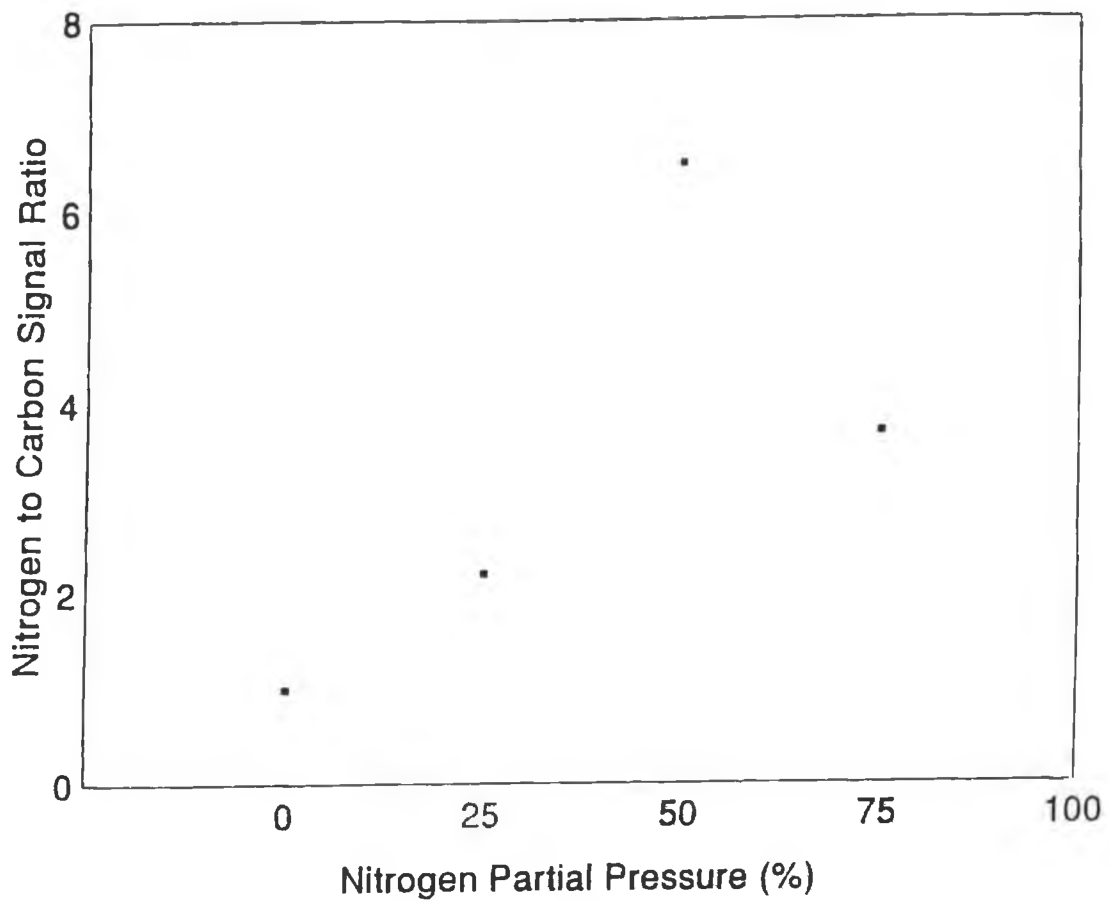


**Figure 6.19** $^{14}N$ to $^{13}C$ signal ratio as a function of $N_2$% partial pressure calculated from SIMS data for films deposited at 1A magnetron current, $5x10^{-3}$ mbar system pressure and at -50V d.c. substrate bias.

| Sample | Magnetron Current | System Pressure | $N_2$% Partial Pressure | Substrate Bias |
|---|---|---|---|---|
| A0 | | | 0% | |
| A1 | | $5 \times 10^{-3}$ | 25% | |
| A2 | 1 Amp | mbar | 50% | Floating (≈ -17V) |
| A3 | | | 75% | |
| B0 | | | 0% | |
| B1 | | $5 \times 10^{-3}$ | 25% | |
| B2 | 2 Amps | mbar | 50% | Floating (≈ -17V) |
| B3 | | | 75% | |
| C0 | | | 0% | |
| C1 | | $5 \times 10^{-3}$ | 25% | |
| C2 | 2.5 Amps | mbar | 50% | Floating (≈ -17V) |
| C3 | | | 75% | |
| D0 | | | 0% | |
| D1 | | $8 \times 10^{-3}$ | 25% | |
| D2 | 1 Amp | mbar | 50% | Floating (≈ -17V) |
| D3 | | | 75% | |
| E0 | | | 0% | |
| E1 | | $8 \times 10^{-3}$ | 25% | |
| E2 | 2 Amp | mbar | 50% | Floating (≈ -17V) |
| E3 | | | 75% | |
| F0 | | | 0% | |
| F1 | | $8 \times 10^{-3}$ | 25% | |
| F2 | 2.5 Amps | mbar | 50% | Floating (≈ -17V) |
| F3 | | | 75% | |
| G0 | | | 0% | |
| G1 | | $5 \times 10^{-3}$ | 25% | |
| G2 | 1 Amp | mbar | 50% | -50 V d.c. |
| G3 | | | 75% | |
| H0 | | | 0% | |
| H1 | | $5 \times 10^{-3}$ | 25% | |
| H2 | 2 Amps | mbar | 50% | -50 V d.c. |
| H3 | | | 75% | |
| J0 | | | 0% | |
| J1 | | $5 \times 10^{-3}$ | 25% | |
| J2 | 2.5 Amps | mbar | 50% | -50 V d.c. |
| J3 | | | 75% | |
| K0 | | | 0% | |
| K1 | | $8 \times 10^{-3}$ | 25% | |
| K2 | 1 Amp | mbar | 50% | -50 V d.c. |
| K3 | | | 75% | |
| L0 | | | 0% | |
| L1 | | $8 \times 10^{-3}$ | 25% | |
| L2 | 2 Amps | mbar | 50% | -50 V d.c. |
| L3 | | | 75% | |
| M0 | | | 0% | |
| M1 | | $8 \times 10^{-3}$ | 25% | |
| M2 | 2.5 Amps | mbar | 50% | -50 V d.c. |
| M3 | | | 75% | |

Table 6.1 **Deposition parameters of the $CN_x$ samples analysed.**

| Sample | C1s B.E., eV (FWHM) | C1s % At Conc. | O1s B.E., eV (FWHM) | O1s % At Conc. | N1s B.E., eV (FWHM) | N1s % At Conc. | Si2p B.E., eV (FWHM) | Si2p % At Conc. | Ar2p B.E., eV (FWHM) | Ar2p % At Conc. |
|---|---|---|---|---|---|---|---|---|---|---|
| F0 | 285.0 (2.1) | 88.7 | 532.8 (2.7) | 9.9 | 400.5 (2.0) | 1.0 | ------- | * | ----- | --- |
| F1 | 285.0 (2.7) | 77.4 | 532.6 (3.1) | 11.6 | 400.4 (3.8) | 10.1 | 102.3 (1.90) | 0.9 | ----- | --- |
| F2 | 285.0 (3.0) | 73.7 | 531.7 (3.1) | 10.7 | 399.6 (4.0) | 15.5 | ------- | * | ----- | --- |
| F3 | 285.0 (3.1) | 72.1 | 531.9 (3.2) | 9.2 | 398.8 (3.8) | 18.5 | ------- | * | ----- | --- |
| J0 | 285.0 (2.1) | 90.8 | 531.8 (2.8) | 8.3 | 400.2 (1.9) | 0.5 | 100.5 (2.1) | 0.5 | ----- | --- |
| J1 | 285.0 (2.7) | 76.8 | 532.2 (3.1) | 13.3 | 400.3 (4.1) | 9.6 | ------- | * | ----- | --- |
| J2 | 285.0 (3.0) | 72.6 | 532.1 (3.2) | 13.4 | 399.5 (3.8) | 13.4 | 102.0 (1.7) | 0.6 | ----- | --- |
| J3 | 285.0 (3.0) | 74.1 | 531.8 (3.1) | 9.5 | 398.8 (4.2) | 15.7 | 100.9 (1.9) | 0.7 | ----- | --- |
| M0 | 285.0 (2.2) | 87.6 | 532.6 (2.9) | 11.0 | 400.4 (1.8) | 0.6 | 102.5 (1.8) | 0.8 | ----- | --- |
| M1 | 285.0 (2.8) | 77.2 | 531.9 (2.9) | 8.5 | 399.1 (4.3) | 12.1 | 103.2 (2.0) | 2.2 | ----- | --- |
| M2 | 285.0 (3.0) | 75.2 | 532.0 (3.1) | 9.2 | 399.3 (4.0) | 14.7 | 101.6 (1.9) | 0.9 | ----- | --- |
| M3 | 285.0 (3.0) | 77.6 | 532.1 (3.1) | 8.4 | 398.4 (4.0) | 13.9 | -------- | * | ----- | --- |
| K1 | 285.0 (3.2) | 71.8 | 531.4 (3.1) | 9.6 | 399.0 (3.7) | 18.1 | 101.8 (1.7) | 0.5 | ----- | --- |
| $Si_{substrate}$ | 285.0 (2.2) | 9.4 | 532.4 (2.1) | 23.1 | ----------- | * | 99.8 (1.7) | 67.5 | ------ | --- |

section (a) analysis conducted in Northern Ireland

| Sample | C1s B.E., eV (FWHM) | C1s % At Conc. | O1s B.E., eV (FWHM) | O1s % At Conc. | N1s B.E., eV (FWHM) | N1s % At Conc. | Si2p B.E., eV (FWHM) | Si2p % At Conc. | Ar2p B.E., eV (FWHM) | Ar2p % At Conc. |
|---|---|---|---|---|---|---|---|---|---|---|
| H0 | 284.5 (1.3) | 90.1 | 532.4 (2.4) | 7.9 | 399.9 (2.9) | 1.5 | -------- | --- | 242.1 (0.9) | 0.5 |
| H1 | 284.7 (1.9) | 82.6 | 532.4 (2.6) | 6.2 | 400.7 (3.9) | 11.2 | -------- | --- | ------- | --- |
| H2 | 285.0 (2.7) | 75.2 | 532.3 (2.6) | 6.6 | 398.8 (3.5) | 18.2 | -------- | --- | ------- | --- |
| H3 | 284.8 (2.3) | 80.5 | 532.1 (2.7) | 6.3 | 398.7 (3.7) | 13.2 | -------- | --- | ------- | --- |

section (b) analysis conducted in Finland

**Table 6.2** **XPS data comprising the B.E.(eV) positions for C1s, O1s, N1s and, where appropriate, Si2p and Ar2p for $CN_x$ samples. Analysis for section (a) was conducted in Northern Ireland, with section (b) completed in Finland.**

# Chapter 7

# $CN_x$ Deposition on Steel

# Chapter 7 - $CN_x$ Deposition on Steel

## 7.1 Introduction

The theoretical hardness values of carbon nitride films indicate that carbon nitride coatings have possible applications in tribological situations as the coatings may possess low wear rates. Additional applications as a decorative coating are also perceivable as it possesses a dark metallic lustrous appearance.

In an investigation of the end-use of $CN_x$ coatings for real applications, experiments were undertaken to determine the tribological properties of the coatings. Hardness and co-efficient of friction values were also determined. The coating comprises carbon bonded to nitrogen, and as neither element is metallic in nature, carbon nitride could possibly be an interesting coating in the area of biomedical implants. $CN_x$ could also provide a hermetic seal, effectively sealing in any harmful metallic species in the prostheses that could migrate into the surrounding tissue. An investigation of the properties of the coating was conducted on films deposited onto both a tool steel (AISI D2, for mechanical use) and a surgical steel (AISI 316L, for biomedical use).

## 7.2 Experimental Parameters

All samples were polished to a 1μm surface finish, and ultrasonically cleaned in 1,1,1 trichloroethane, then in acetone, and finally in methanol. The normal sputter etch was conducted for 15 minutes at a bias voltage of -1000 V d.c. in an argon plasma, whilst both the titanium and carbon targets were degassed and cleaned by energising them to 2 Amps respectively. The interlayer deposition consisted of Ti, TiN and TiC as outlined in *Table 7.1*. All interlayers were deposited for 5 minutes, and at a bias of -50V d.c. A bias of either -50 or -100V r.f. applied during the $CN_x$ layer deposition. TiN was deposited using the Reactaflo optical feedback system, ensuring that stoichiometric TiN was deposited at each instance. The

TiC layer was deposited using 10sccm of butane in an argon plasma. The deposition of the $CN_x$ layer occurred for 60 minutes in either a 75% or 100% nitrogen partial pressure. All samples were cooled in the chamber for 30 minutes to prevent thermal delamination.

## 7.3 Results

The effect of the wear resistance and film hardness were investigated as a function of the deposition parameters. Thickness values were recorded for the films and are given in *Table 7.2*, along with the wear resistance and the hardness values.

### 7.3.1 Hardness

Knoop indentation was conducted on the samples, and hardness values in the range 620 to 2196 HK were recorded. Substrate hardness values of 570 HK were recorded for 316L stainless steel and a value of 1020 HK was recorded for D2 tool steel. Individual hardness values of the films are given in *Table 7.2*. The films were very brittle under load and an audible "pinging" was often heard from the films during indentation. This brittle nature caused cracking and delamination reflecting the high compressive stress evident in the coatings. Under some loads, no visible indent was perceived, suggesting large elastic recovery effects. Little correlation between the deposition conditions and the hardness values was found, but may be attributed to the difficulties incurred in the measurement of these films.

In general, the films deposited at the higher (i.e. more negative) bias exhibited higher hardness values. Hardness values also depended, as expected, on the substrate material, with hardest $CN_x$ values recorded for films deposited onto the harder D2 tool steel substrate, *Table 7.3*. This can be explained by the fact that, despite the indentation technique and the correction factor for hardness values of a thin film on a thick substrate, the indentation method enables the diamond indenter to penetrate the coating and indent the substrate material. This is often

reflected in high hardness values for harder substrates. This indicates that the correction procedure may be inaccurate in the case of very thin films.

There was no apparent effect of the TiC interlayer on hardness values, but this may have been due to the limitations posed by the measurement technique. A more suitable technique would be to investigate the nano-hardness response of the films.

### 7.3.2 Thickness

Thickness of the films was measured using the ball cratering technique. The typical thickness observed are shown in *figure 7.1*, which shows film AA4 at a magnification of 200. The centre portion is the steel substrate with Ti, TiN, TiC and $CN_x$ layers from centre to edge. Typical thickness values of the interlayers are as follows:

| | |
|---|---|
| $CN_x$ | 1.6 μm (average) |
| TiC | 0.4 μm (average) |
| TiN | 0.3 μm (average) |
| Ti | 0.2 μm (average) |

Total average thickness values were 2.5 μm, with individual values in the range 1.63 to 3.39 μm. The difference in the thickness values is explained by the fact that thickness, dependent on the deposition rate, is a function of the interlayer thickness, the bias on the substrate and the nitrogen partial pressure. As each sample had a different combination of the variable parameters one would expect the resultant films to be of different thicknesses. Thickness values for each sample are given in *Table 7.2*. The film processed in 100% nitrogen plasma consistently produced thicker coatings compared to those films processed at 75% nitrogen partial pressure. The effect of the substrate bias, substrate material or interlayers were not obvious.

### 7.3.3 Friction and Wear

Friction was measured using the pin-on-disk tribometer. Using a tungsten carbide ball on a $CN_x$ on tool steel sample, the tribometer was left running for 24 hours. Hertzian pressure calculations for a tungsten carbide ball on a $CN_x$ film yielded a Hertzian pressure of 3.9219GPa, on a contact diameter of 17.84µm. The resulting friction value was 0.25, and no appreciable wear of the sample was noted when examined under an optical microscope. A similar test was undertaken for the measurement of the coefficient of friction for an ultra-high-molecular-weight-polyethylene (UHMWPE) pin and a $CN_x$ on 316L steel disk. Hertzian calculations yielded a pressure of 0.1179GPa on a contact area of 102.9198 µm. The coefficient of friction was noted to be 0.23, very similar to the previous result. Upon examination of the pin and the wear track, no appreciable signs of wear were seen.

Abrasive wheel wear tests were conducted on the samples as outlined in section 4.4. All samples were worn to the same degree, and under the same conditions. Typical wear tracks are depicted in *figure 7.2*. The number of revolutions per micron thickness were recorded and are noted in *Table 7.2*. The number of revolutions per micron film thickness ranges from 1027 to 8475, with a dependency on the film thickness. In addition, it was found that in general, films deposited onto the harder tool steel substrate had increased wear life in order of 3 times as long, *Table 7.4*. Whether this is due to the increased hardness of the substrate, thus yielding a harder coating and hence a more wear resistant coating or due to the overall film thickness increase and wear life increase observed in the D2 samples thus yielding prolonged wear performance is difficult to decipher, but it is probably a combination of the substrate (and hence film hardness) and film thickness.

## 7.4 Discussion

The difficulties encountered in the evaluation of the Knoop hardness of the films arose mainly from the brittle nature of the films, and hence any results observed, even when corrected for thin films according to section 4.2.1 were subject to uncertainty. Thus, any correlation of the thickness values to either the deposition parameters or the film properties such as thickness and wear resistance are questionable. However, it can be obviously seen that the films deposited onto the harder tool steel substrate produced harder Knoop values. No obvious correlation between the interlayers or the nitrogen partial pressure was observed. Generally, it was found that films processed at the more negative substrate bias (-100V r.f.) produced harder films. The thickness values were dependent on the nitrogen partial pressure and on the substrate material, with films deposited on the tool steel and at 100% nitrogen partial pressure having greatest thickness values. The reasons for this are not readily obvious. Wear resistance as measured by number of revolutions per micron thickness shows the immediate correlation between wear resistance and film thickness. The wear resistance for the tool steel samples was greatest, of order 3 times greater than the 316L steel samples. In addition, films processed in the 100% nitrogen plasma exhibited greatest wear resistance. There was no correlation between wear resistance and substrate bias or the TiC interlayer.

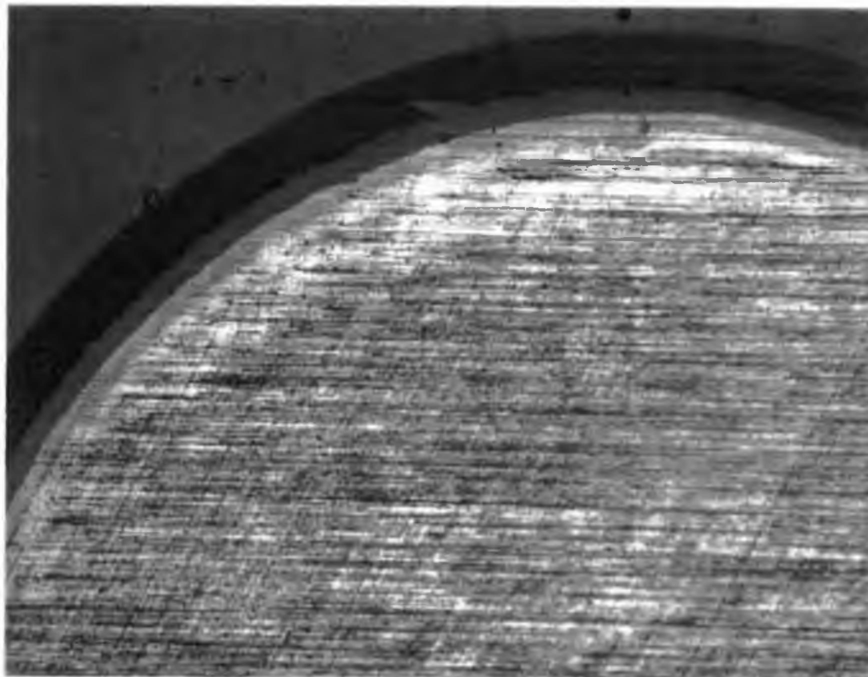

**Figure 7.1** **Photograph of a ball cratering cap of a film deposited onto a 316L substrate with interlayers Ti/TiN/TiC at -100 V r.f. in a 75% nitrogen partial pressure plasma. Magnification x 200.**

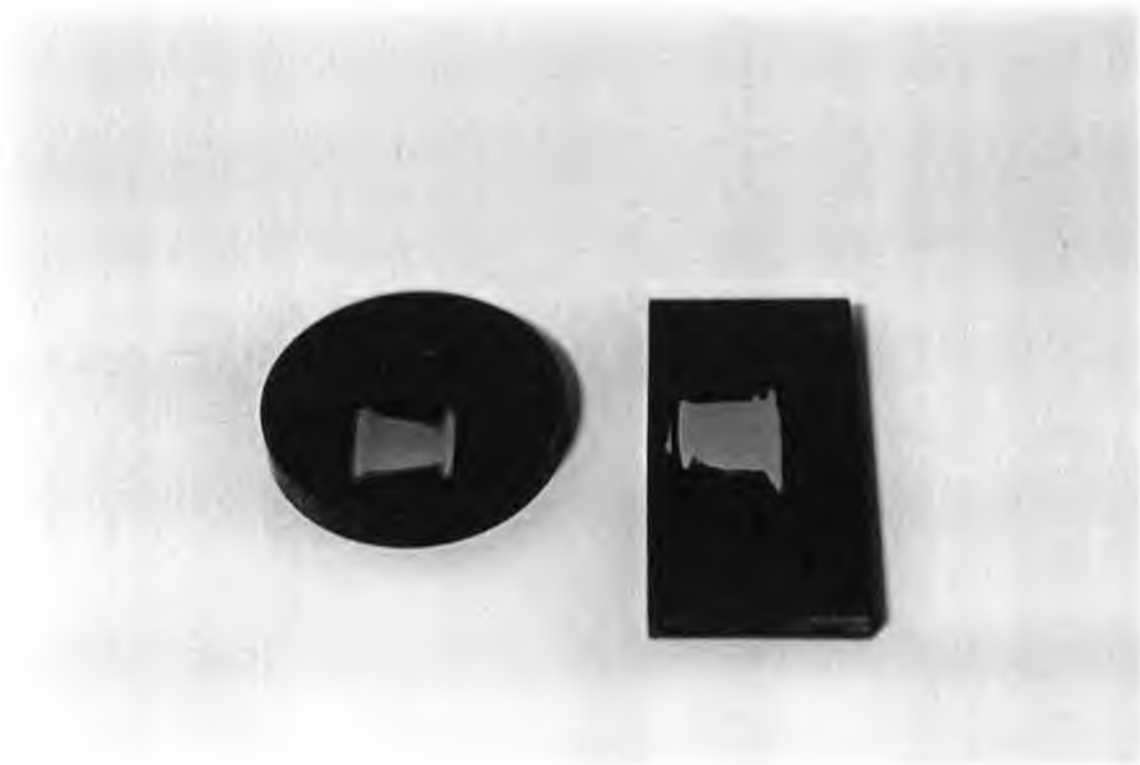

**(a)** **(b)**

**Figure 7.2** **Wear scars produced on CNx coated samples by the rubber wheel abrasive wear test.**
**a) 316L substrate b) D2 substrate**

| Sample | $N_2$% Partial Pressure |
|---|---|
| AA1 | 75% |
| AA2 | 75% |
| AA3 | 75% |
| AA4 | 75% |
| BB1 | 100% |
| BB2 | 100% |
| BB3 | 100% |
| BB4 | 100% |
| CC1 | 75% |
| CC2 | 75% |
| CC3 | 75% |
| CC4 | 75% |
| DD1 | 100% |
| DD2 | 100% |
| DD3 | 100% |
| DD4 | 100% |

**Table 7.1**

| Substrate Bias (V, r.f.) | Interlayers | Substrate |
|---|---|---|
| -50 | Ti/TiN | 316L |
| -100 | Ti/TiN | 316L |
| -50 | Ti/TiN/TiC | 316L |
| -100 | Ti/TiN/TiC | 316L |
| -50 | Ti/TiN | 316L |
| -100 | Ti/TiN | 316L |
| -50 | Ti/TiN/TiC | 316L |
| -100 | Ti/TiN/TiC | 316L |
| -50 | Ti/TiN | D2 |
| -100 | Ti/TiN | D2 |
| -50 | Ti/TiN/TiC | D2 |
| -100 | Ti/TiN/TiC | D2 |
| -50 | Ti/TiN | D2 |
| -100 | Ti/TiN | D2 |
| -50 | Ti/TiN/TiC | D2 |
| -100 | Ti/TiN/TiC | D2 |

**Deposition variables of $CN_x$ on steel**

| Sample | Knoop Hardness (kg/mm$^2$) |
|---|---|
| AA1 | 1667 |
| AA2 | 1165 |
| AA3 | 846 |
| AA4 | 863 |
| BB1 | 1140 |
| BB2 | 1823 |
| BB3 | 2196 |
| BB4 | 1481 |
| CC1 | 2070 |
| CC2 | 1667 |
| CC3 | 1106 |
| CC4 | 1268 |
| DD1 | 620 |
| DD2 | 1684 |
| DD3 | 1379 |
| DD4 | 1902 |

**Table 7.2**

| Thickness (μm) | Wear Resistance (revs/μm thickness) |
|---|---|
| 1.92 | 1344 |
| 1.89 | 1134 |
| 1.63 | 1027 |
| 2.14 | 1312 |
| | |
| 2.21 | 1406 |
| 2.14 | 1284 |
| 2.63 | 3419 |
| 3.27 | 4251 |
| | |
| 2.22 | 3996 |
| 2.77 | 4155 |
| 2.26 | 4068 |
| 1.72 | 3440 |
| | |
| 3.21 | 5778 |
| 3.37 | 8425 |
| 3.39 | 8475 |
| 3.21 | 6263 |

**Analytical results of $CN_x$ on steel**

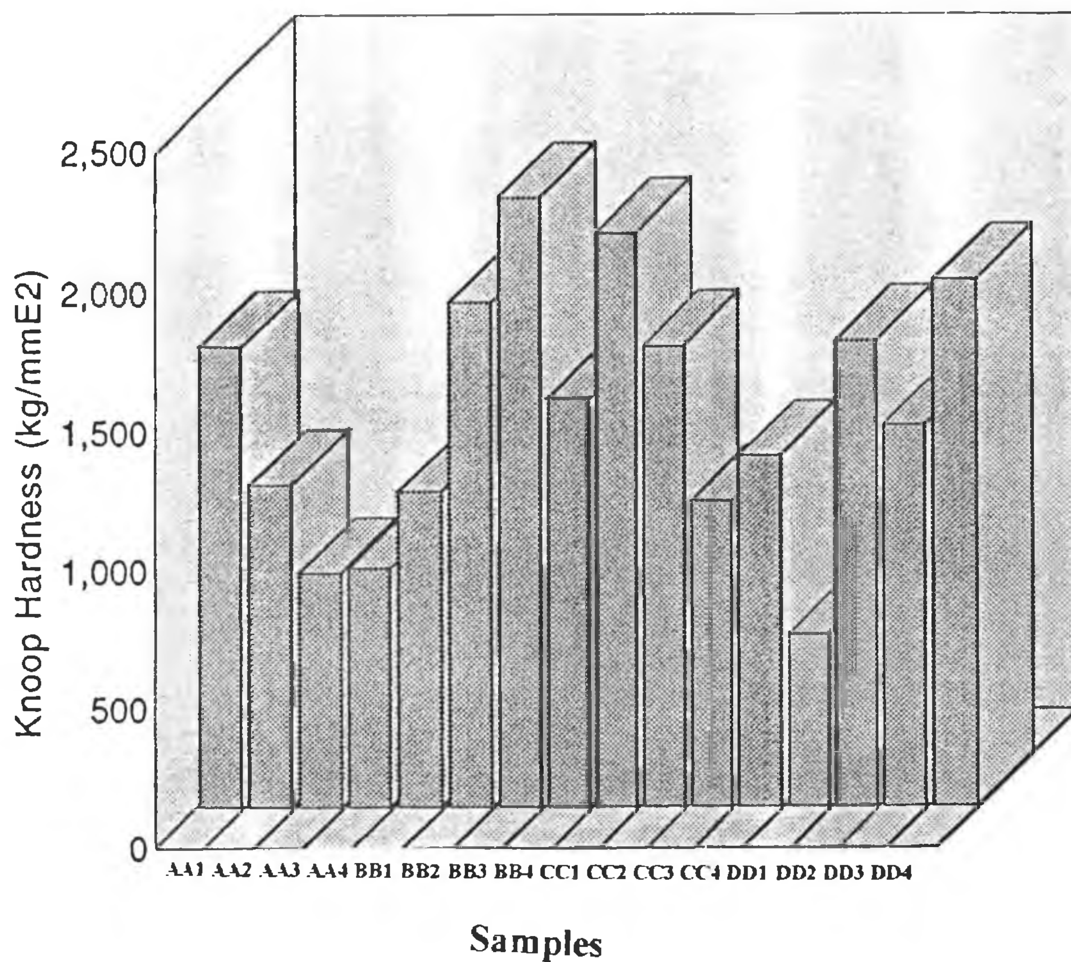


Table 7.3 The variation in $CN_x$ film hardness on steel substrates

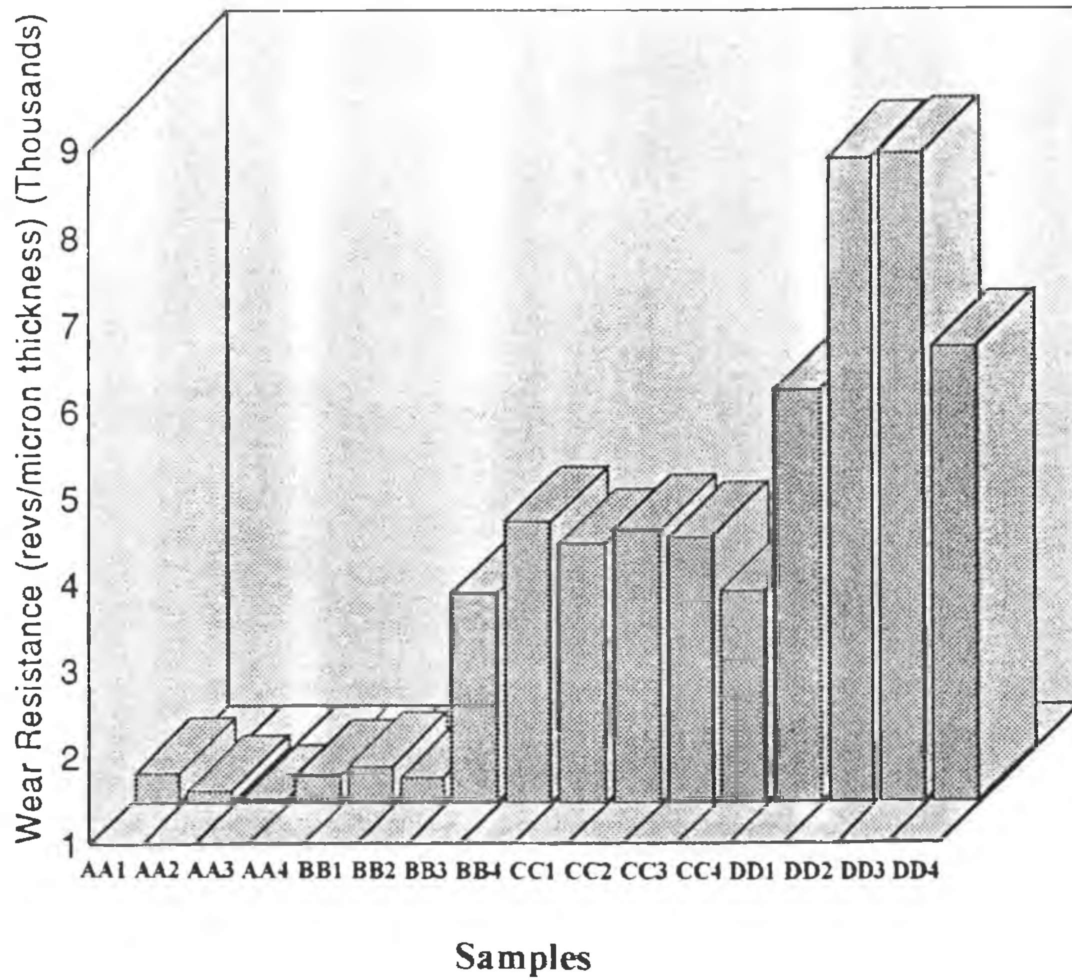


Table 7.4 The variation in $CN_x$ wear resistance on steel substrates

# Chapter 8

# Conclusions

# Chapter 8 - Conclusions

## 8.1 Conclusions - TiN biocompatible coatings

The optimisation of dense coatings for corrosion protection must consider the application for which these coatings will be best suited. Magnetron sputtered TiN films were found to be strongly dependent on magnetron power and substrate bias, the latter being of marginally higher importance. Although the coatings exhibited good coverage etc., some pinhole defects did exist, which would provide corrosion initiation sites on prostheses, possibly reducing their effectiveness. Further experiments will need to be conducted at even greater magnetron powers and larger substrate biases. However, using the unbalanced magnetron system as outlined previously, the substrate ion current saturates at approximately -50V. Hence r.f. biasing should be employed in an attempt to mitigate the pinhole corrosion sites and provide a more hermetic seal. Increased densification of the coating could also be achieved, as discussed previously, by lowering the system pressure, which has the overall effect of increasing the energy of the ion impacting the substrate surface. This, however, is also a major contributory factor to the loss of adhesion due to the introduction of large compressive stress at the coating-substrate interface.

At the substrate bias employed in these investigations, adhesion of the TiN coating to the steel substrate was a major difficulty. Attempts to relieve the stress by the introduction of a Ti interlayer proved successful. The Ti interlayer acted as a compliant interface between the TiN and the steel substrate. In addition, the interlayer also acted as a passivation layer once it oxidised to $TiO_2$ and aided corrosion resistance.

TiN is resistant to saline corrosion. Any access of the corrosive solution to the substrate material through the pinholes will cause local corrosion which can reduce the adhesion of the coating which will then no longer be an effective barrier at that point. Thus any possible application would have to eliminate these pinholes.

Electrographic printing is a simple and clear technique affording distinct visualisation of coating porosity. It is a useful and versatile method of detecting pinhole defects and discontinuities in the coating and can be utilised for many different coating/substrate combinations. However, due to the corrosive nature of the printing fluid, the detection of pinhole defects can also cause corrosion of the substrate material at these defect sites. The subsequent loss of mechanical support for the films due to the corrosion of the base material can cause film cracking and failure, resulting in an overall increase in pinhole size. Thus electrographic printing has limitations whereby the results so obtained should also account for the effect of the printing fluid. Any results should therefore be treated as qualitative rather than quantitative.

A more suitable method of pinhole detection may be the use of a fluid which is fluorescent in ultra-violet (UV) light as a means for visual detection. By applying the fluid to the film surface such that only the pinholes were "wetted" (i.e. the coating itself would have low "wettability"), and by then inspecting the film surface under a UV microscope, the pinholes could readily be detected.

The pinholes could be caused by the "shadowing" effect of particles of dust on the substrate surface. This is a function of chamber cleanliness and though care was taken to keep the chamber clean at all times, the deposition of the coating on the inner surface of the vacuum chamber can result in flaking of this deposit and subsequently could come to rest on the substrate surface during deposition.

The overall conclusion to be made is that whilst TiN may be biocompatible and resistant to saline corrosion, the coating quality in terms of. pinhole defects is of primary importance. Any further densification of the coating by increased ion bombardment due to lowering the system pressure, increasing the substrate bias, using r.f. substrate bias, or increasing the magnetron current must address the pinhole defect density on the coating surface. Concurrent with the densification process by using the above methods will be an increase in the compressive stress in the coating which causes delamination. Thus this must also be addressed, by possibly, the use of interlayers.

## 8.2 Conclusions - $CN_x$ Thin Films

The hardness values of the $CN_x$ films lie in the region predicted by Chen et al [132] however there is no obvious influence of the amount of nitrogen. As the nitrogen partial pressure increased, the levels of $sp^2$ bonding also increased. Energetically, the $sp^3$ bonding, indicative of harder, less graphitic films, is less favourable, and so it is suggested that the bonding in the carbon nitride films is an indication of the energy levels imparted to the growing films. To increase the overall film hardness by increasing $sp^3$ bonding, an increase in the energy imparted to the film would need to occur. This can be achieved in several ways. An increase in the substrate bias, magnetron current, a decrease in the system pressure or an external method such as another energised magnetron, or a nitrogen ion beam. However, the substoichiometric films possess good tribological properties and are adherent. To increase their hardness values and hence increase their wear resistance would thus ensure that carbon nitride films could find numerous uses in mechanical and biomedical applications. The hardness measurement technique should, however consider the fact that the films are extremely thin. The refractive indices of the $CN_x$ films were lower than that of the pure C films under all deposition conditions due to increased graphitic content but showed evidence of nitrogen incorporation which caused relative increases with higher nitrogen-containing gas mixtures. The values of refractive index for the carbon nitride films are similar to graphite, which also indicates the nature of the films deposited. Amorphous carbon coatings possess refractive index values in the range 2 to 2.7. Values in this range were obtained for those films deposited at high magnetron current, again concluding that the energy levels at the film surface are of great importance in determining the nature of the deposited films. Infra-red spectroscopy confirmed results found previously [133,155] which predict that the overall absorption decreases as nitrogen is increased. The absorption also increases as magnetron current is increased. The existence of C≡N bonds was evident from the absorption peak at approximately 2200 $cm^{-1}$. Some absorption due to the C=C (1650 $cm^{-1}$) bonds exist in all films, but the addition of nitrogen greatly increases the absorption at these wavenumbers, indicating increased $sp^2$ bonding. There was no distinct evidence of $sp^3$ bonded carbon nitride.

XRD proved to be a powerful tool in predicting the structural order of the films deposited dependent on the deposition parameters. It was found that films deposited under conditions of increased nitrogen and total gas pressure, low magnetron currents and low magnitude of negative substrate bias possessed an increased level of graphitisation due to the increased structural order in the film. All the above parameters impart little energy to the growing film. Thus, to minimise graphitisation, the deposition parameters should be high magnetron currents, low system pressure and large negative substrate bias. Nitrogen content played a small role in determining the graphitic content. The most significant factor was magnetron current.

The main conclusion to be drawn is that the nitrogen content of the films increased with the partial pressure of nitrogen during deposition, although the results are rather contradictory at the highest partial pressures and may indicate that there is a maximum value that can be attained by this method. This overall result is confirmed by XPS, SIMS, Raman and IR Spectroscopy. It is clear from the XPS, Raman and IR spectroscopy that the bonding between carbon and nitrogen is characterised mainly by C≡N and C=N bonds, with XPS results showing only a little variation in the relative proportion as the nitrogen content of the films increases, as evidenced by the unchanging shape of the N1s peak. The maximum nitrogen content found was 18.5 at.% and SIMS analysis has shown that the composition is uniform throughout the films. The oxygen content is largely due to surface absorption. Increased levels of nitrogen incorporation could perhaps be achieved by increasing the levels of ionisation in the plasma by the use of a thermionic emission source to increase electron emission and hence ionisation by electron collisions.

The carbon-carbon bonding structure is typical of that observed in DLC films with some graphitic content. The films have a disordered structure but the main feature is $sp^2$ bonding as shown by XRD, Raman and IR Spectroscopy. As the nitrogen content is increased, all these techniques show that the $sp^2$-type nature of the bonding becomes more significant. XRD, however, shows that the general deposition conditions have a greater effect on the bonding character than the nitrogen partial pressure alone.

The surface morphology of the films is generally featureless, but some films show evidence of round or irregular granular structures with the existence of some macro-particles. It is not yet clear whether this

difference is due to a difference in internal structure or is only a surface effect. No correlation has yet been detected between surface morphology and deposition conditions. The average surface roughness, however, does show a variation with deposition conditions, with a more negative substrate bias and higher deposition pressure giving smoother surfaces.

In the deposition of carbon nitride thin films onto steel substrates, it was found that hardness, thickness and wear resistance were all dependent on the substrate material, yielding larger values for the tool steel samples. This is probably due to the extremely thin films reflecting the substrate properties. Nanohardness measurements would result in more accurate film hardness values. Observed film properties were not related to the TiC interlayer in all cases. Hardness was also dependent on the substrate bias employed, with greatest values for the more negative bias (-100 V r.f.). Film thickness and wear resistance were dependent on the nitrogen partial pressure, with increased values for the samples processed in a pure nitrogen plasma. The wear resistance was related to the thickness of the films. Thicker films increase wear resistance results due to the increased number of cycles taken to abrade the coating to reach the substrate material. However, due to the difficulties involved in obtaining true hardness values, neither thickness nor wear could be related to hardness values.

Thus for the most wear resistant films, samples of tool steel should be processed in a pure nitrogen plasma with (possibly) a large negative bias on the sample. The coefficient of friction was low, approximately 0.23. The sample preparation reflects the final coating properties, and thus a substrate polished to a ¼μm $R_a$ finish would produce a film with lower frictional coefficients.

These tests illustrated the effectiveness of carbon nitride as a tribological coating, however, the main problem associated with film growth on steel is adhesion. The delamination of the film at the film-substrate surface caused great concern, but was overcome by the introduction of compliant interlayers to relieve residual stress formed during deposition. The corrosion resistance of the carbon nitride coatings is another property to be investigated as many mechanical applications involve the use of lubricants and cooling fluids during machining operations.

In biocompatible applications, the initial wear tests are promising, though in-vitro testing should be conducted. Toxicity, and wear debris effects could then be ascertained. Both TiN and $CN_x$ are theoretically biocompatible but the corrosion sites found at the pinholes need to be addressed comprehensively. In addition, a technique to assess pinhole defect density needs to be developed.

## 8.3 Recommended Work

Further work should address the basic problems of pinhole formation on the substrates during film growth. This could be investigated as a function of r.f. bias on the sample. An investigation leading to the comparison of film properties as a function of r.f. versus d.c. bias would also be worthwhile. These investigations could be undertaken on either (or both) the TiN and $CN_x$ coatings. Similarly, a comparison of film properties deposited by the conventional d.c. powered magnetron and an r.f. powered magnetron could be conducted.

These initial investigations may form the basis for extended work on the nitrogen incorporation into carbon nitride films. Possible external sources for increased ionisation within the plasma may need to be addressed (i.e. thermionic source or ion beam). The use of interlayers to relieve stress in the growing films should be investigated thoroughly, perhaps with experiments conducted to determine the optimum interlayer (Ti, TiN, TiCN) thickness needed to enhance film adhesion to steel substrates. The effect of surface roughness on the film morphology and topography could also be addressed, utilising substrates of differing surface roughness.

Stress measurements in the carbon nitride films as a function of nitrogen incorporation, substrate bias (both d.c. and r.f.), magnetron power and interlayer combination could also be quantified. AFM profiles of the films could also be extended to measure the film roughness and a comparison of these values to substrate roughness values prior to deposition may provide an insight into the "smoothing" abilities of the carbon nitride films, and may also serve to quantify the film thickness necessary to obtain low surface roughness values.

In the area of biocompatibility of the carbon nitride coatings, initial corrosion tests by potentiostatic cycling may provide information regarding the film behaviour in corrosive environments. In addition, submersion tests in solutions simulating synovial fluid (i.e. Ringers solution) should be conducted. Following from these tests, cycotoxicity and haemocompatibility of the carbon nitride films should be assessed.

The deposition of films onto three-dimensional substrates addressing the coverage of samples would need to incorporate the rotation of the substrate table, preferably with computerised control facilities.

Particular areas of interest for further research could include the determination of the Carbon-Nitrogen phase diagram. Scanning and Tunnelling Microscopy (SEM, TEM) in conjunction with XPS may aid in the identification of the phases formed under different deposition parameters. In addition, the mechanism of nitrogen incorporation into the growing films could be investigated. The predominant mechanisms proposed are chemical bonding and/or entrapment by the effect of ion bombardment. A comparison of films deposited by CVD, (which would produce films by chemical bonding), to films deposited by sputtering ( i.e. films deposited under the influence of ion bombardment) may provide some information on the growth mechanism.

# Appendix A

# APPENDIX A

## A1 Glow Discharges

When a voltage (using a high-impedance power supply) is applied to a low-pressure gas, a very small current flows, due to the presence of a very small number of ions and electrons. The current is initially nearly constant, because all of the charge present is moving. As the voltage is increased, sufficient energy is imparted to the existing charged particles so that they produce more charged particles by collisions with neutral gas atoms. Thus more current flows, but the voltage is limited by the output impedance of the power supply. This region is known as the *Townsend Discharge*.
Eventually, an avalanche occurs in which the ions striking the cathode release secondary electrons, which form more ions by collision with neutral gas atoms. These ions then return to the cathode, produce more electrons. When the number of electrons generated is just sufficient to produce enough electrons to regenerate the same number of electrons, the discharge is self-sustaining. The gas begins to glow, the voltage drops, and the current rises abruptly. This is called the *Normal Glow*. The colour of this luminous region is characteristic of the excitation gas used. Since the secondary electron emission ratio of most materials is of the order of 0.1, more than one ion must strike a given area of the cathode to produce another secondary electron. The bombardment of the cathode in the normal glow region self-adjusts in the area to accomplish this. Initially, the bombardment is not uniform, but concentrated near the edges of the cathode or at other irregularities on the surface. As more power is supplied, the bombardment increasingly covers the cathode surface until a nearly-uniform current density is achieved.

A further increase in power produces both increased voltage and current density in the discharge. This *abnormal glow* is the mode used for sputtering. If the cathode is not cooled, at a current density of approximately 0.1A/cm$^2$, thermionic electrons are emitted in addition to secondary electrons, followed by a further avalanche. The output impedance of the power supply limits the voltage and the low-voltage high-current arc discharge forms.

The abnormal glow is dependent on the breakdown voltage $V_B$ . This in turn is dependent on the mean-free-path of secondary electrons and the distance between the anode and the cathode. Each secondary electron must produce about 10-20 ions for the original avalanche to occur. If gas pressure is too low, or the cathode-anode separation too small, the secondaries cannot undergo a sufficient number of ionising collisions before they strike the anode.

If the pressure and/or separation distance is too large, ions generated in the gas are slowed by inelastic collisions so that they strike the cathode with insufficient energy to produce secondary electrons (Paschen's Law related $V_B$ to the product of gas pressure and electrode separation).In most sputtering glow discharges, the discharge starting voltage is relatively high.

*Figure A.1* illustrates the luminous regions of a d.c. glow discharge, the voltage distribution, and the net space charge as a function of distance from cathode to anode. Adjacent to the cathode, there is a brilliant luminous layer known as the cathode or negative glow. This is the region in which incoming discharge ions and positive ions produced at the cathode are neutralised by a variety of processes. This is also the region in which secondary electrons begin to accelerate away from the cathode. The light emitted is characteristic of both the cathode material and the incident ion. The Crook's dark space consists of mainly positive ions and the cathode voltage is effectively screened off, resulting in a large potential drop across the region.

Secondary electrons are repelled at high velocity from the cathode and start to make collisions with neutral gas atoms at a distance away from the cathode corresponding to their mean free path. This leaves a dark space which is very well defined. Since the electrons rapidly lose their energy by collisions, nearly all of the applied voltage appears across this dark space. The dark space is also the region in which positive ions are accelerated toward the cathode. Since the mobility of ions is very much less than that of electrons, the predominant species in the dark space are ions. Acceleration of secondary electrons from the cathode results in ionising collisions in the negative glow region.

The Faraday dark space and positive column are nearly field-free regions whose sole function is to connect electrically the negative glow to the anode. They are not at all essential to the operation of a glow discharge. In most sputtering systems, the anode is located in the negative glow and these other regions so not exist. The length of an unobstructed negative glow is exactly equal to the range of electrons that have been accelerated from the cathode. When the negative glow is truncated, higher voltages must be applied to make up for the ions that would have been generated in the part of it that is blocked by the anode. In general, for uniform cathode bombardment, the anode should be located at least 3-4 times the thickness of the dark space away from the cathode. This distance is inversely proportional to the gas pressure.

## A2 R.F. Glow Discharges

As the frequency of an applied a.c. signal is increased above 50 kHz, electrons oscillating in the glow region acquire sufficient energy to cause ionising collisions, thus reducing the dependence of the discharge on secondary electrons and lowering the breakdown voltage, and the electrodes are no longer required to be electrical conductors since r.f. voltages can be coupled through any kind of impedance. Thus it is possible to sputter any material.

Typical r.f. frequencies used for sputtering are 5-30 MHz, and when either or both electrodes are coupled to the rf generator, through a series capacitor, a pulsating, negative voltage will develop on the electrode. Due to the difference in mobility between electrons and ions, the I-V characteristic is typical of a leaky rectifier, *figure A.2*. Upon application of an r.f. voltage through the capacitor, a high initial current flows to the electrode. On the second half of the cycle, only a relatively small ion current can flow. Since no charge can be transferred through the capacitor, the voltage on the electrode surface must self-bias negatively until the net current (averaged over each cycle) is zero. This results in the pulsating negative potential shown, *Figure A.2.* The average d.c. value of this potential ($V_s$) is nearly equal to the peak voltage applied.

To obtain sputtering from only one electrode in an r.f. system, the electrode which is to be the sputtering target must be an insulator or must be capacitively coupled to the r.f. generator and the area of that electrode must be small compared to that of the directly coupled electrode. Also, the ratio of the voltage between the glow space and the small capacitively coupled electrode ($V_c$) to the voltage between the glow space and the large directly coupled electrode ($V_d$) is

$$\frac{Vc}{Vd} = (Ad / Ac)^4$$

where $A_d$ and $A_c$ are the areas of the directly and capacitively coupled electrodes, respectively. In practice, the directly coupled electrode is the system ground, including baseplates, walls, etc., and is quite large with respect to $A_c$. Thus, the average sheath potential varies between the target electrode and ground, as shown in *figure A.2.* Clearly, to minimise bombardment of grounded fixtures, the area of all grounded parts should be very large by comparison to that of the target.

Approximately 1% of the energy incident on the target surface goes into the ejection of sputtered particles, 75% into heating of the target, and the remainder is dissipated by secondary electrons that bombard and heat the substrate. The heat generated is usually removed by water cooling the backing plates to which the target is attached.

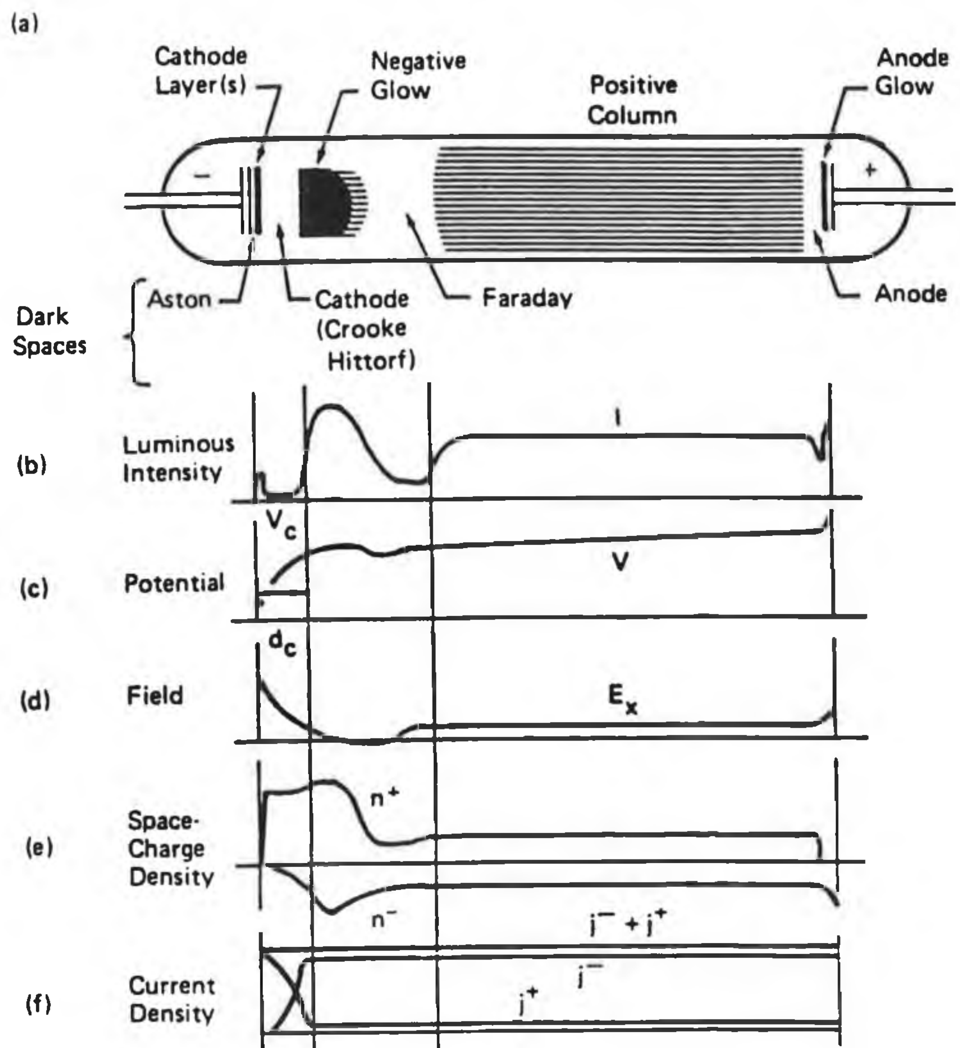


**Figure A.1** **Schematic representation of a D.C. glow discharge**

# Appendix B

| REV. | DESCRIPTION | BY | DATE |
|---|---|---|---|
| | | | |

DRG. No.

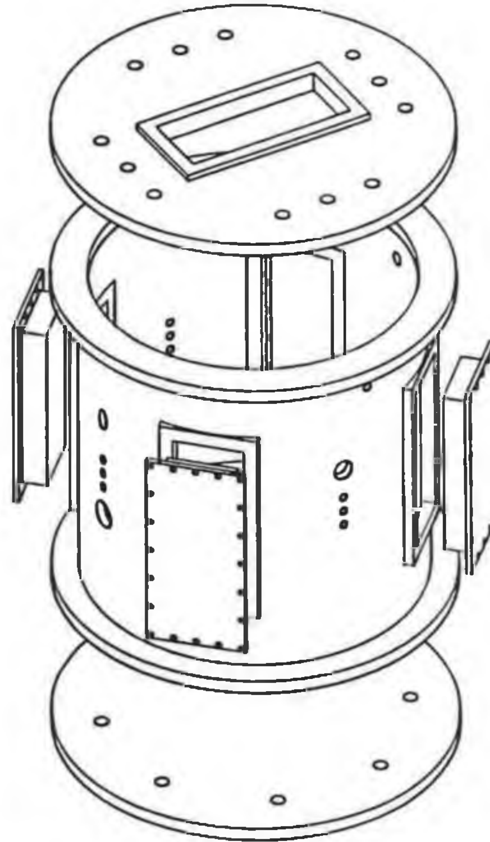

| FIRST ANGLE PROJECTION | TOLERANCES UNLESS SPECIFIED | DCU MECHANICAL ENG. DEPT. | | |
|---|---|---|---|---|
| DRAWN P. KOLA | FRACTIONS | ASSEMBLY | | |
| DATE 13-5-'93 | DECIMALS ± | | | |
| | ANGLES ± | | | |
| | SURFACE FIN. | | | |
| CHECKED | MAT'L | QTY. | ASS'Y DRG. | PARTS LIST |
| APPROVED | HEAT TREAT. NONE | SCALE NONE | PROJECT Magnetron | SHEET 1 OF 18 |

PART No.

A8

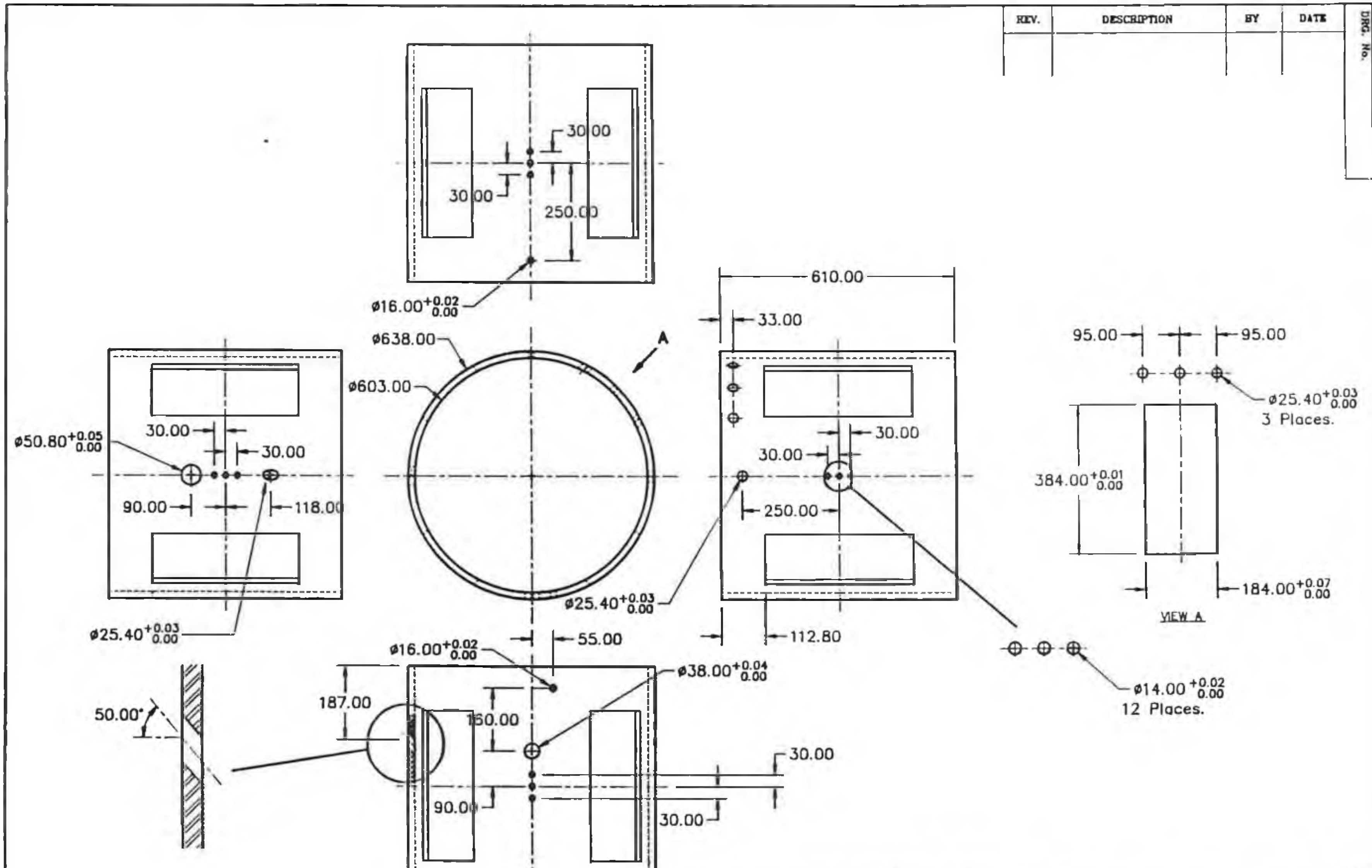

A9

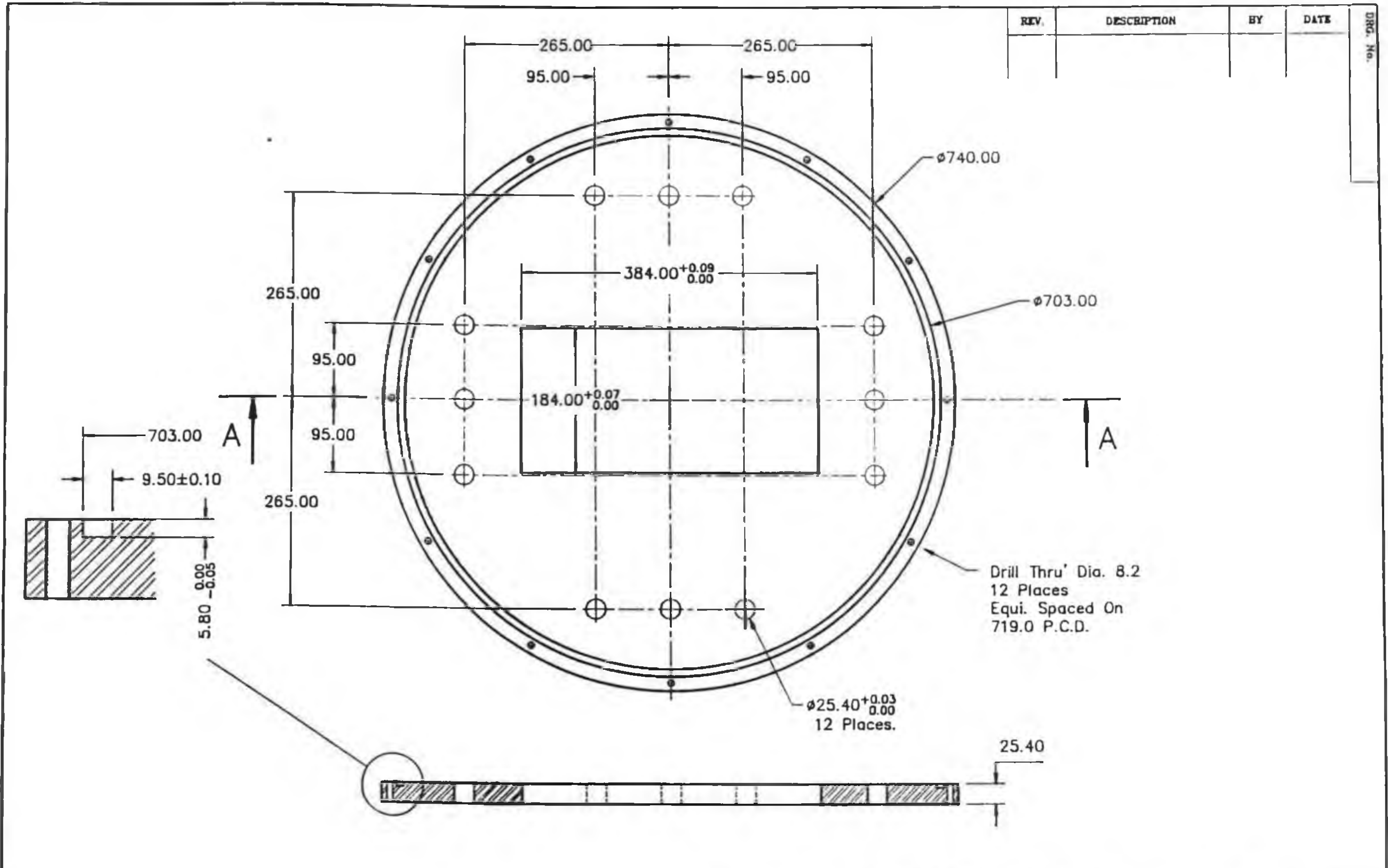

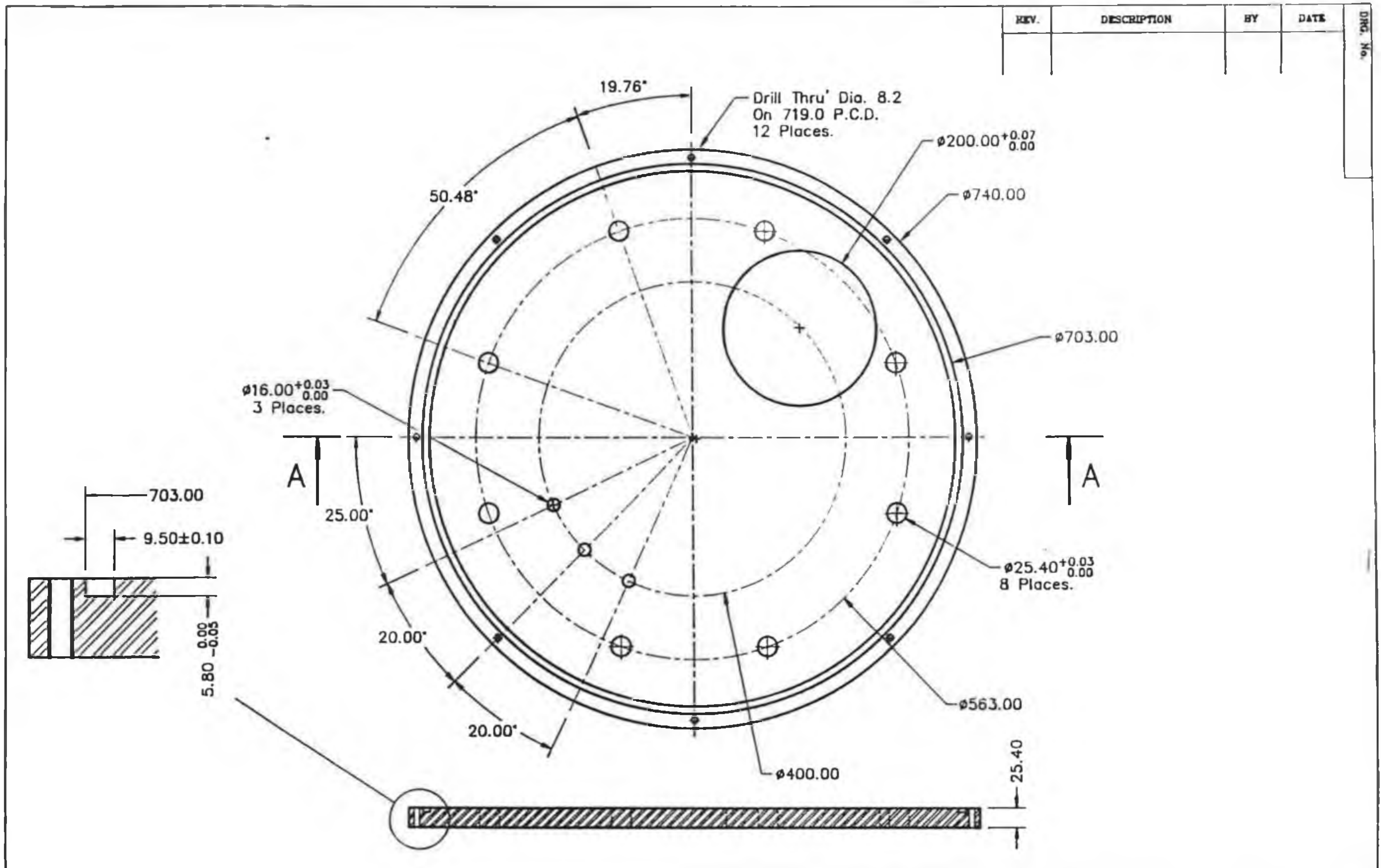


A10

| REV | DESCRIPTION | BY | DATE |
| --- | --- | --- | --- |
| | | | |

DRG. No.

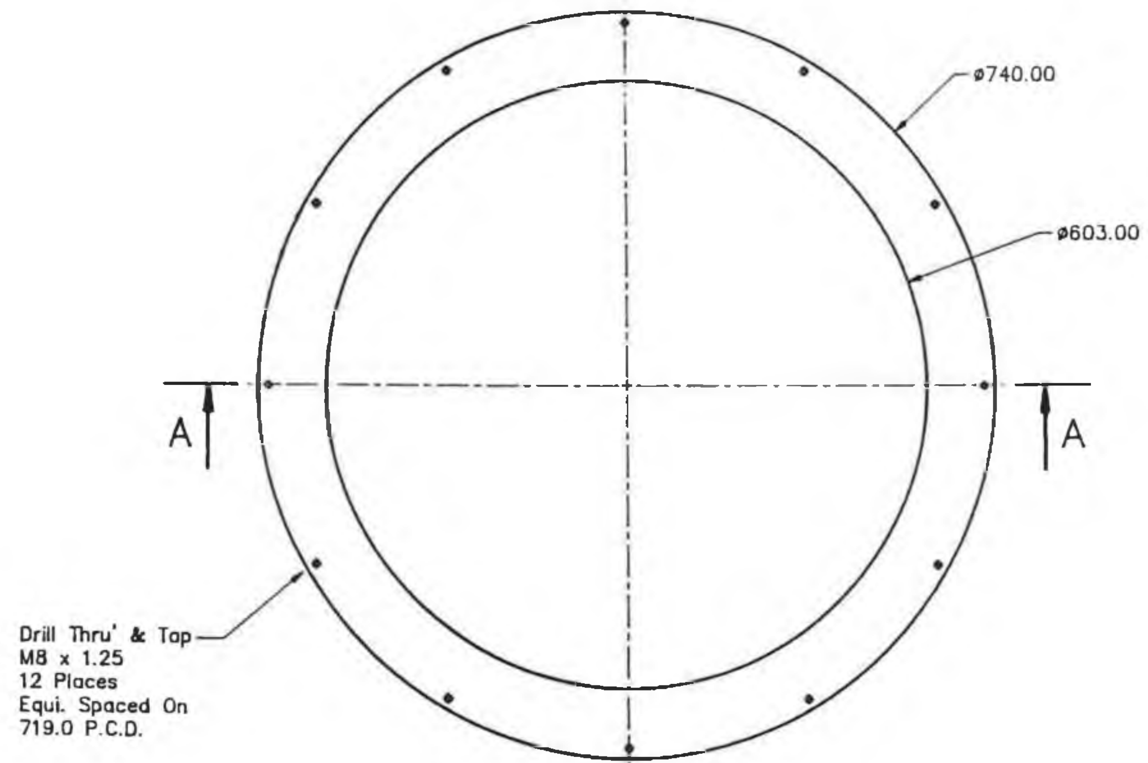

SECTION A–A

| FIRST ANGLE PROJECTION | TOLERANCES UNLESS SPECIFIED | DCU MECHANICAL ENG. DEPT. | | |
| --- | --- | --- | --- | --- |
| DRAWN P.KOLA | FRACTIONS<br>DECIMALS ±0.25mm<br>ANGLES ±1° | CHAMBER FLANGE | | |
| DATE 12-5-'93 | SURFACE FIN. | | | |
| CHECKED | MAT'L 304 STAINLESS STEEL | QTY 2 | ASS'Y DRG. | PARTS LIST |
| APPROVED | HEAT TREAT. NONE | SCALE NONE | PROJECT Magnetron | SHEET 5 OF 18 |

PART No.

A12

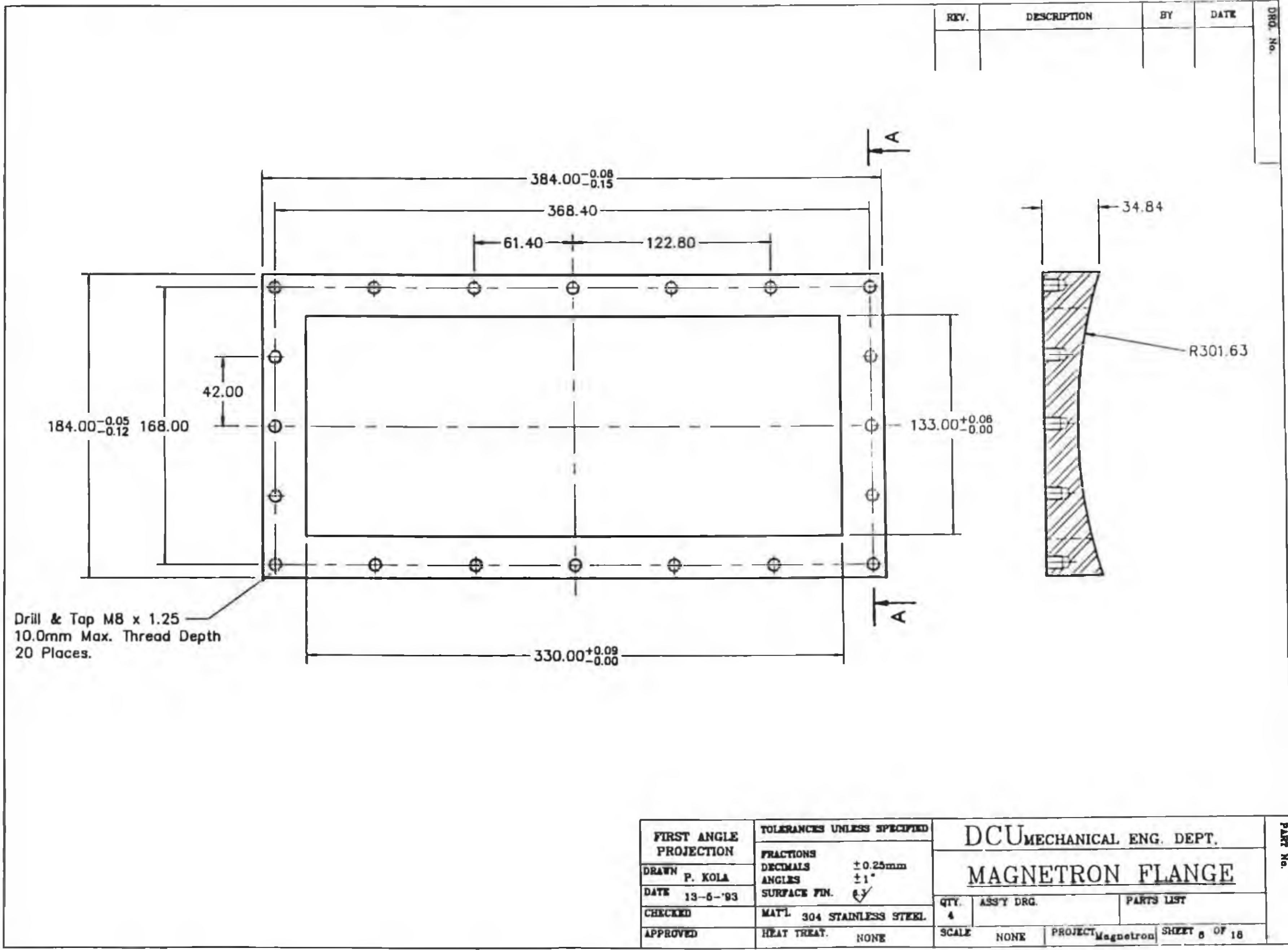

A13

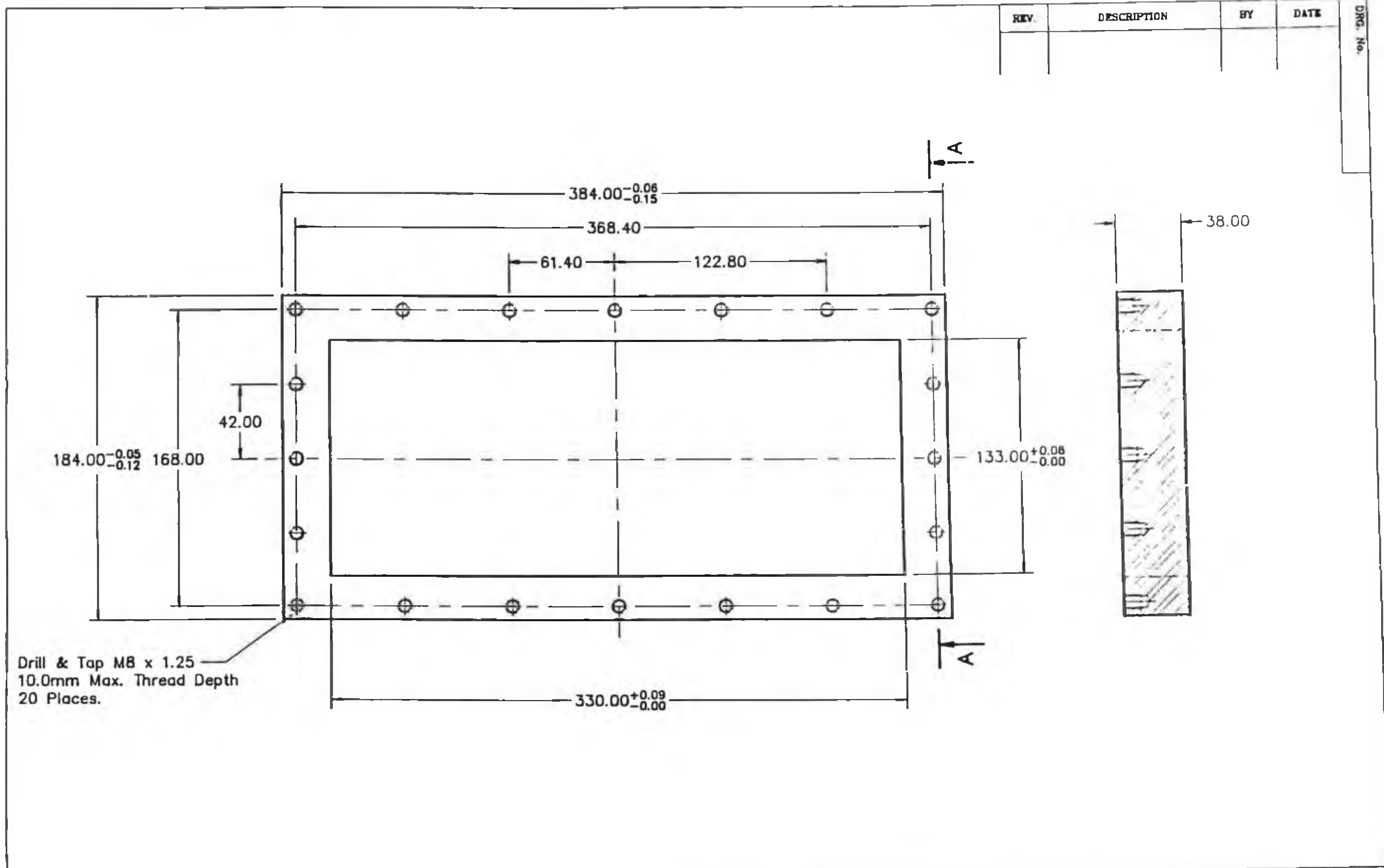

| REV. | DESCRIPTION | BY | DATE |
| --- | --- | --- | --- |
| | | | |

DRG. No.

Drill Thru' & Tap M5 x 0.8
8 Places
Equi. Spaced on a 42.7 P.C.D.

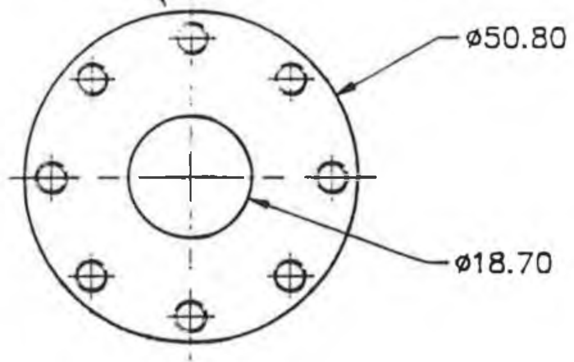


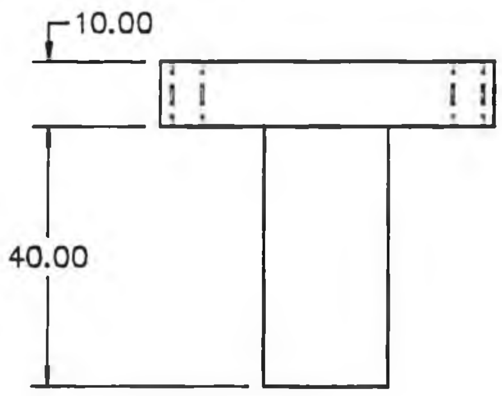


| FIRST ANGLE PROJECTION | TOLERANCES UNLESS SPECIFIED | DCU MECHANICAL ENG. DEPT. | | |
| --- | --- | --- | --- | --- |
| DRAWN P. Kola | FRACTIONS<br>DECIMALS ±0.05mm<br>ANGLES ±1° | SHUTTER BLANKING PLATE | | |
| DATE 3-3-'93 | SURFACE FIN. 0.3 | | | |
| CHECKED | MAT'L 304 Stainless Steel | QTY. 20 | ASS'Y DRG. | PARTS LIST |
| APPROVED | HEAT TREAT. NONE | SCALE NONE | PROJECT Magnetron | SHEET 8 OF 18 |

PART No.

| REV. | DESCRIPTION | BY | DATE |
|---|---|---|---|
| | | | |

DRG. No.

Drill Thru' & Tap M6 x 1.0
6 Places
Equi. Spaced on a 87.5 P.C.D.

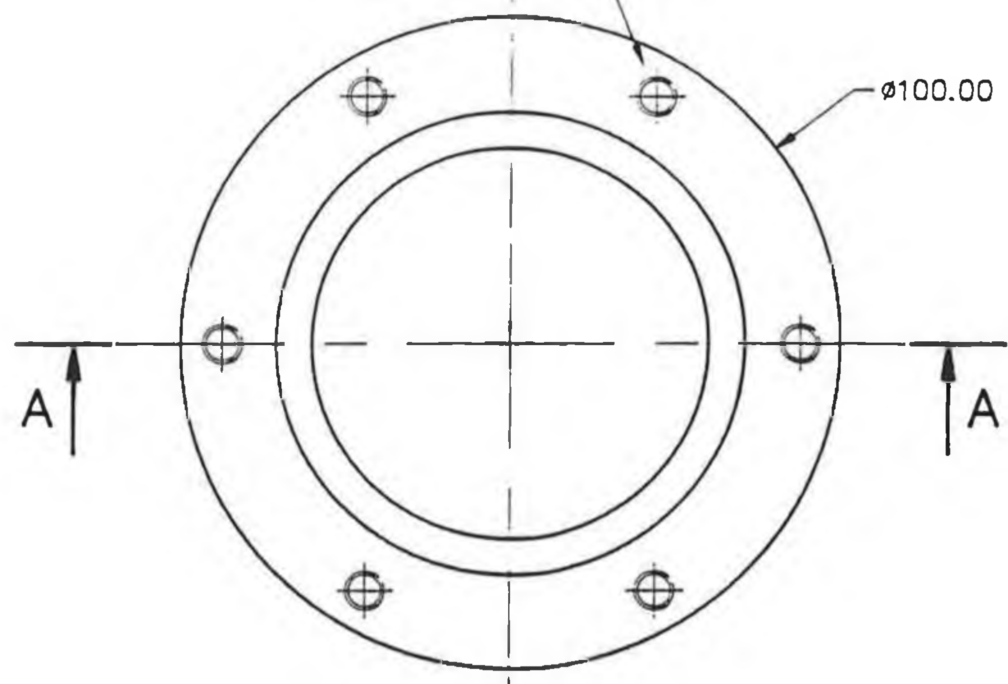


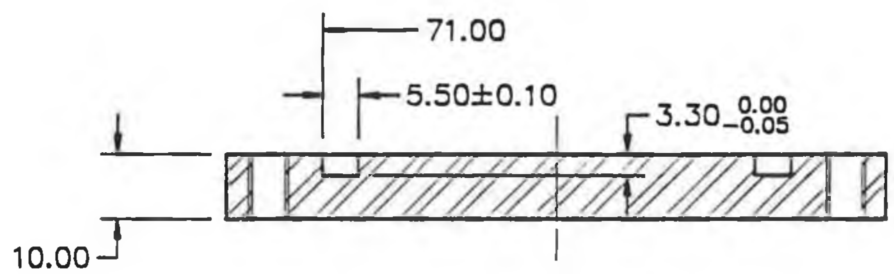


SECTION A–A

| FIRST ANGLE PROJECTION | TOLERANCES UNLESS SPECIFIED | DCU MECHANICAL ENG. DEPT. | | |
|---|---|---|---|---|
| DRAWN P. Kola | FRACTIONS<br>DECIMALS ±0.05mm<br>ANGLES ±1° | TABLE PORT BLANKING PLATE | | |
| DATE 3-3-'98 | SURFACE FIN. 6.3 | QTY. 1 | ASS'Y DRG. | PARTS LIST |
| CHECKED | MAT'L 304 Stainless Steel | | | |
| APPROVED | HEAT TREAT. NONE | SCALE NONE | PROJECT Magnetron | SHEET 9 OF 18 |

PART No.

| REV. | DESCRIPTION | BY | DATE |
|---|---|---|---|
| | | | |

DRG. No.

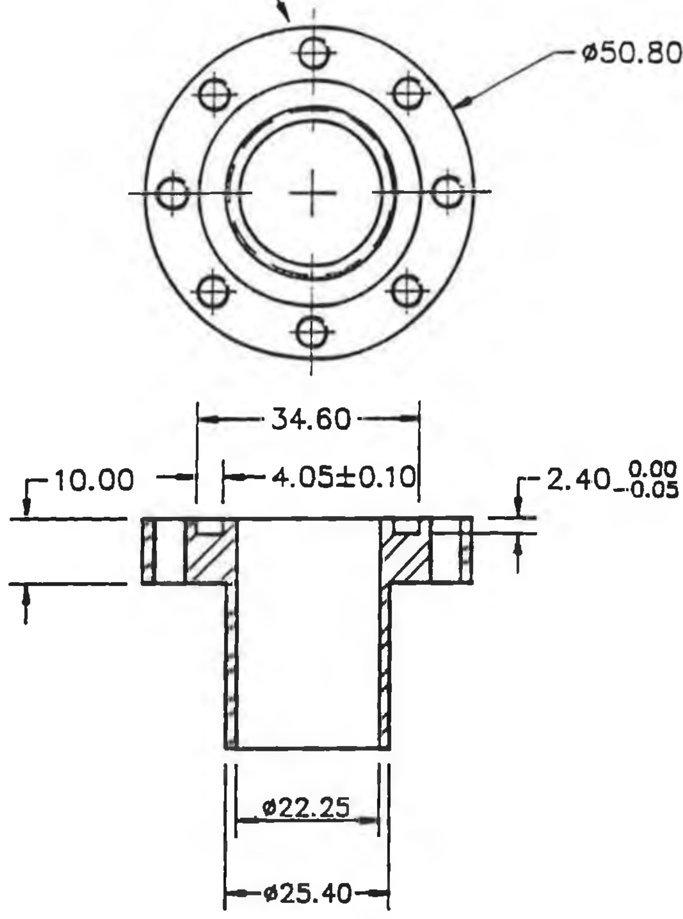


| FIRST ANGLE PROJECTION | TOLERANCES UNLESS SPECIFIED | DCU MECHANICAL ENG. DEPT. | | | PART No. |
|---|---|---|---|---|---|
| DRAWN P. Kola | FRACTIONS | BLANKING PLUG | | | |
| DATE 3-3-'93 | DECIMALS ±0.05mm; ANGLES ±1°; SURFACE FIN. | | | | |
| CHECKED | MAT'L 304 Stainless Steel | QTY. 20 | ASS'Y DRG. | PARTS LIST | |
| APPROVED | HEAT TREAT. NONE | SCALE NONE | PROJECT Magnetron | SHEET 10 OF 18 | |

| REV. | DESCRIPTION | BY | DATE | DRG. No. |
|---|---|---|---|---|
| | | | | |

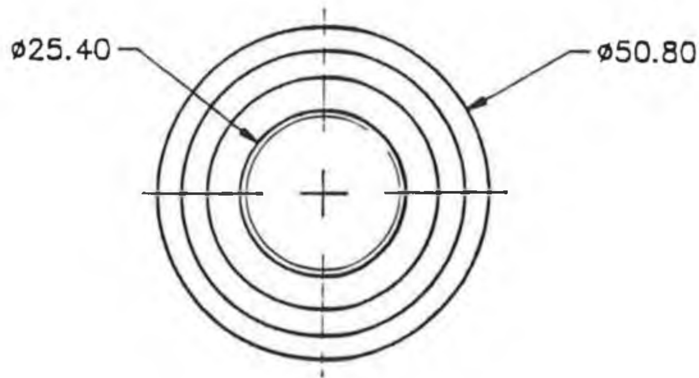


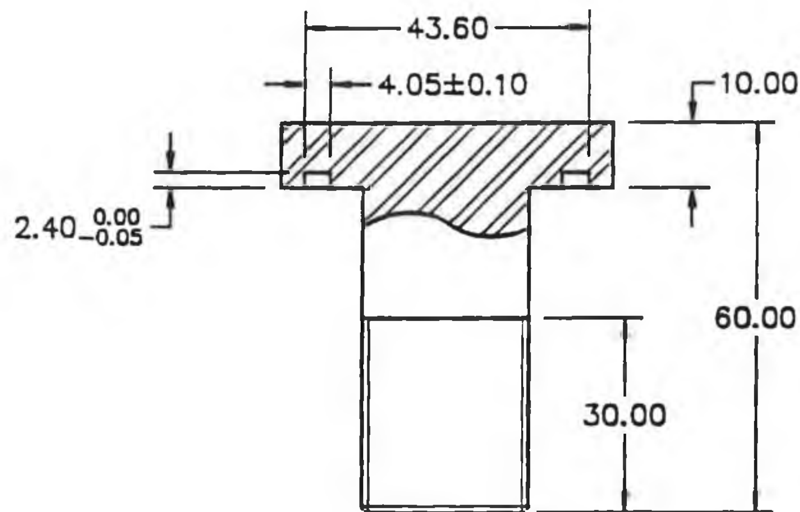


| FIRST ANGLE PROJECTION | TOLERANCES UNLESS SPECIFIED | DCU MECHANICAL ENG. DEPT. | | | PART No. |
|---|---|---|---|---|---|
| DRAWN P. Kola | FRACTIONS<br>DECIMALS ±0.05mm<br>ANGLES ±1°<br>SURFACE FIN. | SPECTROMETER BLANKING PLUG | | | |
| DATE 3-3-'93 | | | | | |
| CHECKED | MAT'L 304 Stainless Steel | QTY. 6 | ASS'Y DRG. | PARTS LIST | |
| APPROVED | HEAT TREAT. NONE | SCALE NONE | PROJECT Magnetron | SHEET 11 OF 18 | |

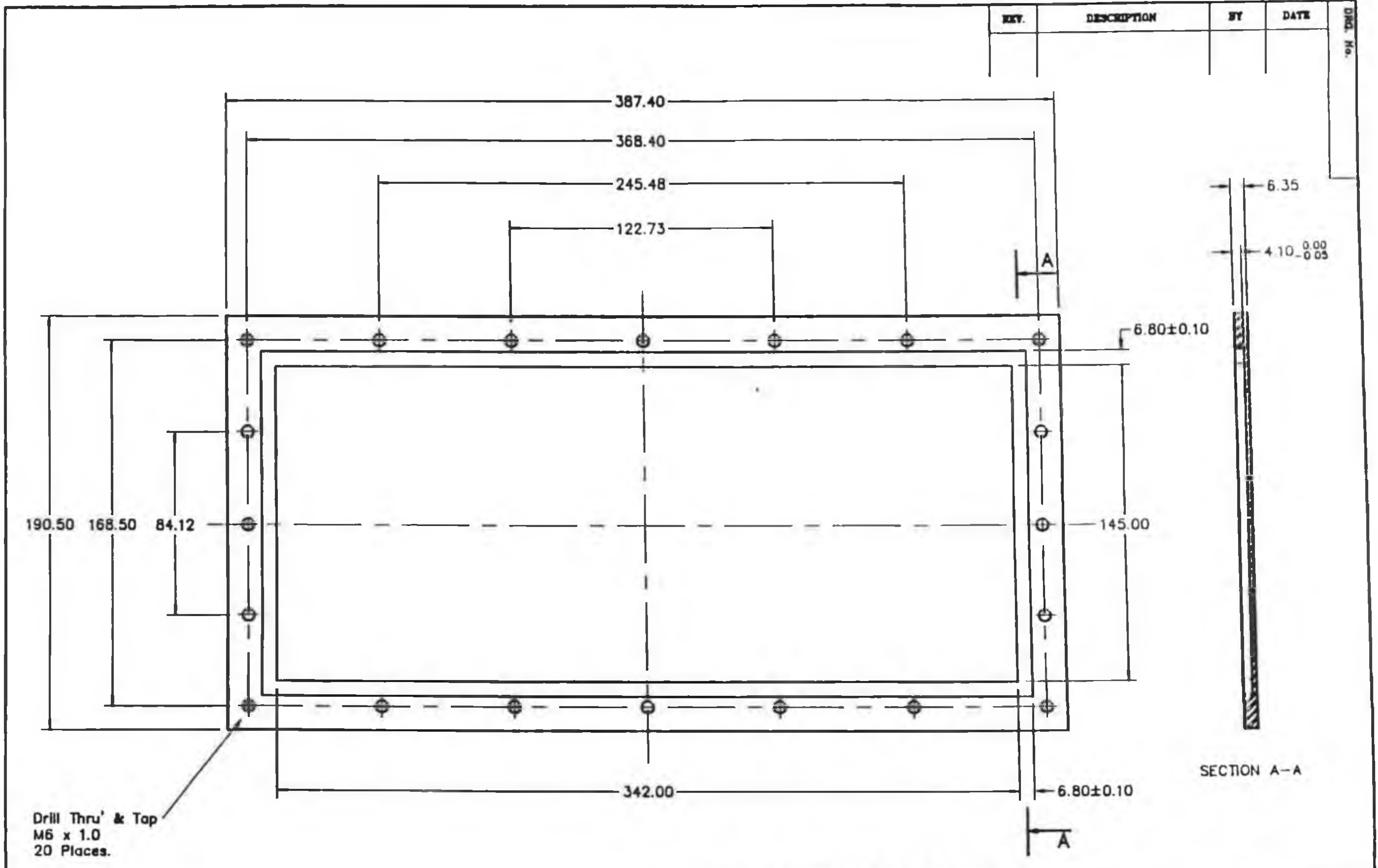

REV.
DESCRIPTION
BY
DATE
DRG. No.
387.40
368.40
245.48
122.73
A
6.35
4.10 0.00 -0.05
6.80±0.10
190.50
168.50
84.12
145.00
342.00
6.80±0.10
SECTION A-A
Drill Thru' & Tap
M6 x 1.0
20 Places.
FIRST ANGLE PROJECTION
DRAWN P. KOLA
DATE 4-2-'93
CHECKED
APPROVED
TOLERANCES UNLESS SPECIFIED
FRACTIONS
DECIMALS ±0.25mm
ANGLES ±1°
SURFACE FIN.
MAT'L 304 STAINLESS STEEL
HEAT TREAT. NONE
DCU MECHANICAL ENG. DEPT.
BLANKING PLATE
QTY. 5
ASS'Y DRG.
PARTS LIST
SCALE NONE
PROJECT MAGNETRON
SHEET 12 OF 18
PART No.

A19

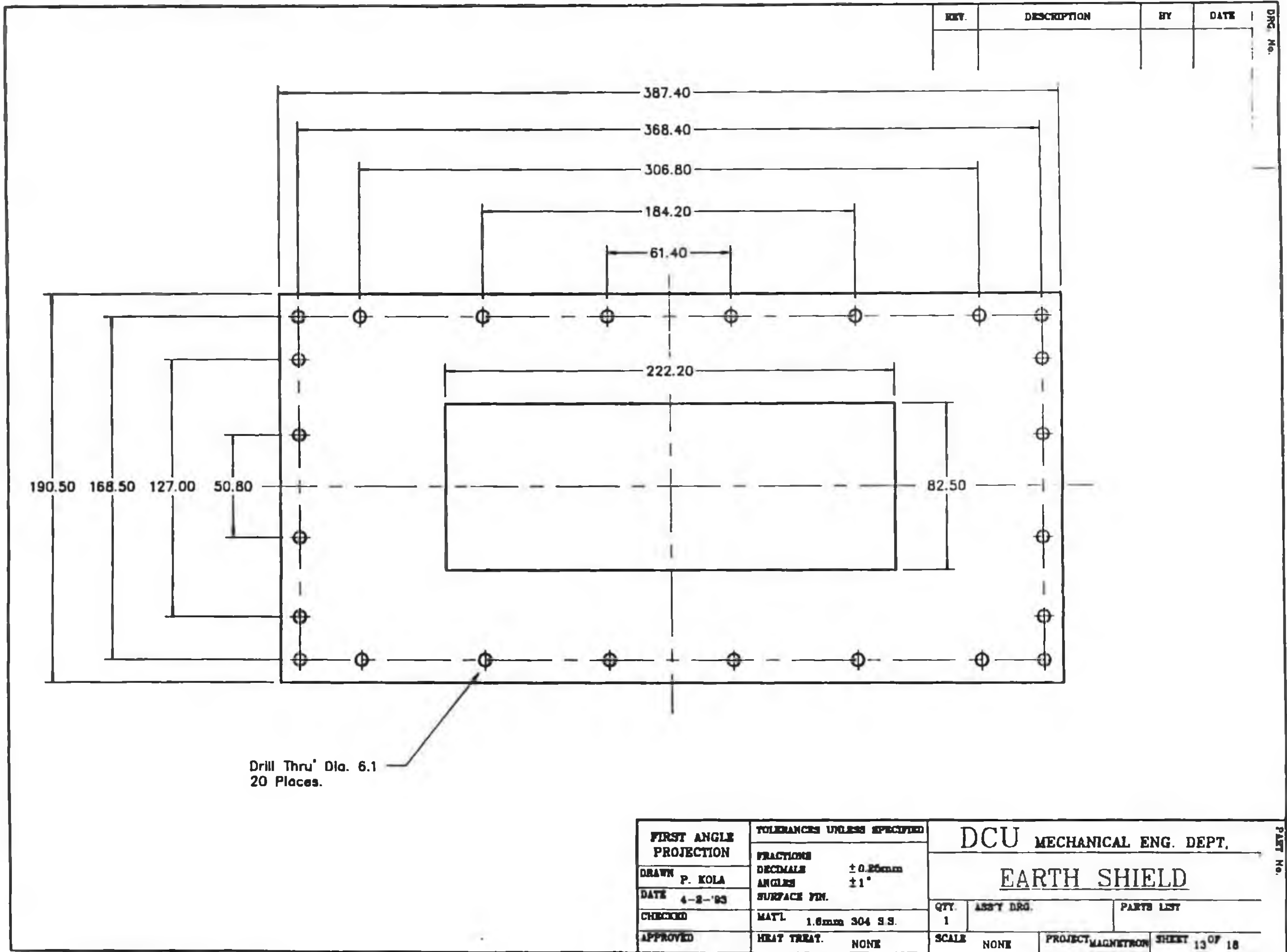

A20

| REV. | DESCRIPTION | BY | DATE | DRG. No. |
|---|---|---|---|---|
| | | | | |

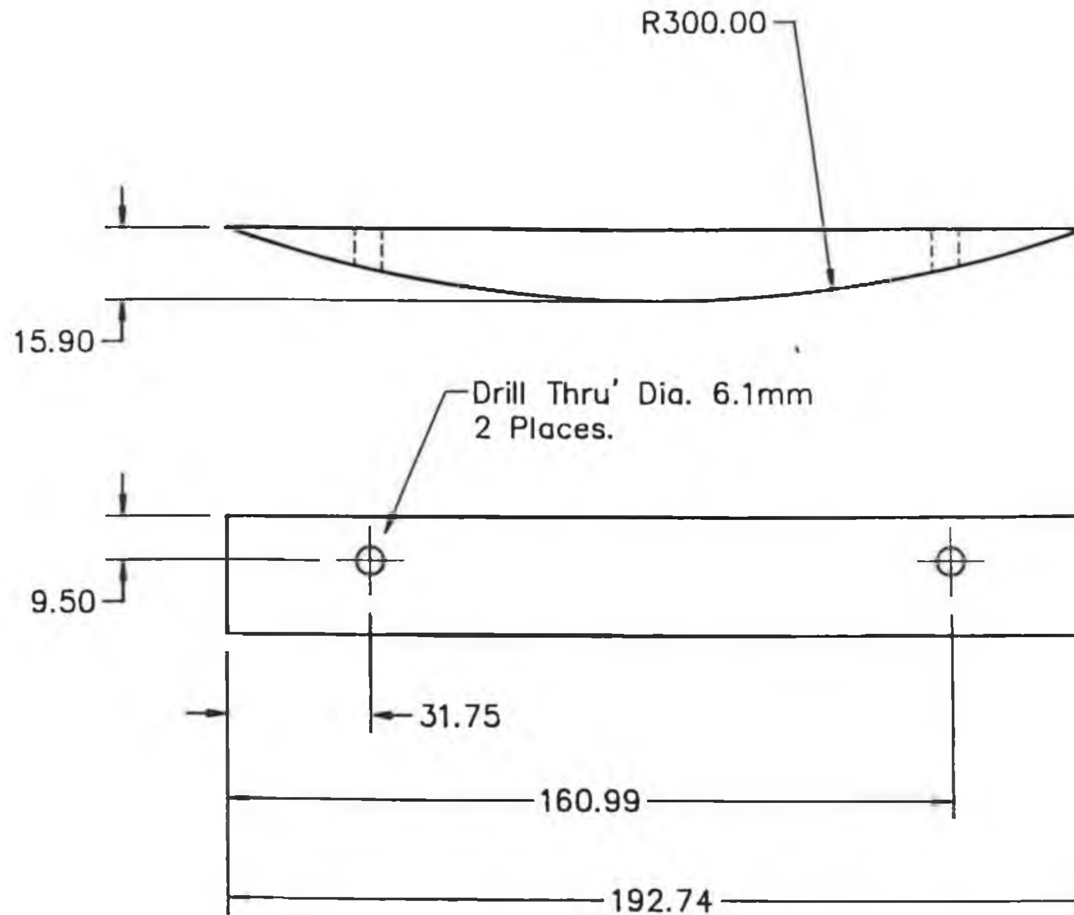


| FIRST ANGLE PROJECTION | TOLERANCES UNLESS SPECIFIED | DCU MECHANICAL ENG. DEPT. | | | PART No. |
|---|---|---|---|---|---|
| DRAWN P. KOLA | FRACTIONS<br>DECIMALS ±0.1mm<br>ANGLES ±1° | EARTH SHIELD SPACER 'A' | | | |
| DATE 4-8-'93 | SURFACE FIN. | QTY. 1 | ASS'Y DRG. | PARTS LIST | |
| CHECKED | MAT'L 304 STAINLESS STEEL | | | | |
| APPROVED | HEAT TREAT. NONE | SCALE NONE | PROJECT MAGNETRON | SHEET 14 OF 18 | |

| REV. | DESCRIPTION | BY | DATE |
|---|---|---|---|
| | | | |

DRG. No.

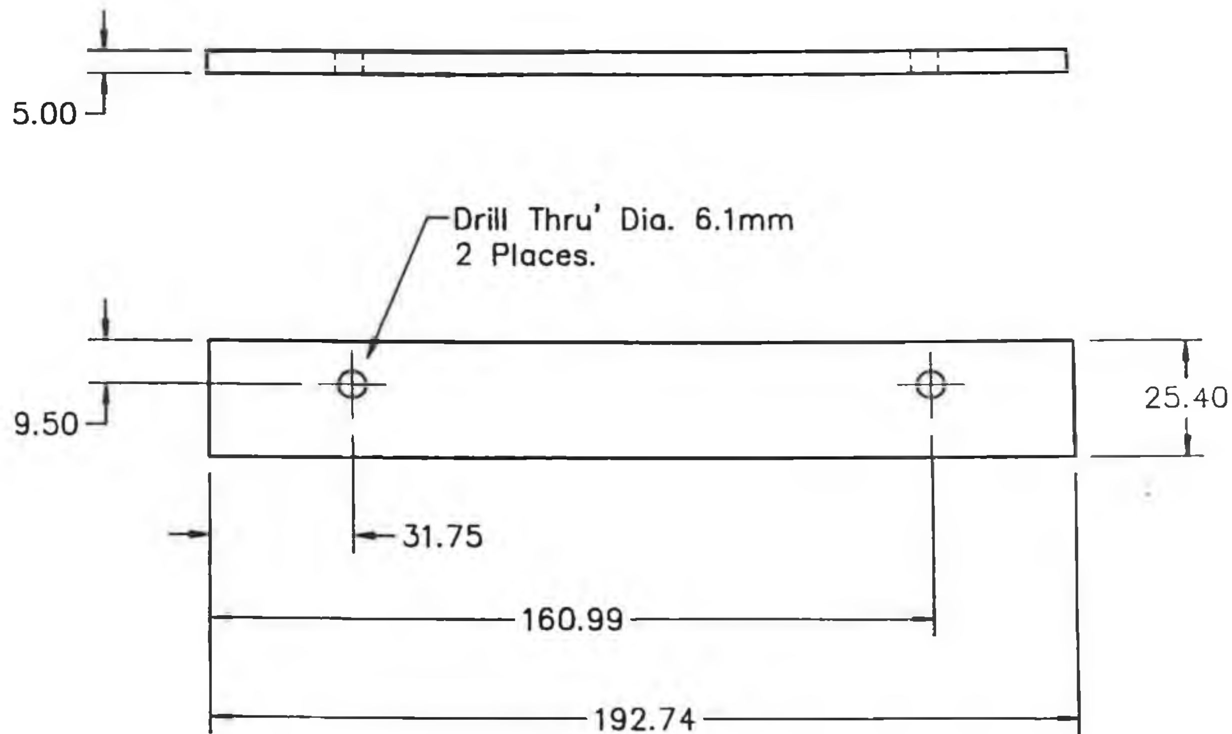


| FIRST ANGLE PROJECTION | TOLERANCES UNLESS SPECIFIED | DCU MECHANICAL ENG. DEPT. | | | PART No. |
|---|---|---|---|---|---|
| DRAWN P. KOLA | FRACTIONS | EARTH SHIELD SPACER 'B' | | | |
| DATE 4-2-'93 | DECIMALS ± 0.1mm<br>ANGLES ±1°<br>SURFACE FIN. | QTY. 1 | ASS'Y DRG. | PARTS LIST | |
| CHECKED | MAT'L 304 STAINLESS STEEL | | | | |
| APPROVED | HEAT TREAT. NONE | SCALE NONE | PROJECT MAGNETRON | SHEET 15 OF 18 | |

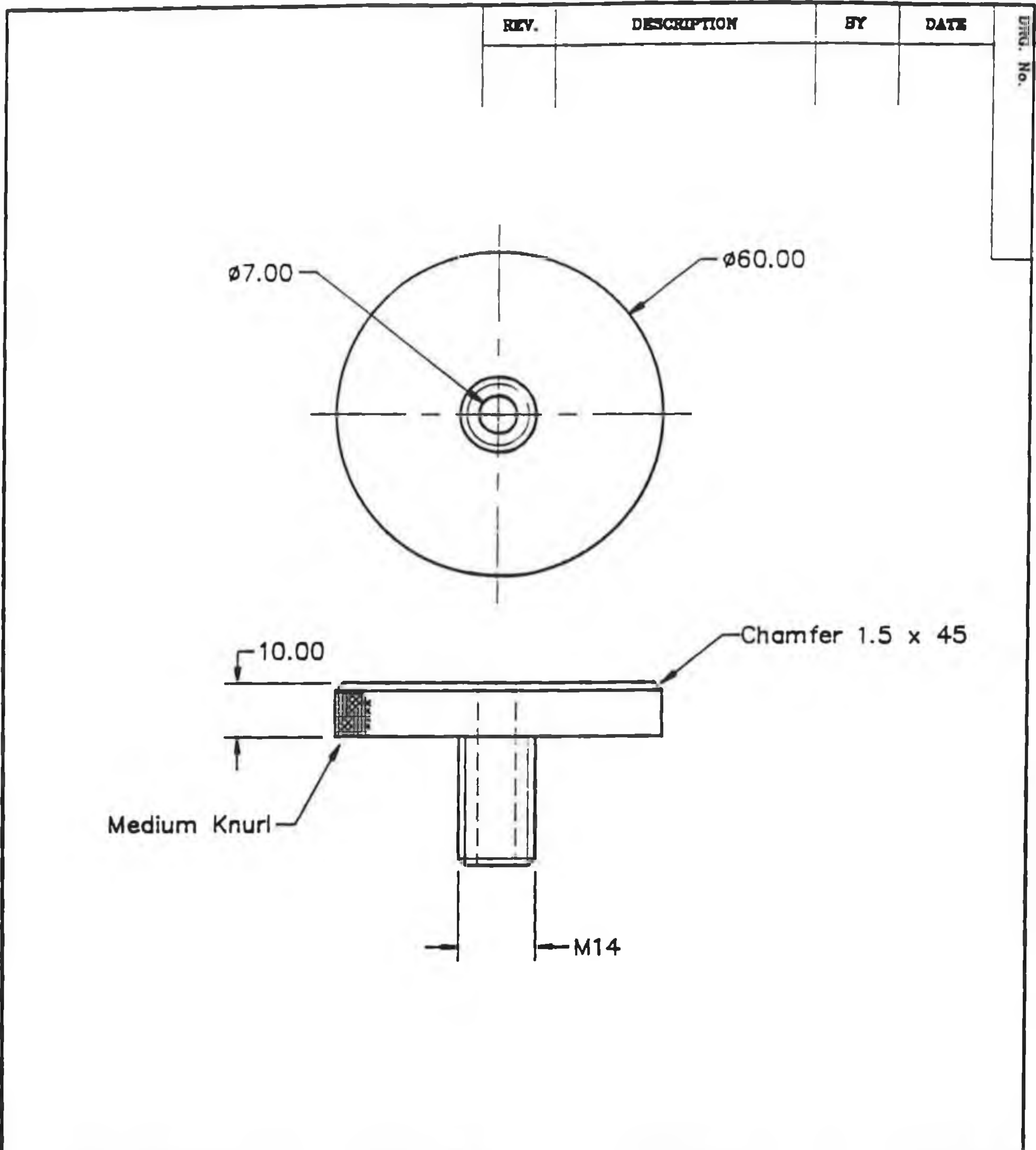


FIRST ANGLE PROJECTION

DRAWN P. Kola

DATE 3-3-'93

CHECKED

APPROVED

TOLERANCES UNLESS SPECIFIED

FRACTIONS
DECIMALS ±0.05mm
ANGLES ±1°
SURFACE FIN. 6.3

MAT'L 304 Stainless Steel

HEAT TREAT. NONE

DCU MECHANICAL ENG. DEPT.

WILSON BOLT

QTY. 20 | ASS'Y DRG. | PARTS LIST

SCALE NONE | PROJECT Magnetron | SHEET 18 OF 18

PART No.

| REV. | DESCRIPTION | BY | DATE |
|---|---|---|---|
| | | | |

DRG. No.

Drill Thru' Dia. 5.4mm
C'bore Dia. 9.0mm
6.0mm Deep
8 Places
42.7mm P.C.D.

ø63.50

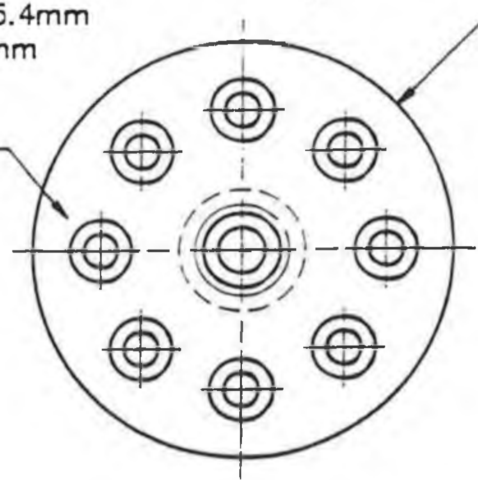

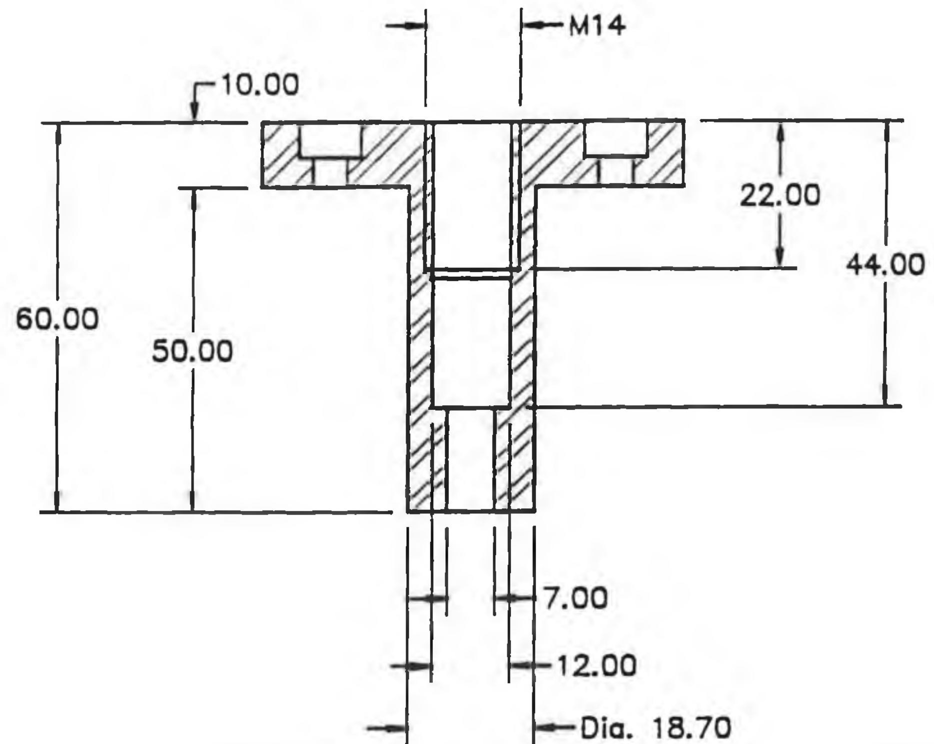


| FIRST ANGLE PROJECTION | TOLERANCES UNLESS SPECIFIED | DCU MECHANICAL ENG. DEPT. |
|---|---|---|
| DRAWN P. Kola | FRACTIONS<br>DECIMALS ±0.05mm<br>ANGLES ±1° | WILSON HOUSEING |
| DATE 3-3-'93 | SURFACE FIN. 6.3 | |
| CHECKED | MAT'L 304 Stainless Steel | QTY. 20 / ASS'Y DRG. / PARTS LIST |
| APPROVED | HEAT TREAT. NONE | SCALE NONE / PROJECT Magnetron / SHEET 17 OF 18 |

PART No.

| REV. | DESCRIPTION | BY | DATE |
|---|---|---|---|
| | | | |

DRG. No.

7.00

12.00

22.00

| FIRST ANGLE PROJECTION | TOLERANCES UNLESS SPECIFIED | DCU MECHANICAL ENG. DEPT. | | | |
|---|---|---|---|---|---|
| DRAWN P. Kola | FRACTIONS<br>DECIMALS ±0.05mm<br>ANGLES ±1°<br>SURFACE FIN. 6.3 | WILSON SPACER | | | |
| DATE 3-3-'93 | | QTY. 20 | ASS'Y DRG. | PARTS LIST | |
| CHECKED | MAT'L 304 Stainless Steel | | | | |
| APPROVED | HEAT TREAT. NONE | SCALE NONE | PROJECT Magnetron | SHEET 18 OF 18 | |

PART No.

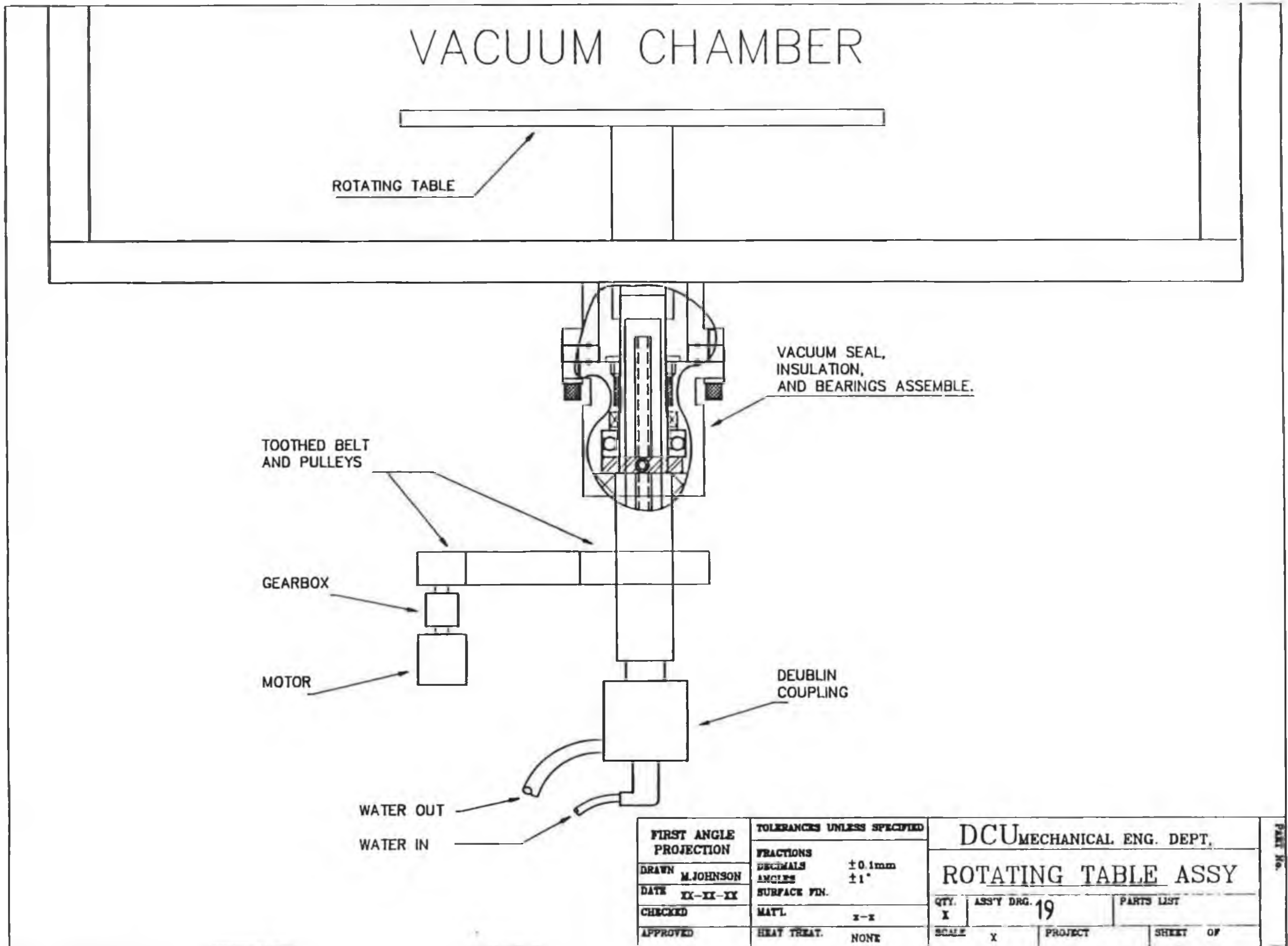
VACUUM CHAMBER
ROTATING TABLE
VACUUM SEAL,
INSULATION,
AND BEARINGS ASSEMBLE.
TOOTHED BELT
AND PULLEYS
GEARBOX
MOTOR
DEUBLIN
COUPLING
WATER OUT
WATER IN
FIRST ANGLE PROJECTION
DRAWN M.JOHNSON
DATE XX-XX-XX
CHECKED
APPROVED
TOLERANCES UNLESS SPECIFIED
FRACTIONS
DECIMALS ±0.1mm
ANGLES ±1°
SURFACE FIN.
MAT'L x-x
HEAT TREAT. NONE
DCU MECHANICAL ENG. DEPT.
ROTATING TABLE ASSY
QTY. X
ASS'Y DRG. 19
PARTS LIST
SCALE X
PROJECT
SHEET OF
PART No.

# Appendix C

# APPENDIX C

## C1 Operational and Safety Procedure

The operation of the magnetron sputtering system is outlined below, however, attention is drawn to the safety requirements for the preservation of both the operator and the system.

*Safety:*

1. Ensure that the required utilities (water, compressed air and ventilation are adequate for safe operation of the system, referring to the operational manuals of the equipment)

2. The diffusion pump attains a high temperature during normal operation - ensure that neither the operator nor any wires/tubing come in contact with the hot surface. Ensure that the water cooling to the diffusion pump is "on" prior to switching on the pump.

3. Ensure that the magnetrons are never touched during deposition, as this can result in a serious electrical shock. Also, ensure that the water cooling to the magnetrons is switched on prior to deposition.

4. Ensure that the ventilation is adequate to remove any fumes from the pumps and also to prevent asphyxiation from the deposition gases.

5. Ensure that proper care is taken in the use of solvents during cleaning of the samples. The use of gloves, mask and safety spectacles is recommended. Note that these solvents (1,1,1 trichloroethane, acetone, methanol and propanol) are all highly flammable.

6. The usual care should be exercised in the operation of high voltage power supplies.

*Operation:*

The procedure for "*starting up*" the rig is outlined below.

**1.** Switch on the water cooling to the *Diffusion Pump*, ensuring that the water pressure booster pump is also on. Plug in all appliances. Check compressed air levels.

**2.** Turn on the *Rotary Pump* (for rough vacuum). When the pressure on gauge 2 (Pirani) on the backing line is approximately 3x $10^{-2}$ mbar, open the *Backing Valve*. Once the pressure on gauge 2 has fallen below 3 x $10^{-2}$ mbar, turn on *Diffusion Pump*, and let it warm up for 40 minutes.

**3.** Once the *Diffusion Pump* is warmed up, the system is ready for evacuation. If the chamber is at atmospheric pressure (gauge 3, the Penning gauge should read 2 x $10^{3}$ mbar), a sample can be loaded into the chamber, and after closing the air inlet valve, the chamber is evacuated thus: The *Backing Valve* is closed, and the *Roughing Valve* is opened. When the pressure on gauge 1 (Pirani gauge) is below 3 x $10^{-1}$ mbar, the *Roughing Valve* is closed and the *Backing Valve* is opened. The *High Vacuum Valve* is then opened. The chamber is now evacuating. Check that the pressure reading on gauge 3 (Penning gauge) is falling, and deposition can commence once a suitable base pressure has been attained.

**4.** Deposition is undertaken by admitting the inert gas (e.g. Argon) through the mass flow meter and energising the magnetron (after checking that the water cooling has been switched on). The addition of reactive gas by use of the mass flow controller or another mass flow meter can also be achieved if compound coatings are desired (e.g. TiN). After the deposition sequence, the magnetrons and gases are switched off, and the chamber is isolated by closing the *High Vacuum Valve*. The system is now in the same status as when "*warming up*". The air inlet valve is opened, and the sample is taken out of the chamber by lifting off the chamber assembly. Another sample can be loaded or the system closed up, the air inlet valve closed, and the system evacuated as outlined above.

Occasionally, the system may need to be "*powered down*" for maintenance etc.

1. Close the *High Vacuum Valve* to isolate the chamber. Turn off the *Diffusion Pump*, and let cool for 40 minutes. The *Backing Valve* and *Rotary Pump* can be switched off once the *Diffusion Pump* is cool. Switch off all cooling water, gases, and plug out all appliances.

***Note:*** It is usual in vacuum operations to allow the chamber to evacuate continuously, even whilst no deposition is taking place. This ensures a clean chamber environment in which to conduct experiments.

# References

## REFERENCES:


[1] S. Zhang and W. Zhu, J. Mat. Proc. Tech., Vol.39, No.1-2, (1993), 165.

[2] T. Bell, Suface Engineering, Vol. 6, No. 1, (1990), 31.

[3] R.F. Bunshah et al, *Deposition Technologies for Films and Coatings*, Noyes Publications, Park Ridge, NJ, (1982).

[4] J.L. Vossen and W. Kern (eds.), *Thin Film Processes*, Academic Press, London, (1978).

[5] K.K. Schuegraf (ed.), *Handbook of Thin Film Deposition Processes & Technologies*, Noyes Publications, New Jersey, (1988).

[6] W.R. Grove, Philos. Trans. Faraday Soc., 87, (1852).

[7] B. Berghaus, *Improvements in and Relating to the Coating of Articles by Means of Thermally Vaporized Material*, Br. Patent 510, 933, August 26, 1937.

[8] D.M. Mattox, Electrochem Tech., 2, (1964), 295.

[9] B. Bhushan and B.K. Gupta, *Handbook of Tribology, Materials, Coatings and Surface Treatments* , McGraw-Hill, (1991).

[10] R. Barrell and D.S. Rickerby, Met. Mater., (1989), 468.

[11] J.B. Almedie, Vacuum, Vol 39, No. 7/8, (1989), 717.

[12] S. M. Rossnagel, J. Vac. Sci. Technol., A6(6), (1988), 3049.

[13] R. Adachi and K. Takeshita, J. Vac. Sci. Technol., 20, (1982), 98.

[14] J.J. Cuomo and S.M. Rossnagel, J.Vac. Sci. Technol., A4, (1986), 393.

[15] T. Hata, E. Noda, O. Marimoto and T. Hada, Appl. Phys. Lett.,37, (1980), 633.

[16] B. Window and N. Savvides, J. Vac. Sci. Technol., A4, (1986), 196.

[17] A.G. Spencer, K. Oka, R.W. Lewin, and R.P. Howson, Vacuum, 38, (1988), 857.

[18] T. Fukami, F. Shintani, and M. Naoe, Thin Solid Films, 149, (1987), 373.

[19] S. Kadlec, J.Musil, Research Report, Institute of Physics, CSAS, No. 055/88, Nov (1988).

[20] J. Vyskočil, J. Musil, S. Kadlec, and W.D. Münz, in E. Brozeit et al (eds.), Plasma Surface Engineering, DGM Informations Gesellschaft, Oberasel, Vol.1, (1989), 661.

[21] S. Kadlec, J. Musil, W. D. Munz, G. Hakanson and J.E. Sundgren, Surface and Coatings Technology, 39/40, (1989), 487.

[22] W.D. Munz, Surface and Coatings Technology, 48, (1991), 81.

[23] J. Musil, S. Kadlec, J. Vyskočil, and V. Poulek, Surface and Coatings Technology, 39/40, (1989), 301.

[24] J.R. Doyle, A. Nuruddin, J.R. Abelson, J. Avc. Sci. & Technol., Vol 12, No. 3, (1994), 886.

[25] F. Elstner, A. Ehrlich, H. Giegengack, H. Kupfer, F. Richter, J. Vac. Sci. & Technol., Vol 12, No. 3, (1994), 886.

[26] S.L. Rohde, A. J. Nelson, A. Mason, W.D. Sproul, J. Vac. Sci. Technol., A10(4), (1992), 1797.

[27] S.R. Yoo, W.U. Oh, J.S. Choi, S.H. Paek, D.S. Shin, J.E. Oh, Y.N. Kim, T.E. Shim, J.G. Lee, Journal of the Korean Institute, Vol. 29A(8), (1992), 49.

[28] B.A. Movchan and A.V. Demchishin, Fiz. Met. Metalloved, 28, (1969), 653.

[29] J.A. Thornton, Ann. Rev. Mater. Sci., 7, (1977), 239.

[30] R. Meissier, A.P. Giri, R.A. Roy, T. Vac. Sci. Technol., A2, (1984), 500.

[31] A.G. Dirks and H.J. Leamy, Thin Solid Films, 47, (1977), 219.

[32] D. Henderson, M.H. Brodsky, P. Chaudhari, Appl. Phys. Lett., 25, (1974), 641.

[33] K.H. Müller, Surface Science, 184, (1987), L375.

[34] J. Michalski and T. Wierzchoń, Materials Science and Engineering, A140, (1991), 499.

[35] D. Y. Jouan, G. Lemperiere, Thin Solid Films, Vol. 237, No. 1-2, (1994), 200.

[36] D. Maheo, J-M. Poitevin, Thin Solid Films, Vol. 237, No. 1-2, (1994), 78.

[37] G. Paller, B. Matthes, W. Herr, E. Broszeit, Materials Science and Engineering, A140, (1991), 647.

[38] F. Richter, H. Kupfer, H. Gigengack, G. Schaarschmidt, F. Scholz, F. Elstner, G. Hecht, Surface and Coatings Technol., 54/55, (1992), 338.

[39] D.S. Rickerby, J. Vac. Sci. Technol., A4, (1986), 2809.

[40] D.S. Rickerby, A.M. Jones, A.J. Perry, Surface and Coatings Technology, 36, (1988), 631.

[41] D.S. Rickerby, G. Eckold, K.T. Scolt, and I.M. Buckley-Golder, Thin Solid Films, 154, (1987), 125.

[42] D.S. Rickerby, A.M. Jones, and B.A. Bellamy, Surf. Coat. Technol, 37, (1989), 111.

[43] V. Valvode, R. Cerny, R. Kuzel, J. Musil, V. Poulek, Thin Solid Films, 158, (1988), 225.

[44] D.P. Upton, Trans. of the Inst. of Metal Finishing, (Nov. 1990), Vol. 68, No. 4, 118.

[45] D.S. Rickerby and P.J. Burnett, Thin Solid Films, 157, (1988), 195.

[46] M. Benmalek, P. Gimenez, J.P. Peyre and C. Tournier, Surface and Coatings Technology, 48, (1991), 181.

[47] T. Spalvins, J.S. Przybyszewski, D.H. Buckley, NASA TND-3707, (1966).

[48] S.J. Bull, A.M. Jones, A.R. McCabe, Surface and Coatings Technology, 54/55, (1992), 173.

[49] I. Petrov, L. Hultman, J-E. Sundgren. J.E. Greene. J. Vac. Sci. Technol., A10(2), (1992), 265.

[50] D.G. Teer and R.D. Arnell, *Recent Developments in Surface Coating and Modification Processes*, Organised by Prof. J. Hallig, Seminar at IMechE, 10th Oct. 1985, 21.

[51] G.A. Clarke, N.R. Osbourne, R.R. Parsons, J. Vac. Sci. Technol., (1991), 1166.

[52] C.C. Cheng, A. Erdemir, and G.R. Fenske, Surface and Coatings Technol., 39/40, (1989), 366.

[53] J.A. Thornton in R.F. Bunshah (ed), *Deposition Technologies for Films and Coatings*, Noyes Publications, Park Ridge, NJ, (1982), 231.

[54] Y-I. Chen, J-G. Duh, Surface and Coatings Technology, 46, (1991), 371.

[55] J. Valli, U. Makela, A. Matthews and V. Murawa, J. Vac. Sci. Technol., A3, (1985), 2411.

[56] V. Helmersson, B.O. Johansson, J.E. Sundgren, H.T.G. Hentzell and P. Billgren, J. Vac. Sci. Technol., A3, (1985), 308.

[57] M. Van Strappen, B. Malliet, L. De Schepper, L.M. Stals, J.P. Celis and J. Roos, 7th IPAT Meeting, Geneva, Ed. CEP Consultants, Edinburgh, (1989), 209.

[58] D.S. Rickerby and S.J. Bull, Surface and Coatings Technol., 39/40, (1989), 315.

[59] D.M. Mattox and G.J, Kominiat, J.Vac. Sci. Technol, A2, (1984), 500.

[60] U. Helmersson, J.E. Sundgren and J.E. Greene, J. Vac. Sci. Technol, 4, (1986), 500.

[61] A.J. Perry, M. Jagner, W.D. Sproul, P.J. Rudnik, Surface and Coatings Technology, 39/40, (1989), 387.

[62] D.M. Turley, Surface and Coatings Technol., 39/40, (1989), 135.

[63] W.D. Sproul. P. J. Rudnik, C.A. Gogol, Research and Development, (Nov. 1989), 79.

[64] S.L. Rohde, W.D. Sproul, J.R. Rohde, J. Vac. Sci. Technol., A9(3), (1991), 1178.

[65] R.D. Arnell, Surface and Coatings Technology, 59, (1993), 105.

[66] M.J. Ahern, *Surface Engineering Through Low Temperature Deposition of Wear Resistant Layers by Reactive Magnetron Sputter Ion Plating*, MEng Thesis, (1991).

[67] B. Jönsson and S. Hogmark, Thin Solid Films, 114, (1984), 257.

[68] Metals Handbook, Vol. II, *Nondestructive Inspection and Quality Control*, 8th edition, The American Society for Metals, (1976).

[69] W.H. Steel, *Interferometry*, 2nd. edition, Cambridge University Press, (1983).

[70] H.P. Lorenz, C. Schuler, *Hard Layer Coatings - Electrochemical Characterization*, Siemens AG, (1987).

[71] A. Tvarusko, H.E. Hinterman, Surface Technology, 9, (1979), 209.

[72] J.P. McCloskey, J. Electrochem. Soc., Vol 114, 6, (1967), 643.

[73] H.R. Miller, E.B. Friedl, Plating, Vol 47, (1960), 520.

[74] H.G. Tompkins, *A Users Guide to Ellipsometry*, Academic Press Inc., San Diego, (1993).

[75] K. Riedling, *Ellipsometry for Industrial Application*, Springer-Verlag Wien, New York, (1988).

[76] N.B. Colthup, L.H. Daly, S.E. Wiberly, *Intoduction to IR and Raman Specctroscopy*, Academic Press, San Diego, (1990).

[77] H.P. Klug. L.E. Alexander, *X-Ray Diffraction Procedures*, John Wiley & Sons, New York, (1954).

[78] M. Prutton, *Surface Physics*, Oxford University Press, (1983).

[79] I.A. Blech, H.A. Vanderplas, J. Appl. Phys., 54, (1982), 3489.

[80] J.A. Thornton, Surface Engineering, Vol. 2, No. 4, (1986), 283.

[81] H-J. Spies, K. Hoeck, E. Broszeit, B. Matthes, W. Herr, Surface and Coatings Technology, 60, (1993), 441.

[82] Zhang Shi Xing, Proc. Int. Conf. on Plasma Sci. and Tech., June 4-7, 1986, Beijing, China, Published by Science Press and VCH, (1986).

[83] N. Yasumaru, K.Tsuchida, E. Saji, T. Ibe, Materials Transactions, JIM, 34(8), (1993), 696.

[84] A. Matthews and H.D. Sundquist in T. Tagaki (ed), Proc. Int. Ion Engineering Congress, ISIDT '83, Kyoto, Japan, Sept. 1983, IEEE (Japan), Tokyo, (1983), 1325.

[85] B. Zhu, Y.Wang, G. Bai and Y. Qi, European Engineering Research and Technology Transfer Congress, Session 6 ( Metals), Materials and Processes, publ. IMechE, Eurotech Direct '91.

[86] A. Neckel, *The Physics and Chemistry of Carbides, Nitrides and Borides*, ed. R. Freer, Kluwer Academic, N.Y. , (1990), 485.

[87] J.E. Sundgren, B. O. Johansson, A. Rockett, S.A. Barnett, J.E. Greene, in *Physics and Chemistry of Protective Coatings*, edited by W.D. Sproul, J.E. Greene, J.A. Thornton, American Institute of Physics Conference Proceedings No. 149, New York, (1986), 95.

[88] H.A. Jehn, International Journal of Materials and Production Technology, Vol. 8(2-4), (1993), 170.

[89] H.M. Gabriel in T. Tagaki (ed), Proc. Int. Ion Engineering Congress, ISIDT '83, Kyoto, Japan, Sept. 1983, IEEE (Japan), Tokyo, (1983), 1311.

[90] M. Kobayashi and Y. Doi, Thin Solid Films, 54, (1978), 67.

[91] J.E. Sundgren and H.T.G. Hentzell, J. Vac. Sci. Tech., A4, (1986), 2259.

[92] P.J. Burnett and D.S. Rickerby, Surface Engineering, 3, (1987), 69.

[93] J. Stansilav, J. Sikac, M. Cermak, Thin Solid Films, 1991, (1991), 255.

[94] M.E. O'Hern, R. H. Parrish, W.C. Oliver, Thin Solid Films, 181, (1989), 357.

[95] U. Beck, G. Reiners, U. Kopacz, H.A. Jehn, Surface and Coatings Technology, 60, (1993), 389.

[96] R. Manory, Surface Engineering, Vol.3, No.3, (1987), 233.

[97] J. Chevallier, J.P. Chabert and J. Spitz, Proc. Int. Conf. IPAT '81, Amsterdam, 1981, CEP Consultants, Comptes Rendus DMG 21/81, Centre d'Étude Nucléaire, Grenoble, (1981).

[98] R. Avni, and T. Spalvins, NASA Tm-83798, National Aeronautics and Space Administration, Cleveland, Ohio, U.S.A., (1984).

[99] Yoshihito Matsumura, Proc. 30th Japan Congress on Matls. Res., Sept. (1986), Kyoto, Japan, 213.

[100] U. Beck, G. Reiners, I. Urban, K. Witt, Thin Solid Films, 220, (1992), 234.

[101] P.M. Marquis, *New Implant Materials*, Eurotech Direct'91, (1991), C412/071.

[102] E. Lugscheider, Th. Weber, M. Knepper and F. Vizethum, Mater. Sci. and Engineering, A139, (1991), 45.

[103] J.A. Jansen, J.G.C. Wolke, S. Swann, J.P.C.M. van der Waerden, K. de Groot, The *Applications of Magnetron Sputtering for Producing Ceramic Coatings on Implant Materials*, The 17th Annual Meeting of the Soc. for Biomater., May 1991, Scottsdale, Arizona, U.S.A.

[104] C. Sella, J.C. Martin, J. Lecoeur, A. Le Chanu, M.F. Harmand, A. Naji, J.P. Davidas, Mater. Sci. and Engineering, A139, (1991), 49.

[105] S.F. Hulbert, J.R. Matthews, J.J. Klawitter, B.M. Saller, R.B. Leonard, J. Biomed. Mater. Res. Symposium, No.5, Part 1, (1974), 85.

[106] P. Griss, B. Krempien, H.F. von Andrian-Werburg, G. Heimke, R. Fleiner, T. Diehm, J. Biomed. Mater. Res. Symposium, No.5, Part 1, (1974), 39.

[107] H. Hildebrand, M. Champs, *Biocompatibility of Co-Cr-Ni Alloys*, Plenum, New York, (1989).

[108] S.F. Hulbert, *Materials of Construction for Surgical Implants*, Paper presented at the Annual Joint Meeting of the South Carolina Chapter of the American Soc. of Civil Engineers, Columbia, S.C., Jan 12, (1968).

[109] S.C. Woodward, *Plastics in Surgical Implants ASTM STP 386*, Symposium presented by Committee F-4 on Surgical Implant Materials, Indianapolis, Ind., (1964).

[110] C.P.A.T. Klein, K.de Groot, and A.A. Driessen, Biodegradation of Calcium Phosphate Ceramics, in P. Vincenzini (ed.), *Ceramics in Surgery*, Elsevier, Amsterdam, (1983), 105.

[111] F.H. Lin, M.H. Hon, J. Med. Eng., ROC, (1985), 5, 33

[112] F.H. Lin, M.H. Hon, J. Mater. Sci. Letters, (1987), 5, 33.

[113] R. Shirandami, I.I. East, J. Biomed. Eng., (1990), Vol. 13, 19.

[114] F.H. Lin, Y.Y. Huang, M.H. Hon, S.C. Wu, J. Biomed. Eng., (1991), Vol 13.

[115] B.J. Tighe, S.J. Holland, Eurotech Direct '91, C412/069.

[116] J.J. Klawitter, S.F. Hulbert, J. Biomed. Mater. Res. Symposium, No.2, Part1, (1971), 161.

[117] J. Narayan, W.D. Fan, R.J. Naryan, P. Tiwari, H.H. Stademaier, Materials Science and Engineering, B25, (1994), 5.

[118] The 1983 Adam Thompson Lecture, *The Role of Biomaterials in the Applications of Artificial Organs*, by H. Klinkmann, Biomaterials in Artificial Organs, Paul, Gaylor, Courtney and Gilchrist (eds.), Proceedings of a Seminar on Biomaterials held at the University of Strathclyde, Glasgow, Sept. 1983.

[119] A. Wisby, P.J. Gregson, M. Tuke, Biomaterials, (1987), Vol 8, Nov., 477.

[120] Y. Mitamuo, T. Mikami, T. Yuton, et al, Development of a Fine Ceramic Heart Valve for use as a Cardiac Prosthesis, Trans. Am. Soc. Artif. Intern. Organs, 32, (1986), 444-448.

[121] O. Knotek, F. Löffler, K. Weitkamp, Surface and Coatings Technology, 54/55, (1992), 536.

[122] I. Dion, C. Baquey, B. Candelon, J.R. Montes, Intnl. J. Artificial Organs, Vol 15, No.10, (1992), 617.

[123] H. Berhandt, A. Lunk, Mater. Sci. and Engineering, A139, (1991), 58.

[124] H. Brauner, Surface and Coatings Technology, 62, (1993), 618.

[125] K. Buth, Gold-Coloured Titanium Nitride Coating of Nonprecious Metal Adhesive Bridge, Dent. Labor. (German), Vol. 39 (4), (1991), 491-492.

[126] P.R. Mezger, N.H.J. Creugers, J. Dent., 1992, Vol 20, 6, 342.

[127] L.L. Hench, E.C. Ethridge, *Biomaterials - An Interfacial Approach*, Biophysics and Bioengineering Series, Vol 4, Acedemic Press, (1982), 18.

[128] Y. Massiani, A. Medjahed, J.P. Crousier, P. Gravier and I. Rebatel, Surface and Coatings Technol., 45, (1991), 115.

[129] J.A. Thornton, Surface Engineering, Vol 2, No.4, (1986), 283.

[130] A.Y. Liu and M.L. Cohen, Science, 245, (1989), 841.

[131] A.Y. Liu and M.L. Cohen, Phys. Rev., B41, (1990), 10727.

[132] M.Y. Chen, X. Lin, V.P. Dravid, Y.W. Chung, M.S. Wong and W.D. Sproul, Surface and Coatings Technology, 54/55, (1992), 360.

[133] M.Y. Chen, D. Li, X. Lin, V.P. Dravid, Y.W. Chung, M.S. Wong and W.D. Sproul, J. Vac. Sci. Technol., A11(3), (1993), 521.

[134] J.J. Cuomo, P.A. Leary, D. Yu, W. Reuter and M. Frish, J. Vac. Sci. Technol., 16, (1976), 299.

[135] C.J. Torng, J.M. Siversten, J.H. Judy and C. Chang, J. Mater. Res., 5, (1990), 2490.

[136] N.H. Cho, D.K. Veirs, J.W. Ager III, M.D. Rubin, C.B. Hopper and D.B. Bogy, J. Appl. Phys., 71(5), (1992), 2243.

[137] N.H. Cho, K.M. Krishnan, D.K. Veirs, M.D. Rubin, C.B. Hopper, B. Bhushan and D.B. Bogy, J. Mater. Res., 5(11), (1990), 2543.

[138] T.A. Yeh, C.L. Lin, J.M. Siversten, J.H. Judy, IEEE Trans. Magn., MAG-27, (1991), 5163.

[139] F. Rossi, B. Andre, A. van Veers, P.E. Mijnarends, H. Schut, F. Labohm, H. Dunlop, M.P. Delplancke and K. Hubbard, *Physical properties of a-C:N films produced by ion beam assisted deposition*, submitted for publication.

[140] C. Niu, Y.Z. Lu and C.M. Lieber, Science, 261, (1993), 334.

[141] J.Seth, R. Padiyath, S.V. Babu, Diamond and Related Materials, 3, (1994), 210.

[142] Y. Lifshitz, G.D. Lempert, S. Rotter, I. Avigal, C. Uzan-Saguy, R. Kalish, J. Kulik, D. Marton and J.W. Rabalais, Diamond and Related Materials, 3, (1994), 542.

[143] D. Marton, A.H. Al-Bayati, S.S. Todorov, K.J. Boyd, J.W. Rabalais, Nucl. Instrum. Methods Phys. Res., B90, (1994), 277.

[144] J.F.D. Chubaci, T. Sakai, T. Yamamoto, K. Ogata, A. Ebe, and F. Fujimoto, Nuclear Instruments and Methods in Physics Research, Section B, 80(1), (1993), 463.

[145] M. Ricci, M. Trinquecoste, F. Auguste, R. Canet, P. Delhaes, C. Guimon, G. Pfister-Guillouzo, B. Nysten and J.P. Issi, J. Mater. Res., 8(3), (1993), 480.

[146] M. Iwaki, K. Takahashi, A. Sekiguchi, J. Mater. Res., 5, (1990), 2562.

[147] M.J. Kenny, J.T.A. Pollock, L.S. Wielunski, Nucl. Instrum. Methods Phys. Res., B39, (1989), 704.

[148] Y. Inoue, Y. Satou, K. Tanaka, Adv. Info. Storage System, 4, (1992), 263.

[149] Z.J. Zhang, S. Fan and C.M. Lieber, App. Phys. Lett., 66(26), (1995), 3852.

[149] H. Sjöström, I. Ivanov, M. Johansson, L. Hultman, J-E Sundgren, S.V. Hainsworth, T.F. Page, L.R. Wallenberg, Thin Solid Films, 246, (1994), 103.

[150] H.X. Han and B.J. Feldman, Solid State Commun., 65, (1988), 921.

[151] N. Nakayama, Y. Tsuchiya, S. Tamada, K. Kosuge, S. Nagata, K. Takahiro, S. Yamaguchi, Jpn. J. Appl. Phys., 32, (1993), L1465.

[152] I. Sugai, M. Oyaizu, T. Hattori, K. Kawasaki, T. Yamo, H.M. Uto, T. Takahasi, K. Yamazaki, Nucl. Instrum. Methods. Phys. Res., A303, (1991), 59.

[153] K.M. Yu, M.L. Cohen, E.E. Haller, W.L. Hansen, A.Y. Liu, I.C. Wu, Physical Review, B49, 7, (1994), 5034.

[154] D. Li, Y.W. Chung, M.S. Wong, W.D. Sproul, J. Appl. Phys., 74(1), (1993), 219.

[155] J. Schwan, W. Dworschak, K. Jung, H. Ehrhardt, Diamond and Related Materials, 3, (1994), 1034.

[156] K. Donnelly, D.P. Dowling, E. Davitt, T.P. O'Brien and T.C. Kelly, in M.S.J.Hashmi (ed.), Proceedings of Advances in Materials and Processing Technologies, Dublin, August 23-27 1993, publ. Dublin City University Press, Vol 2, (1993), 769.

[157] G. Sreenivas, S.S. Ang, W.D. Brown, J. Electronic Materials, 23(6), (1994), 569.

[158] A. Grill, V. Patel, Diamond Films and Technology, Vol2(2-3), (1992), 61.

[159] A. Mansour, D. Ugolini, Physical Review, B(47), 16, (193), 10201.

[160] F.L. Friere Jr., G. Mariotto, C.A. Achete, D.F. Franceschini, *Amorphous Hydrogenated Carbon Nitride Films by Plasma-Enhanced Chemical Vapour Deposition*, presented at Plasma Surface Engineering 1994, Garmisch-Partenkirchen, Sept. 19th-23rd 1994, submitted for publication.

[161] G. Socrates, Infrared Characteristic Group Frequencies, Wiley Interscience, 1980.

[162] J.H. Kaufman, S. Metin and D.D. Saperstein, Phys. Rev, B39, (1989), 1053.

[163] S. Kumar, T.L. Tansley, Solid State Communications, 88(10), (1993), 803.

[164] J.A. Taylor, G.M. Lancaster, A. Ignatiev, J.W. Rabalais, J. Chem. Phys., 68, (1978), 1776.

[165] A. Hoffman, I. gouzman, R. Brener, Appl. Phys. Lett., 64(7), (1994), 845.

[166] D. Mendoza, J. Aguilar-Hernandez and G. Contreras-Puente, Solid State Commun., 84(11), (1992), 1025.

[167] R.J. Nemanich and S.A. Solin, Phys. Rev., 20(2), (1979), 392

[168] G.L. Doll, J.P. Heremans, T.A. Perry, J.V. Mantese, J. Mater. Res., 2(1), (1994).

[169] F. Tuinstra and J.L. Koenig, J. Chem. Phys., 53(3), (1970), 1126.

[170] B.N. Chapman, *Glow Discharge Processses: Sputtering & Plasma Etching*, John Wiley & Sons, New York, (1980).

[171] D. Li, S. Lopez, Y.W. Chung, M.S. Wong and W.D. Sproul, J. Vac. Sci. Tech., A13(3), (1995), 1063.

[172] *Encyclopedia of Inorganic Chemistry*, R. Bruce King (ed.), John Wiley and Sons, Vol. 5, (1994), 2505.

## Published Work

**PUBLISHED WORK:**

"*Magnetron Sputtering of TiN Protective Coatings for Biomedical Applications*". P.V. Kola, S. Daniels, D.C. Cameron and M.S.J. Hashmi, in M.S.J. Hashmi (ed.), Proc. Advances in Materials and Processing Technologies, Dublin, 23-27 August 1993, Vol 2, Dublin City University Press, (1993), 769, J. Mater. Proc. Technol. (in press).

"*Magnetron Sputtering of Carbon Nitride Films*", P.V. Kola, D.C. Cameron and M.S.J. Hashmi, Surface and Coatings Technology, 68/69, (1994), 188

"*Magnetron Sputtered Carbon Nitride Films*", P.V. Kola, D.C. Cameron, B.J. Meenan, K.A. Pischow, C.A. Anderson, N.M.D. Brown and M.S.J. Hashmi, presented as a *Keynote Address* at **Plasma Surface Engineering '94**, Garmisch-Partenkirchen, Germany, 20-23 September 1994, accepted for publication in Surface and Coatings Technology, pending publication Oct. 1995, Surface and Coatings Technology (in press).